Understanding Quaternary aeolian landscape-climate interaction in the piedmonts of Central Asia using luminescence and electron spin resonance techniques

Dissertation
zur Erlangung des Grades
„Doktor der Naturwissenschaften“
im Promotionsfach Geologie/Paläontologie

am Fachbereich Chemie, Pharmazie,
Geographie und Geowissenschaften
Johannes Gutenberg-Universität, Mainz

Aditi Krishna Dave
geb. in New Delhi, Indien

Johannes Gutenberg-Universität Mainz
angefertigt am Max-Planck-Institut für Chemie

Mainz, 2021

1. Berichterstatter: [redacted]
2. Berichterstatter: [redacted]

Tag der mündlichen Prüfung: 25.08.2021

Declaration

I hereby declare that I wrote the submitted dissertation without any unauthorized external assistance and used only sources acknowledged in the work. All textual passages which are appropriated verbatim or paraphrased from published and unpublished texts as well as all information obtained from oral sources are duly indicated and listed in accordance with bibliographical rules. In carrying out this research, I complied with the rules of standard scientific practice as formulated in the statutes of Johannes Gutenberg University Mainz to insure standard scientific practice.

Mainz, 15.07.2021

_____
(Aditi Krishna Dave)

Eidesstattliche Erklärung

Ich versichere hiermit die vorliegende Arbeit eigenständig und nur mit den angegebenen Hilfsmitteln und Quellen verfasst zu haben. Die Dissertation ist weder komplett noch in Teilen an einer anderen Universität oder Fakultät als wissenschaftliche Arbeit oder zu einer Prüfung vorgelegt worden.

Mainz, 15.07.2021

_____
(Aditi Krishna Dave)

To my constants,

MS^2

Thank you for living this with me.

&

To H…….for being his handsome self.

“I must confess that the more I have studied the subject, the more difficult I have found it to form a satisfactory theory”

C. Lyell, 1834

Observations on the loamy deposit called ‘loess’ of the basin of the Rhine
In ‘The Edinburgh New Philosophical Journal’, pp-120

But perhaps, I have learnt to raise the right questions…….

Abstract

Deposits of wind-blown dust, or loess, are excellent terrestrial archives of past climate change. These deposits form stacked sequences of primary loess and buried soils – commonly known as loess-palaeosol sequences - that are largely hypothesised to reflect colder, drier, more windy phases, and more humid, warmer, less windy periods, respectively. The extensive loess deposits that drape the piedmonts of the Asian high mountains in Arid Central Asia (ACA) are one of the major loess deposits in the world. They lie at the core of the Eurasian loess belt and, thus provide a key link between European and East Asian terrestrial paleoenvironmental records. The ACA loess deposits are influenced by, and therefore record the imprint of, two major drivers of the Northern hemisphere climate system: the mid-latitude Westerlies and the Siberian High. The location of the ACA loess thus makes these deposits invaluable for understanding the relationship between loess accumulation and climate. Yet, relatively little is known about the role of ACA in global climate dynamics past and present. Emerging datasets from Central Asian loess records suggest that (i) the prevailing assumptions linking increased loess accumulation with cold glacial conditions do not entirely hold for this region, (ii) the 'rate of accumulation' and the 'timing of accumulation peaks' in loess vary considerably between sites, (iii) we need to reassess the role of deserts as dust sources, as posited by early models for loess formation, and that (iv) we need to better understand the link between past wind regimes and dust transport pathways in the region.

This thesis aims to address these issues in two ways, by reconstructing the timing and provenance of loess deposits across ACA. In order to do so, this thesis explores different applications of trapped charge techniques of Luminescence and Electron Spin Resonance (ESR), namely as classical dating methods and as a provenance tool. These techniques are applied to two of the most ubiquitous mineral types found within loess, quartz and feldspar.

Firstly, this work addresses the question of how loess accumulation responds to climate in ACA. Towards this goal, luminescence dating of both quartz and feldspar is used to generate a high-resolution chronological framework for five new loess sites located along a c. 200 km transect of the understudied piedmonts in the Ili Basin of southeast Kazakhstan. Bayesian age modelling of the age-depth profiles is performed in order to optimise the precision of the datasets and to facilitate the calculation of mass accumulation rates (MARs) through time. The new chronology shows that loess accumulation along the piedmont spans the mid-Holocene to beyond the last interglacial, and reveals spatio-temporal inhomogeneity in loess accumulation. To understand the nature and possible drivers of this non-uniformity in sedimentation patterns, the spatial coverage of this investigation was extended by calculating MARs from published luminescence ages from 30 additional sites across the Ili basin, from neighbouring basins in ACA and from across the Chinese loess plateau. This synthesis

suggests that loess deposits represent a complex response to the interaction of local wind regimes, topography, sediment supply and availability, indicating that interpretations of loess packages as climate archives made hitherto are oversimplified and need to be reassessed. This thesis proposes that the response of loess MAR's can be viewed as a composite of two parameters: 'net accumulation' and 'timing of peaks in accumulation'. The net sedimentation rate at a given site responds both to local topographic context and sediment availability, and to climate. By contrast, the 'timing of peaks in accumulation' largely represents a response to large scale climate dynamics in a region only if derived from an aggregate dataset from multiple sites. An aggregate of MARs from multiple sites removes site-specific bias and provides a more robust tool for understanding past climate dynamics across a region.

Secondly, this thesis deals with the question of loess provenance. Identifying the source rock or location of loess-forming sediments, as well as changes in source through time, can provide insight into dust transport pathways, and consequently facilitate reconstruction of past atmospheric circulation in the region. Ultimately this also helps us to understand the processes of loess genesis, transport, and deposition. This thesis provides the first crucial step towards this goal by developing a new proxy for identifying the provenance of quartz. This new technique utilises the intensities of two paramagnetic centres in quartz, the natural E' and peroxy centres, that are measured using electron spin resonance (ESR). It is based on the premise that these centres arise from Schottky-Frenkel defect pairs, which increase with the age of the quartz-bearing host rock. Following experimental observations that confirm the physical basis of the method, this new approach was applied to a suite of 114 fine-grained loessic quartz samples from two sedimentary basins in Kazakhstan and Tajikistan respectively. Loess within the two basins are known to have different dust source regions and derive from source rocks of very different ages. The results yield a positive correlation between natural E' and peroxy intensities and demonstrate that quartz derived from older rocks (Kazakhstan) yields stronger signals than those sourced from younger rocks (Tajikistan), thus reaffirming the basis of the new method. This new provenance tool was then applied to successfully identify source changes down a long loess-palaeosol sequence in Tajikistan. The natural E'-peroxy centre provenance approach represents a simplified measurement protocol in comparison to other existing ESR-based techniques, is highly applicable to aeolian records, and holds great potential for application to other sedimentary systems.

The application of this new technique was extended further by combining it with an investigation of optically stimulated luminescence (OSL) and thermoluminescence (TL) characteristics of quartz. The intensity of E' defect centre in quartz represents a single defect, while luminescence sensitivity represents an aggregate of charge traps influenced both by the thermal history of the quartz-bearing source rocks and the sedimentary history of the grain. Variation in OSL and TL sensitivity of quartz down long loess-palaeosol sequences have been linked to climate-driven shifts in provenance. Nevertheless, the processes responsible for the observed variations in luminescence sensitivity of quartz, including its link to the

original rock source and/or its sedimentary history, remains a topic of contention. This thesis investigates both paired E'-peroxy intensities and luminescence sensitivity characteristics of quartz in parallel down a long loess sequence from southern Tajikistan, to gain a more nuanced insight into how these different trapped-charge indicators reflect source change through time. OSL and TL sensitivity of quartz within buried soil units (palaeosol) show a distinct increase compared to primary loess units. Using natural E' and peroxy intensities from quartz as an indicator of provenance, the observed increase in OSL and TL sensitivity of loessic quartz is attributed largely to repeated cycles of natural irradiation and bleaching, facilitated by low deposition rates during pedogenesis.

The applications and method development explored in this thesis have important implications not only for the study of Central Asian loess deposits, but also more generally for reconstructing past climatic changes from terrestrial sediment archives. The comprehensive assessment of the response of loess MAR's to climate, in context of geomorphic and topographic constraints, provides a more realistic framework for the interpretation of loess sites as land-based climate records. The development of a new proxy for the provenance of quartz using ESR opens exciting new avenues for application of this technique to other sedimentary systems.

d

Zusammenfassung

Ablagerungen von windverwehtem Staub, oder Löss, sind hervorragende terrestrische Archive vergangener Klimaänderungen. Diese Ablagerungen bilden geschichtete Sequenzen von primärem Löss und Bodenbildung - allgemein bekannt als Löss-Paläobodenabfolge -, von denen weitgehend angenommen wird, dass sie jeweils kältere, trockenere, windreichere Phasen bzw. feuchtere, wärmere, weniger windreiche Perioden widerspiegeln. Die ausgedehnten Lössablagerungen, welche die Piemonte des Asiatischen Hochgebirges in Arid Central Asia (ACA) bedecken, sind eine der größten Lössablagerungen der Welt. Sie liegen im Kern des eurasischen Lössgürtels und stellen somit eine wichtige Verbindung zwischen europäischen und ostasiatischen terrestrischen Paläoumweltarchiven dar. Die ACA-Lössablagerungen werden von zwei Haupttreibern des Klimasystems der nördlichen Hemisphäre beeinflusst und zeichnen daher ihre Spuren auf: die Westwinde der mittleren Breiten und das Sibirische Hoch. Die Lage des ACA-Lösses macht diese Ablagerungen daher von unschätzbarem Wert für das Verständnis der Beziehung zwischen Lössakkumulation und Klima. Dennoch ist relativ wenig über die Rolle von ACA in der globalen Klimadynamik der Vergangenheit und Gegenwart bekannt. Neue Datensätze aus zentralasiatischen Lössaufzeichnungen deuten darauf hin, dass (i) die vorherrschenden Annahmen, die eine erhöhte Lössakkumulation mit kalten glazialen Bedingungen in Verbindung bringen, für diese Region nicht vollständig zutreffen, (ii) die "Akkumulationsrate" und der "Zeitpunkt der Akkumulationsspitzen" im Löss zwischen den Standorten erheblich variieren, (iii) wir die Rolle von Wüsten als Staubquellen neu bewerten müssen, wie es frühe Modelle für die Lössbildung postulierten, und dass (iv) wir die Verbindung zwischen vergangenen Windregimen und Staubtransportwegen in der Region besser verstehen müssen.

Diese Arbeit zielt darauf ab, diese Fragen auf zweierlei Weise anzugehen, indem sie den Zeitpunkt und die Herkunft von Lössablagerungen über ACA rekonstruiert. Um dies zu erreichen, werden verschiedene Anwendungstechniken der Lumineszenz und der Elektronen-Spin-Resonanz (ESR) untersucht, und zwar zum einen als klassische Datierungsmethode und zum anderen als Werkzeug zur Herkunftsbestimmung. Diese Techniken werden auf zwei der am häufigsten vorkommenden Mineraltypen im Löss, Quarz und Feldspat, angewendet.

Erstens beschäftigt sich diese Arbeit mit der Frage, wie die Lössakkumulation in ACA auf das Klima reagiert. Zu diesem Zweck wird die Lumineszenzdatierung von Quarz und Feldspat verwendet, um einen hochauflösenden chronologischen Rahmen für fünf neue Lössstandorte zu erstellen, welche sich entlang eines ca. 200 km langen Transekts in den untersuchten Piemonte des Ili-Beckens im Südosten Kasachstans erstrecken. Eine Bayes'sche Altersmodellierung der Alters-Tiefen-Profile wird durchgeführt, um die Genauigkeit der Datensätze zu optimieren und die Berechnung der Massenakkumulationsraten (MARs) über die Zeit zu erleichtern. Die neue Chronologie zeigt, dass die Lössakkumulation entlang des Piemonts das mittlere Holozän bis über das letzte Interglazial hinaus umfasst und zeigt eine

räumlich-zeitliche Inhomogenität der Lössakkumulation. Um die Natur und die möglichen Ursachen dieser Inhomogenität in den Sedimentationsmustern zu verstehen, wurde die räumliche Abdeckung dieser Untersuchung durch die Berechnung von MARs aus veröffentlichten Lumineszenzaltern von 30 zusätzlichen Standorten im Ili-Becken, aus benachbarten Becken in ACA und aus dem gesamten chinesischen Lössplateau erweitert. Diese Synthese legt nahe, dass Lössablagerungen eine komplexe Reaktion auf das Zusammenspiel von lokalen Windregimen, Topographie, Sedimentangebot und -verfügbarkeit darstellen, was darauf hindeutet, dass bisherige Interpretationen von Lösspaketen als Klimaarchive zu sehr vereinfacht sind und überdacht werden müssen. In dieser Arbeit wird die MAR als eine Kombination aus zwei Parametern vorgeschlagen: "Nettoakkumulation" und "Zeitpunkt der Akkumulationsspitzen". Die Netto-Sedimentationsrate an einem bestimmten Standort reagiert sowohl auf den lokalen topographischen Kontext und die Sedimentverfügbarkeit als auch auf das Klima. Im Gegensatz dazu stellt der "Zeitpunkt der Akkumulationsspitzen" nur dann eine Reaktion auf die großräumige Klimadynamik in einer Region dar, wenn er aus einem aggregierten Datensatz von mehreren Standorten abgeleitet wird. Eine Ansammlung von MARs von mehreren Standorten beseitigt ortsspezifische Verzerrungen und bietet ein robusteres Werkzeug für das Verständnis der vergangenen Klimadynamik in einer Region.

Zweitens beschäftigt sich diese Arbeit mit der Frage der Herkunft des Lösses. Die Identifizierung des Ursprungsgesteins oder -standorts von Lösssedimenten sowie die Veränderungen der Quelle im Laufe der Zeit können Einblicke in Staubtransportwege geben und folglich die Rekonstruktion der vergangenen atmosphärischen Zirkulation in der Region erleichtern. Letztendlich hilft uns dies auch, die Prozesse der Lössgenese, des Transports und der Ablagerung zu verstehen. Diese Arbeit liefert einen ersten entscheidenden Schritt in Richtung dieses Ziels, indem sie eine neue Proxy-Methode zur Identifizierung der Herkunft von Quarz entwickelt. Diese neue Technik nutzt die Intensitäten von zwei paramagnetischen Zentren in Quarz, den natürlichen E'- und Peroxy-Zentren, die mittels Elektronenspinresonanz (ESR) gemessen werden. Sie basiert auf der Prämisse, dass diese Zentren aus Schottky-Frenkel-Defektpaaren entstehen, die mit dem Alter des quarzhaltigen Wirtsgesteins zunehmen. Nach experimentellen Beobachtungen, welche die physikalische Grundlage der Methode bestätigen, wurde dieser neue Ansatz auf eine Reihe von 114 feinkörnigen Löss-Quarzproben aus zwei Sedimentbecken in Kasachstan und Tadschikistan angewendet. Es ist bekannt, dass der Löss in den beiden Becken unterschiedliche Staubquellgebiete besitzt und aus Quellgesteinen mit sehr unterschiedlichen Altern stammt. Die Ergebnisse liefern eine positive Korrelation zwischen natürlichem E' und Peroxy-Intensitäten und zeigen, dass Quarz, der aus älteren Gesteinen (Kasachstan) stammt, stärkere Signale aufweist als Quarz aus jüngeren Gesteinen (Tadschikistan), was die Grundlage der neuen Methode bestätigt. Diese neue Methode zur Herkunftsbestimmung wurde anschließend angewandt, um erfolgreich Ursprungsänderungen entlang einer langen Löss-Paläobodenabfolge in Tadschikistan zu identifizieren. Der Ansatz zur Herkunft von natürlichen E'-Peroxy-Zentren stellt ein

vereinfachtes Messprotokoll im Vergleich zu anderen existierenden ESR-basierten Techniken dar, ist in hohem Maße auf äolische Aufzeichnungen anwendbar und birgt großes Potenzial für die Anwendung auf andere sedimentäre Systeme.

Die Anwendung dieser neuen Technik wurde weiter ausgebaut, indem sie mit einer Untersuchung der optisch stimulierten Lumineszenz (OSL) und Thermolumineszenz (TL) von Quarz kombiniert wurde. Die Intensität des E'-Defektzentrums in Quarz repräsentiert einen einzelnen Defekt, während die Lumineszenzempfindlichkeit eine Anhäufung von Ladungsfallen darstellt, die sowohl von der thermischen Geschichte des quarzhaltigen Ausgangsgesteins als auch von der Sedimentationsgeschichte des Korns beeinflusst werden. Variationen in der OSL- und TL-Empfindlichkeit von Quarz in langen Paläobodenabfolgen wurden mit Sedimentquellenverschiebungen in Verbindung gebracht, die mit klimatischen Schwankungen über glazial-interglaziale Zeitskalen zusammenhängen. Dennoch bleiben die Prozesse, die für die beobachteten Variationen der Lumineszenzempfindlichkeit von Quarz verantwortlich sind, einschließlich ihrer Verbindung zur Gesteinsquelle und/oder ihrer Sedimentationsgeschichte, ein strittiges Thema. In dieser Arbeit werden sowohl die E'-Peroxy-Intensitäten als auch die Lumineszenz-Empfindlichkeitscharakteristika von Quarz entlang einer langen Lösssequenz aus dem südlichen Tadschikistan untersucht, um einen differenzierteren Einblick in die Art und Weise zu erhalten, wie die verschiedenen Indikatoren für eingeschlossene Ladung die Veränderung der Quelle im Laufe der Zeit widerspiegeln. Die OSL- und TL-Empfindlichkeit von Quarz innerhalb vergrabener Bodeneinheiten (Paläoböden) zeigt einen deutlichen Anstieg im Vergleich zu primären Lösseinheiten. Unter Verwendung der natürlichen E'- und Peroxy-Intensitäten von Quarz als Indikator für die Herkunft wird der beobachtete Anstieg der OSL- und TL-Empfindlichkeit von Lössquarz auf wiederholte Zyklen natürlicher Bestrahlung und Bleiche zurückgeführt, die durch geringe Ablagerungsraten während der Pedogenese begünstigt wurden.

Die in dieser Arbeit erforschten Anwendungen und Methodenentwicklungen haben wichtige Implikationen nicht nur für das Studium der zentralasiatischen Lössablagerungen, sondern auch allgemein für die Rekonstruktion vergangener klimatischer Veränderungen aus terrestrischen Sedimentarchiven. Die umfassende Bewertung der Reaktion von Löss-MARs auf das Klima, im Kontext der geomorphologischen und topographischen Bedingungen, bietet einen realistischeren Rahmen für die Interpretation von Lössablagerungen als landbasierte Klimaaufzeichnungen. Die Entwicklung eines neuen Proxys für die Herkunft von Quarz unter Verwendung der ESR eröffnet spannende neue Wege für die Anwendung dieser Technik auf andere sedimentäre Systeme.

Table of Contents

List of Figures

List of Tables

List of Figures in Appendix

List of Tables in Appendix

1. Chapter 1

Introduction

1.1. Dust and Climate: Past, present and future

'Saharan dust: Orange skies and sandy snow in southern Europe'
-*BBC News*[1], 06.02.2021

'Apocalyptic skies as Beijing hit by worst sandstorm in a decade'
-*BBC News*[2], 15.03.2021

'S. Korea suffocated by extremely powerful yellow dust storm'
-*The Korea Herald*[3], 29.03.2021

Dust is an important constituent of the lithosphere, the atmosphere, the hydrosphere, and is now increasingly becoming a component of everyday news. Now more than ever, dust has a significant impact on society and climate. Dust commonly refers to fine grained airborne mineral particles. According to the 'Glossary of Atmospheric Chemistry Terms' (IUPAC[4], 1990), dust is defined as "Small, dry, solid particles projected into the air by natural forces, such as wind, volcanic eruption, and by mechanical or man-made processes such as crushing, grinding, milling, drilling, demolition, shovelling, conveying, screening, bagging, and sweeping. Dust particles are usually in the size range from about 1 to 100 μm in diameter, and they settle slowly under the influence of gravity". A hazardous amount of dust in the air, combined with toxic industrial pollution can lead to severe respiratory diseases (Hefflin et al., 1994; Tao et al., 2012; Khaniabadi et al., 2017), and is a major health concern, especially in Asian countries. Apart from serious risks to human health, a recent UNCCD[5] report also lists sand and dust-storms as major deterrents to socio-economic development, as these events lead to monetary loss and major disruption of agricultural and industrial activities, transportation, and infrastructural loss. Although dust emission (i.e., suspension and transport of dust by wind) usually occurs as a natural phenomenon, these processes have accelerated under human influence leading to enhanced desertification and dryland expansion, mostly due to unsustainable land-use practices and climate change. A glaring example of an environmental disaster due to human influence, as a result of mismanaged land-use practice, can be seen with the drying of the Aral Sea in the 1960's, once the fourth

[1] BBC News: https://www.bbc.com/news/av/world-europe-55966867. Accessed on: 27.06. 2021, 1128 hrs
[2] BBC News: https://www.bbc.com/news/world-asia-china-56399267. Accessed on -27.06.2021, 1811hrs
[3] The Korea Herald: http://www.koreaherald.com/view.php?ud=20210329000209. Accessed on – 27.06. 2021, 1135 hrs
[4] IUPAC (International Union of Pure and Applied Chemistry): see citation in references
[5] UNCCD (United Nations Convention to Combat Desertification): https://www.unccd.int/actions/sand-and-dust-storms. Accessed on: 27.06.2021, 1500 hrs

largest lake in the world. The drive to increase cotton production in the late 1950's led to the diversion of waters of the major rivers feeding the Aral, to the surrounding desert regions to fuel agricultural activity. This led to gradual lowering of the lake-levels and subsequent desiccation of this land-locked lake (Glantz and Zonn, 2005). Another human environmental disaster 'in waiting' concerns the drying of Lake Balkhash. The second largest lake in Central Asia, Lake Balkhash is witnessing declining lake levels and increased salinity, predominantly due to the divergence of its main inflow, the Ili River, to the Kapshagay reservoir (UNDP[6], 2006; Mischke et al., 2020). Today, the Kapshagay reservoir, that was built in the 1970's to boost agricultural productivity in the relatively semi-arid region of the Ili basin as well as the increased divergence of water due to urbanization in the Chinese side of the Ili basin, is threatening the fate of Lake Balkhash. Therefore, climatic variability coupled with anthropogenic climate change and increasing human requirements is leading to increased desertification of drylands (IPCC[7], 2019).

Climate modelling studies by Huang et al (2016) predicts that increasing population, aridity, and warming climate, will enhance desertification and lead to a projected increase of 11-23% (relative to 1961 to 1990) in dryland expansion by the end of this century (Fig. 1.1). The impending consequences of enhanced desertification (increasing aridity, food insecurity, decreasing agricultural productivity, loss of biodiversity), will be particularly severe for vulnerable ecosystems and populations inhabiting these regions, especially in developing countries (Huang et al., 2016; IPCC[7], 2019). Therefore both, the present and our immediate future, demands collective action towards suitable and adequate countermeasures to control detrimental land-use practices and prevent further land-degradation.

At the same time, dust also responds to climate. The production, transport and deposition of dust reflects an earth surface response to climate. Mineral dust thus acts a trigger and tracer of climate change. Therefore, one way of understanding the long-term impact of dust on climate is to study its impact on past climate. Consequently, traces of 'palaeo' dust records found in ice cores (Svennson et al., 2000; Simonsen et al., 2019), ocean sediments (Nakai et al., 1993; Letelier et al., 2019) and as terrestrial deposits (mostly in the form of loess deposits or as aeolian input in lakes; Chu et al., 2009; Munroe et al., 2021), can provide insight into past climate. Of these, wind-blown dust deposits, known as loess are recognized as excellent terrestrial archives of past climate change (Pye, 1987; Smalley et al., 2011;

[6] UNDP (United Nations Development Programme) Report, 2006: Water Conflict and Cooperation in Central Asia. By Erika Weinthal

[7] IPCC (Intergovernmental Panel for Climate Change): see citation in references

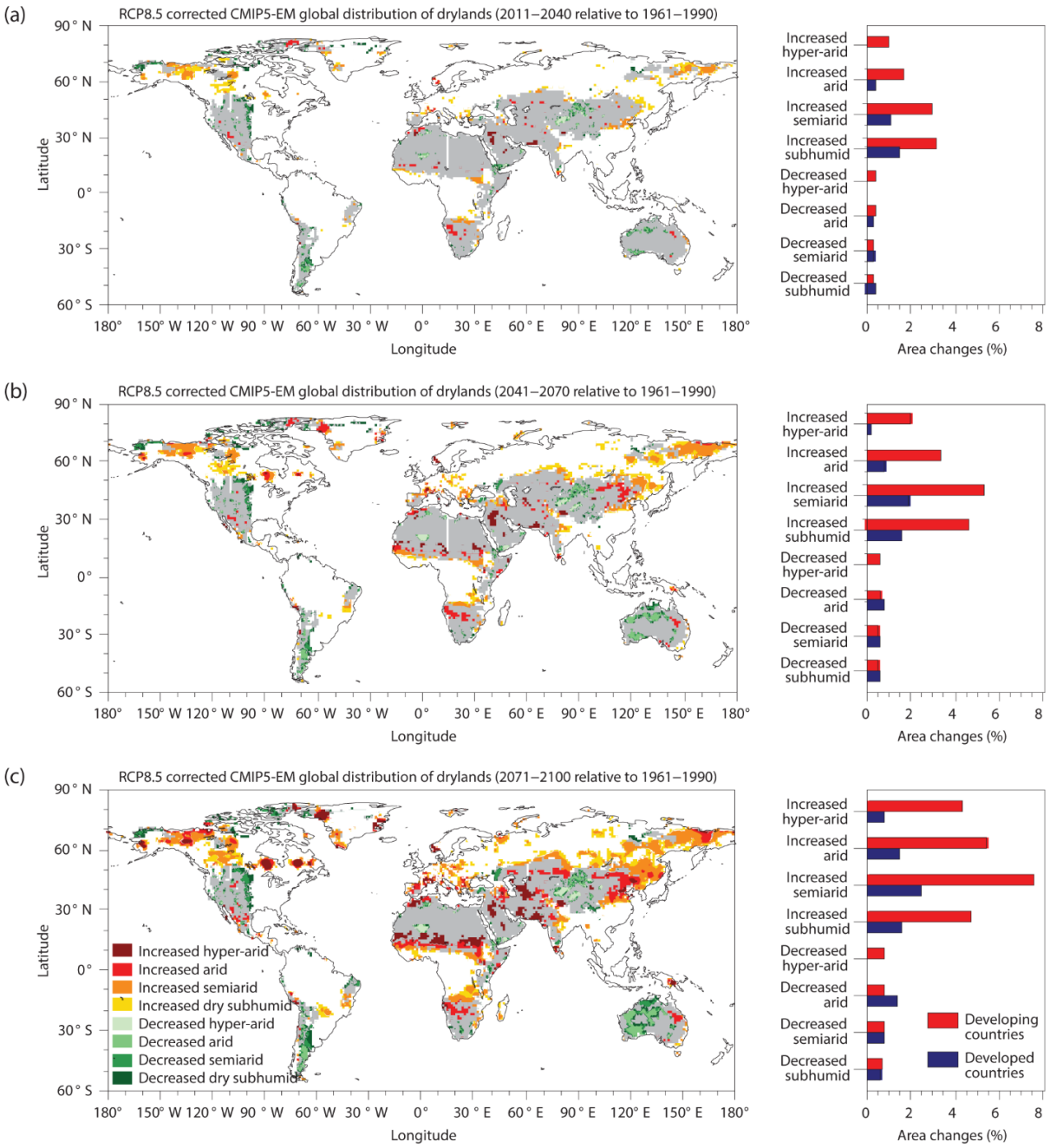

Fig. 1.1. Illustration of projected changes to distribution of dryland subtypes from corrected CMPI5-EM (ensemble mean of the Fifth Coupled Model Intercomparison Project, corrected for historical data) and RCP8.5 (representative concentration pathways) relative to baseline period (1961-1990) for (a) 2011-2040, (b) 2041-2070 and (c) 2071-2100 (adapted from Huang et al., 2016, with permission from Nature).

Schaetzl et al., 2018). The high sedimentation of loess deposits as compared to other archives, not only allows us to infer past climate variability over millennial timescales (Porter and An, 1995; Li et al., 2016a; Zeeden et al., 2018) but also allows one to estimate the 'atmospheric dust load' in the past, which is one of the most essential parameters for

understanding the role of dust feedback mechanisms within the climate system (Albani and Mahowald, 2019; Schaffernicht et al., 2020).

1.2. Loess: An archive of past climate and environment

Loess refers to wind-blown (aeolian) sediment, predominantly composed of silt sized particles. Loess deposits are recognized as excellent terrestrial archives of past climate and environmental change, especially during the Quaternary (Dodonov and Baiguzina, 1995; Muhs et al., 2014a; Schaetzl et al., 2018). These deposits usually occur as alternating beds of loess accumulation and buried soils (palaeosols). Conventionally, it is assumed that loess accumulation increases during drier, colder and more windy conditions, while it decreases and is overprinted by soil development during more humid, warmer and less windy periods (Marković et al., 2015). This hypothesis forms the basis of the association of loess accumulating phases with glacial conditions and soil development with interglacial periods and thus, lays the foundation for correlations between loess profiles and other climate archives (Kukla et al., 1977, 1988; Kohfeld and Harrison, 2003; Sun and An, 2005; Fitzsimmons et al., 2012; Marković et al., 2015). In addition, identifying the source of loess sediments can allow reconstruction of potential dust transport pathways and consequently atmospheric circulation in the region (e.g. Ding et al., 2000; Bird et al., 2015). Grain size distributions as well as the loess accumulation rates are often used as proxies to infer wind strength (Sun et al., 2012; Stevens et al., 2018). For instance, increasing grain size and loess accumulation rates during glacial periods in northwest loess sites of the Chinese loess plateau (CLP) are linked to increasing strength of the East Asian Winter Monsoon (Vriend et al., 2011; Liu et al., 2020). Thus, loess archives provide valuable records of past climate change.

Loess deposits also act as indicators of past environment. Occurrences of gastropod assemblages, land snail and mollusks in loess records act as important palaeoecological indicators. Identification of the species of these assemblages can yield valuable information about their habitat and ecology, and can help infer past ecology and climate (Moine et al., 2002, 2008; Marković et al., 2007). Isotopic analysis of fossil shells of these species can help infer local vegetation and temperature (Banak et al., 2016). Biomarkers like branched GDGT's (glycerol dialkyl-glycerol tetraethers) extracted from loess sediments can provide quantitative temperature estimates (Peterse et al., 2011), while biomarkers like n-alkanes and n-alkanols can provide qualitative insight into past vegetation (Zech et al., 2012; Li et al., 2016b). Pollen in loess records can also help infer local to regional record of past vegetation, and consequently climate (Sun et al., 2017). In recent years, a new proxy based on isotopic analysis ($\delta^{18}O$ and $\delta^{13}C$) of earthworm calcite granules, that predominantly occurs in palaeosols, has been used for quantitative estimation of temperature and precipitation conditions as well as palaeovegetation (Prud'homme et al., 2016; 2018). Hence, loess

sediments preserve a suite of environmental proxies that provide quantitative as well as qualitative estimate of past environmental conditions in the region.

1.2.1. Defining 'Loess'

The term loess comes from the German word 'löss', meaning 'loose', which was first used by Karl Caesar von Leonhard in the early 1800's to describe the crumbly and porous appearance of silty deposits in the Rhine valley near Heidelberg (Pye, 1995). Since then, the interpretation of the concept of loess, its genesis and its characteristic features have been constantly debated and discussed (Obruchev, 1945; Tsoar and Pye, 1987; Smalley and Derbyshire, 1990; Pécsi, 1990; Rozycki, 1991; Smalley, 1995; Smalley et al., 2011). It is generally believed that how one defines loess, depends on whether one takes a sedimentological or pedogenetic approach (Sprafke and Obreht, 2016). The definitions of loess and its characteristic features have been discussed over two centuries (Smalley et al., 2011; Sprafke and Obreht, 2016; Smalley and Obreht, 2018) and a summarised account of the history of these debates and how they shape our current understanding of loess is described below.

Defining loess from 1800's to 2000's (based on the comprehensive compilations of Smalley et al., 2001; 2011; Sprafke and Obreht, 2016 and Ding et al., 2019):

In 1824, Karl Caesar von Leonhard first coined the term loess to describe the friable, silty deposits in the Rhine valley. This term was popularized by English geologist Charles Lyell in 1834, who extensively elaborated on the formation of these deposits and assumed them to be floodplain deposits of fluvial origin. The pioneer of the 'aeolian' theory for loess deposits is debated. Pécsi and Richter (1996) believe it was Virlet D'Aoust who first proposed the aeolian origin of loess in 1858. While Smalley et al (2001), credit Ferdinand von Richthofen, as a pioneer of the aeolian theory of loess formation. Richthofen, in 1882, published elaborate observations of the characteristics of loess in the Chinese loess plateau and proposed an aeolian origin for the silty material. Prior to Richthofen's aeolian theory for Chinese loess, Pumpelly in 1866, proposed a 'lacustrine theory' for formation of Chinese loess. Pumpelly argued that the fine material for the loess was brought in by rivers that drained into a big lake that now forms the loess deposits; however, Pumpelly's arguments were based on the observation of freshwater shells and loam found in the different basins of the Inner Mongolia region of Northern China, which lies north of the well-known loess plateau of China. Richthofen's observations were however, based on the extensive deposits in Shaanxi province of China, which lie at the heart of the Chinese loess plateau.

The next important development came in 1890, with the association of loess features with climate change by John Hardcastle (Smalley et al., 2001). Hardcastle presented an elaborate

observation of loess features of Timaru loess in New Zealand and linked these with change in climatic conditions. He was probably the first to also suggest the production of fine material by glaciers during colder conditions. However, it was Pavel Tutkovskii in 1899, who proposed the formation of loess deposits by 'foehn' winds blowing from glaciated regions and later, further explored the association of loess formation with glaciers and their concurrent occurrence during glacial periods. Meanwhile, L.S. Berg in 1916 proposed the idea of in situ formation of loess, according to which loess was formed as a result of pedogenesis, weathering and/or reworking of the underlying substrate or parent material, with no aeolian input. This theory was adopted by geologist R.J. Russel in 1944 to describe a soil formation theory for loess in the Mississippi valley of USA. Although, the 'soil science' approach to loess received a lot of criticism, these theories gave rise to the idea of 'loessification'. The term loessification refers to a quasi-pedogenetic and/or quasi-diagenetic process that results in the aggregation of loess and/or the development of the loess structure (as defined by Sprafke and Obreht, 2016). However, the definition of loessification and its role in loess genesis still remains an active topic of discussion (Pécsi, 1990, 1995; Cilek, 2001; Svirčev et al., 2013; Smalley et al., 2011; Sprafke and Obreht, 2016).

Another important concept in loess was put forward by Russian geologist Vladimir Afanas'evich Obruchev in 1911 and later in 1945, who identified two types of loess: 'warm' and 'cold' loess. Obruchev referred to dust transported from the warm desert margins as 'warm' loess while that transported from glaciated regions and/or associated fluvioglacial deposits as 'cold' loess (Obruchev, 1945). This concept laid the foundation of the current debates on the 'glacial' versus 'non-glacial' loess (mostly associated with 'desert' loess) formation theory (Tsoar and Pye, 1987; Smalley and Derbyshire, 1990; Smalley, 1995; Wright, 2001; Lancaster, 2020).

Global attention to loess as a quaternary climate archive came with the work of Liu Tung-sheng in 1961, who reported loess with multiple buried soil (palaeosols) in various loess sections in the Chinese loess plateau as representative of changing climatic conditions (Ding et al., 2019). This increased attention to loess archives was further enhanced by G. Kukla, who was the first to correlate loess-palaeosol sequences to marine sediments (Kukla, 1977). Since then, loess archives have been established as quasi continuous archives of past climate change (Ding et al., 2002). They have also gained the status of terrestrial stratotype for the global Quaternary chronostratigraphic scheme by the International Commission on Stratigraphy (Cohen et al., 2013).

Post 1970's, saw an increase in investigation of loess as archives of past climate (Heller and Tung-sheng, 1982; Kukla, 1988; Liu, 1985; Hovan et al., 1989; An et al., 1991a,b). Nevertheless, the question of its 'genesis' still remains a topic of debate. Pye (1987) described loess simply as the accumulation of dust, thus, ascribing it an aeolian nature. This was later followed by the work of Pécsi (1990) who stated "loess is not just the accumulation

of dust". Pécsi (1990) substantiated the importance of post-depositional processes in loess formation and suggested that wind-blown dust becomes loess only after a certain period of time, after undergoing certain diagenetic processes. It is hard to completely negate either of the arguments. The features observed in loess in different contexts and in different geographical areas can be explained in parts, by both the arguments (i.e., 'aeolian' and 'not just aeolian'). Nevertheless, loess deposits are now widely recognised and accepted as wind-blown deposits (Muhs et al., 2014b; Schaetzl et al., 2018).

1.2.2. Loess formation: Production, transport and deposition

Loess formation processes generally encompass production of silt sized material, its transport from the source to the sink, and the final deposition of the material as loess. As discussed in the previous section, various hypotheses have been proposed for the different processes involved in loess formation. Parts of these theories, though altered and modified from the original hypotheses, still form a major part of the current hypotheses on loess formation. For instance, Obruchev's, 'warm' versus 'cold loess' hypothesis gave rise to the 'desert' loess formation theory (Smalley et al., 2014). Production of silt-sized material is believed to essentially occur in two ways:

(a) By glacial grinding (Smalley, 1966, 1995) – wherein silt sized loess particles are produced as a result of grinding of bedrock by large continental ice-sheets and by glaciers in mountains; the silt sized loess sediments generated in this way are commonly referred to as 'glacial loess'.

(b) By 'non-glacial' processes such as weathering of bedrock due to frost shattering, salinisation, aeolian abrasion and biological processes (Wright, 2001; Smith et al., 2002). A major part of this classification comprises of the 'desert' loess hypothesis, wherein silt sized loess particles are hypothesised to be formed by repeated cycles of abrasion, chipping and spalling of sand grains in desert areas (Smalley and Vita-Finzi, 1968; Wright, 2001; Lancaster, 2020). The desert loess hypothesis is quite debated and many authors suggest that loess often characterised as 'desert loess' doesn't fit the criteria of true loess (Smalley, 1995). For example, desert loess sites in Africa and Middle east usually have a predominantly coarser mean grain size (c. 50-80 µm; Crouvi et al., 2010), unlike loess sediments which are dominated by silt sized particles (c. 2-50 µm; Muhs et al., 2014c).

Once the silt-sized material is formed (either by glacial or non-glacial processes), various models (usually with multiple steps) have been proposed for the transport of material from the source (mountains and/or deserts) to the sink (loess deposit). Most of these transport processes usually involve a stage, wherein rivers transport sediment to the deflation zones,

before its final deposition as loess by aeolian processes (Wright, 2001; Smalley et al., 2009). In a recent review, Li et al (2020a) comprehensively summarized the different source areas and transport pathways of major loess areas into three modes of loess formation (Fig. 1.2):

(a) *Continental glacier provenance - River transport mode (CR mode)* - In this mode, the silt sized loess material is produced by continental glacier regions and then transported by rivers to the glaciofluvial outwash plains, from where it is directly deflated to loess depositional areas (Li et al., 2020a). The CR mode is mostly associated with loess found in the marginal zones of continental ice sheets. For example, loess in Central United States (commonly known as Mississippi loess) as well as in Eastern Europe (Ukraine, Belarus and southwest Russia) has been associated with this mode, as the material for loess is primarily formed from the margins of Laurentide ice sheets and the Fennoscandian ice sheet respectively (Forman et al., 1992; Muhs and Bettis, 2003; Rousseau et al., 2007). It is then transported by rivers from glacial outwash areas to alluvial plains and finally entrained by wind to form loess deposits.

(b) *Mountain provenance-River transport mode (MR mode)* - In this mode, high altitude mountain glaciers are the main source for production of silt-sized loess material which is then transported by rivers to alluvial plains from where it is directly deflated by wind to form loess deposits (Li et al., 2020a). This mode of loess formation is quite widespread. Loess in Central and Western Europe, Argentina, North America (Alaska and Northwestern United States) are some of the regions classified under the MR mode. For instance, the Rhine, the Po, the Danube and the Volga river originating from the high-altitude Alps and the Carpathian Mountains form the main source and transport mode of aeolian deposits of Central and Western Europe (Rousseau et al., 2007; Smalley et al., 2009)

(c) *Mountain provenance-river transport-desert transition mode (MRD mode)* – In this mode, the production of source material usually occurs in high altitude mountains and is then transported by rivers to desert basins, which act as interim storage/transition zones from where the material is deflated by wind to form loess deposits. Li et al (2020a) categorized Central Asian loess deposits, loess deposits in China, pampas loess in South America as well as the 'desert loess' sites in Africa and Middle east under the MRD mode. The classification of some of these regions under MRD loess genesis mode is debatable. For instance, some studies in Central Asia support the MRD mode of loess genesis (Obruchev, 1945; Sun, 2002a; Machalett et al., 2006). However, a recent comment on this classification by Li and Song (2020), suggests that Central Asian loess deposits, especially in the Ili basin of southeast (SE) Kazakhstan, should be categorized under MR mode of loess genesis. They base their arguments on provenance studies using grain size modelling and geochemical analyses (Li et al., 2018a,

2019a), as well as on modern meteorological observations of dust storms (e.g. Huo et al., 2014; Li and Song, 2020 and references therein). However, classifying loess areas within Central Asia as either MR or MRD mode is not straightforward. For instance, the loess deposits in the Tacheng basin, north of the Ili basin, do not have any apparent glacial mountain source or prominent river systems and it is assumed that the sediment for loess is obtained from the neighbouring Saryesik-Atyrau desert (Li et al., 2019b). This may also be the reason why loess deposits in the Tacheng basin have low sedimentation rates (also discussed in Chapter 3). A similar argument can also be made for sites in the Chinese loess plateau, where both MR and MRD mode of genesis have been argued for (Sun, 2002b; Yang and Ding, 2008; Stevens et al., 2013; Smalley et al., 2014; Nie et al., 2015; Meng et al., 2019). Therefore, classifying different loess areas of Central Asia or China *sensu-stricto* in either one of the modes is difficult.

There is thus, a need for systematic investigation into provenance of loess sediments to better constrain the source areas and transport pathways of dust to loess sites.

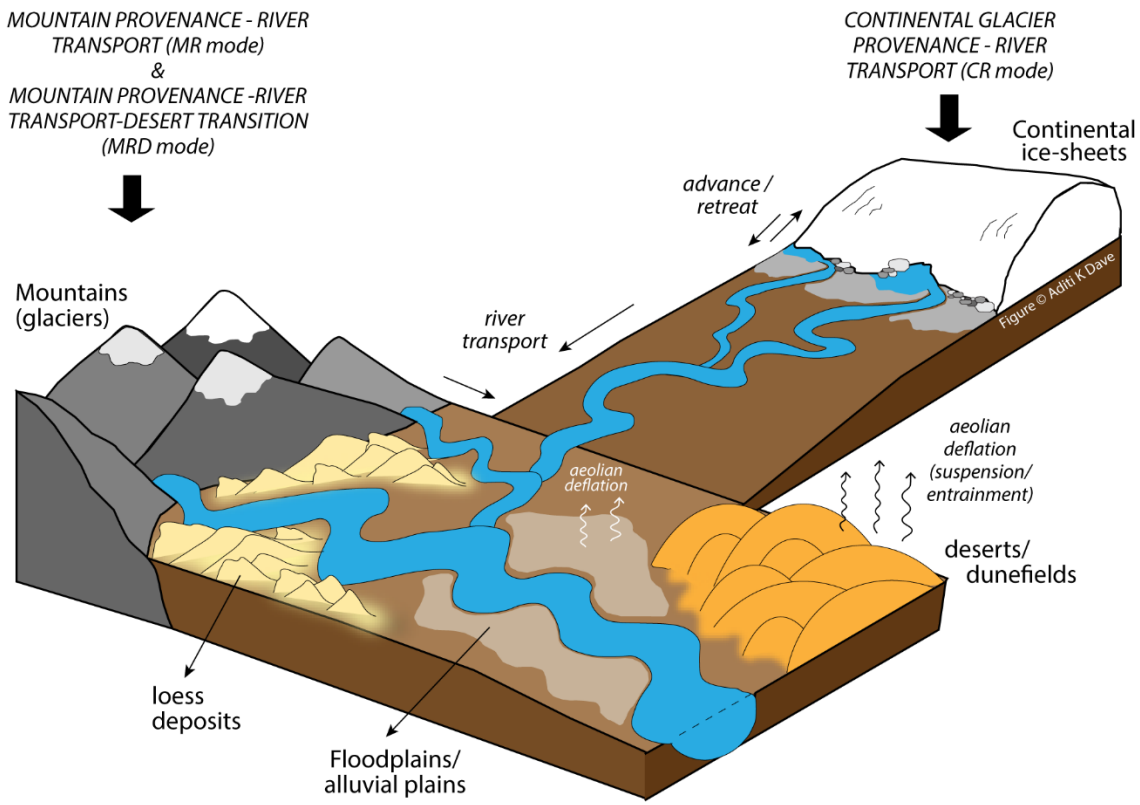

Fig. 1.2. Schematic representation of the different modes of loess genesis based on the textual descriptions of Li et al (2020a).

Once deposited, the loess deposits undergo post depositional alteration due to climate. This ideally results in alternating sequences of loess and palaeosols, a consequence of accumulation of loess in response to colder, drier and more windy periods, and decreased accumulation and soil development during warmer, wetter and less windy conditions. This represents a simplified account of post-depositional change in loess sequences. However, from a soil-science perspective, post-depositional changes in loess involves a complex array of diagenetic and pedogenetic processes that occur during loess deposition (Pécsi, 1990; 1995). An objective understanding of these processes can be found in Sprafke and Obreht (2016).

1.2.3. Extent and distribution of loess

Loess deposits are known to cover at least 10% of the world's land surface (Pécsi, 1968). These deposits usually occur in dry sub-humid to semi-arid climate zones of temperate latitudes (Fitzsimmons, 2017). Fig. 1.3. shows a map of major loess regions in the world. Most of the loess deposits occur close to continental ice sheets, high altitude mountains/ glacier systems and in some cases (arguably) near desert sources. They are favoured by well-established glacial river systems, topographic setting and semi-arid/temperate climatic conditions (Li et al., 2020a). Such settings provide optimal conditions for loess formation and accumulation. Some of the major loess deposits are found in the Chinese loess plateau, in the piedmonts of the Asian high mountains of Central Asia, the Siberian loess plateau and the Russian plains, across Europe (Middle and lower Danube basin, the middle Rhine basin and the lower Seine region), Mississippi basin in North America, Alaska, the Pampean plains of Argentina and Uruguay in South America, and in New Zealand (Schaetzl et al., 2018; Li et al., 2020a). Occurrence of loess at desert margins are reported for various regions in Africa (Tunisia, Namibia, Libya, Algeria and Nigeria) and Middle East (Israel, Yemen and United Arab Emirates), as well as in some isolated pockets of Western United States (Crouvi et al., 2010). Moreover, localised pockets of loess also occur in parts of South Asia (Pakistan, Afghanistan, Kashmir loess in India). Of the major loess regions in the world, some of the thickest and most extensive loess deposits can be found in the Chinese loess plateau of central northern China, with deposits exceeding more than 200 m in thickness (Liu, 1985; Yang and Ding, 2010). Equally comparable in thickness, though otherwise largely understudied, deposits are also found in the Afghan-Tajik depression in Tajikistan. The Tajik deposits are > 150 m thick and extend beyond the Brunhes-Matuyama palaeomagnetic reversal (Dodonov, 1991; Dodonov and Baiguzina, 1995; Ding et al., 2002). On the contrary, loess deposits in mid-latitude America and Alaska are just tens of meters thick (Schaetzl et al., 2018). Thus, the distribution and thickness of loess deposits varies widely across different regions as well as locally within a basin and/or region itself (Li et al., 2020a).

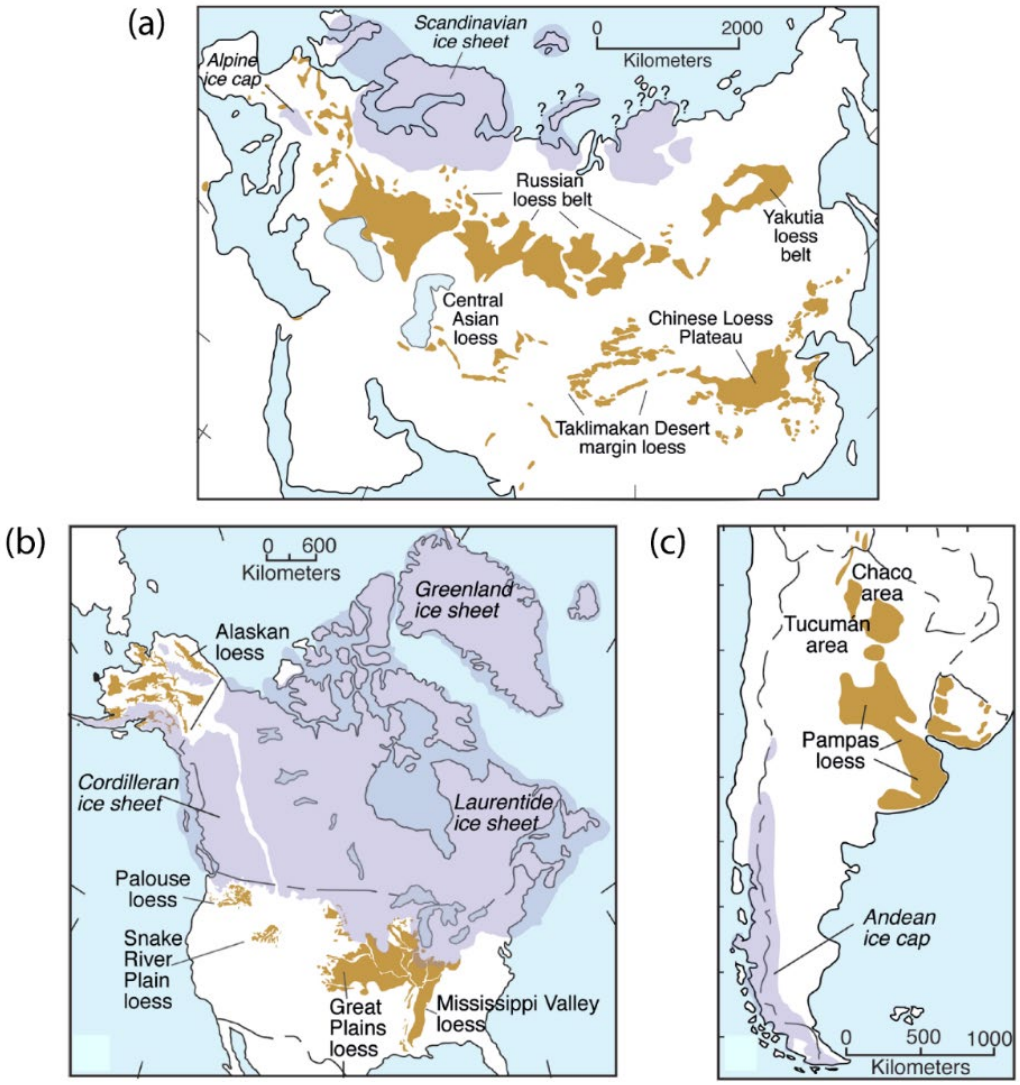

Fig. 1.3. Distribution of major loess deposits across (a) Eurasia, (b) North America and (c) South America (modified from Muhs et al., 2014a and originally from Muhs et al., 2007; adapted with permission from Elsevier).

1.3. Central Asian loess deposits

Central Asia (also known as Arid Central Asia, ACA) is one of the driest regions in the world with extensive and widespread loess deposits, and is a major contributor to global atmospheric dust (Kok et al., 2021). ACA is often used as a generic term that covers a wide geographical area of the dry-sub humid, semi-arid to arid region of continental Asia. For the purpose of this thesis, we define the extent of Central Asia as given by Schaetzl et al (2018). The ACA extends from the Mongolian Hangay mountain margins in the east to the foothills of the Elbruz mountains (northern Iran) in the west, encompassing the basins of the actively uplifting Pamir, Alai, Altai and Tien Shan ranges. This definition of ACA excludes the loess deposits of the Russian plains, but includes the loess deposits in the margins of the Tarim

basin. This region features loess-draped piedmonts, alluvial fans, dunefields and the large endorheic basins of the Aral Sea and Lake Balkhash. It experiences an extremely continental, semi-arid climate, which is influenced mainly by the mid latitude Westerlies, northerly polar fronts, Siberian High-pressure system and East Asian and Indian monsoon system (Machalett et al., 2008; Schaetzl et al., 2018). The influence of the East Asian and Indian monsoon in most parts of Central Asia (especially the rain shadow of the Asian high mountains) is limited, as the Asian high mountains act as a barrier, preventing the moisture laden winds from reaching the interiors of the basin. However, this hypothesis is debated based on contradicting evidence from the region. Speleothems from the Kesang cave in eastern Tien Shan supports the incursion of the East Asian monsoon in this region (Cheng et al., 2012), while the multiple loess records in this region contradicts that idea (Chen et al., 2016; Yan et al., 2019; Li et al., 2020b).

The piedmont loess deposits in Central Asia are quite extensive, yet unevenly distributed and vary in thickness between basins and within the basin itself. For instance, the loess deposits in the eastern part of the Ili basin are thicker than the central part of the Ili basin, which is quite patchy and unevenly distributed (Li et al., 2015a; Sprafke et al., 2018). At the same time, loess deposits in the Afghan-Tajik basin exceeds more than a hundred meters in thickness, and as previous studies show, are fairly continuous (quasi-continuous) and well preserved (Forster and Heller, 1994; Ding et al., 2002). In comparison, the loess deposits in the piedmonts of the Tien Shan ranges are inhomogeneous and unevenly distributed (see Song et al., 2014; Li et al., 2015a).

1.3.1. *Why Central Asia?* Significance

The central focus of this thesis is on the piedmont loess deposits of Central Asia, particularly the Ili basin of southeast (SE) Kazakhstan and the Afghan-Tajik depression in Tajikistan. The semi-arid and arid region of Central Asia forms a major component of the world's dryland systems. Future climate change is predicted to not only cause dryland expansion, but also increase desertification and 'drought like' events, threatening the vulnerable dryland ecosystems, the health and livelihood of people as well as socio-economic development in the region (Huang et al., 2016; IPCC, 2019). Therefore, to understand the impact of future climate change on dryland systems, especially in Central Asia, it is imperative to understand how aeolian landforms in these dryland systems responded to climate change in the past.

Climatically, Central Asia lies at the intersection of two major drivers of the Northern hemisphere – the mid latitude Westerlies and the Siberian High. Therefore, the aeolian deposits in this region are highly susceptible to changing wind regimes in the region and hence, can act as archives for reconstructing atmospheric circulation. A recent study by Fitzsimmons et al (2020) looked at climate reanalysis of wind trajectories and likely dust

transport to loess piedmonts in the Central part of the Ili basin in SE Kazakhstan. According to this, both Westerly and Northerly winds (influenced by the Siberian High) are currently responsible for transporting dust to this region, suggesting multiple potential source areas for the piedmont loess sites, which may have changed dominance through time. Thus, making Central Asian loess deposits a valuable tool in understanding the nature of interaction between these climatic subsystems through time and space.

Central Asia comprises of different aeolian landforms, from dunefields to extensive loess deposits, which provides a natural laboratory to not only understand how different aeolian systems respond to climate but also the interaction between these landform features. For instance, one of the prevailing debates in the aeolian community is to understand the genetic link between deserts and loess deposits (Lancaster, 2020). Therefore, the extensive dunefields of Central Asia, the steep rugged terrain of the Asian high mountains, as well as the prevailing wind dynamics in the region provides an optimal setting to not only study loess formation processes in piedmont regions but, also help understand the nature of interaction between different landforms and thus, gain an insight into earth surface processes and its response to climate.

1.3.2. Key issues in Central Asian loess records

As discussed in the previous section, Central Asian loess deposits form significant archives of past climate change, yet relatively little is known about the past climate and environment in this region. In the past decade however, there has been increasing scientific investigation of loess deposits in this region (Machalett et al., 2006, 2008; ChongYi et al., 2012; Song et al., 2012, 2015; Youn et al., 2014; Kang et al., 2015; Li et al., 2015b, 2016a,c, 2018b, 2019c, 2020c; Fitzsimmons et al 2017, 2018, 2020; Jia et al., 2018; Wang et al., 2019a,b). These emerging datasets based mostly on application of absolute dating techniques and quantitative and qualitative palaeoclimatic proxies have brought forward interesting insights and hypothesis that challenge our conventional understanding of loess formation processes as well as palaeoclimatic inferences from this region. Since this thesis is particularly focused on piedmont loess deposits in Central Asia, especially in the rain shadow of the Asian high mountains; therefore, this section discusses key issues in Central Asian loess records pertaining to this region:

a) Recent studies (Li et al., 2016c, 2018b; Fitzsimmons et al., 2018) suggest that loess accumulation rates in the piedmonts of Central Asia are asynchronous with expected variability over glacial–interglacial timescales, as observed from loess deposits in the Chinese loess plateau (CLP). The asynchronies with loess flux in the CLP, challenges prevailing assumptions that connect increased loess accumulation with cold glacial

periods, thus suggesting that these assumptions do not hold in the piedmont deposits of Central Asia.

b) A synthesis of loess accumulation rates from multiples sites in the ACA (Li et al., 2018b; Fitzsimmons et al., 2018) reveals a disparity in the rate and timing of peaks in loess accumulation between sites. This raises questions on the nature of relationship between loess accumulation and palaeoclimate, and a need to interrogate the role of topography (palaeotopography), local sediment supply as well as wind regimes in the high terrain environments of ACA.

c) Early loess formation models for Central Asia (e.g. Obruchev, 1945) posit that the Saryesik-Atyrau and Taukum dunefields to the north of the Ili plain act both as transitional sedimentary sink for sediments transported to the piedmonts as well as sources of dust for entrainment and transport to the loess sites. It is therefore, classified under the MRD mode (as discussed in section 1.2.2) by Li et al (2020a). This loess formation theory for Central Asian loess deposits was widely accepted based on the prevailing circulation patterns and wind dynamics in the area, proximity of deserts to loess sites (Obruchev, 1945; Machalett et al., 2006) and mineralogical and grain size properties (Sun, 2002a). However, recent geochemical investigations (Li et al., 2018a) on loess deposits as well as surrounding source areas such as proximal dunefields, river alluvium and floodplain deposits suggest a predominantly MR mode (discussed in section 1.2.2). Thus, in order to better understand the nature and mechanism of loess formation, there is a need to establish a robust provenance approach to characterize the source signature and to identify its imprint on loess deposits.

d) Grain size variations at multiple loess sites in the Central Asian piedmonts have been correlated to millennial scale oscillations linked to the transport of the North Atlantic signal by the Westerlies (Li et al., 2016a; Wang et al., 2019a). At the same time, the predominance of the Northerly winds associated with the Siberian High-pressure system has been proposed as a major driver of loess accumulation in Central Asia, especially during glacial periods (Cheng et al., 2021). Thus, the nature of interaction as well as the spatio-temporal predominance of these two Northern hemispheric climatic subsystems in the region is not well understood and lacks conclusive evidence.

1.4. Study region

This thesis is focused on piedmont loess deposits in the Ili basin of SE Kazakhstan and in the northern margins of the Afghan-Tajik basin in Tajikistan. Fig. 1.4 shows a detailed map of the regional setting and the location of loess sites investigated in this thesis. A detailed account of the stratigraphy of the loess sites is presented in subsequent chapters. The photographs of

the loess sections sampled in this study are shown in Figure 1.5 and Figure 1.6. A general description of the regional setting of the sites is summarized below.

1.4.1. Ili basin, SE Kazakhstan

This thesis investigates four loess sites located across a c. 200 km east-west transect along the Zalisky Alatau range front in the Ili basin of SE Kazakhstan (Fig. 1.4 and Fig. 1.5). The four sites under investigation are:

Panfilov (*PAN*; c.5 m thick; 43^{o} 22.295' N, 77^{o} 07.670' E; 710 m a.s.l.)
Ashubulak (*ASH*; c.5 m thick; 43^{o} 28.671' N, 77^{o} 47.379' E; 760 m a.s.l.)
Taukaraturyuk (*TAU*; c.7.5 m thick; 43^{o} 29.445' N, 78^{o} 01.509' E; 769 m a.s.l.)
Malubai (*MAL*; c.6 m thick; 43^{o} 26.312' N, 78^{o} 19.763' E; 815 m a.s.l.)

These sites are part of extensive loess deposits that drape the piedmonts of the Central and Eastern Tien Shan ranges, where they form margins of the Ili river catchment in SE Kazakhstan and NW China. The Ili River (also referred to as Yili) is the main tributary of Lake Balkhash endorheic basin. The river catchment forms a triangular, east-west oriented valley (hereafter referred to as the Ili basin) which opens to the west at the present day Kapshagay Reservoir onto the 'Ili plain', an open region of alluvial deposits, dunefields and a large delta, before terminating at Lake Balkhash. The Ili basin is enclosed by the Dzungarian Alatau to the north, the Chinese Borohoro ranges to the east and the Central and Eastern Tien Shan to the south and southeast, respectively. These mountain ranges constrain the flow of the Ili river and its tributaries (the Kashi, Tekes and Kunes Rivers; Fig. 1.4), and also acts as a topographic trap for loess accumulation in the enclosed basin.

The Ili basin experiences a continental semi-arid climate. This region is predominantly influenced by the interaction of the mid latitude Westerlies and the high-altitude polar front, linked to the Siberian High-pressure system. Nevertheless, many seasonal near-surface air flow and pressure systems also influence the region (Lydolph, 1977; Machalett et al., 2008). Apart from the prevailing Westerly influence in the region, during the summer this region is also influenced by Northerly and Northwesterly winds, artic and polar air flows as well as cyclonic winds resulting from the thermal depression over the Central Asian mainland. While, during the winter, this region is dominated by anticyclonic Northeasterly winds linked to the Siberian High-pressure system as well as a southward shift of the polar front leading to stronger cyclones and precipitation (Lydolph, 1977; Machalett et al., 2008). Thus, the seasonal variations in wind direction and precipitation are strongly influenced by the interaction between these wind and pressure systems and the orography of the region (Lydolph, 1977).

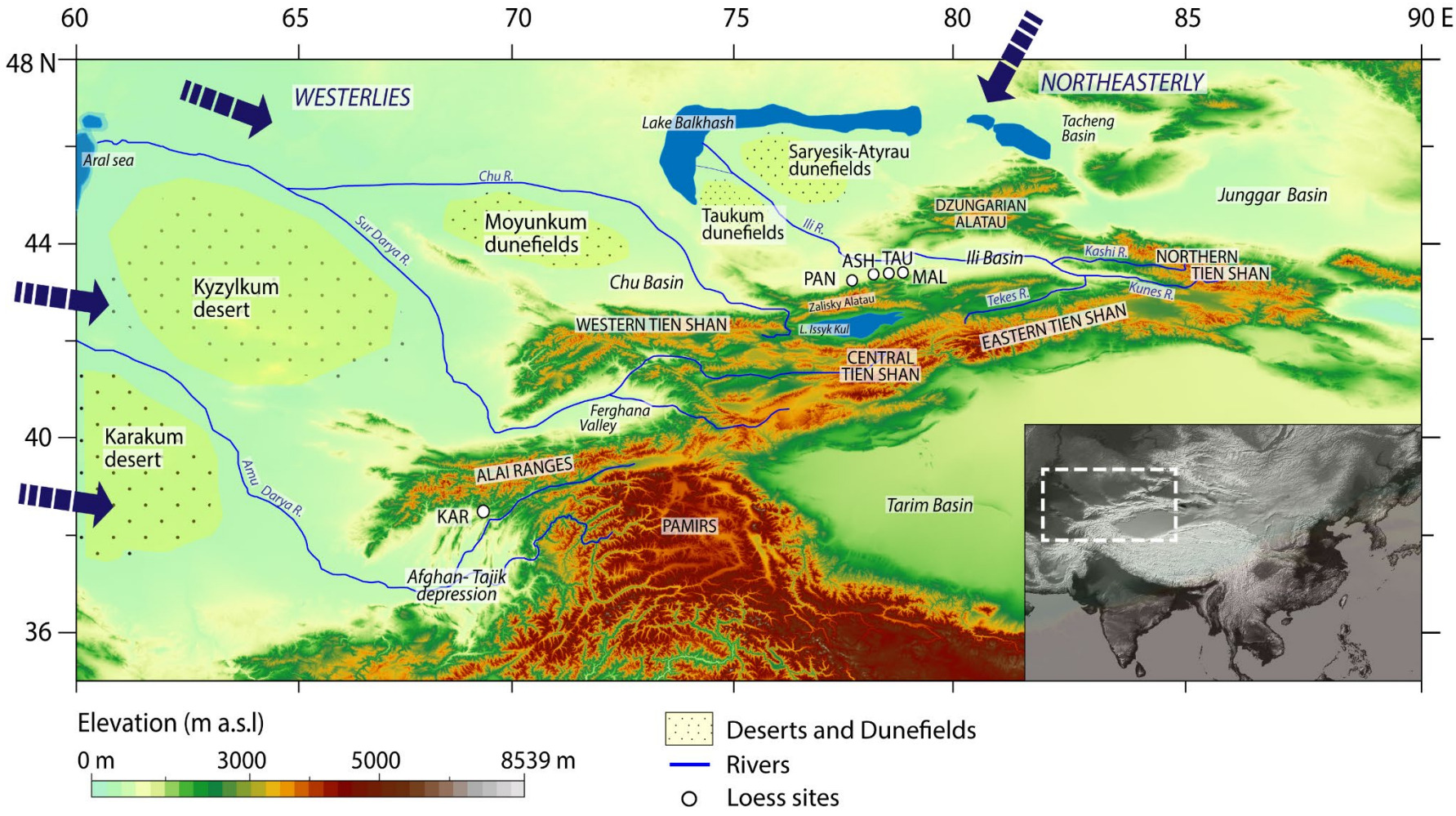

Fig. 1.4. Regional setting and location of loess sites investigated in this thesis. The elevation map was created using open source SRTM (Shuttle Radar Topography Mission) data provided by AW3D of the Japan Aerospace Exploration Agency.

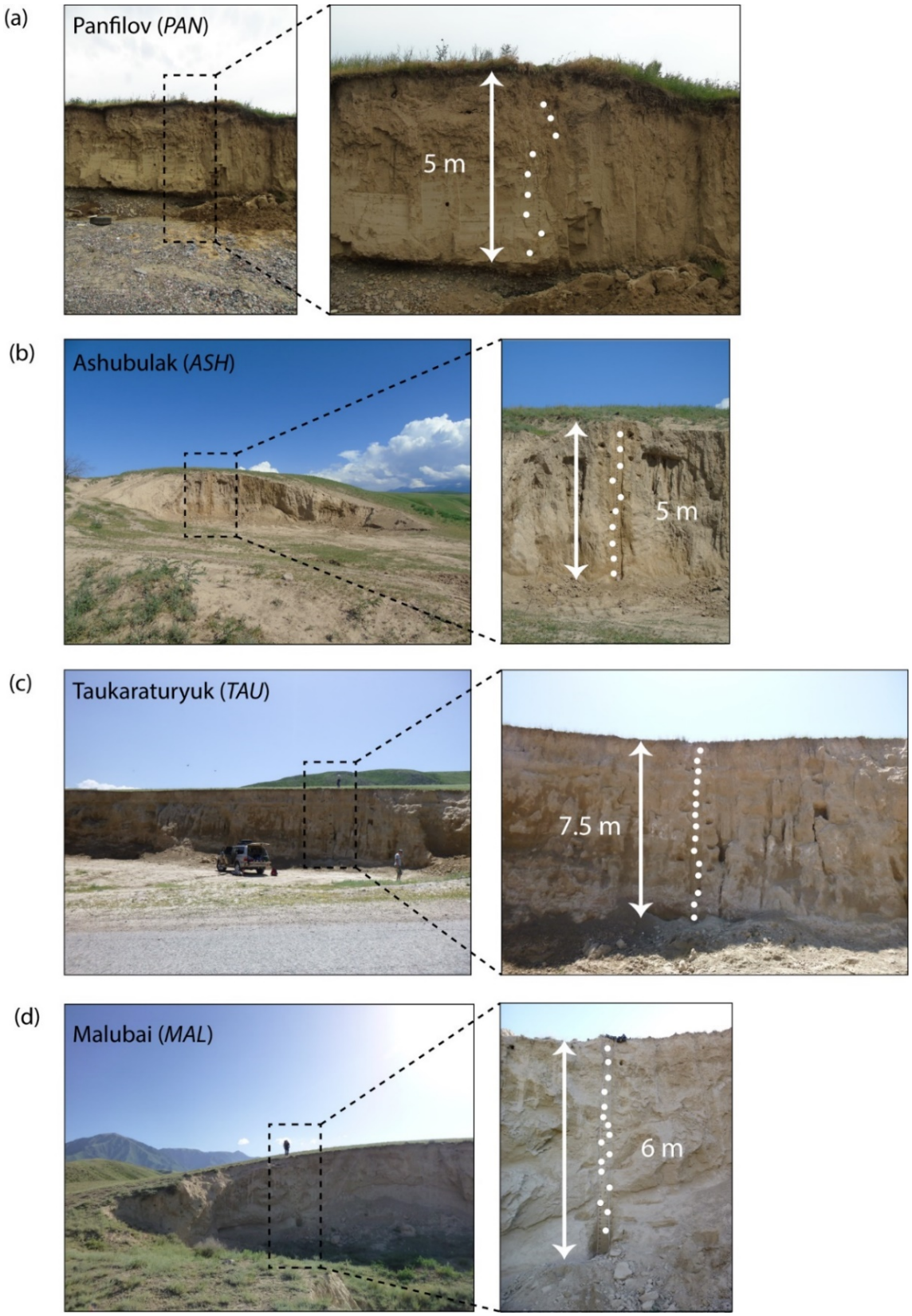

Fig. 1.5. Photographs of the loess sections, along with sampling location (for purposes of dating and provenance) are shown for site (a) Panfilov (PAN), (b) Ashubulak (ASH), (c) Taukaraturyuk (TAU) and (d) Malubai (MAL) from the Ili basin of SE Kazakhstan (Field campaign - 2017 and 2019).

1.4.2. Afghan-Tajik depression, Tajikistan

This thesis investigates a c. 60 m thick loess-palaeosol sequence of Karamaidan (KAR; 38°34'33.47'' N, 69°16'40.79'', 1629 m a.s.l) located c. 45 km east to Dushanbe, the capital of Tajikistan (Fig. 1.4 and Fig. 1.6). The site of KAR investigated in this thesis is a subsection of four overlapping sections that was sampled as part of the 2018 field expedition in Tajikistan (Fig. 1.6). KAR lies in the foothills of the Gissar Range on the northern margins of the Afghan-Tajik depression and is situated between two major tributaries of the Amu-Darya River, the Kofarnihon to the north and the Vakhsh to the south. The Afghan-Tajik depression is a seismically active sedimentary basin, the northern part of which is punctuated by a series of north-south folds and ridges (McNab et al., 2019), that are traversed by a number of rivers and streams arising from the glaciated Alai, Trans-Alai and Pamir ranges; providing vast glacio-/fluvial outwash and alluvial plains that act as dust source regions. This provides an optimal topographic and geomorphic setting for dust deposition. In addition, the Karakum and Kzylkum deserts located to the West also act as dust sources for loess deposits in the basin (Li et al., 2019b). Hence, the Tajik basin acts as a depositional sink for loess, and as such, this region is known to preserve some of the longest and quasi continuous loess records spanning the past million years (Forster and Hellar, 1994; Dodonov and Baiguzina, 1995; Ding et al., 2002). The loess deposits at KAR, provide one such record and are known to preserve a fairly continuous record of climate change over the past 1 Ma (Forster and Heller, 1994). This provides us with an ideal test site to investigate factors and processes controlling long term variations in source, in response to climatic oscillations.

Tajikistan experiences a continental, subtropical to semi-arid climate, with a variable precipitation regime. The eastern parts of the country receive higher annual precipitation then the western part (Li et al, 2019a). The Westerlies are the prevailing wind regime in this region, and interact seasonally with (i) the southward shifting polar front from the north and intruding northwesterly artic air in the winters and (ii) with cyclonic winds resulting from a thermal depression during the summers (Lydolph, 1977). Previous studies based on grain size analysis and climate modelling (Ding et al., 2002; Vandenberghe et al., 2006) in the region suggest that Westerlies form the predominant dust transporting winds to the basin. However recent studies based on mineralogy and geochemistry of sediments (Li et al., 2019a), suggests that local surface air-flow wind patterns within the basin were primarily responsible for dust accumulation within the basin; nevertheless, they also hypothesise minor contributions from Westerly transported dust from the Karakum and Kzylkum deserts. Hence, the nature of interaction between different dust transporting wind regimes remains poorly understood and needs further investigation.

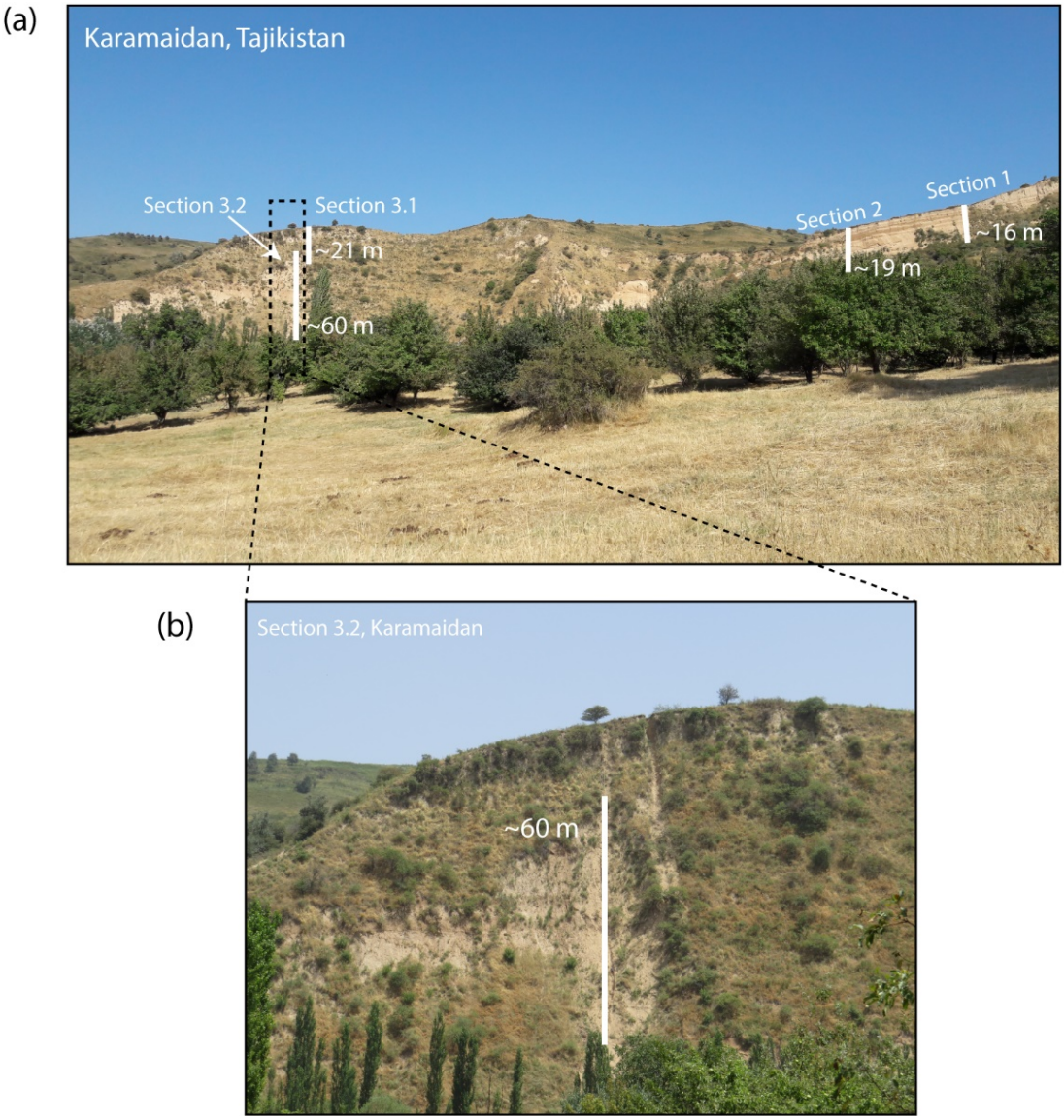

Fig. 1.6. (a) The exposed loess cliff at Karamaidan (KAR) with four overlapping sections (b) The c. 60m thick loess section at KAR investigated in this thesis. Photographs were taken during the 2018 field campaign in Tajikistan.

1.5. Research aims and chapter outline

1.5.1. Research objectives

This thesis aims at understanding Quaternary aeolian landscape – climate interaction by reconstructing the timing and provenance of loess deposits in Central Asia using trapped charge techniques – Luminescence and Electron spin resonance. This thesis aims at understanding two main issues in Central Asian loess deposits:

(a) *How does loess accumulation respond to climate in the piedmonts of Central Asia?*
This generic question encapsulates one of the key issues of loess records from the piedmonts of Central Asia. In this thesis, we aim to address three main aspects of this issue:

- climatic and geological constraints on loess accumulation in piedmont regions.
- spatio-temporal inhomogeneity in loess records in the Central Asian piedmonts.
- response of loess accumulation to glacial-interglacial cyclicity as well as its asynchronous disparities with loess flux from the Chinese loess plateau.

(b) *The question of provenance?*
Identifying the provenance of loess sediments can help address two key issues of loess research in Central Asia: (i) establishing dust transport pathways, thereby providing insight into climate circulation patterns in the past, (ii) understanding processes of loess genesis, transport and deposition; therefore, shedding light on the much debated 'desert loess' versus 'glacial loess' hypothesis in Central Asia. However, up until now, the provenance approach applied to piedmont loess sediments in this region involve 'bulk sediment' grain size modelling and elemental geochemistry (Li et al., 2018a). These methods have been unable to hitherto provide conclusive evidence for provenance. Therefore, there is a need of a provenance tool that targets specific minerals in sediments to enable robust characterization of source in loess sediments.

This thesis investigates these issues utilising trapped charge techniques of Luminescence and Electron Spin Resonance (ESR), in a two-fold approach:
First, as 'classical' dating tools. This thesis utilises 'Luminescence technique' as a dating tool to develop high-resolution chronological framework for loess deposits in the Central Asian piedmonts. The absolute ages are statistically modelled using Bayesian age-depth modelling tools to obtain mass accumulation rates and evaluate spatio-temporal distribution of loess in the region.

Second, as provenance tools. This thesis proposes a new proxy for provenance of quartz using naturally accumulated defect centres in quartz, measured by ESR. This new technique is applied to various loess sections in different basins in Central Asia, with the aim to better understand the provenance of loess sediments in the region. This thesis also investigates luminescence sensitivity in parallel with defect centre characteristics of quartz down a long loess sequence, to gain a more nuanced insight into how these different trapped-charge indicators reflect source change through time.

All the above investigations are supported by stratigraphic data, magnetic susceptibility measurements, grain size analyses and micromorphology, which provide support and also lay the foundation for palaeoclimatic interpretations for the investigated sites.

1.5.2. Outline of chapters

The outline and primary goal of each chapter is listed below:

Chapter 2 – Methodology: Basic principles and Concepts.
This chapter provides an elaborate account of the underlying principles and concepts of the methodological tools used in this thesis. The sample preparation procedures and the instrumentation are described in subsequent chapters as per the requirements of the proposed research question.

Chapter 3 – The patchwork loess of Central Asia: Implications for interpreting aeolian dynamics and past climate circulation in piedmont regions (Status: Submitted to Quaternary Science Reviews)
This chapter addresses the issue of 'loess accumulation and its response to climate' in the piedmonts of Central Asia. In this study we investigate the relationship between loess mass accumulation rates (MAR's) and climate, in the context of topography, sediment availability and supply and past circulation particularly in the Ili basin of SE Kazakhstan, and more widely within ACA and the CLP. This study draws a local to regional perspective on loess accumulation across various piedmont settings in semi-arid to sub-humid temperate latitudes. This is undertaken by firstly, generating a high-resolution chronological framework based on luminescence ages for five new loess sites in the rather understudied Central part of the Ili basin in SE Kazakhstan. Secondly, by integrating the new dataset with published luminescence ages from 30 other sites to calculate loess MAR's from within the Ili basin, and more broadly from neighbouring basins in the ACA and the CLP. This study interprets loess MARs as a composite of two parameters, 'net accumulation' and 'timing of accumulation peaks' in loess, and systematically assesses how loess MARs respond to climate, geomorphic and geological controls, to better understand loess depositional dynamics in the piedmonts of Central and East Asia.

Chapter 4 - A novel proxy for tracking the provenance of dust based on paired E'-peroxy paramagnetic defect centres in fine-grained quartz (Status: Submitted to Geophysical Research Letters)
This chapter provides the first crucial step towards resolving the 'question of provenance' by developing a novel approach for provenance of quartz. In this study, we propose a new method for identifying sediment provenance by exploiting the characteristics of two defect centres in quartz, namely the E' and the peroxy centre using Electron Spin Resonance (ESR). This new approach is based on the premise that the intensity of E' and peroxy signals in natural quartz arises from Schottky-Frenkel defect pairs and is proportional to the age of the quartz host rock (Odom and Rink, 1989). To test whether the new approach is successful in distinguishing between loess sediments, we apply the new measurement protocol to a suite of 114 fine-grained quartz loess samples from two sedimentary basins in Kazakhstan and

Tajikistan respectively. These samples are known to have different dust source regions and also derive from source rocks of very different ages. We also test the applicability of the new technique to evaluate temporal variability in source within a loess sequence, by investigating the natural E' and peroxy signal variability down a long loess-palaeosol sequence. This new approach presents a simplified measurement protocol in comparison to other ESR-based provenance techniques, which, while highly applicable to long aeolian records, also holds great potential for application to other sedimentary systems.

Chapter 5 – Variations in luminescence characteristics and paramagnetic defect centres of fine-grained quartz from a loess-palaeosol sequence in Tajikistan: Implications for provenance studies in aeolian environments (Status: In preparation)

This chapter evaluates loess depositional dynamics of a long loess palaeosol record based on combined approach utilising luminescence characteristics and paramagnetic defect centres in quartz. Variations in luminescence characteristics of quartz from long loess-palaeosol sequences have been linked to sediment source shifts related to long term climatic fluctuations. However, the natural processes of loess transport and deposition that lead to change in sensitivity of quartz remain contended. In this study, we investigate the natural defect centres (based on the new approach) as well as the luminescence characteristics of quartz from a c. 60 m thick loess palaeosol sequence in Tajikistan. We then utilise the defect centres in quartz as a provenance indicator, to evaluate the natural processes of loess transport and deposition that lead to observed variability in luminescence characteristics of quartz.

Chapter 6 – Conclusions and Outlook

This chapter summarises the main findings and observations from this thesis. It also discusses a suite of open questions and areas of investigation for future studies in this field.

References

Albani, S., & Mahowald, N. M. (2019). Paleodust Insights into Dust Impacts on Climate. Journal of Climate, 32(22), 7897–7913. https://doi.org/10.1175/JCLI-D-18-0742.1

An, Z., Kukla, G. J., Porter, S. C., & Xiao, J. (1991a). Magnetic susceptibility evidence of monsoon variation on the Loess Plateau of central China during the last 130,000 years. Quaternary Research, 36(1), 29–36. https://doi.org/10.1016/0033-5894(91)90015-W

An, Z., Kukla, G., Porter, S. C., & Xiao, J. (1991b). Late quaternary dust flow on the chinese Loess Plateau. Catena, 18(2), 125–132. https://doi.org/10.1016/0341-8162(91)90012-M

Arimoto, R. (2001). Eolian dust and climate: Relationships to sources, tropospheric chemistry, transport and deposition. Earth-Science Reviews, 54(1), 29–42. https://doi.org/10.1016/S0012-8252(01)00040-X

Atkinson, J. D., Murray, B. J., Woodhouse, M. T., Whale, T. F., Baustian, K. J., Carslaw, K. S., Dobbie, S., O'Sullivan, D., & Malkin, T. L. (2013). The importance of feldspar for ice nucleation by mineral dust in mixed-phase clouds. Nature, 498(7454), 355–358. https://doi.org/10.1038/nature12278

Banak, A., Mandic, O., Sprovieri, M., Lirer, F., & Pavelić, D. (2016). Stable isotope data from loess malacofauna: Evidence for climate changes in the Pannonian Basin during the Late Pleistocene. Climate Change in the Balkan-Carpathian Region during Late Pleistocene and Holocene, 415, 15–24. https://doi.org/10.1016/j.quaint.2015.10.102

Bird, A., Stevens, T., Rittner, M., Vermeesch, P., Carter, A., Andò, S., Garzanti, E., Lu, H., Nie, J., Zeng, L., Zhang, H., & Xu, Z. (2015). Quaternary dust source variation across the Chinese Loess Plateau. Palaeogeography, Palaeoclimatology, Palaeoecology, 435, 254–264. https://doi.org/10.1016/j.palaeo.2015.06.024

Bristow, C. S., Hudson-Edwards, K. A., & Chappell, A. (2010). Fertilizing the Amazon and equatorial Atlantic with West African dust: African Fertilizer for Amazon and Atlantic. Geophysical Research Letters, 37(14), n/a-n/a. https://doi.org/10.1029/2010GL043486

Chen, F., Jia, J., Chen, J., Li, G., Zhang, X., Xie, H., Xia, D., Huang, W., & An, C. (2016). A persistent Holocene wetting trend in arid central Asia, with wettest conditions in the late Holocene, revealed by multi-proxy analyses of loess-paleosol sequences in Xinjiang, China. Quaternary Science Reviews, 146, 134–146. https://doi.org/10.1016/j.quascirev.2016.06.002

Cheng, H., Zhang, P. Z., Spötl, C., Edwards, R. L., Cai, Y. J., Zhang, D. Z., Sang, W. C., Tan, M., & An, Z. S. (2012). The climatic cyclicity in semiarid-arid central Asia over the past 500,000 years: Climatic cyclicity in Arid Central Asia. Geophysical Research Letters, 39(1), n/a-n/a. https://doi.org/10.1029/2011GL050202

Cheng, L., Song, Y., Wu, Y., Liu, Y., Liu, H., Chang, H., Zong, X., & Kang, S. (2021). Drivers for Asynchronous Patterns of Dust Accumulation in Central and Eastern Asia and in Greenland During the Last Glacial Maximum. Geophysical Research Letters, 48(5). https://doi.org/10.1029/2020GL091194

ChongYi, E., Lai, Z., Sun, Y., Hou, G., Yu, L., & Wu, C. (2012). A luminescence dating study of loess deposits from the Yili River basin in western China. Quaternary Geochronology, 10, 50–55. https://doi.org/10.1016/j.quageo.2012.04.022

Chu, G., Sun, Q., Zhaoyan, G., Rioual, P., Qiang, L., Kaijun, W., Han, J., & Liu, J. (2009). Dust records from varved lacustrine sediments of two neighboring lakes in northeastern China over the last 1400 years. Quaternary International, 194(1), 108–118. https://doi.org/10.1016/j.quaint.2008.08.005

Cilek, V. (2001). The loess deposits of the Bohemian Massif: Silt provenance, palaeometeorology and loessification processes. Quaternary International, 76–77, 123–128. https://doi.org/10.1016/S1040-6182(00)00096-3

Cohen, K. M., Finney, S. C., Gibbard, P. L., & Fan, J.-X. (2013). The ICS International Chronostratigraphic Chart. Episodes, 36(3), 199–204. https://doi.org/10.18814/epiiugs/2013/v36i3/002

Crouvi, O., Amit, R., Enzel, Y., & Gillespie, A. R. (2010). Active sand seas and the formation of desert loess. Quaternary Science Reviews, 29(17), 2087–2098. https://doi.org/10.1016/j.quascirev.2010.04.026

Ding, Z. L., Rutter, N. W., Sun, J. M., Yang, S. L., & Liu, T. S. (2000). Re-arrangement of atmospheric circulation at about 2.6Ma over northern China: Evidence from grain size records of loess-palaeosol and red clay sequences. Quaternary Science Reviews, 19(6), 547–558. https://doi.org/10.1016/S0277-3791(99)00017-7

Ding, H., Li, Y., Yang, Y., & Jia, X. (2019). Origin and evolution of modern loess science – 1824 to 1964. Journal of Asian Earth Sciences, 170, 45–55. https://doi.org/10.1016/j.jseaes.2018.10.024

Ding, Z. L., Derbyshire, E., Yang, S. L., Yu, Z. W., Xiong, S. F., & Liu, T. S. (2002). Stacked 2.6-Ma grain size record from the Chinese loess based on five sections and correlation with the deep-sea δ18O record. Paleoceanography, 17(3), 5-1-5–21. https://doi.org/10.1029/2001PA000725

Dodonov, A. E. (1991). Loess of Central Asia. GeoJournal, 24(2). https://doi.org/10.1007/BF00186015

Dodonov, A. E., & Baiguzina, L. L. (1995). Loess stratigraphy of Central Asia: Palaeoclimatic and palaeoenvironmental aspects. Aeolian Sediments in the Quaternary Record, 14(7), 707–720. https://doi.org/10.1016/0277-3791(95)00054-2

Fitzsimmons, K. E., Marković, S. B., & Hambach, U. (2012). Pleistocene environmental dynamics recorded in the loess of the middle and lower Danube basin. Quaternary Science Reviews, 41, 104–118. https://doi.org/10.1016/j.quascirev.2012.03.002

Fitzsimmons, K. E. (2017). Reconstructing palaeoenvironments on desert margins: New perspectives from Eurasian loess and Australian dry lake shorelines. Quaternary Science Reviews, 171, 1–19. https://doi.org/10.1016/j.quascirev.2017.05.018

Fitzsimmons, K. E., Iovita, R., Sprafke, T., Glantz, M., Talamo, S., Horton, K., Beeton, T., Alipova, S., Bekseitov, G., Ospanov, Y., Deom, J.-M., Sala, R., & Taimagambetov, Z. (2017). A chronological framework connecting the early Upper Palaeolithic across the Central Asian piedmont. Journal of Human Evolution, 113, 107–126. https://doi.org/10.1016/j.jhevol.2017.07.006

Fitzsimmons, K. E., Sprafke, T., Zielhofer, C., Günter, C., Deom, J.-M., Sala, R., & Iovita, R. (2018). Loess accumulation in the Tian Shan piedmont: Implications for palaeoenvironmental change in arid Central Asia. Quaternary International, 469, 30–43. https://doi.org/10.1016/j.quaint.2016.07.041

Fitzsimmons, K. E., Nowatzki, M., Dave, A. K., & Harder, H. (2020). Intersections between wind regimes, topography and sediment supply: Perspectives from aeolian landforms in Central Asia. Palaeogeography, Palaeoclimatology, Palaeoecology, 540, 109531. https://doi.org/10.1016/j.palaeo.2019.109531

Forman, S. L., Arthur Bettis, E., Kemmis, T. J., & Miller, B. B. (1992). Chronologic evidence for multiple periods of loess deposition during the Late Pleistocene in the Missouri and Mississippi River Valley, United States: Implications for the activity of the Laurentide ice sheet. Palaeogeography, Palaeoclimatology, Palaeoecology, 93(1), 71–83. https://doi.org/10.1016/0031-0182(92)90184-7

Forster, Th., & Heller, F. (1994). Loess deposits from the Tajik depression (Central Asia): Magnetic properties and paleoclimate. Earth and Planetary Science Letters, 128(3–4), 501–512. https://doi.org/10.1016/0012-821X(94)90166-X

Glantz, M. H., & Zonn, I. S. (2005). The Aral Sea: Water, Climate and Environmental Change in Central Asia. Geneva: World Meteorological Organization.

Hefflin, B. J., Jalaludin, B., McClure, E., Cobb, N., Johnson, C. A., Jecha, L., & Etzel, R. A. (1994). Surveillance for Dust Storms and Respiratory Diseases in Washington State, 1991. Archives of Environmental Health: An International Journal, 49(3), 170–174. https://doi.org/10.1080/00039896.1994.9940378

Heller, F., & Tung-sheng, L. (1982). Magnetostratigraphical dating of loess deposits in China. Nature, 300(5891), 431–433. https://doi.org/10.1038/300431a0

Hovan, S. A., Rea, D. K., Pisias, N. G., & Shackleton, N. J. (1989). A direct link between the China loess and marine δ18O records: Aeolian flux to the north Pacific. Nature, 340(6231), 296–298. https://doi.org/10.1038/340296a0

Huang, J., Yu, H., Guan, X., Wang, G., & Guo, R. (2016). Accelerated dryland expansion under climate change. Nature Climate Change, 6(2), 166–171. https://doi.org/10.1038/nclimate2837

Huo, W., et al. (2014), Simulation of Tacheng 3.12 east-wind sandstorm, Desert Oasis Meteorol., 8(4), 26–31. (In Chinese with English abstract). (n.d.).

Jia, J., Liu, H., Gao, F., & Xia, D. (2018). Variations in the westerlies in Central Asia since 16 ka recorded by a loess section from the Tien Shan Mountains. Palaeogeography, Palaeoclimatology, Palaeoecology, 504, 156–161. https://doi.org/10.1016/j.palaeo.2018.05.021

Kang, S., Wang, X., Lu, Y., Liu, W., Song, Y., & Wang, N. (2015). A high-resolution quartz OSL chronology of the Talede loess over the past ∼30 ka and its implications for dust accumulation in the Ili Basin, Central Asia. LED14 Proceedings, 30, 181–187. https://doi.org/10.1016/j.quageo.2015.04.006

Khaniabadi, Y. O., Fanelli, R., De Marco, A., Daryanoosh, S. M., Kloog, I., Hopke, P. K., Conti, G. O., Ferrante, M., Mohammadi, M. J., Babaei, A. A., Basiri, H., & Goudarzi, G. (2017). Hospital admissions in Iran for cardiovascular and respiratory diseases attributed to the Middle Eastern Dust storms. Environmental Science and Pollution Research, 24(20), 16860–16868. https://doi.org/10.1007/s11356-017-9298-5

Kohfeld, K. E., & Harrison, S. P. (2003). Glacial-interglacial changes in dust deposition on the Chinese Loess Plateau.Quaternary Science Reviews, 22(18), 1859–1878. https://doi.org/10.1016/S0277-3791(03)00166-5

Kok, J. F., Adebiyi, A. A., Albani, S., Balkanski, Y., Checa-Garcia, R., Chin, M., Colarco, P. R., Hamilton, D. S., Huang, Y., Ito, A., Klose, M., Li, L., Mahowald, N. M., Miller, R. L., Obiso, V., Pérez García-Pando, C., Rocha-Lima, A., & Wan, J. S. (2021). Contribution of the world's main dust source regions to the global cycle of desert dust. Atmospheric Chemistry and Physics Discussions, 2021, 1–34. https://doi.org/10.5194/acp-2021-4

Krinner, G., Boucher, O., & Balkanski, Y. (2006). Ice-free glacial northern Asia due to dust deposition on snow. Climate Dynamics, 27(6), 613–625. https://doi.org/10.1007/s00382-006-0159-z

Kukla, G., Heller, F., Ming, L. X., Chun, X. T., Sheng, L. T., & Sheng, A. Z. (1988). Pleistocene climates in China dated by magnetic susceptibility. Geology, 16(9), 811–814. https://doi.org/10.1130/0091-7613(1988)016<0811:PCICDB>2.3.CO;2

Kukla, G. J. (1977). Pleistocene land—Sea correlations I. Europe. Earth-Science Reviews, 13(4), 307–374. https://doi.org/10.1016/0012-8252(77)90125-8

Lancaster, N. (2020). On the formation of desert loess. Quaternary Research, 96, 105–122. Cambridge Core. https://doi.org/10.1017/qua.2020.33

Letelier, R. M., Björkman, K. M., Church, M. J., Hamilton, D. S., Mahowald, N. M., Scanza, R. A., Schneider, N., White, A. E., & Karl, D. M. (2019). Climate-driven oscillation of phosphorus and iron limitation in the North

Pacific Subtropical Gyre. Proceedings of the National Academy of Sciences, 116(26), 12720. https://doi.org/10.1073/pnas.1900789116

Li, Y., Song, Y., Yan, L., Chen, T., & An, Z. (2015a). Timing and Spatial Distribution of Loess in Xinjiang, NW China. PLOS ONE, 10(5), e0125492. https://doi.org/10.1371/journal.pone.0125492

Li, G., Wen, L., Xia, D., Duan, Y., Rao, Z., Madsen, D. B., Wei, H., Li, F., Jia, J., & Chen, F. (2015b). Quartz OSL and K-feldspar pIRIR dating of a loess/paleosol sequence from arid central Asia, Tianshan Mountains, NW China. Quaternary Geochronology, 28, 40–53. https://doi.org/10.1016/j.quageo.2015.03.011

Li, Y., Song, Y., Lai, Z., Han, L., & An, Z. (2016a). Rapid and cyclic dust accumulation during MIS 2 in Central Asia inferred from loess OSL dating and grain-size analysis. Scientific Reports, 6(1), 32365. https://doi.org/10.1038/srep32365

Li, Y., Yang, S., Wang, X., Hu, J., Cui, L., Huang, X., & Jiang, W. (2016b). Leaf wax n-alkane distributions in Chinese loess since the Last Glacial Maximum and implications for paleoclimate. Quaternary International, 399, 190–197. https://doi.org/10.1016/j.quaint.2015.04.029

Li, G., Rao, Z., Duan, Y., Xia, D., Wang, L., Madsen, D. B., Jia, J., Wei, H., Qiang, M., Chen, J., & Chen, F. (2016c). Paleoenvironmental changes recorded in a luminescence dated loess/paleosol sequence from the Tianshan Mountains, arid central Asia, since the Penultimate Glaciation. Earth and Planetary Science Letters, 448, 1–12. https://doi.org/10.1016/j.epsl.2016.05.008

Li, Y., Song, Y., Fitzsimmons, K. E., Chen, X., Wang, Q., Sun, H., & Zhang, Z. (2018a). New evidence for the provenance and formation of loess deposits in the Ili River Basin, Arid Central Asia. Aeolian Research, 35, 1–8. https://doi.org/10.1016/j.aeolia.2018.08.002

Li, G., Chen, F., Xia, D., Yang, H., Zhang, X., Madsen, D., Oldknow, C., Wei, H., Rao, Z., & Qiang, M. (2018b). A Tianshan Mountains loess-paleosol sequence indicates anti-phase climatic variations in arid central Asia and in East Asia. Earth and Planetary Science Letters, 494, 153–163. https://doi.org/10.1016/j.epsl.2018.04.052

Li, Y., Song, Y., Kaskaoutis, D. G., Chen, X., Mamadjanov, Y., & Tan, L. (2019a). Atmospheric dust dynamics in southern Central Asia: Implications for buildup of Tajikistan loess sediments. Atmospheric Research, 229, 74–85. https://doi.org/10.1016/j.atmosres.2019.06.013

Li, Y., Song, Y., Yin, Q., Han, L., & Wang, Y. (2019b) Orbital and millennial northern mid-latitude westerlies over the last glacial period. Climate Dynamics, 53(5–6), 3315–3324. https://doi.org/10.1007/s00382-019-04704-5

Li, Y., Song, Y., Qiang, M., Miao, Y., & Zeng, M. (2019c). Atmospheric Dust Variations in the Ili Basin, Northwest China, During the Last Glacial Period as Revealed by a High Mountain Loess-Paleosol Sequence. Journal of Geophysical Research: Atmospheres, 124(15), 8449–8466. https://doi.org/10.1029/2019JD030470

Li, Y., Shi, W., Aydin, A., Beroya-Eitner, M. A., & Gao, G. (2020a). Loess genesis and worldwide distribution. Earth-Science Reviews, 201, 102947. https://doi.org/10.1016/j.earscirev.2019.102947

Li, Y., Song, Y., Fitzsimmons, K. E., Chen, X., Prud'homme, C., & Zong, X. (2020b). Origin of loess deposits in the North Tian Shan piedmont, Central Asia. Palaeogeography, Palaeoclimatology, Palaeoecology, 559, 109972. https://doi.org/10.1016/j.palaeo.2020.109972

Li, G., Yang, H., Stevens, T., Zhang, X., Zhang, H., Wei, H., Zheng, W., Li, L., Liu, X., Chen, J., Xia, D., Oldknow, C., Ye, W., & Chen, F. (2020c). Differential ice volume and orbital modulation of Quaternary moisture patterns between Central and East Asia. Earth and Planetary Science Letters, 530, 115901. https://doi.org/10.1016/j.epsl.2019.115901

Li, Y., & Song, Y. (2020). Discussion of the paper “Loess genesis and worldwide distribution” by Yanrong Li, Wenhui Shi, Adnan Aydin, et al. Earth-Science Reviews, 103151. https://doi.org/10.1016/j.earscirev.2020.103151

Liu, T. S. (1985). Loess and Environment. China Ocean Press (Beijing).

Liu, Y., Liu, X., Ma, L., Kang, S., Qiang, X., Guo, F., & Sun, Y. (2020). Temporal–spatial variations in aeolian flux on the Chinese Loess Plateau during the last 150 ka. Geological Magazine, 157(5), 757–767. https://doi.org/10.1017/S0016756819001067

Lydolph, P. E. (1977). Climates of the Soviet Union. Elsevier Scientific Pub. Co.

Machalett, B., Frechen, M., Hambach, U., Oches, E. A., Zöller, L., & Marković, S. B. (2006). The loess sequence from Remisowka (northern boundary of the Tien Shan Mountains, Kazakhstan)—Part I: Luminescence dating. Quaternary International, 152–153, 192–201. https://doi.org/10.1016/j.quaint.2005.12.014

Machalett, B., Oches, E. A., Frechen, M., Zöller, L., Hambach, U., Mavlyanova, N. G., Marković, S. B., & Endlicher, W. (2008). Aeolian dust dynamics in central Asia during the Pleistocene: Driven by the long-term migration, seasonality, and permanency of the Asiatic polar front: Aeolian dust dynamics in Central Asia. Geochemistry, Geophysics, Geosystems, 9(8). https://doi.org/10.1029/2007GC001938

Marković, S. B., Oches, E. A., McCoy, W. D., Frechen, M., & Gaudenyi, T. (2007). Malacological and sedimentological evidence for “warm” glacial climate from the Irig loess sequence, Vojvodina, Serbia. Geochemistry, Geophysics, Geosystems, 8(9). https://doi.org/10.1029/2006GC001565

Marković, S. B., Stevens, T., Kukla, G. J., Hambach, U., Fitzsimmons, K. E., Gibbard, P., Buggle, B., Zech, M., Guo, Z., Hao, Q., Wu, H., O’Hara Dhand, K., Smalley, I. J., Újvári, G., Sümegi, P., Timar-Gabor, A., Veres, D., Sirocko, F., Vasiljević, D. A., … Svirčev, Z. (2015). Danube loess stratigraphy—Towards a pan-European loess stratigraphic model. Earth-Science Reviews, 148, 228–258. https://doi.org/10.1016/j.earscirev.2015.06.005

Martin, J. H. (1990). Glacial-interglacial CO 2 change: The Iron Hypothesis. Paleoceanography, 5(1), 1–13. https://doi.org/10.1029/PA005i001p00001

Martínez-García, A., Sigman, D. M., Ren, H., Anderson, R. F., Straub, M., Hodell, D. A., Jaccard, S. L., Eglinton, T. I., & Haug, G. H. (2014). Iron Fertilization of the Subantarctic Ocean During the Last Ice Age. Science, 343(6177), 1347. https://doi.org/10.1126/science.1246848

Meng, X., Liu, L., Zhao, W., He, T., Chen, J., & Ji, J. (2019). Distant Taklimakan Desert as an Important Source of Aeolian Deposits on the Chinese Loess Plateau as Evidenced by Carbonate Minerals. Geophysical Research Letters, 46(9), 4854–4862. https://doi.org/10.1029/2018GL081551

Mischke, S., Zhang, C., & Plessen, B. (2020). Lake Balkhash (Kazakhstan): Recent human impact and natural variability in the last 2900 years. Journal of Great Lakes Research, 46(2), 267–276. https://doi.org/10.1016/j.jglr.2020.01.008

Moine, O., Rousseau, D.-D., & Antoine, P. (2008). Terrestrial molluscan records of Weichselian Lower to Middle Pleniglacial climatic changes from the Nussloch loess series (Rhine Valley, Germany): The impact of local factors. Boreas, 34(3), 363–380. https://doi.org/10.1111/j.1502-3885.2005.tb01107.x

Moine, O., Rousseau, D.-D., Jolly, D., & Vianey-Liaud, M. (2002). Paleoclimatic Reconstruction Using Mutual Climatic Range on Terrestrial Mollusks. Quaternary Research, 57(1), 162–172. Cambridge Core. https://doi.org/10.1006/qres.2001.2286

Muhs, D. R., & Bettis, A. E. (2003). Quaternary loess-Paleosol sequences as examples of climate-driven sedimentary extremes. In M. A. Chan & A. W. Archer, Extreme depositional environments: Mega end members in geologic time. Geological Society of America. https://doi.org/10.1130/0-8137-2370-1.53

Muhs, D. R., Prins, M. A., & Machalett, B. (2014a). Loess as a Quaternary paleoenvironmental indicator. Past Global Changes, 22(2), 84–85. https://doi.org/10.22498/pages.22.2

Muhs, D. R., Cattle, S. R., Crouvi, O., Rousseau, D.-D., Sun, J., & Zárate, M. A. (2014b). Loess Records. In P. Knippertz & J.-B. W. Stuut (Eds.), Mineral Dust (pp. 411–441). Springer Netherlands. https://doi.org/10.1007/978-94-017-8978-3_16

Muhs, D. R. (2014c). Origins and Properties of Quaternary Loess Deposits. In Reference Module in Earth Systems and Environmental Sciences. Elsevier. https://doi.org/10.1016/B978-0-12-409548-9.09431-8

Munroe, J. S., McElroy, R., O'Keefe, S., Peters, A., & Wasson, L. (2021). Holocene records of eolian dust deposition from high-elevation lakes in the Uinta Mountains, Utah, USA. Journal of Quaternary Science, 36(1), 66–75. https://doi.org/10.1002/jqs.3250

Nakai, S., Halliday, A. N., & Rea, D. K. (1993). Provenance of dust in the Pacific Ocean. Earth and Planetary Science Letters, 119(1), 143–157. https://doi.org/10.1016/0012-821X(93)90012-X

Nie, J., Stevens, T., Rittner, M., Stockli, D., Garzanti, E., Limonta, M., Bird, A., Andò, S., Vermeesch, P., Saylor, J., Lu, H., Breecker, D., Hu, X., Liu, S., Resentini, A., Vezzoli, G., Peng, W., Carter, A., Ji, S., & Pan, B. (2015). Loess Plateau storage of Northeastern Tibetan Plateau-derived Yellow River sediment. Nature Communications, 6(1), 8511. https://doi.org/10.1038/ncomms9511

Obruchev, V. A. (1945). Loess types and their origin. American Journal of Science, 243(5), 256–262. https://doi.org/10.2475/ajs.243.5.256

Odom, A. L., & Rink, W. J. (1989). Natural accumulation of Schottky-Frenkel defects: Implications for a quartz geochronometer. Geology, 17(1), 55–58. https://doi.org/10.1130/0091-7613(1988)017<0055:NAOSFD>2.3.CO;2

Pécsi, M., 1968. Loess. In: Fairbridge, R.W. (Ed). Encyclopedia of Geomorphology. Reinhold Book Corporation, New York, 674–678.

Pécsi, M. (1990). Loess is not just the accumulation of dust. Quaternary International, 7–8, 1–21. https://doi.org/10.1016/1040-6182(90)90034-2

Pécsi, M. (1995). The role of principles and methods in loess-paleosol investigations. GeoJournal, 36(2–3), 117–131. https://doi.org/10.1007/BF00813156

Pécsi, M., Richter., G. (1996). Löss: Herkunft – Gliederung – Landschaften Zeitschrift für Geomorphologie N.F. Supplementband, 98. Gebrüder Bornträger, Berlin & Stuttgart.

Peterse, F., Prins, M. A., Beets, C. J., Troelstra, S. R., Zheng, H., Gu, Z., Schouten, S., & Damsté, J. S. S. (2011). Decoupled warming and monsoon precipitation in East Asia over the last deglaciation. Earth and Planetary Science Letters, 301(1), 256–264. https://doi.org/10.1016/j.epsl.2010.11.010

Porter, S. C., & An, Z. (1995). Correlation between climate events in the North Atlantic and China during the last glaciation. Nature, 375(6529), 305–308. https://doi.org/10.1038/375305a0

Prud'homme, C., Lécuyer, C., Antoine, P., Hatté, C., Moine, O., Fourel, F., Amiot, R., Martineau, F., & Rousseau, D.-D. (2018). δ13C signal of earthworm calcite granules: A new proxy for palaeoprecipitation reconstructions during the Last Glacial in western Europe. Quaternary Science Reviews, 179, 158–166. https://doi.org/10.1016/j.quascirev.2017.11.017

Prud'homme, C., Lécuyer, C., Antoine, P., Moine, O., Hatté, C., Fourel, F., Martineau, F., & Rousseau, D.-D. (2016). Palaeotemperature reconstruction during the Last Glacial from δ18O of earthworm calcite granules from Nussloch loess sequence, Germany. Earth and Planetary Science Letters, 442, 13–20. https://doi.org/10.1016/j.epsl.2016.02.045

Pye, K. (1987). Aeolian Dust and Dust Deposits. Academic Press, London.

Pye, K. (1995). The nature, origin and accumulation of loess. Aeolian Sediments in the Quaternary Record, 14(7), 653–667. https://doi.org/10.1016/0277-3791(95)00047-X

Rousseau, D.-D., Derbyshire, E., Antoine, P., & Hatté, C. (2007). Loess Records | Europe. In S. A. Elias (Ed.), Encyclopedia of Quaternary Science (pp. 1440–1456). Elsevier. https://doi.org/10.1016/B0-44-452747-8/00162-9

Rozycki, S. Z. (1991). Loess and Loess-like Deposits. Ossolineum-Polish Academy of Sciences.

Schaetzl, R. J., Bettis, E. A., Crouvi, O., Fitzsimmons, K. E., Grimley, D. A., Hambach, U., Lehmkuhl, F., Marković, S. B., Mason, J. A., Owczarek, P., Roberts, H. M., Rousseau, D.-D., Stevens, T., Vandenberghe, J., Zárate, M., Veres, D., Yang, S., Zech, M., Conroy, J. L., … Zech, R. (2018, May). Approaches and challenges to the study of loess—Introduction to the LoessFest Special Issue. Quaternary Research; Cambridge University Press. https://doi.org/10.1017/qua.2018.15

Schaffernicht, E. J., Ludwig, P., & Shao, Y. (2020). Linkage between dust cycle and loess of the Last Glacial Maximum in Europe. Atmospheric Chemistry and Physics, 20(8), 4969–4986. https://doi.org/10.5194/acp-20-4969-2020

Simonsen, M. F., Baccolo, G., Blunier, T., Borunda, A., Delmonte, B., Frei, R., Goldstein, S., Grinsted, A., Kjær, H. A., Sowers, T., Svensson, A., Vinther, B., Vladimirova, D., Winckler, G., Winstrup, M., & Vallelonga, P. (2019). East Greenland ice core dust record reveals timing of Greenland ice sheet advance and retreat. Nature Communications, 10(1), 4494. https://doi.org/10.1038/s41467-019-12546-2

Smalley, I. (1995). Making the material: The formation of silt sized primary mineral particles for loess deposits. Aeolian Sediments in the Quaternary Record, 14(7), 645–651. https://doi.org/10.1016/0277-3791(95)00046-1

Smalley, I. J. (1966). The properties of glacial loess and the formation of loess deposits. Journal of Sedimentary Petrology, 36(3), 669–676.

Smalley, I. J., & Derbyshire, E. (1990). The definition of ice-sheet and mountain loess. Area, 22(3), 300–301.

Smalley, I. J., Jefferson, I. F., Dijkstra, T. A., & Derbyshire, E. (2001). Some major events in the development of the scientific study of loess. Recent Research on Loess and Palaeosols, Pure and Applied, 54(1), 5–18. https://doi.org/10.1016/S0012-8252(01)00038-1

Smalley, I. J., & Vita-Finzi, C. (1968). The formation of fine particles in sandy deserts and the nature of 'desert' loess. Journal of Sedimentary Petrology, 38(3), 766–774.

Smalley, I., Marković, S. B., & Svirčev, Z. (2011). Loess is [almost totally formed by] the accumulation of dust. The Second Loessfest (2009), 240(1), 4–11. https://doi.org/10.1016/j.quaint.2010.07.011

Smalley, I., & Obreht, I. (2018). The formation of loess ground by the process of loessification: A history of the concept. Geologos, 24(2), 163–170. https://doi.org/10.2478/logos-2018-0015

Smalley, I., O'Hara-Dhand, K., & Kwong, J. (2014). China: Materials for a loess landscape. Loess and Dust Dynamics, Environments, Landforms, and Pedogenesis: A Tribute to Edward Derbyshire, 117, 100–107. https://doi.org/10.1016/j.catena.2013.11.016

Smalley, I., O'Hara-Dhand, K., Wint, J., Machalett, B., Jary, Z., & Jefferson, I. (2009). Rivers and loess: The significance of long river transportation in the complex event-sequence approach to loess deposit formation. Loess in the Danube Region and Surrounding Loess Provinces: The Marsigli Memorial Volume, 198(1), 7–18. https://doi.org/10.1016/j.quaint.2008.06.009

Smith, B. J., Wright, J. S., & Whalley, W. B. (2002). Sources of non-glacial, loess-size quartz silt and the origins of "desert loess". Earth-Science Reviews, 59(1), 1–26. https://doi.org/10.1016/S0012-8252(02)00066-1

Song, Y., Li, C., Zhao, J., Cheng, P., & Zeng, M. (2012). A combined luminescence and radiocarbon dating study of the Ili loess, Central Asia.Quaternary Geochronology, 10, 2–7. https://doi.org/10.1016/j.quageo.2012.04.005

Song, Y., Chen, X., Qian, L., Li, C., Li, Y., Li, X., Chang, H., & An, Z. (2014). Distribution and composition of loess sediments in the Ili Basin, Central Asia. Quaternary International, 334–335, 61–73. https://doi.org/10.1016/j.quaint.2013.12.053

Song, Y., Lai, Z., Li, Y., Chen, T., & Wang, Y. (2015). Comparison between luminescence and radiocarbon dating of late Quaternary loess from the Ili Basin in Central Asia. Quaternary Geochronology, 30, 405–410. https://doi.org/10.1016/j.quageo.2015.01.012

Sprafke, T., & Obreht, I. (2016). Loess: Rock, sediment or soil – What is missing for its definition? Quaternary International, 399, 198–207. https://doi.org/10.1016/j.quaint.2015.03.033

Sprafke, T., Fitzsimmons, K. E., Grützner, C., Elliot, A., Marquer, L., & Nigmatova, S. (2018). Reevaluation of Late Pleistocene loess profiles at Remizovka (Kazakhstan) indicates the significance of topography in evaluating terrestrial paleoclimate records. Quaternary Research, 89(3), 674–690. https://doi.org/10.1017/qua.2017.103

Stevens, T., Buylaert, J.-P., Thiel, C., Újvári, G., Yi, S., Murray, A. S., Frechen, M., & Lu, H. (2018). Ice-volume-forced erosion of the Chinese Loess Plateau global Quaternary stratotype site. Nature Communications, 9(1), 983. https://doi.org/10.1038/s41467-018-03329-2

Stevens, T., Carter, A., Watson, T. P., Vermeesch, P., Andò, S., Bird, A. F., Lu, H., Garzanti, E., Cottam, M. A., & Sevastjanova, I. (2013). Genetic linkage between the Yellow River, the Mu Us desert and the Chinese Loess Plateau. Quaternary Science Reviews, 78, 355–368. https://doi.org/10.1016/j.quascirev.2012.11.032

Sun, J. (2002a). Source Regions and Formation of the Loess Sediments on the High Mountain Regions of Northwestern China. Quaternary Research, 58(3), 341–351. https://doi.org/10.1006/qres.2002.2381

Sun, J. (2002b). Provenance of loess material and formation of loess deposits on the Chinese Loess Plateau. Earth and Planetary Science Letters, 203(3), 845–859. https://doi.org/10.1016/S0012-821X(02)00921-4

Sun, Y., & An, Z. (2005). Late Pliocene-Pleistocene changes in mass accumulation rates of eolian deposits on the central Chinese Loess Plateau. Journal of Geophysical Research, 110(D23), D23101. https://doi.org/10.1029/2005JD006064

Sun, Y., Clemens, S. C., Morrill, C., Lin, X., Wang, X., & An, Z. (2012). Influence of Atlantic meridional overturning circulation on the East Asian winter monsoon. Nature Geoscience, 5(1), 46–49. https://doi.org/10.1038/ngeo1326

Sun, A., Guo, Z., Wu, H., Li, Q., Yu, Y., Luo, Y., Jiang, W., & Li, X. (2017). Reconstruction of the vegetation distribution of different topographic units of the Chinese Loess Plateau during the Holocene. Quaternary Science Reviews, 173, 236–247. https://doi.org/10.1016/j.quascirev.2017.08.006

Svensson, A., Biscaye, P. E., & Grousset, F. E. (2000). Characterization of late glacial continental dust in the Greenland Ice Core Project ice core. Journal of Geophysical Research: Atmospheres, 105(D4), 4637–4656. https://doi.org/10.1029/1999JD901093

Svirčev, Z., Marković, S. B., Stevens, T., Codd, G. A., Smalley, I., Simeunović, J., Obreht, I., Dulić, T., Pantelić, D., & Hambach, U. (2013). Importance of biological loess crusts for loess formation in semi-arid environments. Quaternary International, 296, 206–215. https://doi.org/10.1016/j.quaint.2012.10.048

Swap, R., Garstang, M., Greco, S., Talbot, R., & Kållberg, P. (1992). Saharan dust in the Amazon Basin. Tellus B: Chemical and Physical Meteorology, 44(2), 133–149. https://doi.org/10.3402/tellusb.v44i2.15434

Tao, Y., An, X., Sun, Z., Hou, Q., & Wang, Y. (2012). Association between dust weather and number of admissions for patients with respiratory diseases in spring in Lanzhou. Science of The Total Environment, 423, 8–11. https://doi.org/10.1016/j.scitotenv.2012.01.064

Tsoar, H., & Pye, K. (1987). Dust transport and the question of desert loess formation. Sedimentology, 34(1), 139–153. https://doi.org/10.1111/j.1365-3091.1987.tb00566.x

Vandenberghe, J., Renssen, H., van Huissteden, K., Nugteren, G., Konert, M., Lu, H., Dodonov, A., & Buylaert, J.-P. (2006). Penetration of Atlantic westerly winds into Central and East Asia. Quaternary Science Reviews, 25(17), 2380–2389. https://doi.org/10.1016/j.quascirev.2006.02.017

Vriend, M., Prins, M. A., Buylaert, J.-P., Vandenberghe, J., & Lu, H. (2011). Contrasting dust supply patterns across the north-western Chinese Loess Plateau during the last glacial-interglacial cycle. Quaternary International, 240(1), 167–180. https://doi.org/10.1016/j.quaint.2010.11.009

Wang, L., Jia, J., Xia, D., Liu, H., Gao, F., Duan, Y., Wang, Q., Xie, H., & Chen, F. (2019a). Climate change in arid central Asia since MIS 2 revealed from a loess sequence in Yili Basin, Xinjiang, China. Quaternary International, 502, 258–266. https://doi.org/10.1016/j.quaint.2018.02.032

Wang, L., Jia, J., Zhao, H., Liu, H., Duan, Y., Xie, H., Zhang, D. D., & Chen, F. (2019b). Optical dating of Holocene paleosol development and climate changes in the Yili Basin, arid central Asia. The Holocene, 29(6), 1068–1077. https://doi.org/10.1177/0959683619831432

Wright, J. S. (2001). "Desert" loess versus "glacial" loess: Quartz silt formation, source areas and sediment pathways in the formation of loess deposits. Geomorphology, 36(3), 231–256. https://doi.org/10.1016/S0169-555X(00)00060-X

Yan, D., Xu, H., Lan, J., Zhou, K., Ye, Y., Zhang, J., An, Z., & Yeager, K. M. (2019). Solar activity and the westerlies dominate decadal hydroclimatic changes over arid Central Asia. Global and Planetary Change, 173, 53–60. https://doi.org/10.1016/j.gloplacha.2018.12.006

Yang, S., & Ding, Z. (2008). Advance–retreat history of the East-Asian summer monsoon rainfall belt over northern China during the last two glacial–interglacial cycles. Earth and Planetary Science Letters, 274(3), 499–510. https://doi.org/10.1016/j.epsl.2008.08.001

Yang, S., & Ding, Z. (2010). Drastic climatic shift at ∼2.8Ma as recorded in eolian deposits of China and its implications for redefining the Pliocene-Pleistocene boundary. Plio-Pleistocene Correlation and Global Change, 219(1), 37–44. https://doi.org/10.1016/j.quaint.2009.10.029

Youn, J. H., Seong, Y. B., Choi, J. H., Abdrakhmatov, K., & Ormukov, C. (2014). Loess deposits in the northern Kyrgyz Tien Shan: Implications for the paleoclimate reconstruction during the Late Quaternary. Catena, 117, 81–93. https://doi.org/10.1016/j.catena.2013.09.007

Zech, M., Rass, S., Buggle, B., Löscher, M., & Zöller, L. (2012). Reconstruction of the late Quaternary paleoenvironments of the Nussloch loess paleosol sequence, Germany, using n-alkane biomarkers. Quaternary Research, 78(2), 226–235. Cambridge Core. https://doi.org/10.1016/j.yqres.2012.05.006

Zeeden, C., Hambach, U., Veres, D., Fitzsimmons, K., Obreht, I., Bösken, J., & Lehmkuhl, F. (2018). Millennial scale climate oscillations recorded in the Lower Danube loess over the last glacial period. Palaeogeography, Palaeoclimatology, Palaeoecology, 509, 164–181. https://doi.org/10.1016/j.palaeo.2016.12.029

Footnote References

IUPAC (1990). Glossary of atmospheric chemistry terms. International Union of Pure and Applied Chemistry, Applied Chemistry Division, Commission on Atmospheric Chemistry. Pure and Applied Chemistry 62 (11), 2167-2219.

IPCC (2019): Climate Change and Land: an IPCC special report on climate change, desertification, land degradation, sustainable land management, food security, and greenhouse gas fluxes in terrestrial ecosystems [P.R. Shukla, J. Skea, E. Calvo Buendia, V. Masson-Delmotte, H.-O. Pörtner, D. C. Roberts, P. Zhai, R. Slade, S. Connors, R. van Diemen, M. Ferrat, E. Haughey, S. Luz, S. Neogi, M. Pathak, J. Petzold, J. Portugal Pereira, P. Vyas, E. Huntley, K. Kissick, M. Belkacemi, J. Malley, (eds.)]. In press. Online access: https://www.ipcc.ch/srccl/

2. Chapter 2

Methodology: Basic principles and concepts

This chapter describes the scientific methodology used during the course of this thesis, with a focus on the fundamental principles and concepts of the techniques employed. The sample preparation and instrumentation are described in detail as per its application in the subsequent chapters. In case any aspect of the investigation was conducted by an individual and/or organization other than myself, the relevant contribution has been duly acknowledged here as well as in the relevant chapter.

The core of this doctoral work is focused on utilising two well-known trapped charge techniques: Luminescence and Electron Spin Resonance (ESR), to investigate the timing and provenance of loess deposits in Central Asia. The chronology and provenance work is supported by stratigraphic data, micromorphology, grain size analysis and magnetic susceptibility measurements. This chapter gives a detailed description of the principles and concepts underlying the application of trapped charge techniques as classical dating tools and as provenance indicators. Furthermore, this section also discusses the basis and application of proxy indices (grain size, magnetic susceptibility and micromorphology) to the study of loess archives.

2.1. Geochronology: Luminescence dating

Luminescence comes from the latin word 'lumen' meaning 'light', and refers to the spontaneous emission of light. The phenomenon of luminescence in nature has been reported since historical times with multiple evidences found in mythological texts – whether it's the auroras lighting up the night sky or the fire-flies illuminating a dark night! One of the earliest observations of luminescence from a mineral, was reported by Robert Boyle (Boyle, 1664); when Boyle decided to go to bed with a diamond (!) – well, that lead to one of the first observations of thermoluminescence, i.e., emission of luminescence due to application of heat. The word luminescence was first used by German physicist Eilhardt Wiedemann (Wiedemann, 1888), who later proceeded to differentiate between six different types of luminescence based on the method of excitation: photoluminescence (due to light), thermoluminescence (heat), chemiluminescence (chemical reaction), electroluminescence (electric current), crystalloluminescence (crystallisation processes) and triboluminescence (crushing of crystals). Of these, the phenomena of photoluminescence and thermoluminescence forms the basis of the luminescence dating method.

Luminescence dating is one of the most widely applied absolute dating techniques to sedimentary archives in the Quaternary (Aitken, 1985, 1998; Preusser et al., 2008). Up until the 1940's, Thermoluminescence (TL) was used as a tool to identify minerals, but with the development of a highly sensitive detector such as the photomultiplier tube, other applications of TL gained impetus (Aitken, 1985). TL studies in the field of dating began with its application in dating pottery (Daniels et al., 1953; Aitken et al., 1964; Ralph and Han, 1966). TL was first applied to dating of sediments by Wintle and Huntley (1979). This application was superseded by the application of Optically stimulated luminescence (OSL) that utilises optical stimulation by light to date quartz and feldspar minerals respectively (Huntley et al., 1985; Hütt et al., 1988). Since then, measurement techniques and protocols have advanced greatly, especially with the development of the single aliquot regenerative (SAR) protocol, which has revolutionized the field of luminescence dating (Murray and Wintle, 2000, 2003).

Luminescence dating is a technique that allows one to date the event when mineral grains like quartz and feldspar were last exposed to light or heat (Aitken, 1998). In nature, exposure to sunlight (e.g. during erosion, transport and deposition) or heating to high temperatures (e.g., during firing of pottery or burning of flints in a hearth) can lead to resetting (commonly referred to as 'bleaching') of the geological and /or accrued signal in the mineral grains. After its final burial or deposition, the luminescence signal in the mineral grains starts building up again due to the ionising radiation received from the decay of radioactive isotopes of uranium (U), thorium (Th) and potassium (K) and their daughter products, as well as cosmic rays from the sun (Aitken, 1998). The stored luminescence signal is then measured in the laboratory under optical (OSL) or thermal (TL) stimulation using a photomultiplier tube. This measured luminescence corresponds to the amount of ionising radiation received by the sample during its burial period and is known as the equivalent dose (D_e) or palaeodose. A schematic of the aforementioned process is shown in Fig. 2.1. Now, since one can evaluate the equivalent dose (or radiation received during the burial period) in the laboratory, then by determining the rate of ionising radiation, we can calculate the age of the mineral grains simply by using the equation:

$$Age = \frac{Equivalent\ dose\ [Gy]}{Dose\ rate\left[\frac{Gy}{yr}\right]}$$

(Eq. 2.1)

where,

Gy (Gray) = unit of absorbed radiation dose = J/kg

This technique can be applied to a wide variety of quartz and feldspar containing materials like sedimentary deposits, rocks, heated pottery and burnt flints (Aitken, 1998) A lot of

minerals are known to exhibit luminescence properties; however, one can only effectively date crystalline minerals of quartz and feldspar. This is because, these minerals are easily bleached and their luminescence signal remains stable over geological timescales (Aitken, 1985). They also show minimal change in sensitivity to the applied radiation dose and the physical behaviour of the signal growth curve (i.e., the radiation dose response curve) can be studied using mathematical functions (Preusser et al., 2008). In addition, the ubiquitousness of quartz and feldspar minerals in nature, makes this technique, one of the most commonly applied absolute dating tools in geology and archaeology.

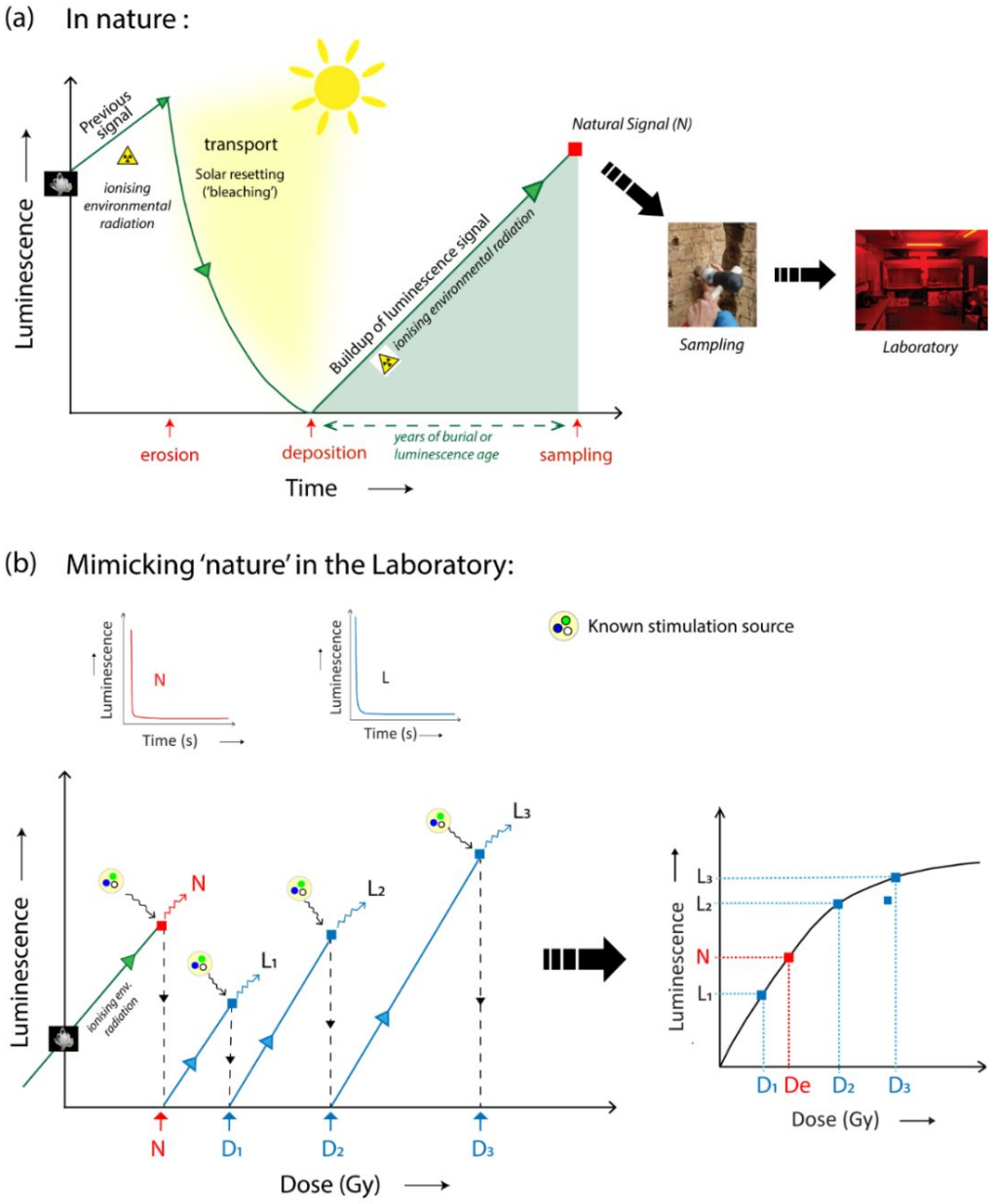

Fig. 2.1. Basic concept of luminescence dating (based on the description of luminescence dating by Aitken, 1998).

Physical phenomena underlying the luminescence dating technique

The physical basis of the luminescence dating technique can be explained via the energy level diagram (commonly known as the 'Band model'; based on Aitken, 1985; Duller, 2008) as shown in Figure. 2.2. Consider a quartz lattice, which on receiving ionising radiation due to the radioactive isotopes of uranium, thorium and potassium in the surrounding sediment, excites electrons from the lower energy valence band to the higher energy conduction band. This leads to generation of holes (or vacancies) in the lower energy valence band. After some time, these excited electrons in the conduction band lose their energy and diffuse out. At this stage they get trapped by stable electron traps (T, Fig. 2.2). These electron traps result from defects in the crystalline lattice of quartz; such that, the deeper the trap is below the high energy conduction band, greater is the lifetime of the trap. When the quartz is optically or thermally stimulated in the laboratory, the trapped electrons are released and recombine with vacant holes in the valence band called the luminescence centre (designated as R, Fig. 2.2), located near the valence band. This recombination of an electron and hole results in the emission of a luminescence signal (due to loss of energy) and is measured by the photomultiplier tube.

2.1.1. Determination of equivalent dose

The equivalent dose (D_e) is defined as the laboratory radiation dose equivalent to that received in the natural environment since the last exposure to sunlight or heat (Aitken, 1985, 1998). OSL dating is an umbrella term for techniques that utilise stimulation by light source to measure the equivalent dose from a sample. Hence, depending upon the wavelength of light used for stimulation, it can be classified further to specify the stimulation source, for e.g. BOSL (Blue-OSL), GOSL (Green-OSL), VSL (Violet stimulated luminescence), IRSL (Infrared stimulated luminescence) and so on (Aitken, 1998). Since the IRSL dating technique has been developed specifically for feldspar, the term IRSL is routinely used independently of the OSL term. In this thesis, we focus on sedimentary quartz and feldspar bleached by exposure to sunlight through the application of Blue-Optically stimulated luminescence (BOSL) and Infrared stimulated luminescence (IRSL) techniques respectively. These techniques are hereon simply referred to as OSL and IRSL dating techniques. Hence in this section, only protocols pertaining to these techniques are discussed in detail.

Single aliquot regenerative-dose (SAR) protocol

One of the most important developments in the application of luminescence dating measurement protocols came with the proposal of the single aliquot regenerative (SAR)-dose protocol after Murray and Wintle (2000, 2003), which is also used in this thesis for D_e determination. The main advantage of this protocol lies in the fact that all the measurements are carried out on a single aliquot, which avoids taking into consideration individual

luminescence properties of grains from different aliquots (Murray and Wintle, 2000). The SAR protocol comprises of a sequence of steps that are implemented on a single aliquot of quartz. The summary of the SAR protocol is presented in Table 2.1 and a brief description of the steps involved is provided here (based on Murray and Wintle, 2000, 2003).

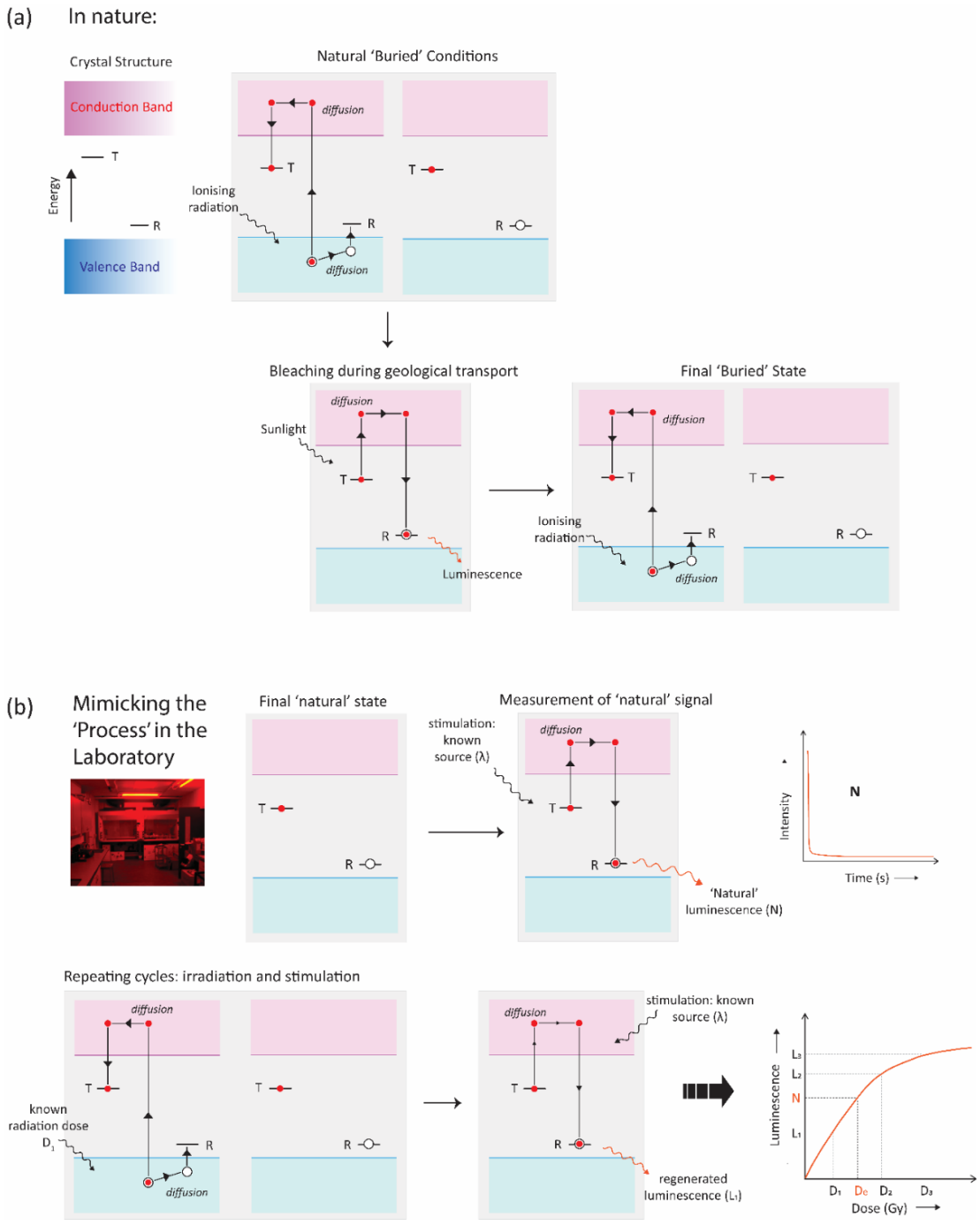

Fig. 2.2. Schematic representation of the electronic processes that occur in crystalline quartz that form the basis of the luminescence dating technique (modified from Aitken (1985) and Duller (2008) to include a complete representation of electronic processes that occur in nature and those induced during laboratory measurements). The solid and empty red circles represent electrons and holes respectively.

- *Step 1: Dose:* This is the first step of the SAR protocol, wherein a single aliquot is irradiated with a beta dose. In the first cycle, the given beta dose always corresponds to zero (i.e., no dose is given), after which a specified amount of dose (known as regeneration dose) is given in the subsequent cycles.
- *Step 2: Preheat*: This step is done to remove the thermally unstable component of the OSL signal and is performed prior to measurement of the OSL signal.
- *Step 3: OSL measurement:* In this step, the aliquot is stimulated with light and the resulting OSL signal is measured by the photomultiplier tube. In the first cycle, since no dose was given, the step measures the natural OSL signal (L_n). In all the subsequent cycles, it measures the OSL signal due to the different regeneration doses given to the aliquot (L_x).
- *Step 4: Test dose:* In this step, a small beta dose is given to the aliquot after each OSL measurement, and this dose is kept constant through all the cycles in the SAR protocol. This step allows us to account for sensitivity change that occurs due to multiple cycles of light stimulation, heating, and radiation dosing, that can cause sensitivity change in the aliquot.
- *Step 5: Cut heat:* This is a brief heating step that is given prior to measurement of the OSL signal from the test dose. This step is carried out to empty the 110^{o}C TL traps and prevent any contribution to the OSL signal from these thermally unstable traps.
- *Step 6: OSL measurement to the test dose*: In this step, the OSL response to the test dose is measured (T_x). When the test dose is measured after the measurement of natural OSL signal it is referred to as T_n
- *Step 7: Repetition of cycles:* Now, the entire cycle from Step 1 to Step 6 is repeated at least four to six times, by giving a specified amount of regeneration dose in each cycle.

Based on these steps, the OSL signal intensity is corrected for sensitivity change by taking a ratio of L_n/T_n for the natural signal and L_x/T_x for each of the regenerated OSL signals. This is then used to construct a dose response curve (growth curve) of sensitivity corrected OSL signal to the given dose, which is subsequently used to evaluate the D_e of the sample.

After this, two additional steps are incorporated at the end of the SAR protocol. These two steps act as intrinsic tests that check the validity and reliability of the SAR protocol and are included as part of routine measurements at the end of the SAR protocol. These tests are included as Step 8 and Step 9 in Table 2.1.

- *Step 8: Recuperation test*: This step is also known as the zero step, in which a sample is given a zero dose and value of L_x/T_x is measured in the same way as described above. Since a zero dose is given, ideally one should obtain a zero signal. Hence, this step is used to assess the effect of charge transfer from the deeper OSL traps on the

OSL signal due to repeated cycles of irradiation, heating, and optical stimulation in the SAR protocol (Murray and Wintle, 2003). According to Murray and Wintle (2000, 2003), the recuperation value should be within 5% of the natural sensitivity corrected OSL signal (L_n/T_n).

- *Step 9: Recycling ratio*: In this step, a regeneration dose is repeated. This is usually the same as the first dose given to the sample and the L_x/T_x is measured. This step is done to assess if the sensitivity changes that arise due to the preceding irradiation, heating, and bleaching cycles, were correctly accounted for (Murray and Wintle, 2000). Therefore, if the sensitivity correction is successful, then the ratio of the luminescence response for the same dose (in this case the first regeneration dose) and that given after the end of all the SAR cycles (for the recycling test) should be unity. Subsequently, only those ratios that lie within 10% of unity are considered acceptable (Murray and Wintle, 2000).

Table 2.1. A summary of the steps involved in the 'classical' SAR protocol (Murray and Wintle, 2000; 2003).

Step	Treatment	Measurement
1	Given dose	-
2	Preheat	-
3	OSL measurement	L_n, L_x
4	Test dose	-
5	Cut heat	-
6	OSL measurement of test dose	T_n, T_x
	Bleach	-
7	Repeat steps 1 to 6: With regeneration dose	-
8	Recuperation	-
9	Recycling	$(L_n/T_n)/ (L_1/T_1) = 1$

Prior to the application of the SAR protocol for determination of D_e, three external tests, namely: a) IR depletion ratio, b) Dose recovery test, and c) Preheat plateau test, are routinely performed. This is done to optimize the parameters of the SAR protocol to the specific sample type as well as check the applicability and reliability of the SAR protocol for a sample.

- *IR depletion ratio:* This was suggested by Duller (2003) to check for potential contamination of quartz sample by feldspathic minerals and assess its purity after chemical treatment. This involves measurement of the ratio of the OSL signal after IR stimulation to the OSL signal measured without an IR stimulation to the same given dose. This test can be performed separately or as part of the routine SAR protocol. It is based on the fact that quartz OSL traps are not sensitive to IR stimulation, while

feldspar traps are. Thus, a ratio of OSL signals to a given dose taken with and without IR stimulation allows us to assess the contamination of quartz by feldspar.

- *Preheat test:* This test is performed to evaluate which preheat temperature should be employed for measuring the D_e of the sample. Preheat (or thermal) treatment allow for the removal of light sensitive shallow traps, particularly those filled by laboratory irradiations, prior to optical stimulation. This test allows us to assess which preheat temperature is sufficient to remove all the unstable traps of the OSL signal, with minimum change in sensitivity. For this purpose, the SAR protocol at different preheat temperatures (usually between 160-280^{o}C) is applied to aliquots of the same sample (Murray and Wintle, 2000). In an ideal situation, if the measured D_e's reach a stable plateau value which is independent of the applied preheat temperature, then the sensitivity change is correctly accounted for in the SAR protocol and the preheat value can be chosen from the plateau region of the preheat plateau test (Wintle and Murray, 2006).
- *Dose recovery test:* This test is done to check the applicability of the SAR protocol and to check the suitability of the pre-heat temperature employed during the SAR protocol by testing whether a given laboratory dose can be efficiently recovered from an aliquot using the SAR protocol (Murray and Wintle, 2003). In optimal conditions, the ratio of given laboratory dose to measured dose should be unity, however such a value is practically not attainable because of inherent factors associated with: (i) laboratory versus natural bleaching conditions, wherein the wavelength and intensity of the light varies in the laboratory and in nature, and (ii) laboratory irradiation versus natural irradiation; where for the same dose, the former is performed over a period of seconds to minutes while the latter occurs over a period of hundreds to thousands of years. Therefore, values within 10% of unity are considered as an acceptable criterion for application of the SAR protocol (Murray and Wintle, 2003).

Another important parameter to note during D_e analysis in luminescence dating is the saturation characteristics of the quartz OSL signal. Every sample is defined by a characteristic dose (D_o) which depends on the reconstructed dose response curve (i.e., it is derived from the exponential function used to fit the curve) of the sample. $2*D_o$ (or $2D_o$) is defined as the signal saturation level. It is taken as 85% of the maximum intensity of the signal, a value at which all the electron traps in the crystal lattice are filled and the OSL signal approaches saturation. For purposes of dating, D_e should be less than $2D_o$ ($D_e < 2D_o$; Wintle and Murray, 2006). Therefore, $2D_o$ is recommended as the upper limit for luminescence dating as any uncertainty in the natural signal leads to a higher asymmetric uncertainty in the evaluated D_e values (Wintle and Murray, 2006).

Double-Single aliquot regenerative-dose (DSAR) protocol

The DSAR protocol was first proposed for calculation of the equivalent dose from the quartz component of the fine grain polymineral sample by Banerjee et al (2001). In this protocol, an extra IR stimulation step was introduced before each OSL measurement in the SAR protocol. Ideally, the 'IR stimulation step' corresponds to an 'IR bleaching step' which essentially allows the removal of the feldspar signal, and the subsequent optical stimulation enables the measurement of the post Infrared-OSL (pIR-OSL) signal from the quartz-component of the polymineral sample. This is because IR stimulation yields luminescence signal from feldspar and not from quartz (Hütt et al., 1988). This method was also proposed as a technique to simultaneously obtain an IRSL and pIR-OSL age from polymineral grains (Banerjee et al, 2001). Following this, a study by Roberts and Wintle (2001) showed that the IRSL and pIR-OSL ages from polymineral fine grains obtained from Chinese loess samples do not yield consistent results, and attributed this to the inability of the DSAR method to adequately monitor sensitivity change related to either one or both of the signals. Later studies by Zhang and Zhou (2007) suggested that optimising the duration of exposure and temperature during the IR bleach step prior to OSL measurement could significantly help in obtaining reliable D_e's from pIR-OSL signal from polyminerals. It was further suggested that the IR bleach at room temperature worked better than those at higher temperature. This aspect of their work was further probed by Jain and Singhvi (2003), who observed that IR stimulation at elevated temperatures can lead to accessing deeper traps of the OSL signal, which can consequently deplete the subsequent pIR-OSL signal. However, a room temperature or lower IR stimulation temperature (<70^{o}C, Jain and Singhvi, 2003; Dave et al., 2019; this study) does not affect the D_e value obtained from the pIR-OSL signal.

Infrared stimulated luminescence (IRSL) dating protocols

OSL dating of quartz is often limited by the saturation of its dose response at c. 200 Gy (equivalent to c. 50-70 ka, assuming a typical dose rate of 3-4 Gy/ka; Buylaert et al., 2008; Roberts, 2008; this study). At the same time feldspar saturates only at much higher doses (c. 2000 Gy; Buylaert et al., 2008), and can extend the age range beyond OSL dating of quartz. However, the IRSL signal from feldspar is prone to anomalous fading (Wintle, 1973), which occurs as a result of quantum mechanical tunnelling (Visocekas, 1985). Due to this phenomena, IRSL ages tend to underestimate the true age. For this purpose, measurement protocols were proposed to estimate the fading of the IRSL signal and correct for this signal loss (Lamothe and Auclair, 1999; Huntley and Lamothe, 2001; Kars et al., 2008). Even then, such corrections are often large and rely on significant assumptions, such as the rate of fading observed at laboratory timescale being equivalent to the geological time scale (Lamothe et al., 2003). This prompted investigations in the feldspar signals that showed no fading.

Investigation of fading rates of different feldspar (Na and K-rich) signals by Thomsen et al (2008) led to the observation that a low temperature (50°C) bleach step followed by an elevated temperature IRSL measurement resulted in lower fading of the signal (i.e. pIR-IRSL) compared to conventional IRSL signal. Following this, several studies based on investigation of feldspar signal behaviour at elevated temperatures were performed (Buylaert et al., 2008; Murray et al., 2009). These studies led to the development and application of elevated temperature post Infrared-Infrared stimulation (pIR-IRSL) signals that exhibited negligible fading rates (Thiel et al., 2011; Buylaert et al., 2012).

2.1.2. Environmental dose rate determination

The other essential component for age determination using luminescence, is the evaluation of the dose rate received by the sample per year (expressed as Gy/yr). In other words, this is equivalent to the rate at which the sample (quartz and feldspar grains) received ionising radiation dose from the surrounding environment. The total dose rate is calculated from three components (Aitken, 1998; Fig. 2.3). The first component is the external dose rate, which comprises of total ionising radiation from the alpha (α), beta (β) and gamma (γ) radiations produced by the decay of radioactive isotopes (^{238}U, ^{232}Th, ^{40}K) in the surrounding sediment. A minor contribution also comes from ^{87}Rb (<1%; Preusser et al., 2008) and other minerals; however, due to their low contribution they are usually neglected. The second component, the internal dose rate, arises due to the presence of radioactive isotopes within the crystal lattice of the quartz or feldspar mineral (Aitken, 1998). Finally, the third component comprises of radiation due to cosmic rays arising from solar and other galactic sources that penetrate the earth's atmosphere and can only be measured under present conditions. The intensity of the cosmic radiation depends on the altitude, location and the depth of the overlying material (Prescott and Hutton, 1994).

Thus, the total dose rate for sediments can be simply represented as:

$$D_o = D_{external} + D_{internal} + D_{cosmic} \quad \text{(Eq. 2.2)}$$

Where,

D = Total dose rate received by the quartz and feldspar

$D_{external} = (D_\alpha + D_\beta + D_\gamma)_{surroundings}$

$D_{internal}$ = radioisotopic inclusions within the quartz or feldspar grains

D_{cosmic} = cosmic rays from outer space

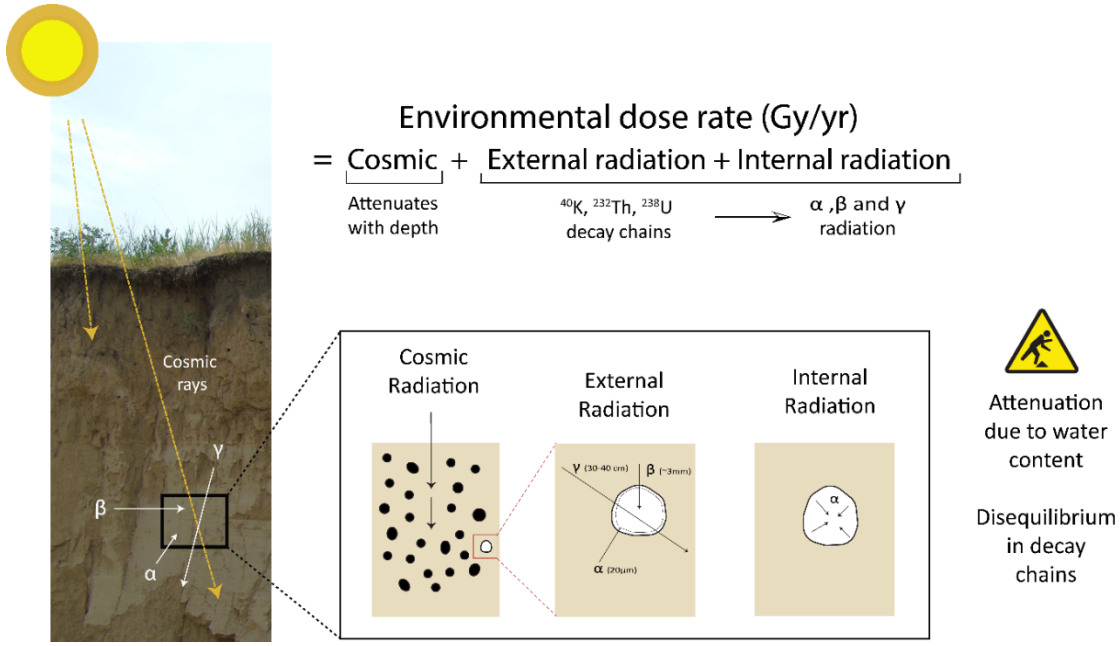

Fig. 2.3. Schematic illustration of environmental dose rate estimation in sedimentary deposits (based on the descriptions in the text).

Fig. 2.3 illustrates the different components of the environmental dose rate and the effect of different ionising radiations on sediment grains. The α-radiations are produced by the decay of ^{238}U and ^{232}Th. They comprise of α-particles, which are essentially helium nuclei (He^{2+}). These particles have a limited penetration depth of c.20 µm in sediments (Preusser et al., 2008). This means that in case of sand sized quartz, it only effects the outer rim of the grain, which is usually etched away (during HF treatment) in coarse grain quartz. The α contribution is therefore negligible in case of coarse grain quartz. However, in feldspar grains and fine grain quartz we account for α-contribution by using appropriate α-efficiency factors (Rees-Jones, 1995). The β radiations consist of β particles which refer to high speed electrons that are emitted during the decay of ^{40}K, ^{238}U and ^{232}Th. The β particles have a travel range of 2-3 mm and hence can completely penetrate all grain sizes. The γ-radiations consist of high energy photons which are emitted during the decay of ^{40}K, ^{238}U and ^{232}Th and have a penetration range of up to 40-50 cm and hence, also effects all grain sizes. The cosmic rays consist of high energy radiations made up of neutrons, muons, electrons, and photons and can permeate through hundreds of meters (Aitken, 1985; Preusser et al., 2008). The fundamental assumption in evaluation of dose rate is that it does not vary with time, hence we assume that the present-day dose rate from the surrounding sediment of the sample is the same as that in the past. The major sources of uncertainty in sediment dose rate may arise from attenuation of β-particles by moisture and/or due to secular disequilibrium in uranium and thorium decay chains (Mejdahl, 1979; Olley et al., 1996). To have a better estimate of moisture content over the entire burial period of sediment, the calculation of

dose rate considers both the in-situ and 'saturated' water content of the sediment sample (Durcan et al., 2015). Secular disequilibrium in U and Th chains occurs when there is an imbalance between the daughter and parent isotopes; this can occur due to introduction of new material or by escape or removal of the daughter isotope (due to leaching in groundwater, absorption or gaseous escape). This disequilibrium frequently occurs in uranium decay chains as ^{238}U produces water soluble daughter nuclei, ^{226}Ra and ^{222}Rn, which can potentially leach out of the system, leading to substantial changes in the dose rate estimation (Olley et al., 1996; 1997). While the thorium decay chains are usually assumed to be in equilibrium as ^{232}Th is insoluble and produces very short-lived daughter nuclei (Olley et al, 1996).

The dose rate of the sediment can be determined by various laboratory (Inductively coupled Plasma-Mass Spectrometry, high resolution germanium gamma spectrometry, Beta counting) and in-situ (gamma spectrometer, dosimeter) techniques. In this thesis, the radionuclide concentrations of ^{238}U, ^{232}Th and ^{40}K were analysed using high-resolution germanium gamma spectrometry, measured at the Felsenkeller, VKTA Dresden. All dose rate calculations for this study were performed using DRAC v.1.2 (Durcan et al., 2015). The parameters for conversion of radionuclide concentrations (Guérin et al., 2011), α-efficiency values for the given sample (Rees-Jones, 1995) and cosmic ray contributions (Prescott and Hutton, 1994) for each sample are discussed in detail in Chapter 3.

Note: The OSL dating of samples from the site of Remizovka (REM) in Chapter 3 were undertaken by Dr. PD K.E. Fitzsimmons.

2.1. Provenance

The ultimate aim of sedimentary provenance analysis is to identify the parent rock assemblages from which sediments are derived (Weltje and von Eynatten, 2004). Fig. 2.4 gives a simplified schematic representation of the concept of provenance in sedimentary settings. However, inferring the final source material, is often complex. This is a result of complex evolution of the sediment's detrital spectrum, especially in terms of its composition (multiple sources) and grain size (variable grain sizes from multiple sources) as the sediment gets transported from the source to the sink (Johnsson and Basu, 1993; Allen, 2008; Caracciolo, 2020). As such, a suite of qualitative and quantitative provenance methods are now employed to study various different geomorphic processes in nature (Weltje and von Eynatten, 2004 and references therein). Some of the 'classic' quantitative provenance tools used in sedimentary geology based on elemental and isotopic composition (rare earth elements, elemental geochemistry, Sr/Nd isotopes; Sun, 2002; Chen et al., 2007; Újvári et al., 2008; Rao et al., 2015) are derived from bulk sediments, which often limits their application (Biscaye et al., 1997; Yang et al., 2001; Bory et al., 2003) and often leads to indeterminate

results. This has led to an increasing interest in development and application of provenance methods that target specific minerals and their characteristics, such as cathodoluminescence of quartz (Nagashima et al., 2017), electron spin resonance (ESR) centres in quartz (Nagashima et al., 2007; Sun et al., 2007, 2013; Shimada et al., 2013), luminescence characteristics of quartz (Sawakuchi et al., 2018; Gliganic et al., 2017), garnet geochemistry (Alizai et al., 2016; Fenn et al., 2018) and U-Pb ages on detrital zircons (Stevens et al., 2010; Pullen et al., 2011; Clift et al., 2012). In this thesis, we investigate quartz as a proxy for provenance using electron spin resonance and luminescence techniques. Here, the underlying basis of the techniques employed in this thesis have been presented.

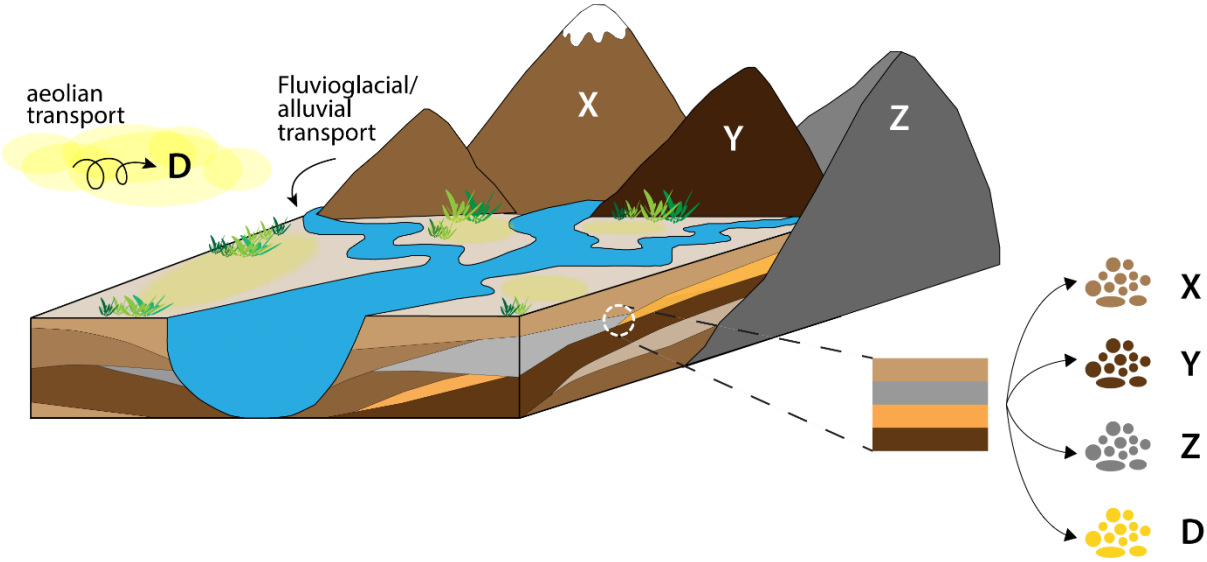

Fig. 2.4. A simplified illustration of the concept of provenance in sedimentary settings.

2.2.1. Luminescence characteristics of quartz

Over the past two decades there has been an increasing interest in the luminescence characteristics of quartz as a tracer for sediment history and provenance (Gray et al., 2019). Quartz luminescence-based techniques exploit various characteristics of the quartz OSL and the TL signals. These include the components of the quartz OSL signal (Pietsch et al., 2008; Tsukamoto et al., 2011; Sawakuchi et al., 2011; Jeong and Choi, 2012; Haddadchi et al., 2016), luminescence sensitivity of the quartz OSL and TL signal (Fitzsimmons, 2011; Sawakuchi et al., 2011, 2018; Zular et al., 2015; Li and Zhou, 2020), and characteristic dose (D_o) of quartz (Gong et al., 2014; Mineli et al., 2021). This thesis primarily focuses on the luminescence sensitivity of quartz and as such, the discussion herein pertains to that.

'Luminescence' in a crystalline quartz lattice is produced as a result of radiative recombination of an electron and hole centre (Aitken, 1998). The amount of luminescence emitted is related to the concentration of the trapped population (of both electron and

holes) as well as the efficiency of the radiative recombination process (Yukihara and McKeever, 2011). Luminescence sensitivity is conventionally defined as the luminescence emitted per unit dose of radiation per unit mass (expressed commonly as photon counts/Gy/kg). That means for a given radiation dose, different samples show different luminescence sensitivities. Current literature suggests that luminescence sensitivity of quartz reflects: i) provenance (i.e., origin - the thermal history and geochemistry of the rock; Fitzsimmons, 2011; Sawakuchi et al., 2011; Guralnik et al., 2015), and/ or (ii) the sedimentary history (i.e., various cycles of erosion-deposition-transport in nature; Pietsch et al., 2008; Zheng et al., 2009; Fitzsimmons et al., 2010; Lü and Sun, 2011; Gliganic et al., 2017). Based on luminescence sensitivity of quartz grains extracted from rocks and from fluvial and coastal sediments in Brazil, Sawakuchi et al (2011) observed that the OSL sensitivity of quartz can be a combination of both, and in some cases the sensitivity change due to natural processes may mask the 'provenance' (or thermal signature of the source rock).

Laboratory experiments with repeated cycles of irradiation, heating and bleaching on quartz (Bøtter-Jensen et al., 1995; Wintle and Murray, 1999; Chen and Li, 2000; Li, 2002) as well as repeated cycles of only irradiation and bleaching (Moska and Murray, 2006; Pietsch et al., 2008; Li and Zhou, 2020) are known to generally increase the sensitivity of quartz. These laboratory-based studies support the phenomena observed in natural settings, where long sedimentary histories (e.g. in deserts) or increased transport distances (e.g. in fluvial systems) can lead to an increase in sensitivity of quartz grains (Pietsch et al., 2008; Fitzsimmons et al., 2010; Sawakuchi et al., 2012). Luminescence sensitivity of quartz grains also depends on the thermal history and geochemistry of rocks, which is observed in studies conducted on quartz extracted from rocks (Sawakuchi et al., 2010; 2011; Guralnik et al., 2015).

Fundamentally, sensitivity of quartz has been linked to various, and/or a combination of parameters inherently related to the quartz crystal lattice, such as the ratio of luminescent (L centres) to non-luminescent (R centres) radiative recombination centres (Li, 2002), trapped water-content in quartz lattice (Sharma et al., 2017), competition between trapping centres in the crystal (Poolton, 2000; Schilles et al., 2001), and the concentration of the trapped population (of both electrons and holes; Yukihara and McKeever, 2011). Nevertheless, how and to what extent the two factors, thermal and/or sedimentary history of the quartz, control the inherent sensitivity of the crystalline quartz lattice is still poorly understood (Fitzsimmons, 2011; Sawakuchi et al., 2011; Mineli et al., 2021). Thus, in order to better understand the luminescence sensitivity variations in quartz, there is a need to: (i) get better insight into geomorphic processes that control sensitivity change, and (ii) gain fundamental understanding of the mechanisms and processes within the crystalline lattice that affect the luminescence intensity emitted from quartz.

In aeolian systems, the luminescence characteristics of quartz has been investigated using different components of quartz (Gong et al., 2015), quartz saturation characteristics (Gong et

al., 2014) and luminescence sensitivity of quartz grains (Zheng et al., 2009; Lü and Sun, 2011; Lü et al., 2014; Li and Zhou, 2020; Lü et al., 2021). In this thesis, down-profile variations in luminescence sensitivity of the OSL and TL signal from quartz in loess have been examined. Lü et al (2014) and Lü et al (2021) investigated down-profile variations in OSL and TL sensitivity of quartz from different grain sizes in multiple loess sections located across northern and central Chinese Loess Plateau (CLP). They observed distinct change in luminescence sensitivity of both signals between loess and palaeosol horizons, and attributed these changes to climate driven shifts in provenance. These studies suggest two possible scenarios that lead to change in luminescence sensitivity of quartz in the alternating loess-palaeosol units of a loess sequence: (i) contraction and expansion of deserts in response to climate, leading to respective increase and decrease in transport distance of the dust source from the loess sites, thereby causing sensitivity change in quartz (Lü et al., 2014; 2021), and (ii) response of high altitude mountain-glacier systems to glacial-interglacial cyclicity, leading to contribution of usually dim-glacial origin quartz during more erosive glacial stages (Lü et al., 2014).

In a recent study, Li and Zhou (2020) investigated two loess sections in south-eastern Tajikistan and observed a similar trend in OSL and TL sensitivity between loess and palaeosol horizons (i.e., a distinct increase in sensitivity in soil horizons and a significant decrease during loess accumulation stages; as also observed by Lü et al., 2014, 2021). However, they argue that the change in sensitivity of quartz arises as a result of differential weathering of different rock types over glacial-interglacial periods; therefore, leading to availability of different sediment compositions containing quartz of varied origin through time, ultimately causing change in sensitivity over glacial (loess stages) and inter-glacial stages (palaeosol-stages). Up until now, only a limited number of down-profile variations in sensitivity have been conducted on loess sequences (Lü et al., 2014, 2021; Li and Zhou, 2021). Thus, the studies from the CLP and from the Tajik loess show similar trends of increased OSL and TL sensitivity in palaeosols and decreased sensitivity in loess units, which have ultimately been attributed to change in provenance of quartz as a result of climatic-shifts. However, the geomorphic process leading to the change in source of loess in response to climate is still under contention. Hence, these studies present interesting ideas and concepts that need to be examined in detail. They also present great potential towards understanding the interaction between loess depositional processes and climate in piedmont regions.

2.2.2. Electron spin resonance-based provenance techniques

Electron Spin Resonance (ESR), also known as Electron Paramagnetic Resonance (EPR) is a technique that studies unpaired electrons in materials (Weil and Bolton, 2006). The phenomena of ESR was first discovered by Soviet Physicist Evgenii Konstantinovich Zavoisky

in 1944 (Salikhonov and Zavoiskaya, 2015) and since then its application has revolutionised the fields of physics, chemistry, biology and geology. The ESR technique, as a dating tool, was first systematically established in 1975 by Ikeya with the dating of stalactites in Akiyoshi cave in Japan (Ikeya, 1975). Since then, ESR has been established as a widely applied dating tool in archaeology and geosciences (Grün, 1989; Ikeya, 1993; Schellmann et al., 2008) as well as a quartz based-provenance tool (Toyoda et al., 2016). This thesis focuses on exploring the application of ESR characteristics of quartz grains for sedimentary provenance analysis.

Basic concept of ESR Spectroscopy (Weil and Bolton, 2006) explained in context of quartz:

Crystal growth, impurities and diagenetic dislocation of atoms in a crystal can give rise to defects in quartz. When quartz is irradiated with an ionising radiation, the electrons from the valence band are excited into the conduction band. After some time, the electrons in the conduction band diffuse out and get trapped in quasi-stable traps in the 'forbidden' energy levels, some of which can have a lifetime of up to several million years. Traps occupied by a single electron act as paramagnetic centres, whose concentration can be measured using ESR spectroscopy. An electron (as in the case of paramagnetic species) has a magnetic moment and a magnetic spin quantum number, s = 1/2. In the absence of a magnetic field, the magnetic moment (m_s = 1/2 or m_s = -1/2) associated with the spin is randomly oriented and the two energy levels are degenerate. In continuous wave-electron spin resonance (CW-ESR), an external magnetic field (B) is applied to the crystal. This causes a splitting of the degenerate energy levels (Zeeman effect) as the electron spin is oriented either parallel (m_s = +1/2) or antiparallel (m_s = -1/2) to the direction of the magnetic field. The energy of splitting of the two levels, ΔE, is given by the equation:

$$\Delta E = g\mu B$$

(Eq. 2.3)

where,

g = spectroscopic splitting factor, known as Landé factor
μ_B = Bohr magneton
B = magnetic field

At the same time, a constant microwave frequency (ν), with an energy, E = hν, is applied to the system. When the energy of splitting becomes equal to the energy of the applied microwave frequency, i.e.,

$$h\nu = g\mu_B B$$

(Eq. 2.4)

Then, the system is said to be in a state of resonance, i.e., the electron oscillates between the two orientations. This results in an absorption spectrum. This thesis takes the first derivative of the absorption intensity and considers the peak-to-peak amplitude of this derivative as equivalent to the concentration of the measured paramagnetic defect centre (Chesnut, 1977). A schematic of this process is illustrated in Fig. 2.5.

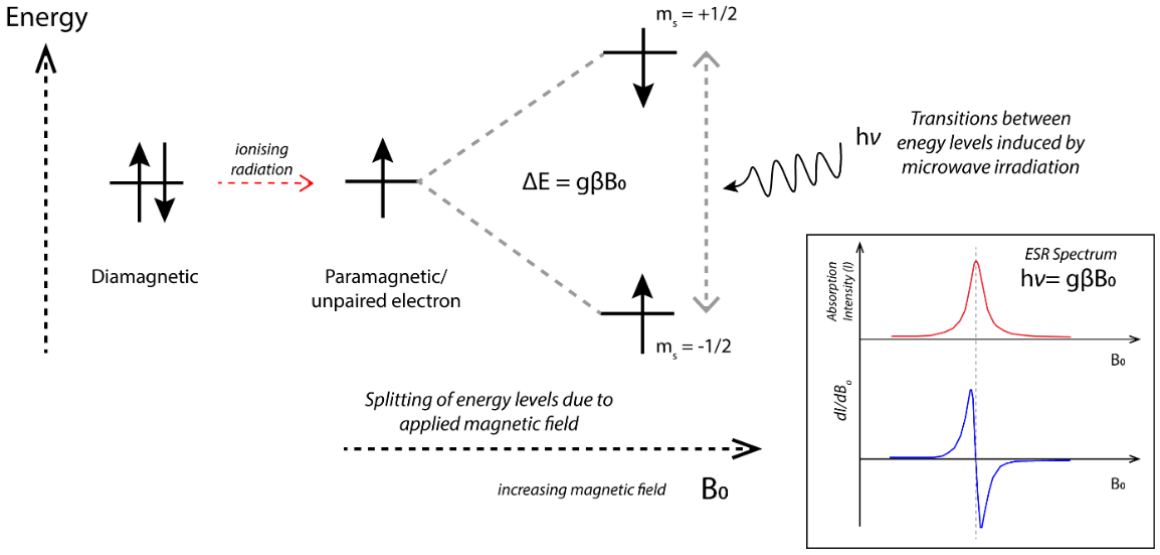

Fig. 2.5. Schematic illustration of measurement of paramagnetic species using electron spin Resonance.

ESR signals in quartz as provenance indicators

Lattice defects and impurities in quartz, in the presence of ionising radiation, give rise to paramagnetic defect centres. These defect centres can be measured using ESR. Up until now, provenance studies based on ESR signals in quartz have mainly utilised the E', Al-hole and Ti centres. A brief description of the centres used in different provenance studies is given below (Fig. 2.6):

(i) E' centre: An E' centre (≡*Si*·) is one of the major defect centres in natural quartz. It is essentially an unpaired electron occupying an oxygen vacancy (Feigl et al., 1974).

(ii) Al-hole centre (Weil, 1984; Ikeya, 1993): The aluminium-hole centre (Al-hole centre, $[AlO_4/h^+]^0$) is an impurity related defect centre in natural quartz. Al occurs as impurity in a quartz crystal and can replace a silicon (Si) atom in the quartz crystal lattice. Since Al has an extra electron, this replacement is accompanied by an alkali ion for charge compensation, leading to the formation of a neutral defect $[AlO_4/M^+]^0$; where, M = monovalent cation (Na, Li, etc). On irradiation, the neutral centres trap a hole, and releases an alkali ion to form an Al-hole centre, $[AlO_4/h^+]^0$ (see Fig. 2.6c)

(iii) Ti centre (Weil, 1984): The titanium centre ($[TiO_4/M^+]^0$, where M = Li, Na, H) in quartz is also an impurity related defect centre. This defect centre is formed when a Ti atom replaces a Si atom, and forms $[TiO4]^0$. Being diamagnetic, it occurs without any charge compensation. On irradiation, an electron and an alkali centre are trapped together for charge compensation to form a paramagnetic Ti centre $[TiO_4/M^+]^0$ (see Fig. 2.6d)

(iv) In this thesis, the use of peroxy centre (as measured by Odom and Rink, 1989) is proposed as an indicator of provenance. The peroxy centre is an oxygen-related hole centre. Stapelbroeck et al (1979) identified two types of oxygen-associated trapped hole centres (OHC) in fused silica after γ-irradiation, namely the dry OHC (i.e., a peroxy radical, ≡*Si*-O-O·) and a wet OHC (i.e., a non-bridging oxygen hole centre, ≡*Si*–O·). In natural quartz, one can only measure the 'peroxy' centre (as observed by McMorris, 1970; Odom and Rink, 1989). Recent studies (Salh, 2011; Skuja et al., 2020) make us consider the possibility that the aforementioned 'peroxy' signal is likely to be an overlap of a peroxy radical (≡*Si*-O-O·, POR) and non-bridging oxygen hole centre (≡*Si*–O·, NBOHC). Refer to Fig. B8 in appendix B for illustration of the same. However, this hypothesis does not affect our present work and requires further investigation which is beyond the scope of investigation in this thesis.

Al-hole and Ti-Li centres in quartz have been utilised in various studies to differentiate between the provenance of fluvial sediments. (Shimada et al., 2013, 2016; Tissoux et al., 2015; Wei et al., 2020). These methods are primarily based on the observations that the concentration of Al-hole centre positively correlates to the Al content (in ppm) of quartz (Usami et al, 2009), and that the non-bleachable component of Al-hole centres is sample dependant and depends on the crystallisation conditions or metamorphic history of the quartz (Tissoux et al., 2012). A majority of the provenance studies based on quartz ESR signals are focused on the use of the heat-treated E' (HT-E') centre (Toyoda and Naruse, 2002; Toyoda and Hattori, 2000; Toyoda et al., 2016). The intensity of HT-E' centres in combination with the crystallinity index of quartz (Nagashima et al., 2007) is amongst the most commonly applied ESR-based provenance method to sedimentary systems.

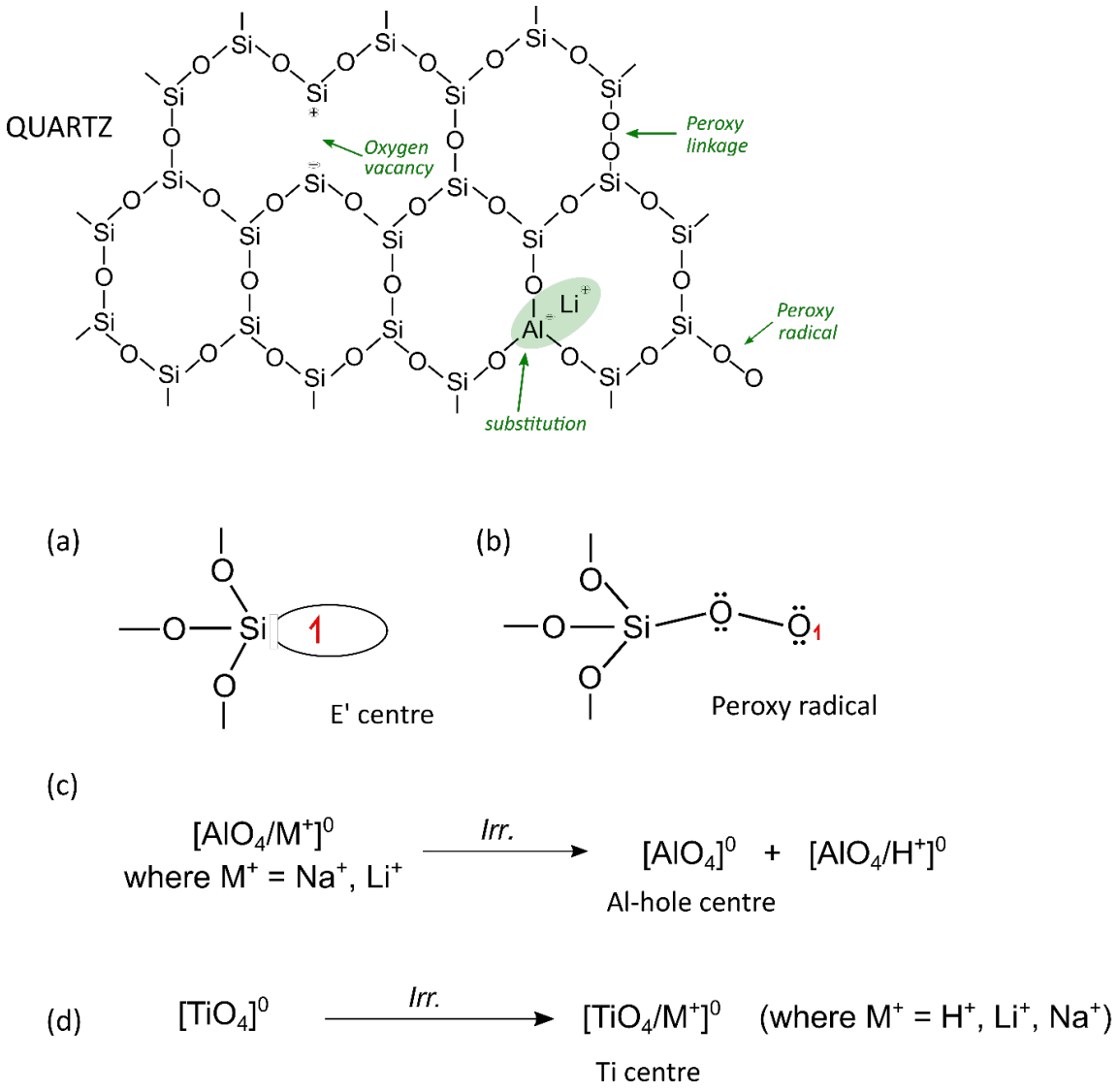

Fig. 2.6. Common intrinsic and extrinsic defects in natural quartz (adapted from Götze et al., 2001). Paramagnetic defect centres in quartz probed for ESR-based provenance analysis: (a) E' centre, (b) peroxy radical (c) Al-hole centre and (d) Ti centre.

Basis of Heat treated - E' (HT-E') approach

One of the most widely known approach in provenance of quartz using ESR, utilises the measurement of the E' signal in quartz after γ-irradiation and thermal treatment (Toyoda and Hattori, 2000; Toyoda and Naruse, 2002; Toyoda et al., 2016). This modified signal is commonly referred to as the heat treated-E' (HT-E') signal. This approach is based on the premise that the total number of diamagnetic oxygen vacancies are characteristic of the rock type and increase with the age of the source rock (Toyoda and Hattori, 2000; Toyoda et al., 2016).

Weeks and Nelson (1960) observed that the intensity of E' centre increases on heating in synthetic quartz. Following this, Jani et al (1983) proposed a mechanism for this increase in synthetic quartz, according to which heating releases holes from the Al-hole centre. These holes recombine with one of the two electrons of the diamagnetic oxygen vacancy, converting them into ESR measurable E' centres. On the basis of this approach, Toyoda and Ikeya (1991) proposed a protocol to measure the total oxygen vacancies in natural quartz by irradiating (with γ-rays) and heating the quartz. This was further supported by the work of Toyoda and Hattori (2000), who reaffirmed the mechanism of formation of HT-E', by studying the dose response curves of Al-hole centres and HT-E' centres. Therefore, HT-E' was assumed to reflect the total number of oxygen vacancies in quartz. In addition, Toyoda and Hattori (2000) showed that the HT-E' signal intensity in quartz was proportional to the age of the host granite. These results led to the use of HT-E' as a proxy for provenance. However, Usami et al (2009), found that quartz with low Al concentration had a weak HT-E' intensity and vice versa, suggesting that the concentration of HT-E' centres was dependent not only on the total oxygen vacancies in the rock, but also on the Al concentration. This raises questions on whether HT-E' is a true reflection of the total number of oxygen vacancies in a quartz crystal.

Basis of the paired E'-peroxy approach (this study)

This thesis investigates the utilisation of natural accumulation of E' and peroxy paramagnetic centres in quartz as a proxy for provenance. This approach is based on the observations by Odom and Rink (1989) that E' and peroxy centres in natural quartz arise from Schottky-Frenkel (SF) defect pairs. The SF defect pairs consist of an oxygen vacancy (=*Si*=*Si*=) and peroxy linkage (≡*Si*-*O*-*O*-*Si*≡) that are formed by the displacement of an O atom in the quartz crystal lattice (≡*Si*-*O*-*Si*≡). The holes generated by the Al-hole centre combines with the diamagnetic SF defect pairs to yield paramagnetic E' and peroxy centres. A schematic of formation of the E' and peroxy centre is shown in Fig. 2.7. This phenomenon was first observed in fused silica (Stapelbroek et al., 1979; Friebele et al., 1979). Odom and Rink (1989) first observed that the E' and proxy centres in granitic quartz are correlated to the age of the rock and arise from SF defect pairs in quartz. They therefore proposed this as a potential geochronometer. Following which, Rink and Odom (1991) proposed that observed E' and peroxy centres were formed by recoil of α-emitting nuclides present as impurities in rocks. They suggested this based on comparison of concentration of paramagnetic centres with lattice vacancy calculations associated with alpha-recoil damage in quartz. Their results were supported by previous observations by McMorris (1970), who based on the similarity of the peroxy signal to that of an ESR centre generated in synthetic quartz due to fast neuron generation (Weeks, 1956), proposed that the peroxy signal was produced by α-recoil nuclei emitted by impurities (U and Th) in rocks.

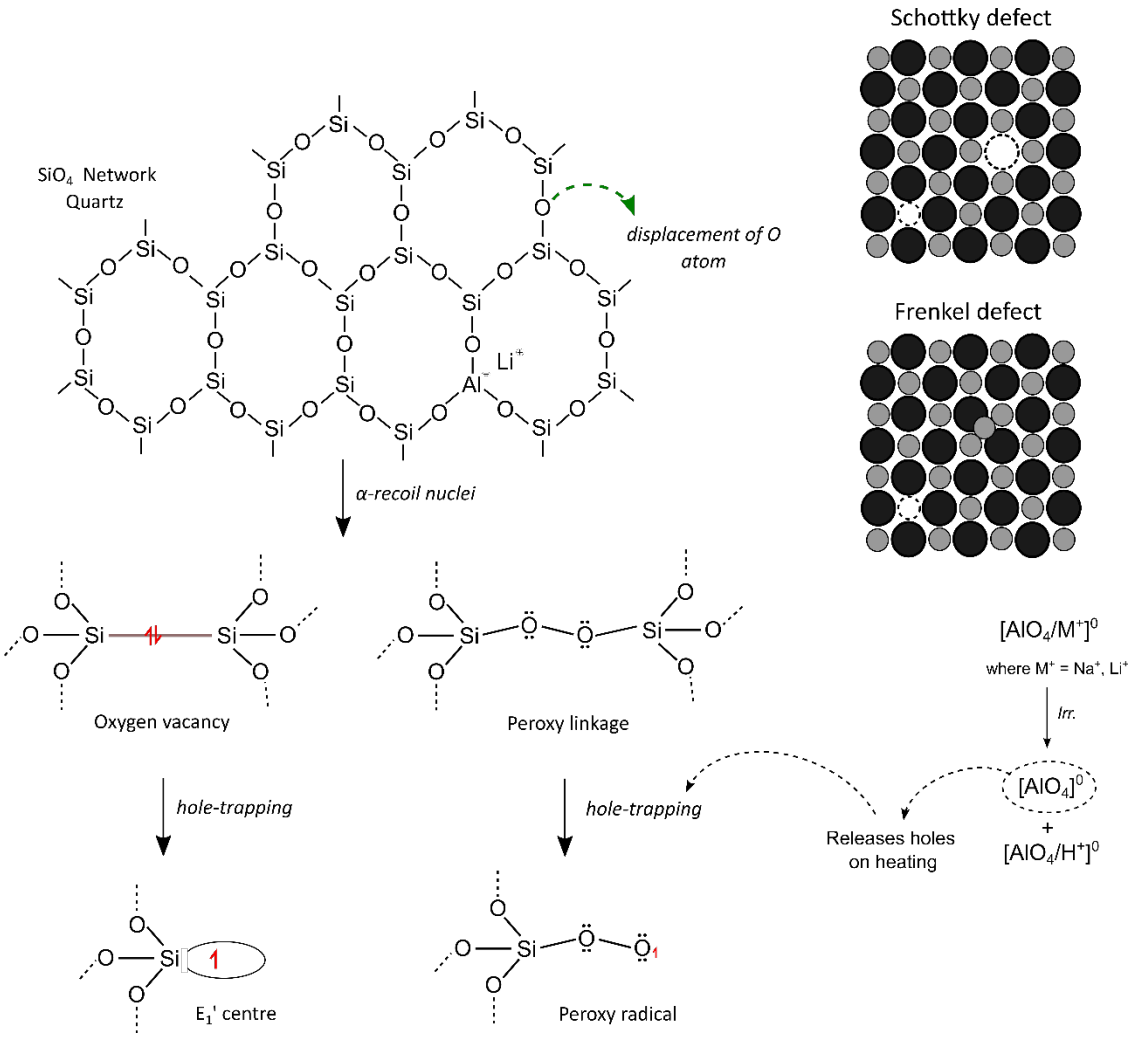

Fig. 2.7. Schematic 2-D representation of the reaction mechanism proposed for formation of the E' and peroxy centres in quartz (based on the description by Jani et al., 1983 and Odom and Rink, 1989).

Natural E' versus HT-E'

Apart from the difference in the basis of the two methods, one of the major disagreements between the natural and HT-E' centre lies in understanding which radiation(s) is (are) responsible for the formation of the precursor of E' centre (i.e., oxygen vacancies) in natural quartz. Investigations on the behaviour of E' centre after γ irradiation post-annealing, as well as the spin-spin relaxation times of the E' centre, suggest that β and γ radiations lead to formation of oxygen vacancies in nature (Toyoda et al., 1992, 2005). However, based on experimental and theoretical calculations on production of oxygen vacancies in Li and B-doped quartz and natural quartz, Toyoda et al (2001) suggested that α-recoil nuclei are more likely to have contributed to production of oxygen vacancies in natural quartz. This is in tune with previous observations made by Rink and Odom (1991) based on lattice vacancy calculations associated with α-damage in quartz. Hence, to better understand the dynamics

of these centres there is a need to understand the factors responsible for their formation in the crystal lattice.

2.3. Supporting proxy analyses

In this thesis, the chronology and provenance work on sediments, is supported by 'classical' indices used in the study of loess archives: grain size, micromorphology, and magnetic susceptibility. These analyses, along with the stratigraphy of the loess sections, lay the foundation on which the primary work of this thesis and subsequent interpretations are based.

2.3.1. Grain size

Grain size analysis of loess archives provides an important quantitative tool to infer palaeoclimatic conditions (An et al., 1991a; Ding et al., 2002; Sun et al., 2012), loess transport and depositional processes (Vandenberghe, 2013; Li et al, 2018), and the effect of post-depositional (secondary) processes in loess deposits (Vandenberghe et al., 2018). Grain size and associated statistical measures act as powerful indicators of wind strength; based on the assumption that increased wind strength enables aeolian transport of coarser grains to the loess site (An et al., 1991a; Lu and Sun, 2000; Sun et al., 2012; Stevens et al., 2018). For example, such studies have been widely applied across the Chinese loess plateau (CLP) to infer the strength of the East Asian winter monsoon (Lu and An, 1998; Lu and Sun, 2000; Vriend et al., 2011), and across various regions in Arid Central Asia and Europe to infer the influence of the Westerly wind strength (Li et al., 2016; Rousseau et al., 2007; Antoine et al., 2009). These studies have consequently led to interpretation of the influence of large-scale climate systems. For instance, increase in grain size in sites in north-western CLP during glacial periods have been linked to increased EAWM wind strength, therefore suggesting a strengthened Siberian High during glacial stages (Sun et al., 2012; Stevens et al., 2018). Correlation of grain size variations at various Westerly influenced loess sites in ACA and Europe with abrupt climatic changes associated with the North Atlantic signal suggests that Westerlies respond to changes in the North Atlantic (Rousseau et al., 2007; Li et al., 2016).

Although, grain size indices can provide a powerful tool for inferring terrestrial paleoclimates, such reconstructions must always be performed in context of local geomorphic settings. An example of the effect of local geomorphic setting on grain size records can be found in Chapter 3 (see Fig. 3.9). Furthermore, grain size distributions and associated end member modelling approaches can provide an excellent tool for characterizing aeolian transport processes and provenance (Vandenberghe, 2013; Paterson and Heslop, 2015; Yu et al., 2016; Dietze and Dietze, 2019). For example, on the basis of variation in different grain size sub-populations of sediments from eastern Ili basin in Kazakhstan, Li et al (2018) suggested that

the piedmont loess in this region was sourced primarily from proximal sources, and that rivers provide a major source for loess as compared to the surrounding deserts. In addition, characterization of grain size can also provide a useful method to determine the nature and degree of post depositional alteration in aeolian deposits (Vandenberghe et al., 2018). For instance, Sun et al (2006) used grain size distributions to identify pedogenic alteration of the red clay sequence (late Miocene to middle Pliocene; Liu, 1985) as compared to the overlying loess-paleosol sequence at multiple sites in the CLP. A similar study was also undertaken by Kovács (2008) in the Pannonian basin in Hungary to identify pedogenic alteration of red clay deposits, which are primarily aeolian in nature. Nevertheless, identification of post depositional processes in loess deposits is quite complex and cannot always be explained via grain size analyses. In such cases, one needs to rely on other sedimentological tools (e.g., mineralogy) and proxy indices (like micromorphology and magnetic susceptibility) coupled with stratigraphic data and geomorphic setting of the sites.

Note: In this thesis, the grain size analysis in Chapter 3 was undertaken by Dr. Lenka Lisá at the Institute for Geology, Czech Academy of Sciences, Prague.

2.3.2. Micromorphology

Micromorphological analysis of thin sections from loess-palaeosol sequences provides a valuable tool in the study of paleoenvironmental conditions during processes of loess accumulation and soil formation (Kemp, 1999). Micromorphological features like coatings around grains, cryogenic features and calcitic concentrations can provide important insight into sedimentary processes during loess accumulation and as well as pedogenic processes during soil formation. This can help infer climatic conditions (Courty and Fedoroff, 1987; Fedoroff et al., 1990), vegetation (Fedoroff and Goldberg, 1982), depositional processes, as well as post-depositional alteration in loess sequences (Mücher and Vreeken, 1981; Kemp, 1997; Kielhofer et al., 2020).

Note: The micromorphological investigations in this thesis (Chapter 3) were undertaken by Dr. Lenka Lisá at the Institute for Geology, Czech Academy of Sciences, Prague.

2.3.3. Magnetic susceptibility

Magnetic susceptibility is a 'classic' proxy index to infer palaeoclimatic conditions in loess-palaeosol sequences, based on alternating loess and soil horizons (Kukla, 1988; Heller and Liu, 1986; An et al., 1991b; Evans and Heller, 1994). Magnetic susceptibility (κ) measures the degree to which sediment can be temporarily magnetised in the presence of an external magnetic field. κ is a dimensionless quantity and is defined as (Evans and Heller, 2003):

$$\kappa = \frac{M}{H}$$

(Eq. 2.5)

where, M = acquired magnetisation, and; H= applied magnetic field

In this thesis, bulk magnetic susceptibility measurements were performed. This quantity is defined as:

$$\chi_m = \frac{\kappa}{\rho}$$

(Eq. 2.6)

where,

ρ = density of the material.

The enhancement in the magnetic susceptibility signal is usually determined by the concentration, composition, and grain size of the iron (Fe)-bearing minerals. These Fe-minerals are usually categorised as para-, ferro-, antiferro- and ferrimagnetic depending on their magnetic properties (Buggle et al., 2009). The magnetisation ability of these minerals are shown in the Table 2.2, with Ferro- and Para- demonstrating the most and least respectively (Thomsen and Oldfield, 1986).

Table 2.2. Different types of Fe-minerals listed in order of decreasing magnetisation ability (based on data from Thomson and Oldfield, 1986).

Type	Example
Ferro-	Fe, Co, Ni and their alloys
Ferri-	magnetite, maghemite
Antiferro-	hematite
Para-	biotite, pyrite

Other than mineralogy, magnetic susceptibility is also influenced by grain size. Usually, grains ≤30 nm are categorised as superparamagnetic (SP), i.e., they align instantly in the presence of applied magnetic field and therefore enhance magnetic susceptibility (Buggle et al., 2009). While grains > 30 nm, acquire single domain (SD) and multidomain (MD) properties. SD or MD refers to grains that have either one or multi regions of coupled magnetic moments respectively. This means that as these regions increase in a grain, its ability to magnetise decreases, i.e., its magnetic susceptibility decreases. This is one of the reasons why soils,

which have a higher proportion of ultrafine iron-oxides (SP) have higher magnetic susceptibility than loess horizons, where SD or MD grains predominate (Thomson and Oldfield, 1986; Buggle et al., 2009). The enhancement of magnetic susceptibility in soils and its decrease in loess units is commonly observed across most European and Chinese loess sites (Kukla, 1988; Maher and Thompson, 1992; Evans and Heller, 1994; Panaiotu et al., 2001). However, some loess sequences in Alaska and Siberia (Begét and Hawkins, 1989; Begét et al., 1990; Liu et al., 1999; Matasova et al., 2001), show an opposite trend, where magnetic susceptibility decreases in the soil units. These inverse trends in magnetic susceptibility in loess-palaeosol sequences from different regions gave rise to two models: the pedogenic enhancement and the wind vigour model (Evans and Heller, 1994; Bradak et al., 2021). These models have been widely used to explain the enhancement of magnetic susceptibility values in loess-palaeosol sequence.

The pedogenic enhancement model explains the commonly observed phenomena of magnetic enhancement in soils. According to this model, since soil formation occurs during warmer and more humid (interglacial) conditions, it has a higher concentration of ultrafine superparamagnetic (SP) component which leads to higher magnetic susceptibility in soils compared to loess (Maher and Taylor, 1988). On the other hand, the wind vigour model provides an explanation for the magnetic enhancement of loess units which is commonly observed in Alaskan and Siberian loess. As per the wind vigour model, strong winds in a region (especially during glacial periods) can lead to entrainment of higher fraction of dense iron oxide grains from the source region, leading to enhancement of magnetic susceptibility during loess accumulating phases (Evans, 2001). Nevertheless, many studies have shown that not all sites can be explained via the aforementioned models and the enhancement of magnetic susceptibility in loess-palaeosol is a far more complex process (Sun and Liu, 2000; Wang et al., 2006; Kravchinsky et al., 2008; Liu et al., 2012). For instance, a loess-palaeosol sequence (Talede) in the Ili basin of SE Kazakhstan exhibited higher low-frequency magnetic susceptibility (χ_{lf}) values in the loess, while it showed higher frequency-dependent magnetic susceptibility (χ_{fd}) values in the soil (Liu et al.,2012). These observed differences in χ_{lf} values have been attributed to higher concentration of magnetic minerals in loess as compared to palaeosols and presence of coarse SD and MD grains in both loess and palaeosol units. At the same time, palaeosols have a higher proportion of ultrafine component leading to higher χ_{fd} values in the soil units.

Note: The magnetic susceptibility (MS) measurements in Chapter 3 were undertaken by self at the Alpine Palaeomagnetism Laboratory, Peveragno, Italy. The portable in-situ MS measurements at Karamaidan (Tajikistan) in Chapter 4 were carried out by Dr. G. Scardia (Universidade Estadual Paulista, Brazil).

References

Aitken, M. J., Tite, M. S., & Reid, J. (1964). Thermoluminescence Dating of Ancient Ceramics. Nature, 202(4936), 1032–1033. https://doi.org/10.1038/2021032b0

Aitken, M.J. (1985). Thermoluminescence dating. Academic Press, London.

Aitken, M.J. (1998). An introduction to Optical dating: The dating of quaternary sediments by the use of photon-stimulated luminescence. Oxford University Press, Oxford.

Alizai, A., Clift, P. D., & Still, J. (2016). Indus Basin sediment provenance constrained using garnet geochemistry. Journal of Asian Earth Sciences, 126, 29–57. https://doi.org/10.1016/j.jseaes.2016.05.023

Allen, P. A. (2008). From landscapes into geological history. Nature, 451(7176), 274–276. https://doi.org/10.1038/nature06586

An, Z., Kukla, G., Porter, S. C., & Xiao, J. (1991a). Late quaternary dust flow on the chinese Loess Plateau. Catena, 18(2), 125–132. https://doi.org/10.1016/0341-8162(91)90012-M

An, Z., Kukla, G. J., Porter, S. C., & Xiao, J. (1991b). Magnetic susceptibility evidence of monsoon variation on the Loess Plateau of central China during the last 130,000 years. Quaternary Research, 36(1), 29–36. https://doi.org/10.1016/0033-5894(91)90015-W

Antoine, P., Rousseau, D.-D., Moine, O., Kunesch, S., Hatté, C., Lang, A., Tissoux, H., & Zöller, L. (2009). Rapid and cyclic aeolian deposition during the Last Glacial in European loess: A high-resolution record from Nussloch, Germany. Quaternary Science Reviews, 28(25), 2955–2973. https://doi.org/10.1016/j.quascirev.2009.08.001

Banerjee, D., Murray, A. S., Bøtter-Jensen, L., & Lang, A. (2001). Equivalent dose estimation using a single aliquot of polymineral fine grains. Radiation Measurements, 33(1), 73–94. https://doi.org/10.1016/S1350-4487(00)00101-3

Begét, J. E., & Hawkins, D. B. (1989). Influence of orbital parameters on Pleistocene loess deposition in central Alaska. Nature, 337(6203), 151–153. https://doi.org/10.1038/337151a0

Begét, J. E., Stone, D. B., & Hawkins, D. B. (1990). Paleoclimatic forcing of magnetic susceptibility variations in Alaskan loess during the late Quaternary. Geology, 18(1), 40–43. https://doi.org/10.1130/0091-7613(1990)018<0040:PFOMSV>2.3.CO;2

Biscaye, P. E., Grousset, F. E., Revel, M., Van der Gaast, S., Zielinski, G. A., Vaars, A., & Kukla, G. (1997). Asian provenance of glacial dust (stage 2) in the Greenland Ice Sheet Project 2 Ice Core, Summit, Greenland. Journal of Geophysical Research: Oceans, 102(C12), 26765–26781. https://doi.org/10.1029/97JC01249

Bory, A. J.-M., Biscaye, P. E., & Grousset, F. E. (2003). Two distinct seasonal Asian source regions for mineral dust deposited in Greenland (NorthGRIP). Geophysical Research Letters, 30(4). https://doi.org/10.1029/2002GL016446

Bøtter-Jensen, L., Agersnap Larsen, N., Mejdahl, V., Poolton, N. R. J., Morris, M. F., & McKeever, S. W. S. (1995). Luminescence sensitivity changes in quartz as a result of annealing. Radiation Measurements, 24(4), 535–541. https://doi.org/10.1016/1350-4487(95)00006-Z

Boyle, R. (1664). Experiments and considerations touching colours, Royal Society Proceedings, London, pp. 413-423

Bradák, B., Seto, Y., Stevens, T., Újvári, G., Fehér, K., & Költringer, C. (2021). Magnetic susceptibility in the European Loess Belt: New and existing models of magnetic enhancement in loess. Palaeogeography, Palaeoclimatology, Palaeoecology, 569, 110329. https://doi.org/10.1016/j.palaeo.2021.110329

Buggle, B., Hambach, U., Glaser, B., Gerasimenko, N., Marković, S., Glaser, I., & Zöller, L. (2009). Stratigraphy, and spatial and temporal paleoclimatic trends in Southeastern/Eastern European loess–paleosol sequences. Lower Latitudes Loess-Dust Transport Past and Present, 196(1), 86–106. https://doi.org/10.1016/j.quaint.2008.07.013

Buylaert, J. P., Murray, A. S., Vandenberghe, D., Vriend, M., Corte, F. D., & haute, P. V. den. (2008). Optical dating of Chinese loess using sand-sized quartz: Establishing a time frame for Late Pleistocene climate changes in the western part of the Chinese Loess Plateau. Quaternary Geochronology, 3(1), 99–113. https://doi.org/10.1016/j.quageo.2007.05.003

Buylaert, J.-P., Jain, M., Murray, A. S., Thomsen, K. J., Thiel, C., & Sohbati, R. (2012). A robust feldspar luminescence dating method for Middle and Late Pleistocene sediments. Boreas, 41(3), 435–451. https://doi.org/10.1111/j.1502-3885.2012.00248.x

Caracciolo, L. (2020). Sediment generation and sediment routing systems from a quantitative provenance analysis perspective: Review, application and future development. Earth-Science Reviews, 209, 103226. https://doi.org/10.1016/j.earscirev.2020.103226

Chen, G., & Li, S. H. (2000). Studies of quartz 110 °C thermoluminescence peak sensitivity change and its relevance to optically stimulated luminescence dating. Journal of Physics D: Applied Physics, 33(4), 437–443. https://doi.org/10.1088/0022-3727/33/4/318

Chen, J., Li, G., Yang, J., Rao, W., Lu, H., Balsam, W., Sun, Y., & Ji, J. (2007). Nd and Sr isotopic characteristics of Chinese deserts: Implications for the provenances of Asian dust. Geochimica et Cosmochimica Acta, 71(15), 3904–3914. https://doi.org/10.1016/j.gca.2007.04.033

Chesnut, D. B. (1977). On the Use of the AW2 method for integrated line intensities from first-derivative presentations. Journal of Magnetic Resonance (1969), 25(2), 373–374. https://doi.org/10.1016/0022-2364(77)90032-4

Clift, P. D., Carter, A., Giosan, L., Durcan, J., Duller, G. A. T., Macklin, M. G., Alizai, A., Tabrez, A. R., Danish, M., VanLaningham, S., & Fuller, D. Q. (2012). U-Pb zircon dating evidence for a Pleistocene Sarasvati River and capture of the Yamuna River. Geology, 40(3), 211–214. https://doi.org/10.1130/G32840.1

Courty, M.-A., & Fédoroff, N. (1987). Morphology and distribution of textural features in arid and semiarid regions. In: Fedoroff, N., Bresson, L.-M., Courty, M.-A. (Eds.), Soil Micromorphology. Association Francaise pour l'Etude du Sol, Plaisir, pp. 213–219.

Daniels, F., Boyd, C. A., & Saunders, D. F. (1953). Thermoluminescence as a Research Tool. Science, 117(3040), 343. https://doi.org/10.1126/science.117.3040.343

Dave, A. K., Courty, M.-A., Fitzsimmons, K. E., & Singhvi, A. K. (2019). Revisiting the contemporaneity of a mighty river and the Harappans: Archaeological, stratigraphic and chronometric constraints. Quaternary Geochronology, 49, 230–235. https://doi.org/10.1016/j.quageo.2018.05.002

Dietze, E., & Dietze, M. (2019). Grain-size distribution unmixing using the R package EMMAgeo. E&G Quaternary Science Journal, 68(1), 29–46. https://doi.org/10.5194/egqsj-68-29-2019

Ding, Z. L., Derbyshire, E., Yang, S. L., Yu, Z. W., Xiong, S. F., & Liu, T. S. (2002). Stacked 2.6-Ma grain size record from the Chinese loess based on five sections and correlation with the deep-sea δ18O record. Paleoceanography, 17(3), 5-1-5–21. https://doi.org/10.1029/2001PA000725

Duller, G. A. T. (2003). Distinguishing quartz and feldspar in single grain luminescence measurements. Radiation Measurements, 37(2), 161–165. https://doi.org/10.1016/S1350-4487(02)00170-1

Durcan, J. A., King, G. E., & Duller, G. A. T. (2015). DRAC: Dose Rate and Age Calculator for trapped charge dating. Quaternary Geochronology, 28, 54–61. https://doi.org/10.1016/j.quageo.2015.03.012

Duller, G. A. T. (2008). Luminescence Dating: Guidelines on using luminescence dating in archaeology. English Heritage.

Durcan, J. A., King, G. E., & Duller, G. A. T. (2015). DRAC: Dose Rate and Age Calculator for trapped charge dating. Quaternary Geochronology, 28, 54–61. https://doi.org/10.1016/j.quageo.2015.03.012

Evans, M. E. (2001). Magnetoclimatology of aeolian sediments. Geophysical Journal International, 144(2), 495–497. https://doi.org/10.1046/j.0956-540X.2000.01317.x

Evans, M. E., & Heller, F. (1994). Magnetic enhancement and palaeoclimate: Study of a loess/palaeosol couplet across the Loess Plateau of China. Geophysical Journal International, 117(1), 257–264. https://doi.org/10.1111/j.1365-246X.1994.tb03316.x

Evans, M. E., & Heller, F. (2003). Environmental magnetism: Principles and applications of enviromagnetics. Academic Press. http://site.ebrary.com/id/10201879

Fedoroff, N., Courty, M. A., & Thompson, M. L. (1990). Micromorphological Evidence of Paleoenvironmental Change in Pleistocene and Holocene Paleosols. In L. A. Douglas (Ed.), Developments in Soil Science (Vol. 19, pp. 653–665). Elsevier. https://doi.org/10.1016/S0166-2481(08)70382-9

Fedoroff, N., & Goldberg, P. (1982). Comparative micromorphology of two late Pleistocene paleosols (in the Paris Basin). Catena, 9(1–2), 227–251. https://doi.org/10.1016/S0341-8162(82)80016-7

Feigl, F. J., Fowler, W. B., & Yip, K. L. (1974). Oxygen vacancy model for the E1′ center in SiO2. Solid State Communications, 14(3), 225–229. https://doi.org/10.1016/0038-1098(74)90840-0

Fenn, K., Stevens, T., Bird, A., Limonta, M., Rittner, M., Vermeesch, P., Andò, S., Garzanti, E., Lu, H., Zhang, H., & Lin, Z. (2018). Insights into the provenance of the Chinese Loess Plateau from joint zircon U-Pb and garnet geochemical analysis of last glacial loess. Quaternary Research, 89(3), 645–659. https://doi.org/10.1017/qua.2017.86

Fitzsimmons, K. (2011). An assessment of the luminescence sensitivity of Australian quartz with respect to sediment history. Geochronometria, 38(3), 199–208. https://doi.org/10.2478/s13386-011-0030-9

Fitzsimmons, K. E., Rhodes, E. J., & Barrows, T. T. (2010). OSL dating of southeast Australian quartz: A preliminary assessment of luminescence characteristics and behaviour. 12th International Conference on Luminescence and Electron Spin Resonance Dating (LED 2008), 5(2), 91–95. https://doi.org/10.1016/j.quageo.2009.02.009

Friebele, E. J., Griscom, D. L., Stapelbroek, M., & Weeks, R. A. (1979). Fundamental defect centers in glass: The peroxy radical in irradiated, high-purity, fused silica. Physical Review Letters, 42(20), 1346–1349.

Gliganic, L. A., Cohen, T. J., Meyer, M., & Molenaar, A. (2017). Variations in luminescence properties of quartz and feldspar from modern fluvial sediments in three rivers. Quaternary Geochronology, 41, 70–82. https://doi.org/10.1016/j.quageo.2017.06.005

Gong, Z., Sun, J., & Lü, T. (2015). Investigating the components of the optically stimulated luminescence signals of quartz grains from sand dunes in China. Quaternary Geochronology, 29, 48–57. https://doi.org/10.1016/j.quageo.2015.06.004

Gong, Z., Sun, J., Lü, T., & Tian, Z. (2014). Investigating the optically stimulated luminescence dose saturation behavior for quartz grains from dune sands in China. Quaternary Geochronology, 22, 137–143. https://doi.org/10.1016/j.quageo.2014.01.003

Götze, J., Plötze, M., and Habermann, D. 2001: Origin, spectral characteristics and practical applications of the cathodoluminescence (CL) of quartz - a review. Mineralogy and Petrology, 71, 225-250.

Gray, H. J., Jain, M., Sawakuchi, A. O., Mahan, S. A., & Tucker, G. E. (2019). Luminescence as a Sediment Tracer and Provenance Tool. Reviews of Geophysics, 57(3), 987–1017. https://doi.org/10.1029/2019RG000646

Grün, R. (1989). Electron spin resonance (ESR) dating. Quaternary International, 1, 65–109. https://doi.org/10.1016/1040-6182(89)90010-4

Guérin, G., Mercier, N., & Adamiec, G. (2011). Dose-rate conversion factors: Update. Ancient TL, 29(1), 5–8.

Guralnik, B., Ankjærgaard, C., Jain, M., Murray, A. S., Müller, A., Wälle, M., Lowick, S. E., Preusser, F., Rhodes, E. J., Wu, T.-S., Mathew, G., & Herman, F. (2015). OSL-thermochronometry using bedrock quartz: A note of caution. Quaternary Geochronology, 25, 37–48. https://doi.org/10.1016/j.quageo.2014.09.001

Haddadchi, A., Olley, J., & Pietsch, T. (2016). Using LM-OSL of quartz to distinguish sediments derived from surface-soil and channel erosion. Hydrological Processes, 30(4), 637–647. https://doi.org/10.1002/hyp.10646

Heller, F., & Liu, T. (1986). Palaeoclimatic and sedimentary history from magnetic susceptibility of loess in China. Geophysical Research Letters, 13(11), 1169–1172. https://doi.org/10.1029/GL013i011p01169

Heller, F., Liu, X., Liu, T., & Xu, T. (1991). Magnetic susceptibility of loess in China. Earth and Planetary Science Letters, 103(1), 301–310. https://doi.org/10.1016/0012-821X(91)90168-H

Huntley, D. J., Godfrey-Smith, D. I., & Thewalt, M. L. W. (1985). Optical dating of sediments. Nature, 313(5998), 105–107. https://doi.org/10.1038/313105a0

Huntley, D. J., & Lamothe, M. (2001). Ubiquity of anomalous fading in K-feldspars and the measurement and correction for it in optical dating. Canadian Journal of Earth Sciences, 38(7), 1093–1106. Scopus. https://doi.org/10.1139/cjes-38-7-1093

Hütt, G., Jaek, I., & Tchonka, J. (1988a). Optical dating: K-feldspars optical response stimulation spectra. Quaternary Science Reviews, 7(3), 381–385. https://doi.org/10.1016/0277-3791(88)90033-9

Hütt, G., Jaek, I., & Tchonka, J. (1988b). Optical dating: K-feldspars optical response stimulation spectra. Quaternary Science Reviews, 7(3), 381–385. https://doi.org/10.1016/0277-3791(88)90033-9

Ikeya, M. (1975). Dating a stalactite by electron paramagnetic resonance. Nature, 255(5503), 48–50. https://doi.org/10.1038/255048a0

Ikeya, M. (1993). New Applications of Electron Spin Resonance: Dating, Dosimetry and Microscopy. WORLD SCIENTIFIC. https://doi.org/10.1142/1854

Jain, M., & Singhvi, Ashok. K. (2001). Limits to depletion of blue-green light stimulated luminescence in feldspars: Implications for quartz dating. Radiation Measurements, 33(6), 883–892. https://doi.org/10.1016/S1350-4487(01)00104-4

Jani, M. G., Bossoli, R. B., & Halliburton, L. E. (1983). Further characterization of the E1′ center in crystalline SiO2. Physical Review B, 27(4), 2285–2293. https://doi.org/10.1103/PhysRevB.27.2285

Jeong, G. Y., & Choi, J.-H. (2012). Variations in quartz OSL components with lithology, weathering and transportation. Quaternary Geochronology, 10, 320–326. https://doi.org/10.1016/j.quageo.2012.02.023

Johnsson, M. J., & Basu, A. (1993). The system controlling the composition of clastic sediments. Processes Controlling the Composition of Clastic Sediments, 284(Geological Society of America, Special Paper), 1–19.

Kars, R. H., Wallinga, J., & Cohen, K. M. (2008). A new approach towards anomalous fading correction for feldspar IRSL dating—Tests on samples in field saturation. Proceedings of the 15th Solid State Dosimetry (SSD15), 43(2), 786–790. https://doi.org/10.1016/j.radmeas.2008.01.021

Kemp, R. A. (1999). Micromorphology of loess–paleosol sequences: A record of paleoenvironmental change. Catena, 35(2), 179–196. https://doi.org/10.1016/S0341-8162(98)00099-X

Kemp, R. A., Derbyshire, E., & Xingmin, M. (1997). Micromorphological variation of the S 1 paleosol across northwest China. CATENA, 31(1), 77–90. https://doi.org/10.1016/S0341-8162(97)00028-3

Kielhofer, J., Miller, C., Reuther, J., Holmes, C., Potter, B., Lanoë, F., Esdale, J., & Crass, B. (2020). The micromorphology of loess-paleosol sequences in central Alaska: A new perspective on soil formation and landscape evolution since the Late Glacial period (c. 16,000 cal yr BP to present). Geoarchaeology, 35(5), 701–728. https://doi.org/10.1002/gea.21807

Kovács, J. (2008). Grain-size analysis of the Neogene red clay formation in the Pannonian Basin. International Journal of Earth Sciences, 97(1), 171–178. https://doi.org/10.1007/s00531-006-0150-2

Kravchinsky, V. A., Zykina, V. S., & Zykin, V. S. (2008). Magnetic indicator of global paleoclimate cycles in Siberian loess–paleosol sequences. Earth and Planetary Science Letters, 265(3), 498–514. https://doi.org/10.1016/j.epsl.2007.10.031

Kukla, G., Heller, F., Ming, L. X., Chun, X. T., Sheng, L. T., & Sheng, A. Z. (1988). Pleistocene climates in China dated by magnetic susceptibility. Geology, 16(9), 811–814. https://doi.org/10.1130/0091-7613(1988)016<0811:PCICDB>2.3.CO;2

Lamothe, M., & Auclair, M. (1999). A solution to anomalous fading and age shortfalls in optical dating of feldspar minerals. Earth and Planetary Science Letters, 171(3), 319–323. https://doi.org/10.1016/S0012-821X(99)00180-6

Lamothe, M., Auclair, M., Hamzaoui, C., & Huot, S. (2003). Towards a prediction of long-term anomalous fading of feldspar IRSL. Radiation Measurements, 37(4), 493–498. https://doi.org/10.1016/S1350-4487(03)00016-7

Li, S.-H. (2002). Luminescence sensitivity changes of quartz by bleaching, annealing and UV exposure. Radiation Effects and Defects in Solids, 157(3), 357–364. https://doi.org/10.1080/10420150212998

Li, Y., Song, Y., Lai, Z., Han, L., & An, Z. (2016). Rapid and cyclic dust accumulation during MIS 2 in Central Asia inferred from loess OSL dating and grain-size analysis. Scientific Reports, 6(1), 32365. https://doi.org/10.1038/srep32365

Li, Y., Song, Y., Fitzsimmons, K. E., Chen, X., Wang, Q., Sun, H., & Zhang, Z. (2018). New evidence for the provenance and formation of loess deposits in the Ili River Basin, Arid Central Asia. Aeolian Research, 35, 1–8. https://doi.org/10.1016/j.aeolia.2018.08.002

Li, Y., & Zhou, L. (2020). Variations of thermally and optically stimulated luminescence sensitivity of loess and pedocomplex samples from southern Tajikistan, Central Asia. Geochronometria, 0(0), 000010151520150118. https://doi.org/10.1515/geochr-2015-0118

Liu, T. S. (1985). Loess and Environment. China Ocean Press (Beijing).

Liu, X. M., Hesse, P., Rolph, T., & Begét, J. E. (1999). Properties of magnetic mineralogy of Alaskan loess: Evidence for pedogenesis. Quaternary International, 62(1), 93–102. https://doi.org/10.1016/S1040-6182(99)00027-0

Liu, Y., Shi, Z., Deng, C., Su, H., & Zhang, W. (2012). Mineral magnetic investigation of the Talede loess–palaeosol sequence since the last interglacial in the Yili Basin in the Asian interior. Geophysical Journal International, 190(1), 267–277. https://doi.org/10.1111/j.1365-246X.2012.05527.x

Lu, H., & An, Z. (1998). Paleoclimatic significance of grain size of loess-palaeosol deposit in Chinese Loess Plateau. Science in China Series D: Earth Sciences, 41(6), 626–631. https://doi.org/10.1007/BF02878745

Lu, H., & Sun, D. (2000). Pathways of dust input to the Chinese Loess Plateau during the last glacial and interglacial periods. Catena, 40(3), 251–261. https://doi.org/10.1016/S0341-8162(00)00090-4

Lü, T., & Sun, J. (2011). Luminescence sensitivities of quartz grains from eolian deposits in northern China and their implications for provenance. Quaternary Research, 76(2), 181–189. https://doi.org/10.1016/j.yqres.2011.06.015

Lü, T., Sun, J., Li, S.-H., Gong, Z., & Xue, L. (2014). Vertical variations of luminescence sensitivity of quartz grains from loess/paleosol of Luochuan section in the central Chinese Loess Plateau since the last interglacial. Quaternary Geochronology, 22, 107–115. https://doi.org/10.1016/j.quageo.2014.04.004

Lü, T., Sun, J., Feathers, J. K., & Sun, D. (2021). Spatiotemporal variations and implications of luminescence sensitivity of quartz grains on the Chinese Loess Plateau since the last interglaciation. Quaternary Research, 99, 190–203. Cambridge Core. https://doi.org/10.1017/qua.2020.53

Maher, B. A., & Taylor, R. M. (1988). Formation of ultrafine-grained magnetite in soils. Nature, 336(6197), 368–370. https://doi.org/10.1038/336368a0

Maher, B. A., & Thompson, R. (1992). Paleoclimatic significance of the mineral magnetic record of the Chinese loess and paleosols. Quaternary Research, 37(2), 155–170. https://doi.org/10.1016/0033-5894(92)90079-X

Matasova, G., Petrovský, E., Jordanova, N., Zykina, V., & Kapička, A. (2001). Magnetic study of Late Pleistocene loess/palaeosol sections from Siberia: Palaeoenvironmental implications. Geophysical Journal International, 147(2), 367–380. https://doi.org/10.1046/j.0956-540x.2001.01544.x

McMorris, D. W. (1970). ESR Detection of Fossil Alpha Damage in Quartz. Nature, 226(5241), 146–148. https://doi.org/10.1038/226146b0

Mejdahl, V. (1979). Thermoluminescence dating: beta-dose attenuation in quartz grains. Archaeometry, 21(1), 61–72. https://doi.org/10.1111/j.1475-4754.1979.tb00241.x

Mineli, T. D., Sawakuchi, A. O., Guralnik, B., Lambert, R., Jain, M., Pupim, F. N., Rio, I. del, Guedes, C. C. F., & Nogueira, L. (2021). Variation of luminescence sensitivity, characteristic dose and trap parameters of quartz from rocks and sediments. Radiation Measurements, 144, 106583. https://doi.org/10.1016/j.radmeas.2021.106583

Moska, P., & Murray, A. S. (2006). Stability of the quartz fast-component in insensitive samples. Proceedings of the 11th International Conference on Luminescence and Electron-Spin Resonance Dating (LED 2005), 41(7), 878–885. https://doi.org/10.1016/j.radmeas.2006.06.005

Mücher, H. J., & Vreeken, W. J. (1981). (Re)deposition of loess in southern Limbourg, The Netherlands. 2. Micromorphology of the lower silt loam complex and comparison with deposits produced under laboratory conditions. Earth Surface Processes and Landforms, 6(3–4), 355–363. https://doi.org/10.1002/esp.3290060314

Murray, A. S., & Wintle, A. G. (2000). Luminescence dating of quartz using an improved single-aliquot regenerative-dose protocol. Radiation Measurements, 32(1), 57–73. https://doi.org/10.1016/S1350-4487(99)00253-X

Murray, A. S., & Wintle, A. G. (2003). The single aliquot regenerative dose protocol: Potential for improvements in reliability. Radiation Measurements, 37(4), 377–381. https://doi.org/10.1016/S1350-4487(03)00053-2

Murray, A. S., Buylaert, J. P., Thomsen, K. J., & Jain, M. (2009). The effect of preheating on the IRSL signal from feldspar. Radiation Measurements, 44(5), 554–559. https://doi.org/10.1016/j.radmeas.2009.02.004

Nagashima, K., Tada, R., Tani, A., Toyoda, S., Sun, Y., & Isozaki, Y. (2007). Contribution of aeolian dust in Japan Sea sediments estimated from ESR signal intensity and crystallinity of quartz. Geochemistry, Geophysics, Geosystems, 8(2). https://doi.org/10.1029/2006GC001364

Nagashima, K., Tada, R., Tani, A., Sun, Y., Isozaki, Y., Toyoda, S., & Hasegawa, H. (2011). Millennial-scale oscillations of the westerly jet path during the last glacial period. Journal of Asian Earth Sciences, 40(6), 1214–1220. https://doi.org/10.1016/j.jseaes.2010.08.010

Nagashima, K., Nishido, H., Kayama, M., Kurosaki, Y., Ohgo, S., & Hasegawa, H. (2017). Composition of Asian dust from cathodoluminescence spectral analysis of single quartz grains. Geology, 45(10), 879–882. https://doi.org/10.1130/G39237.1

Odom, A. L., & Rink, W. J. (1989). Natural accumulation of Schottky-Frenkel defects: Implications for a quartz geochronometer. Geology, 17(1), 55–58. https://doi.org/10.1130/0091-7613(1988)017<0055:NAOSFD>2.3.CO;2

Olley, J. M., Murray, A., & Roberts, R. G. (1996). The effects of disequilibria in the uranium and thorium decay chains on burial dose rates in fluvial sediments. Quaternary Science Reviews, 15(7), 751–760. https://doi.org/10.1016/0277-3791(96)00026-1

Olley, J. M., Roberts, R. G., & Murray, A. S. (1997). Disequilibria in the uranium decay series in sedimentary deposits at Allen's cave, nullarbor plain, Australia: Implications for dose rate determinations. Radiation Measurements, 27(2), 433–443. https://doi.org/10.1016/S1350-4487(96)00114-X

Panaiotu, C. G., Panaiotu, E. C., Grama, A., & Necula, C. (2001). Paleoclimatic record from a loess-paleosol profile in southeastern Romania. Physics and Chemistry of the Earth, Part A: Solid Earth and Geodesy, 26(11), 893–898. https://doi.org/10.1016/S1464-1895(01)00138-7

Paterson, G. A., & Heslop, D. (2015). New methods for unmixing sediment grain size data. Geochemistry, Geophysics, Geosystems, 16(12), 4494–4506. https://doi.org/10.1002/2015GC006070

Pietsch, T. J., Olley, J. M., & Nanson, G. C. (2008). Fluvial transport as a natural luminescence sensitiser of quartz. Quaternary Geochronology, 3(4), 365–376. https://doi.org/10.1016/j.quageo.2007.12.005

Poolton, N. R. J., Smith, G. M., Riedi, P. C., Bulur, E., Bøtter-Jensen, L., Murray, A. S., & Adrian, M. (2000). Luminescence sensitivity changes in natural quartz induced by high temperature annealing: A high frequency EPR and OSL study. Journal of Physics D: Applied Physics, 33(8), 1007–1017. https://doi.org/10.1088/0022-3727/33/8/318

Prescott, J. R., & Hutton, J. T. (1994). Cosmic ray contributions to dose rates for luminescence and ESR dating: Large depths and long-term time variations. Radiation Measurements, 23(2), 497–500. https://doi.org/10.1016/1350-4487(94)90086-8

Preusser, F., Degering, D., Fuchs, M., Hilgers, A., Kadereit, A., Klasen, N., Krbetschek, M., Richter, D., & Spencer, J. Q. G. (2008). Luminescence dating: Basics, methods and applications. E&G Quaternary Science Journal, 57(1/2), 95–149. https://doi.org/10.3285/eg.57.1-2.5

Pullen, A., Kapp, P., McCallister, A. T., Chang, H., Gehrels, G. E., Garzione, C. N., Heermance, R. V., & Ding, L. (2011). Qaidam Basin and northern Tibetan Plateau as dust sources for the Chinese Loess Plateau and paleoclimatic implications. Geology, 39(11), 1031–1034. https://doi.org/10.1130/G32296.1

Ralph, E. K., & Han, M. C. (1966). Dating of Pottery by Thermoluminescence. Nature, 210(5033), 245–247. https://doi.org/10.1038/210245a0

Rao, W., Tan, H., Chen, J., Ji, J., Chen, Y., Pan, Y., & Zhang, W. (2015). Nd–Sr isotope geochemistry of fine-grained sands in the basin-type deserts, West China: Implications for the source mechanism and atmospheric transport. Geomorphology, 246, 458–471. https://doi.org/10.1016/j.geomorph.2015.06.043

Rees-Jones, J. (1995). Optical dating of young sediments using fine-grained quartz. Ancient TL, 13, 9–14.

Rink, W. J., & Odom, A. L. (1991). Natural alpha recoil particle radiation and ionizing radiation sensitivities in quartz detected with EPR: Implications for geochronometry. International Journal of Radiation Applications and Instrumentation. Part D. Nuclear Tracks and Radiation Measurements, 18(1), 163–173. https://doi.org/10.1016/1359-0189(91)90108-T

Roberts, H. M. (2008). The development and application of luminescence dating to loess deposits: A perspective on the past, present and future. Boreas, 37(4), 483–507. https://doi.org/10.1111/j.1502-3885.2008.00057.x

Roberts, H. M., & Wintle, A. G. (2001). Equivalent dose determinations for polymineralic fine-grains using the SAR protocol: Application to a Holocene sequence of the Chinese Loess Plateau. Quaternary Science Reviews, 20(5), 859–863. https://doi.org/10.1016/S0277-3791(00)00051-2

Rousseau, D.-D., Sima, A., Antoine, P., Hatté, C., Lang, A., & Zöller, L. (2007). Link between European and North Atlantic abrupt climate changes over the last glaciation. Geophysical Research Letters, 34(22), L22713. https://doi.org/10.1029/2007GL031716

Salh, R. (2011). Defect Related Luminescence in Silicon Dioxide Network: A Review. In S. Basu (Ed.), Crystalline Silicon—Properties and Uses. InTech. https://doi.org/10.5772/22607

Salikhonov, K.M. and Zavoiskaya, N.E. (2015). Zavoisky and the Discovery of EPR. Resonance - Journal of Science Education 20 (11), 963-968.

Sawakuchi, A. O., Blair, M. W., DeWitt, R., Faleiros, F. M., Hyppolito, T., & Guedes, C. C. F. (2011). Thermal history versus sedimentary history: OSL sensitivity of quartz grains extracted from rocks and sediments. Quaternary Geochronology, 6(2), 261–272. https://doi.org/10.1016/j.quageo.2010.11.002

Sawakuchi, A. O., Guedes, C. C. F., DeWitt, R., Giannini, P. C. F., Blair, M. W., Nascimento, D. R., & Faleiros, F. M. (2012). Quartz OSL sensitivity as a proxy for storm activity on the southern Brazilian coast during the Late Holocene. Quaternary Geochronology, 13, 92–102. https://doi.org/10.1016/j.quageo.2012.07.002

Sawakuchi, A. O., Jain, M., Mineli, T. D., Nogueira, L., Bertassoli, D. J., Häggi, C., Sawakuchi, H. O., Pupim, F. N., Grohmann, C. H., Chiessi, C. M., Zabel, M., Mulitza, S., Mazoca, C. E. M., & Cunha, D. F. (2018). Luminescence of quartz and feldspar fingerprints provenance and correlates with the source area denudation in the Amazon River basin. Earth and Planetary Science Letters, 492, 152–162. https://doi.org/10.1016/j.epsl.2018.04.006

Schellmann, G., Beerten, K., & Radtke, U. (2008). Electron sin resonance (ESR) dating of Quaternary materials. E&G Quaternary Science Journal, 57(1/2), 150–178. https://doi.org/10.3285/eg.57.1-2.6

Schilles, T., Poolton, N. R. J., Bulur, E., Bøtter-Jensen, L., Murray, A. S., Smith, G. M., Riedi, P. C., & Wagner, G. A. (2001). A multi-spectroscopic study of luminescence sensitivity changes in natural quartz induced by high-

temperature annealing. Journal of Physics D: Applied Physics, 34(5), 722–731. https://doi.org/10.1088/0022-3727/34/5/310

Sharma, S. K. (2017). Understanding the Reasons for Variations in Luminescence Sensitivity of Natural Quartz Using Spectroscopic and Chemical Studies. Proceedings of the Indian National Science Academy, 92(0). https://doi.org/10.16943/ptinsa/2017/49024

Shimada, A., Takada, M., & Toyoda, S. (2013). Characteristics of ESR signals and TLCLs of quartz included in various source rocks and sediments in Japan: A clue to sediment provenance. Geochronometria, 40(4), 334–340. https://doi.org/10.2478/s13386-013-0111-z

Shimada, A., Takada, M., & Toyoda, S. (2016). Electron spin resonance signals of quartz in present-day river bed sediments and possible source rocks in the Kizu River basin, Western Japan. Geochronometria, 43(1), 155–161. https://doi.org/10.1515/geochr-2015-0039

Skuja, L., Ollier, N., & Kajihara, K. (2020). Luminescence of non-bridging oxygen hole centers as a marker of particle irradiation of α-quartz. Radiation Measurements, 135, 106373. https://doi.org/10.1016/j.radmeas.2020.106373

Stapelbroek, M., Griscom, D. L., Friebele, E. J., & Sigel, G. H. (1979). Oxygen-associated trapped-hole centers in high-purity fused silicas. Electronic Properties and Structure of Amorphous Solids, 32(1), 313–326. https://doi.org/10.1016/0022-3093(79)90079-6

Stevens, T., Palk, C., Carter, A., Lu, H., & Clift, P. D. (2010). Assessing the provenance of loess and desert sediments in northern China using U-Pb dating and morphology of detrital zircons. Geological Society of America Bulletin, 122(7–8), 1331–1344. https://doi.org/10.1130/B30102.1

Stevens, T., Buylaert, J.-P., Thiel, C., Újvári, G., Yi, S., Murray, A. S., Frechen, M., & Lu, H. (2018). Ice-volume-forced erosion of the Chinese Loess Plateau global Quaternary stratotype site. Nature Communications, 9(1), 983. https://doi.org/10.1038/s41467-018-03329-2

Sun, J. (2002). Provenance of loess material and formation of loess deposits on the Chinese Loess Plateau. Earth and Planetary Science Letters, 203(3), 845–859. https://doi.org/10.1016/S0012-821X(02)00921-4

Sun, J., & Liu, T. (2000). Multiple origins and interpretations of the magnetic susceptibility signal in Chinese wind-blown sediments. Earth and Planetary Science Letters, 180(3), 287–296. https://doi.org/10.1016/S0012-821X(00)00175-8

Sun, Y., Lu, H., & An, Z. (2006). Grain size of loess, palaeosol and Red Clay deposits on the Chinese Loess Plateau: Significance for understanding pedogenic alteration and palaeomonsoon evolution. Monsoon and Tectonics of Asia, 241(1), 129–138. https://doi.org/10.1016/j.palaeo.2006.06.018

Sun, Y., Tada, R., Chen, J., Chen, H., Toyoda, S., Tani, A., Isozaki, Y., Nagashima, K., Hasegawa, H., & Ji, J. (2007). Distinguishing the sources of Asian dust based on electron spin resonance signal intensity and crystallinity of quartz. Atmospheric Environment, 41(38), 8537–8548. https://doi.org/10.1016/j.atmosenv.2007.07.014

Sun, Y., Clemens, S. C., Morrill, C., Lin, X., Wang, X., & An, Z. (2012). Influence of Atlantic meridional overturning circulation on the East Asian winter monsoon. Nature Geoscience, 5(1), 46–49. https://doi.org/10.1038/ngeo1326

Sun, Y., Chen, H., Tada, R., Weiss, D., Lin, M., Toyoda, S., Yan, Y., & Isozaki, Y. (2013). ESR signal intensity and crystallinity of quartz from Gobi and sandy deserts in East Asia and implication for tracing Asian dust provenance. Geochemistry, Geophysics, Geosystems, 14(8), 2615–2627. https://doi.org/10.1002/ggge.20162

Thiel, C., Buylaert, J.-P., Murray, A., Terhorst, B., Hofer, I., Tsukamoto, S., & Frechen, M. (2011). Luminescence dating of the Stratzing loess profile (Austria) – Testing the potential of an elevated temperature post-IR IRSL protocol. Quaternary International, 234(1), 23–31. https://doi.org/10.1016/j.quaint.2010.05.018

Thompson, R., & Oldfield, F. (1986). Environmental Magnetism. Springer Netherlands. https://doi.org/10.1007/978-94-011-8036-8

Thomsen, K. J., Murray, A. S., Jain, M., & Bøtter-Jensen, L. (2008). Laboratory fading rates of various luminescence signals from feldspar-rich sediment extracts. Radiation Measurements, 43(9), 1474–1486. https://doi.org/10.1016/j.radmeas.2008.06.002

Tissoux, H., Voinchet, P., Lacquement, F., Prognon, F., Moreno, D., Falguères, C., Bahain, J.-J., & Toyoda, S. (2012). Investigation on non-optically bleachable components of ESR aluminium signal in quartz. Radiation Measurements, 47(9), 894–899. https://doi.org/10.1016/j.radmeas.2012.03.012

Tissoux, H., Voinchet, P., Lacquement, F., & Despriée, J. (2015). ESR as a method for the characterization of alluvial sediments. Radiation Measurements, 81, 2–8. https://doi.org/10.1016/j.radmeas.2015.05.010

Toyoda, S., & Ikeya, M. (1991). Thermal stabilities of paramagnetic defect and impurity centers in quartz: Basis for ESR dating of thermal history. Geochemical Journal, 25(6), 437–445. https://doi.org/10.2343/geochemj.25.437

Toyoda, S., Ikeya, M., Morikawa, J., & Nagatomo, T. (1992). Enhancement of oxygen vacancies in quartz by natural external β and γ ray dose: A possible ESR Geochronometer of Ma-Ga range. Geochemical Journal, 26(3), 111–115. https://doi.org/10.2343/geochemj.26.111

Toyoda, S., & Hattori, W. (2000). Formation and decay of the E1′ center and of its precursor. Applied Radiation and Isotopes, 52(5), 1351–1356. https://doi.org/10.1016/S0969-8043(00)00094-4

Toyoda, S., Rink, W. J., Yonezawa, C., Matsue, H., & Kagami, T. (2001). In situ production of alpha particles and alpha recoil particles in quartz applied to ESR studies of oxygen vacancies. Quaternary Science Reviews, 20(5), 1057–1061. https://doi.org/10.1016/S0277-3791(00)00018-4

Toyoda, S., & Naruse, T. (2002). Eolian dust from the Asian deserts to the Japanese Islands since the last glacial maximum: The basis for the ESR method. Chikei, 23(5), 811–820.

Toyoda, S., Takeuchi, D., Asai, T., Komuro, K., & Horikawa, Y. (2005). Spin–spin relaxation times of the E1′ center in quartz with and without irradiation: Implications for the formation process of the oxygen vacancies in nature. Radiation Measurements, 39(5), 503–508. https://doi.org/10.1016/j.radmeas.2004.09.002

Toyoda, S., Nagashima, K., & Yamamoto, Y. (2016). ESR signals in quartz: Applications to provenance research – A review. Quaternary International, 397, 258–266. https://doi.org/10.1016/j.quaint.2015.05.048

Tsukamoto, S., Nagashima, K., Murray, A. S., & Tada, R. (2011). Variations in OSL components from quartz from Japan sea sediments and the possibility of reconstructing provenance. Loess in Eurasia, 234(1), 182–189. https://doi.org/10.1016/j.quaint.2010.09.003

Újvári, G., Varga, A., & Balogh-Brunstad, Z. (2008). Origin, weathering, and geochemical composition of loess in southwestern Hungary. Quaternary Research, 69(3), 421–437. https://doi.org/10.1016/j.yqres.2008.02.001

Usami, T., Toyoda, S., Bahadur, H., Srivastava, A. K., & Nishido, H. (2009). Characterization of the E1′ center in quartz: Role of aluminum hole centers and oxygen vacancies. Physica B: Condensed Matter, 404(20), 3819–3823. https://doi.org/10.1016/j.physb.2009.07.075

Vandenberghe, J. (2013). Grain size of fine-grained windblown sediment: A powerful proxy for process identification. Earth-Science Reviews, 121, 18–30. https://doi.org/10.1016/j.earscirev.2013.03.001

Vandenberghe, J., Sun, Y., Wang, X., Abels, H. A., & Liu, X. (2018). Grain-size characterization of reworked fine-grained aeolian deposits. Earth-Science Reviews, 177, 43–52. https://doi.org/10.1016/j.earscirev.2017.11.005

Visocekas, R. (1985). Tunnelling radiative recombination in labradorite: Its association with anomalous fading of thermoluminescence. Nuclear Tracks and Radiation Measurements, 10(4), 521–529. https://doi.org/10.1016/0735-245X(85)90053-5

Vriend, M., Prins, M. A., Buylaert, J.-P., Vandenberghe, J., & Lu, H. (2011). Contrasting dust supply patterns across the north-western Chinese Loess Plateau during the last glacial-interglacial cycle. Quaternary International, 240(1), 167–180. https://doi.org/10.1016/j.quaint.2010.11.009

Wang, X., Lu, H., Xu, H., Deng, C., Chen, T., & Wang, X. (2006). Magnetic properties of loess deposits on the northeastern Qinghai-Tibetan Plateau: Palaeoclimatic implications for the Late Pleistocene. Geophysical Journal International, 167(3), 1138–1147. https://doi.org/10.1111/j.1365-246X.2006.03007.x

Weeks, R. A. (1956). Paramagnetic Resonance of Lattice Defects in Irradiated Quartz. Journal of Applied Physics, 27(11), 1376–1381. https://doi.org/10.1063/1.1722267

Weeks, R. A., & Nelson, C. M. (1960). Trapped Electrons in Irradiated Quartz and Silica: II, Electron Spin Resonance. Journal of the American Ceramic Society, 43(8), 399–404. https://doi.org/10.1111/j.1151-2916.1960.tb13682.x

Wei, C., Yin, G., Li, Y., Liu, C., Li, W., & Guo, R. (2020). Quartz electron spin resonance signal intensity of Al and Ti–Li centers as a provenance indicator: An example from the Yangtze River Basin. Quaternary International, 562, 76–84. https://doi.org/10.1016/j.quaint.2020.06.023

Wiedemann, E. (1888) "Über Fluorescenz und Phosphorescenz, I. Abhandlung" (On fluorescence and phosphorescence), Annalen der Physik 34 (1888) 446-463.

Weil, J. A. (1984). A review of electron spin spectroscopy and its application to the study of paramagnetic defects in crystalline quartz. Physics and Chemistry of Minerals, 10(4), 149–165. https://doi.org/10.1007/BF00311472

Weil, J. A., & Bolton, J. R. (2006). Electron Paramagnetic Resonance. John Wiley & Sons, Inc. https://doi.org/10.1002/0470084987

Weltje, G. J., & von Eynatten, H. (2004). Quantitative provenance analysis of sediments: Review and outlook. Quantitative Provenance Analysis of Sediments, 171(1), 1–11. https://doi.org/10.1016/j.sedgeo.2004.05.007

Wintle, A. G. (1973). Anomalous Fading of Thermo-luminescence in Mineral Samples. Nature, 245(5421), 143–144. https://doi.org/10.1038/245143a0

Wintle, A. G., & Huntley, D. J. (1979). Thermoluminescence dating of a deep-sea sediment core. Nature, 279(5715), 710–712. https://doi.org/10.1038/279710a0

Wintle, A. G., & Murray, A. S. (1999). Luminescence sensitivity changes in quartz. Radiation Measurements, 30(1), 107–118. https://doi.org/10.1016/S1350-4487(98)00096-1

Wintle, A. G., & Murray, A. S. (2006). A review of quartz optically stimulated luminescence characteristics and their relevance in single-aliquot regeneration dating protocols. Radiation Measurements, 41(4), 369–391. https://doi.org/10.1016/j.radmeas.2005.11.001

Yang, J.-D., Chen, J., Tao, X.-C., Li, C.-L., Ji, J.-F., & Chen, Y. (2001). Sr isotope ratios of acid-leached loess residues from Luochuan, China: A tracer of continental weathering intensity over the past 2.5 Ma. Geochemical Journal, 35(6), 403–412. https://doi.org/10.2343/geochemj.35.403

Yu, S.-Y., Colman, S. M., & Li, L. (2016). BEMMA: A Hierarchical Bayesian End-Member Modeling Analysis of Sediment Grain-Size Distributions. Mathematical Geosciences, 48(6), 723–741. https://doi.org/10.1007/s11004-015-9611-0

Yukihara, E. G., & McKeever, S. W. S. (2011). Optically Stimulated Luminescence: Fundamentals and Applications. John Wiley & Sons, Ltd. https://doi.org/10.1002/9780470977064

Zhang, J. F., & Zhou, L. P. (2007). Optimization of the 'double SAR' procedure for polymineral fine grains. Radiation Measurements, 42(9), 1475–1482. https://doi.org/10.1016/j.radmeas.2007.06.007

Zheng, C. X., Zhou, L. P., & Qin, J. T. (2009). Difference in luminescence sensitivity of coarse-grained quartz from deserts of northern China. Radiation Measurements, 44(5), 534–537. https://doi.org/10.1016/j.radmeas.2009.02.013

Zular, A., Sawakuchi, A. O., Guedes, C. C. F., & Giannini, P. C. F. (2015). Attaining provenance proxies from OSL and TL sensitivities: Coupling with grain size and heavy minerals data from southern Brazilian coastal sediments. Radiation Measurements, 81, 39–45. https://doi.org/10.1016/j.radmeas.2015.04.010

3. Chapter 3

The patchwork loess of Central Asia: Implications for interpreting aeolian dynamics and past climate circulation in piedmont regions

Aditi K. Dave[1], Lenka Lisá[2], Giancarlo Scardia[3], Saida Nigmatova[4], Kathryn E. Fitzsimmons[1]

[1]Research Group for Terrestrial Palaeoclimates, Max Planck Institute for Chemistry, Mainz, Germany
[2]Institute of Geology, Czech Academy of Sciences, Prague, Czech Republic
[3]Instituto de Geociências e Ciências Exatas, Universidade Estadual Paulista (UNESP), 13506-900 Rio Claro SP, Brazil
[4]Institute of Geological Sciences K. Satpaeva, Ministry for Education and Science of the Republic of Kazakhstan, Almaty, Kazakhstan

Status

Submitted to Quaternary Science Reviews

Highlights

- Aeolian sedimentation dynamics in the Ili Basin are controlled by a complex interaction between wind regime, sediment availability and supply, and topography.
- Loess mass accumulation rates (MARs) at a given site are driven both by climate dynamics and local geomorphic setting.
- OSL investigations on fine-grain quartz from the Ili Basin yields reliable ages back to c. 70 ky.

Abstract

The reconstruction of mass accumulation rates (MARs) in loess deposits is widely used for interpreting long-term aeolian transport and climate dynamics in terrestrial environments. Interpretations of MAR records are predicated on the assumption that variability at a given site is representative of the wider region and overwhelmingly reflects climatic change. In part, these interpretations are driven by the preponderance of reconstructions based on individual sites, or limited numbers of selected sites. This can lead to bias in the interpretation of past conditions for a region, particularly if other proxy information is lacking. Recent syntheses of loess accumulation rates from multiple sites in Arid Central Asia (ACA) have revealed disparities in the timing of peak accumulation between sites, which were also found to be asynchronous with loess flux in the Chinese Loess Plateau (CLP). These results challenge the presumed link between climate and dust flux, suggesting a more complex interplay between drivers of loess accumulation.

We investigate this issue by 1) extending the spatial cover of loess chronologies across ACA by adding five new sites from the western Ili Basin, and 2) calculating MAR records for 30 sites across ACA and the CLP over the last 60 ky. Our luminescence-dating based chronologies from five sites along the Central Tien Shan piedmont (ACA) yield not only variable MARs, but also diverse histories of loess accumulation, ranging from the mid-Holocene to beyond the last interglacial. Our results indicate spatio-temporal inhomogeneity in the timing and rate of loess deposition at different scales along the Tien Shan piedmont and more broadly across ACA and underscore the importance of interrogating local and regional influences on dust supply and transport. Our calculations of loess MARs from 30 published sites from across both ACA and the CLP facilitate further exploration of the causal link between loess accumulation, climatic and geological controls. We find that the timing of peak dust flux across a region, as an indicator of large-scale climate dynamics, is best derived from an aggregate of sites to remove site-specific bias where local processes or topographic setting outweigh the climate signature.

Keywords: Loess, Quartz, Luminescence dating, Mass accumulation rates, Central Asia, Chinese loess plateau, Ili Basin, Pleistocene

3.1. Introduction

Dust is an important constituent of the climate system. It can act as a trigger for climate change, whether directly by altering the radiative balance of the Earth, or indirectly by changing the optical properties of clouds (Arimoto et al., 2001; Andrea and Rosenfeld, 2008). Iron in mineral dust acts as a limiting nutrient in oceans, increasing ocean productivity and thereby atmospheric greenhouse gas concentrations, thus acting as an additional indirect driver of climate change (Martin, 1990; Martinez-Garcia et al., 2014). Conversely, the production, transport and deposition of dust reflects an earth-surface response to climatic conditions. Consequently, deposits of wind-blown dust, known as loess (Pye,1987; Pecsi, 1990), are recognised as significant terrestrial archives of past climate change (Liu, 1985; Smalley et al., 1995, 2005; Muhs, 2007), especially in the semi-arid and sub-humid temperate latitudes (Fitzsimmons, 2017).

Reconstruction of changes in loess accumulation rates is one of the most commonly used parameters for inferring past climatic conditions and atmospheric dust load. The quantification of loess sedimentation as mass accumulation rates (MARs) not only facilitates direct comparison between different sites, but also the reconstruction of large-scale dust flux patterns over glacial-interglacial timescales (Kohfeld and Harrison, 2003). In addition, loess MAR datasets provide input to models to better understand the role of dust feedback

mechanisms within the climate system (Albani and Mahowald, 2019; Schaffernicht et al., 2020). On this basis, it is essential to ensure that interpretation of MAR datasets reflects a solid understanding of the various geological and climatic factors affecting loess accumulation rates in a given region.

Loess MAR's as a gauge for palaeoenvironmental conditions is based on the widespread assumption that loess accumulation increases during drier, colder and/or windier climate phases, and decreases and is overprinted by soil development during wetter, warmer and/or less windy periods. It is this hypothesis on which correlations between loess profiles are overwhelmingly predicated, both within (e.g., Kukla et al., 1988; Kohfeld and Harrison, 2003; Sun and An, 2005; Fitzsimmons et al., 2012) and between regions (Markovic et al., 2015). Calculations of loess accumulation are mostly based on luminescence dating, which determines the timing of burial of ubiquitous quartz and feldspar minerals and which, having a higher upper dating limit than radiocarbon, can therefore extend the chronological length of the quantitative record (Singhvi et al., 2001; Stevens, 2019). Recently, an increase in studies applying high-resolution luminescence dating to loess deposits has started to suggest a lack of uniformity in accumulation rates (Ujvari et al., 2010; Fitzsimmons et al., 2017), even at individual sites (e.g., Fitzsimmons and Hambach, 2014; Sprafke et al., 2018; Stevens et al, 2018; Fenn et al., 2020). These results call into question the presumed primary association between loess accumulation and climatic controls, and prompt a reconsideration of geological controls on aeolian flux.

Central Asia (hereafter Arid Central Asia or ACA), defined here as the region to the north of the Asian high mountains and between the Caspian Sea and Mongolia, is an arid region at the intersection between two major Northern hemisphere climate systems, the mid-latitude Westerlies and the Siberian High. ACA is assumed to be a major contributor to the global dust cycle (Narsima, 2007; Kok et al., 2021), based on both its climatic context and widespread thick loess deposits. The region therefore represents an invaluable natural laboratory for exploring loess accumulation as a response to climate. Recently produced chronological datasets from loess sites in ACA (Li et al., 2016a, 2018a; Fitzsimmons et al., 2018) indicate a high degree of variability in the timing and peak of loess accumulation between sites, therefore challenging prevailing assumptions linking aeolian flux to cold, dry phases, and with the timescales of glacial-interglacial climate variability. It has since been suggested, on the basis of modelled dust trajectories, that the topographic complexity and diverse landscape features (desert dunes, stony pavements, alluvial deposits and floodplains) in ACA lead to a complex interaction between topography, wind dynamics, sediment availability and supply (Fitzsimmons et al., 2020). We therefore expect that it is not just climate that plays a major role in dictating the pattern and distribution of loess flux in this region and possibly elsewhere, but that other factors must be taken into equal consideration.

In this study, we investigate spatial variability in timing and rates of loess accumulation across the Ili Basin of southeast (SE) Kazakhstan, and in ACA more widely. We undertake a two-fold approach. Firstly, we obtain a high-resolution chronological record based on luminescence dating for five loess sites in the as-yet understudied central and western part of the Ili Basin; providing an additional 200 km of spatial coverage to the loess record in the region. We integrate our new chronologies with published luminescence dated loess records from eastern part of the basin to derive a conceptual understanding of aeolian dynamics within the Ili Basin with respect to timing and topography. Secondly, we calculate MARs for all reliably dated Ili Basin loess sites, as well as for additional sites across ACA and the Chinese Loess Plateau (CLP), to synthesise the spatial distribution of dust flux and the timing of peak accumulation with respect to geographic setting and larger scale climate drivers across Central and East Asia.

3.2. Regional setting

Arid Central Asia (ACA) is a predominantly arid to semi-arid region, defined here as extending from the Caspian Sea in the west to the Mongolian Hangay uplands in the east (Schaetzl et al., 2018). ACA forms a wide belt in the rain shadow north of the Asian high mountains, including the actively uplifting Pamir, Alai and Tien Shan (Schurr et al 2014; Grützner et al., 2017). The region features loess-draped piedmonts, alluvial fans, dune fields, and the large endorheic basins of the Aral Sea and Lake Balkhash. ACA experiences an extremely continental, semi-arid climate. Its present-day climate is driven by the interaction between two main climatic features – the mid-latitude Westerlies and the high-altitude polar front, linked to the Siberian High-Pressure system, from the north. Seasonal variations in wind direction and precipitation are strongly influenced by the interaction between these subsystems and the orography of the region (Lydolph, 1977; Machalett et al., 2008).

This study focuses on the loess deposits that drape the piedmonts of the central and eastern Tien Shan mountain ranges within the Ili Basin, located in SE Kazakhstan and northwest China. The Ili River (also referred to as Yili, Fig. 3.1) is the main inflow of Lake Balkhash; its main tributaries include the Kashi, Tekes and Kunes Rivers, which originate in the upper, Chinese part of the basin. The Ili Basin is surrounded by the Tien Shan mountain ranges to the south, the Chinese Borohoro range to the east, and the Dzhungarian Alatau and northern Tien Shan to the northeast, forming a funnel shape that opens to the west, exposing it to the prevailing westerly and northerly winds and the associated dust transport pathways believed to facilitate loess accumulation along the piedmonts. The basin opens out at the “Ili Gate” onto the alluvial fans, plains and dunefields of the “Ili plain”. The Ili River terminates in a large delta at Lake Balkhash.

The source of loess in the Ili Basin and along the Tien Shan piedmont of the Ili plain is still unclear. Early models (e.g., Obruchev, 1945) posit that the dune fields of the Ili plain to the north, including the Saryesik-Atyrau and Taukum (Fig. 3.1), act both as sediment sinks for material transported from the Tien Shan, and as sources for dust entrainment and transport back onto the piedmont. Recent investigations based on loess bulk chemistry and grain-size from the eastern, Chinese side of the Ili Basin (Li et al., 2018b) suggest that the loess is predominantly locally sourced, with distal, desert-derived material increasing in contribution westward along the piedmont. Models for fine-grained sediment transport suggest that both local and distal transport, as well as the funnelling or obstructing effect of topography, play a role (Fitzsimmons et al., 2020). The setting of individual sites with respect to topography and sediment transport would therefore likely influence the degree to which loess sediments accumulate and preserve responses to past climatic conditions.

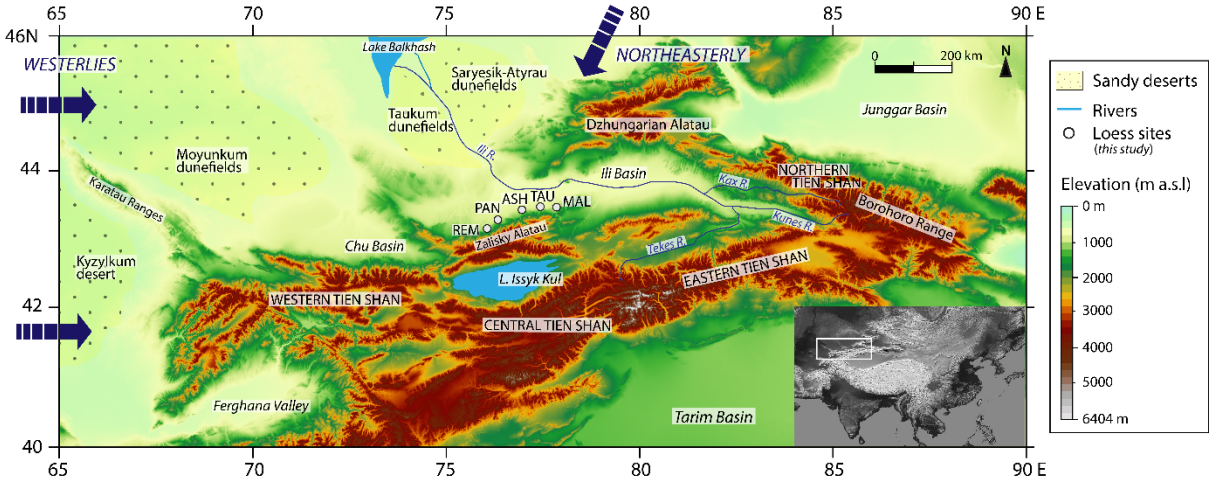

Fig. 3.1. Regional setting and location of loess sites under study.

Loess deposits in the Ili catchment vary substantially in thickness, from more than 100 m (Song et al., 2014) to less than 1 metre. The distribution and thickness of loess in the eastern (Chinese) part of the Ili Basin was described by Song et al. (2014); as yet there is minimal data available for the western and central (Kazakh) part of the basin. Likewise, in the past decade, a number of high-resolution dated loess records have been published from the eastern (Chinese) part of the Ili basin (E et al., 2012; Song et al., 2012, 2015; Kang et al., 2015; Li et al., 2018a, 2020a; Wang et al., 2019a,b; Yang et al., 2020), while the central, Kazakh part of the basin remains largely unexplored. Field observations along the Kazakh Ili piedmonts in 2015 (Sprafke et al., 2018) and again in 2017 suggest that loess deposits here, in contrast to the Chinese Ili (Song et al., 2014) are discontinuous, highly variable in thickness and are

distributed along the mountain foothills, infilling valleys and draping alluvial plains along the range front.

Here we investigate five loess sections from a c. 200 km east-west transect along the Tien Shan piedmont within the Ili catchment, from the enclosed part of the basin, through the Ili Gate and to the Ili plain. This part of the Tien Shan is known as the Zalisky Alatau (Fig. 3.1). It is seismically active; evidence for surface rupture has been observed within the loess at several locations along the range front (Seelander et al., 2012; Grützner et al., 2017). For this reason, we examined our sampling sites for evidence of local tectonic deformation. We found none at our sites, which assures us of their integrity as archives of accumulation independent of tectonics.

3.3. Material and Methods

3.3.1. Field work and site description

We sampled five loess sections from a c. 200 km E-W transect along the Zalisky Alatau range front in SE Kazakhstan (Fig. A1 in appendix A). Since all sites were exposed as vertical cliff sections, we undertook fieldwork by abseil to ensure continuous down-profile observations and sampling. Prior to sampling, we cleared back at least 50 cm of the surface sediment to prevent contamination by recent sediment relocation and to expose undisturbed sections. A brief description of our site locations is given below.

Remizovka (hereafter REM, 43° 13.2' N, 76° 51' E; 1070 m a.s.l.) is a >25 m-thick section exposed on a hillslope, originally excavated for the construction of ski jump facilities on the southern margins of Almaty city. Loess at the site has previously been described and dated by luminescence (Machalett et al., 2006, 2008; Fitzsimmons et al., 2018; Sprafke et al., 2018). A radiocarbon-dated subsection, which has since been removed during road construction (referred to as Tramplin, Feng et al., 2011), was recently placed in stratigraphic context to clarify ambiguity between studies (Sprafke et al., 2018). Our study here focusses on the uppermost 7 m of the main section.

Panfilov (PAN, 43° 22.295' N, 77° 07.670' E; 710 m a.s.l.), is a c. 5 m thick site located just southwest of the village of Panfilovo, c. 40 km northeast of Almaty. The loess section has been exposed as a result of erosion by the Tsyganski Creek, which flows northward from the Tien Shan.

Ashubulak (ASH, 43° 28.671' N, 77° 47.379' E; 760 m a.s.l.) is located at the southern edge of the village of the same name, c. 50 km east of the PAN section. The exposed outcrop at this site is 5.1 m-thick and is entirely composed of pale yellowish primary loess. Like PAN, the ASH

site is also located along the peripheral edge of the piedmont loess, where the loess deposits taper out northwards onto alluvial fans.

Taukaraturyk (TAU, 43° 29.445' N, 78° 01.509' E; 769 m a.s.l.), is a 7.5 m-thick profile located on the southern edge of the village of Taukaraturyuk, c. 20 km east of ASH and c. 100 km eastward of Almaty, at approximately the narrowest part of the Ili Gate. Unlike the loess-marginal sites of PAN and ASH, which are located in more open, exposed sections c. 10 km out from the range front, the TAU site is located much closer to the mountain ranges (c. 1 km north of the first ridge of the Zalisky Alatau).

Malubai (MAL, 43° 26.312' N, 78° 19.763' E; 815 m a.s.l.), is located c. 20 km south of the city of Chilik (Shelek) and c. 25 km east of TAU. The MAL site lies on the northern slope of a northeast-southwest bifurcating flank of the Zalisky Alatau, and is consequently more sheltered than the other sites. We observed a deformed gravel bed c. 6 m north of the MAL section but did not identify any disturbance in the loess packing within our sampled section; we therefore assume the MAL section sampled is essentially undisturbed by recent tectonic activity. The exposed outcrop at MAL is 6 m-thick.

3.3.2. Proxy indices

Samples for micromorphology, grain-size analyses and magnetic susceptibility were collected from four sites (PAN, ASH, TAU and MAL) at 10 cm intervals. We collected these samples in 8 cm^3 plastic boxes hammered into the cleaned-back profiles. The same sample material was used for all three analyses in the order described below. Grain size and magnetic susceptibility data for the site of REM was already available from previous work (Fitzsimmons et al, 2018; Schulte et al., 2018).

3.3.2(a) Magnetic susceptibility

Magnetic susceptibility measurements were performed on 228 samples from four sites (PAN, ASH, TAU, MAL) using AGICO Kappabridge MFK2 at the Alpine Palaeomagnetism Laboratory (Peveragno, Italy). The samples were air dried at 50 °C and measured at room temperature with an alternating current magnetic field with an amplitude of 20 A/m at 976 Hz (low frequency). The low frequency measurements were repeated two times for each sample; the mean was taken for the final calculation of normalised mass-specific bulk magnetic susceptibility (χ_m).

3.3.2(b) Micromorphology

Eighteen selected samples were prepared for micromorphological analysis from three loess localities (PAN, ASH and TAU). The samples were impregnated in vacuum chamber using

Polylite 2000 and after curing, the thin sections were observed using a polarising microscope at resolution ranges of 16-800x at the Institute of Geology, Czech Academy of Sciences (Prague). The micromorphological descriptions follow Stoops (2003) and are summarised in Table A1 of the supplementary material (Appendix A).

3.3.2(c) Grain size

Grain-size analyses were undertaken on 228 samples from four sites (PAN, ASH, TAU and MAL) following two different preparation methods: the total dispersion method (Konert and Vandenberghe, 1997) and dispersion in KOH (Łomotowski et al., 2008). For the total dispersion method, samples were dispersed in 10% KOH solution and then treated with HCl and H_2O_2 to remove carbonates and organic matter respectively. The KOH dispersion method involved measurement following sediment dispersion in 10% KOH solution. All grain-size measurements were undertaken at the Institute of Geology at the Czech Academy of Sciences, Prague, using a CILAS 1190 LD laser particle analyser, with a measurement range of 0.04–2000 µm and analytical error of <2 %. We evaluated mean grain size using the GRADISTAT program (Blott and Pye, 2001). Sedimentology and wind-strength interpretations were made on the basis of mean grain size, the proportion of ≤ 4 µm grains (determined using both preparation methods), as well as the grain size index (GSI: %26–52 µm / %<26 µm; Antoine et al., 2009; based on the total dispersion method).

3.3.3. Luminescence dating

Samples for luminescence dating were collected at 1 m intervals from all five profiles (REM, PAN, ASH, TAU and MAL) by hammering 3.5 cm-diameter, 10 cm-long steel tubes into freshly cleaned loess sections. A total of 27 samples were collected from five sites. Additional sediment for dose-rate analysis was collected from the material immediately surrounding the tubes. The exposed outer material from the ends of the steel tubes was used for determining water content; sediment from the inner parts of the tubes was processed for equivalent dose analysis. All samples were processed under subdued red-light conditions at the Institute of Geosciences, Johannes Gutenberg University, and measured at the Max Planck Institute for Chemistry, respectively (Mainz, Germany). Wet sieving of sediment yielded insufficient coarse grains (>63 µm) for measurement; we therefore prepared fine-grained (4–11 µm) quartz and polymineral samples using established protocols (Frechen et al., 1996; Timar-Gabor et al., 2010).

We measured equivalent dose (D_e) using optically stimulated luminescence (OSL) based on the single aliquot regenerative dose (SAR) protocol (Murray and Wintle, 2000; 2003) for the quartz fraction, and elevated temperature post-infrared infrared stimulated luminescence (pIRIR; Thiel et al., 2011) for the polymineral fine-grained (K-feldspar-bearing) material. In

order to negate the suspicion of any feldspar contamination of the OSL signal from the quartz-rich fine grains, we applied the double-SAR approach (DSAR, Banerjee et al 2001; Jain and Singhvi, 2005; Dave et al., 2018), which includes an additional IR stimulation prior to all blue stimulation steps within the SAR protocol. In samples where saturation of the quartz OSL signal was suspected (after Timar-Gabor et al., 2017), elevated pIRIR signals from fine-grained polymineral samples were used for D_e determination.

Radionuclide concentrations for dose-rate determination were analysed using high-resolution germanium gamma spectrometry, measured at the Felsenkeller, VKTA Dresden. Dose rates were calculated from the radionuclide concentrations using published conversion factors (Guerin et al., 2011), combined with measured moisture content and published equations for cosmic-ray dose rate contributions (Prescott and Hutton, 1994). A detailed account of sample preparation, luminescence measurements and protocols, and dose-rate calculations can be found in the supplementary material in appendix A.

3.3.4. Age-depth modelling and mass accumulation rates

Based on our investigations of fine-grained quartz (section 3.4.2.) and the reliability of quartz-based OSL ages, we limited our assessment of loess MARs to the past 60 ka. The presence of a substantial number of dated loess sites within this age range allows for a good representation of loess sedimentation patterns across the Ili Basin, elsewhere in ACA and across the CLP.

We undertook age-depth modelling and calculated sediment accumulation rates for 30 additional sites based on published luminescence ages (based on quartz OSL and feldspar pIRIR ages) that span the time period 0-60 ka. Our analysis was based on high resolution luminescence ages taken from 14 sites across the Ili Basin (including sites from the present study), 8 sites from neighbouring sedimentary basins in ACA, and 11 representative sites from the CLP. Age-depth modelling for all sites was performed using the R package Bacon (Blaauw and Christen, 2011). The age-depth models derived using R-Bacon were used to estimate the corresponding sedimentation rates (SR, cm ka^{-1}), and then to evaluate MAR's (g $cm^{-2}ka^{-1}$) using the equation: $MAR = SR \times \rho_{dry} \times f_{eol}$, where ρ_{dry} is the dry bulk density (g cm^{-3}) and f_{eol} refers to the sediment fraction that is aeolian in nature (Kohfeld and Harrison, 2000). We used a value of $f_{eol} = 1$ for all calculations, since we assume that loess is entirely aeolian in nature. Based on published literature, we utilised mean bulk density values of 1.5 g cm^{-3} for ACA (based on values obtained by Jia et al., 2018; Wang et al., 2019a; Li et al., 2019a) and 1.48 g cm^{-3} for sites in the CLP (Kohfeld and Harrison, 2003; Kang et al, 2015). Details of the sites analysed in this study (and the selection thereof), criteria for the selection of luminescence ages, age-depth model parameters for R-Bacon, the constraints for MAR

calculations and subsequent interpretation of different sites (where relevant) are described in the supplementary material.

3.4. Results

3.4.1. Stratigraphy and sediment characteristics

The stratigraphy of our five investigated sections, including grain size and magnetic susceptibility can be seen in Fig. 3.2. A detailed account of the micromorphological characteristics are summarized in Table A1 of the supplementary material.

We focused on the uppermost 7 m of the REM loess profile, which spans c. 35-15 ka (based on $pIRIR_{290}$ dating; Fitzsimmons et al., 2018). The top 0.8 m of this section is characterised by recent soil formation, including penetration by living plant roots. A carbonate-enriched subhorizon is observed at 0.8–1.5 m depth, below which massive, homogenous primary loess is observed down to 7.2 m. The magnetic susceptibility record shows relatively little variation down the profile below the recent soil. The grain-size record similarly yields minimal variations, with the exception of a slight increase in the coarser fraction at 3.9–4.3 m and 5.9–6.1 m depths (Schulte et al., 2018). Additional observations relating to colour indices and pedology are described in Fitzsimmons et al. (2018).

The PAN section is 5.1 m–thick and overlies a >3 m-thick fluvial gravel bed; the imbrication of cobbles indicates northward flow. The uppermost 0.5 m of the section comprises modern soil, penetrated by present-day roots. At 0.5–0.7 m, we observe a slightly darker humic horizon, which is intercalated with colluvial loess-like material. Below this layer and down to 0.9 m, colluvial angular clasts (2-4 mm) are observed which grade downwards into loess-like sediment. The upper c. 1.2 m yields higher magnetic susceptibility values (c. 130–90 x 10^{-8} m^3kg^{-1}) that support our observations of weathering and soil formation. From c. 0.9–5.1 m, the section is composed of pale yellowish primary loess, with a carbonate-enriched layer at 0.9–1.2 m. Reduced magnetic susceptibility values (c. 60 x 10^{-8} m^3kg^{-1}) below c. 1.2 m are consistent with un-weathered, primary loess deposits. Micromorphological analyses of 4 samples (Table A1) from the uppermost primary loess (0.9 to 2 m depth) shows dominant well sorted, fine-grained aeolian silt mixed with coarser, angular colluvial material (<4 mm); these observations are supported by the grain-size results (Fig. 3.2). The total dispersion method, which dissociates aggregates, yields a higher proportion of very fine clasts (<4 µm) than the KOH method, which indicates high proportion of aggregates from 0.5-2 m. The aggregates are most likely derived from a combination of colluvial clasts, disintegration of carbonate-coated or carbonate-rich clasts, and aggregation by organic matter present in the sediment. We observe an abrupt increase in magnetic susceptibility at the base of the loess just above the gravels, although the reason for this is unclear.

The outcrop at ASH is 5.1 m-thick and is entirely composed of pale yellowish primary loess. The modern soil is c. 30 cm-thick with modern rootlets. While the geographic situation of ASH is similar to PAN, located along the northern margin of the piedmont loess deposits, the ASH sediments are more consistent with homogenous, fine-grained primary loess and no colluvial input was observed. Magnetic susceptibility yields no major variations down the profile, which is consistent with primary loess deposition with no evidence of pedogenesis. Micromorphology of five selected samples (Table A1) provides further evidence of minimal disturbance of the sediments following aeolian deposition.

The TAU section is c. 7.5 m-thick. The uppermost 0.3 m is composed of humic soil with modern rootlets and bioturbation, below which a blocky, carbonate-rich C horizon extends down to 0.7 m. From 0.7–7.5 m depth, the section comprises pale yellowish primary loess, with local occurrences of very coarse sand at depths of 1.5–2.0 m, 2.4–2.8 m, and 3.8–4.9 m. Carbonate mottling was observed at 1.8–2.9 m and 5.5–7.1 m, and minor manganese concretions occur at 2.4–2.8 m and 3.0–3.8 m. The magnetic susceptibility values show subtle variations along the profile. Higher values (c. 90–120 x 10^{-8} m^3kg^{-1}) occur in the uppermost 2.5 m. We interpret these peaks as incipient pedogenesis which was not observed in the field. There is considerable variation in the GSI in the upper 2.5 m, as well as three distinct increases in mean grain size and the GSI at 3.4–3.8 m, 4–5 m, and 6–7.5 m (Fig. 3.2) which occur as subangular very coarse sand (Table A1). We interpret these peaks as evidence of colluvial input from the nearby bedrock outcrops, which are c. 0.7 km south of the site. Micromorphological analysis on six selected samples throughout the profile also identified persistent occurrence of angular gypsum crystals below 1.6 m depth (Table A1), which should represent *in situ* precipitation under arid conditions.

The exposed outcrop of MAL is 6 m-thick. The uppermost c. 0.4 m is composed of modern soil with roots developed within colluvial loess-like material. At 0.4–0.9 m depth, we observe fewer angular clasts within a loess matrix. A discontinuous very coarse sand to gravel layer with silt matrix was observed at 1.1–1.3 m, below which carbonate-rich loess dominates down to c. 2 m. Below 2 m depth, the section is composed of pale yellowish-beige primary loess, with occasional carbonate mottling and Fe-Mn concretions observed at 2.5–5 m. The MAL section yields higher magnetic susceptibility (c. 70 x 10^{-8} m^3kg^{-1}) in the upper 1.5 m, most likely reflecting recent pedogenesis. Mean grain size and GSI vary substantially at 0.5–2.5 m; below 5 m, a sudden decrease in grain size is observed. The grain size variations in the upper 2.5 m most likely reflect variable colluvial input to the silt-dominated aeolian component. Below 2.5 m, the mean grain size, as well as GSI, does not show significant

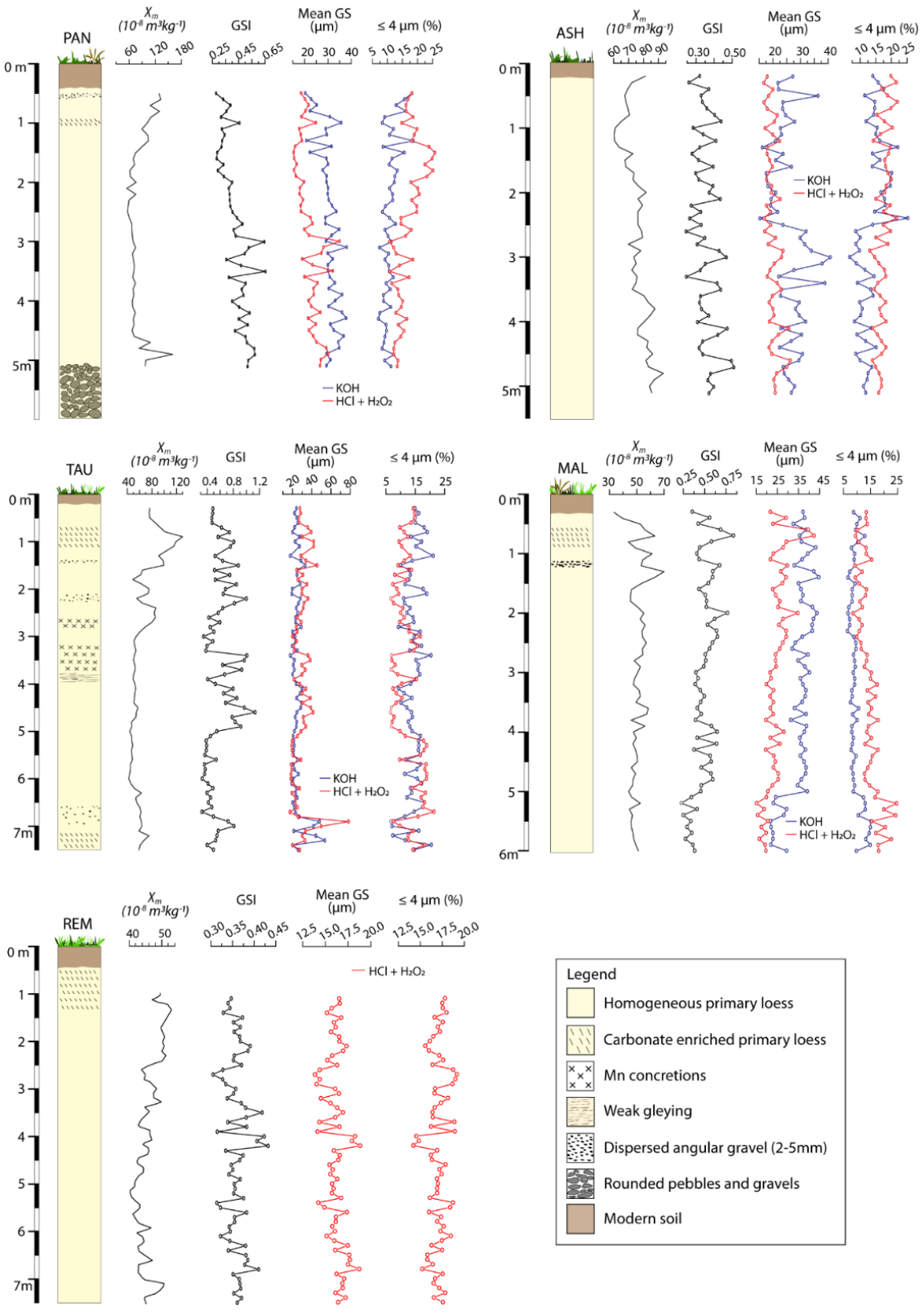

Fig. 3.2. Stratigraphy of the loess sites under study, with down-profile variation in mean grain size (GS), grain size index (GSI) and magnetic susceptibility at the respective sites. The grain size dataset for REM is obtained from Schulte et al. (2018) and the magnetic susceptibility at REM is from Fitzsimmons et al. (2018).

variation and is likely to reflect purely aeolian input to the site. The abrupt decrease of GSI in the primary loess below 5 m most likely indicates a decrease in wind strength (Fig. 3.2).

3.4.2. Luminescence dating

3.4.2(a) Quartz OSL signal characteristics

The natural and regenerative OSL decay curves obtained from fine-grained quartz from all five sites are sufficiently bright for reliable dating, although intensity varies between samples. The generally high sensitivity observed in our samples contrasts with observations from sites further east in the Ili Basin (e.g., Li et al., 2018a). The fine-grained quartz OSL decay curves show rapid decay within the initial 1 s of stimulation, indicating dominance of the rapidly bleached fast component (Fig. A2), and are suitable for luminescence dating using the DSAR protocol.

The thermal stability of signals used for D_e determination was tested using the preheat plateau test on 4–11 µm quartz of two samples, A0021 (PAN) and A0034 (ASH), by varying the temperature from 180 to 280 °C for 10 s (Fig. 3.3a). The results indicate an acceptable pre-heat plateau range between 240 to 260 °C, hence a preheat of 260 °C with a cut heat of 240 °C for 10 s was chosen for all further equivalent dose measurements. We tested the performance of the DSAR protocol on sample A0034 using different infrared (IR) bleaching temperatures and IR bleaching times, and found that lower IR bleaching temperatures (50 °C) are more suitable irrespective of IR exposure time (Fig. 3.3b). Dose-recovery tests were performed on two samples (A0025 from PAN; A0034 from ASH) using both DSAR and the standard SAR protocol using a given beta irradiation dose similar to the equivalent dose (~ 47.5 Gy). Dose recovery ratios were found to be within 10% of unity in all cases (Fig. 3.3a).

Equivalent doses were measured on 16-22 aliquots from each of the fine-grained quartz samples from all five sites. D_e values for the samples from REM were measured using the SAR protocol; those from the other four sites (PAN, ASH, TAU and MAL) were measured using the DSAR protocol (Table A2). The robustness of the measurement protocols for individual aliquots was assessed based on recycling and recuperation ratios, measured after all irradiation steps. Recycling ratios fell within 10% of unity for all samples. Recuperation ratios were <2% of the natural signal for all aliquots, indicating negligible thermal transfer of charge during measurements. D_e's were calculated by integrating the initial 0.8 s, by subtracting the last 8 s of the background from the OSL signal. Since the D_e distributions of all samples are gaussian in form, the Central Age Model (CAM, Galbraith et al., 1999) was used to calculate the D_e for all samples (Table 3.1).

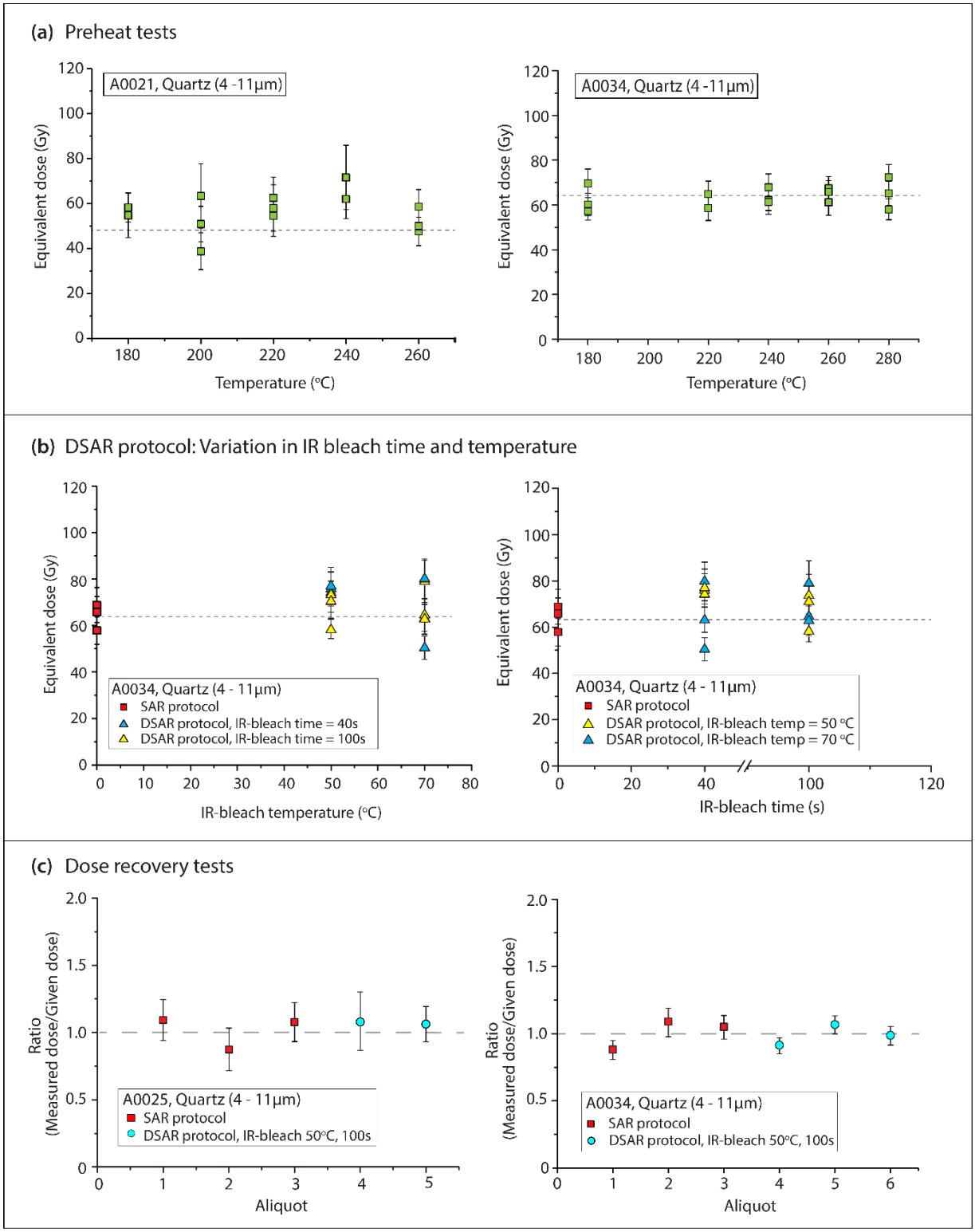

Fig. 3.3. (a) Dependence of equivalent dose (D_e) on preheat temperature during SAR protocols for selected samples A0021 (PAN) and A0034 (ASH) (b) Optimisation of the DSAR protocol: Variation in D_e with varying IR bleach temperature and IR bleach time respectively for sample A0034 (c) Dose recovery tests on selected samples (A0025 and A0034) using both SAR and DSAR protocols.

All samples below 1.5 m depth at TAU and below 1 m at MAL exhibited saturation-like behaviour of the OSL dose-response curve in the lower dose region. We therefore tested the dose response of four selected fine-grained quartz samples from TAU (A0003, A0016) and MAL (A0037, A0050) at higher doses (up to c.1500 Gy) according to Timar-Gabor et al. (2017) (Fig. A3, refer supplementary material in appendix A for details). From these, we derived apparent D_e values of c. 180-190 Gy (c. 70 ka), which indicates the natural saturation values of fine-grained quartz in this region (Table 3.1).

3.4.2(b) pIRIR signal characteristics

Given the apparent (natural) saturation of fine-grained quartz at TAU (>1.5 m depth) and MAL (>0.5 m depth), we undertook pIRIR dating of the polymineral fine-grained fraction for those samples; pIRIR has been shown to saturate at higher doses than quartz OSL (Buylaert et al., 2012). We assessed the applicability of the pIR-IRSL protocol using a stimulation temperature of 290 °C by undertaking dose-recovery tests on sample A0054 (MAL). This yielded a ratio of measured-to-given dose within 10% of unity (Fig. A4) and demonstrated the suitability of the protocol. Subsequent $pIRIR_{290}$ measurements of equivalent dose from four samples each from TAU (below 1.5 m depth) and MAL (below 0.5 m) yielded natural signals close to saturation. We evaluated the closeness of the natural pIRIR signals to saturation by constructing dose response curves at high doses (>3000 Gy) for two polymineral samples taken from the top and bottom of the TAU (A0003 and A0016) and MAL (A0037 and A0050) sites respectively, and assessing the ratio of natural sensitivity-corrected $pIRIR_{290}$ signal to that emitted at a dose of c. 3325 Gy (Fig. 3.4; after Avram et al., 2020). The D_e of all samples lies in the range of 88–92%, which is greater than $2D_o$ (a value defined as 85% of saturation for quartz OSL signal; Wintle and Murray, 2006). The $2D_o$ value is recommended as the upper limit for quartz OSL dating as any uncertainty in the natural signal leads to a higher asymmetric uncertainty in the evaluated D_e values (Wintle and Murray, 2006), however, no equivalent criteria exists for pIRIR signals and as such we evaluate our samples based on the same criteria as quartz OSL. Consequently, the $pIRIR_{290}$ ages from TAU and MAL, summarised in Table A3, are considered minimum ages.

3.4.2(c) Chronology of the Zailisky Alatau loess sections, Central Tien Shan piedmont

The final age estimates from all five loess profiles are summarised in Table 3.1 and Fig. 3.5. Fine-grained quartz OSL ages were derived for 19 samples from four sites (REM, PAN, ASH, and the upper 1m of TAU; Fig. 3.5). Polymineral fine-grain pIRIR dating on 8 selected samples from below 1.5 m and 0.5 m at TAU and MAL respectively yielded minimum age estimates (Table A3). The upper 7 m of the profile REM spans 10–40 ka and falls within the uncertainties of previously published pIRIR ages (Fitzsimmons et al., 2018). Profiles PAN, ASH and the upper 1 m of TAU date to between 6–17 ka. The sediments at MAL and below 1 m at TAU were deposited >180 ka.

Table 3.1. Equivalent dose, dose rate data and luminescence age estimates for fine grained quartz from the Ili basin study sites. The term n_e/n_t refers to the total number of accepted discs to the total number of discs measured.

Site	Sample No.	Depth (m)	Moisture attenuated dose rate (Gy/ka)			Cosmic (Gy/ka)	Total Dose Rate (Gy/ka)	n_e/n_t	De (Gy)	Age (ka)
			Alpha	Beta	Gamma					
Remizovka (REM)	L-EVA-1475	1.1 ± 0.10	0.5 ± 0.1	2.0 ± 0.2	1.2 ± 0.1	0.20 ± 0.02	3.8 ± 0.4	24/24	48.2 ± 0.5	12.8 ± 1.2
	L-EVA-1476	2.1 ± 0.10	0.5 ± 0.1	2.3 ± 0.2	1.3 ± 0.1	0.17 ± 0.02	4.3 ± 0.4	24/24	75.7 ± 1.0	17.8 ± 1.6
	L-EVA-1477	3.1 ± 0.10	0.6 ± 0.1	2.3 ± 0.2	1.4 ± 0.1	0.15 ± 0.02	4.4 ± 0.4	22/24	86.0 ± 1.2	19.7 ± 1.9
	L-EVA-1478	4.1 ± 0.10	0.5 ± 0.1	2.2 ± 0.2	1.3 ± 0.1	0.13 ± 0.01	4.1 ± 0.4	24/24	88.4 ± 1.4	21.7 ± 2.0
	L-EVA-1479	5.1 ± 0.10	0.5 ± 0.1	2.2 ± 0.2	1.2 ± 0.1	0.12 ± 0.01	4.0 ± 0.4	24/24	99.1 ± 1.6	24.9 ± 2.3
	L-EVA-1480	6.1 ± 0.10	0.5 ± 0.1	2.2 ± 0.2	1.2 ± 0.1	0.11 ± 0.01	4.0 ± 0.4	24/24	107.0 ± 2.0	26.5 ± 2.5
	L-EVA-1481	7.1 ± 0.10	0.5 ± 0.1	2.2 ± 0.2	1.3 ± 0.1	0.10 ± 0.01	4.0 ± 0.4	24/24	127.0 ± 2.0	31.5 ± 2.9
Panfilov (PAN)	A0017	1.0 ± 0.05	0.5 ± 0.1	2.2 ± 0.2	1.3 ± 0.1	0.21 ± 0.02	4.2 ± 0.2	19/19	23.1 ± 0.3	5.5 ± 0.3
	A0019	2.0 ± 0.05	0.4 ± 0.1	1.9 ± 0.2	1.1 ± 0.1	0.18 ± 0.02	3.6 ± 0.2	19/19	38.5 ± 0.5	10.6 ± 0.7
	A0021	3.0 ± 0.05	0.5 ± 0.1	2.1 ± 0.2	1.2 ± 0.1	0.16 ± 0.02	3.9 ± 0.2	16/17	47.4 ± 1.8	12.0 ± 1.1
	A0023	4.0 ± 0.05	0.5 ± 0.1	2.0 ± 0.2	1.2 ± 0.1	0.14 ± 0.01	3.9 ± 0.2	20/20	63.4 ± 1.6	16.4 ± 1.3
	A0025	5.0 ± 0.05	0.5 ± 0.1	2.2 ± 0.2	1.3 ± 0.1	0.13 ± 0.01	4.0 ± 0.2	16/17	64.4 ± 2.6	15.9 ± 1.4
Ashubulaq (ASH)	A0026	0.5 ± 0.05	0.4 ± 0.1	1.8 ± 0.2	1.1 ± 0.1	0.24 ± 0.02	3.6 ± 0.2	20/20	45.9 ± 0.6	12.9 ± 0.9
	A0028	1.5 ± 0.05	0.5 ± 0.1	2.1 ± 0.2	1.3 ± 0.1	0.20 ± 0.02	4.1 ± 0.2	20/21	52.6 ± 2.0	12.7 ± 1.1
	A0030	2.5 ± 0.05	0.5 ± 0.1	2.2 ± 0.2	1.3 ± 0.1	0.17 ± 0.02	4.2 ± 0.2	19/20	51.1 ± 2.0	12.3 ± 1.1
	A0032	3.5 ± 0.05	0.5 ± 0.1	2.3 ± 0.2	1.3 ± 0.1	0.15 ± 0.02	4.2 ± 0.2	20/20	63.0 ± 1.3	14.9 ± 1.0
	A0034	4.5 ± 0.05	0.5 ± 0.1	2.2 ± 0.2	1.3 ± 0.1	0.14 ± 0.01	4.1 ± 0.2	21/22	63.5 ± 1.1	15.6 ± 1.1
Taukaraturyuk (TAU)	A001	0.5 ± 0.05	0.4 ± 0.0	1.8 ± 0.1	1.1 ± 0.1	0.24 ± 0.02	3.5 ± 0.2	22/22	46.6 ± 1.4	13.3 ± 1.0
	A002	1.0 ± 0.05	0.5 ± 0.1	2.0 ± 0.2	1.2 ± 0.1	0.21 ± 0.02	3.9 ± 0.2	22/22	44.9 ± 0.7	11.4 ± 0.8
	*A003**	*1.5 ± 0.05*	*0.5 ± 0.1*	*2.0 ± 0.1*	*1.2 ± 0.1*	*0.19 ± 0.02*	*3.9 ± 0.2*	*8/8*	*305.1 ± 13.8*	*78.3 ± 7.1*
	*A0016**	*7.5 ± 0.05*	*0.5 ± 0.1*	*2.3 ± 0.2*	*1.3 ± 0.1*	*0.10 ± 0.01*	*4.2 ± 0.2*	*7/11*	*301.6 ± 22.4*	*71.5 ± 8.5*
Malubai (MAL)	*A0037*[i]	*1.0 ± 0.05*	*0.6 ± 0.1*	*2.0 ± 0.2*	*1.2 ± 0.1*	*0.21 ± 0.02*	*4.0 ± 0.2*	*3/3*	*339.7 ± 17.0*	*84.9 ± 8.5*
	*A0037**	*1.0 ± 0.05*	*0.8 ± 0.1*	*2.4 ± 0.2*	*1.6 ± 0.1*	*0.20 ± 0.02*	*5.0 ± 0.2*	*3/3*	*339.7 ± 17.0*	*67.9 ± 6.1*
	*A0050**	*5.1 ± 0.05*	*0.7 ± 0.1*	*2.5 ± 0.2*	*1.6 ± 0.1*	*0.13 ± 0.01*	*4.9 ± 0.2*	*3/3*	*373.1 ± 18.5*	*76.1 ± 6.8*

A0037 has unusually low Uranium content compared to the samples from the rest of the profile, hence, the age derived here maybe overestimated due to low dose rate. Hence, we use the dose rate of A0038.* The text shown in Italics are saturated ages from Quartz estimated from dose response curves constructed at high dose

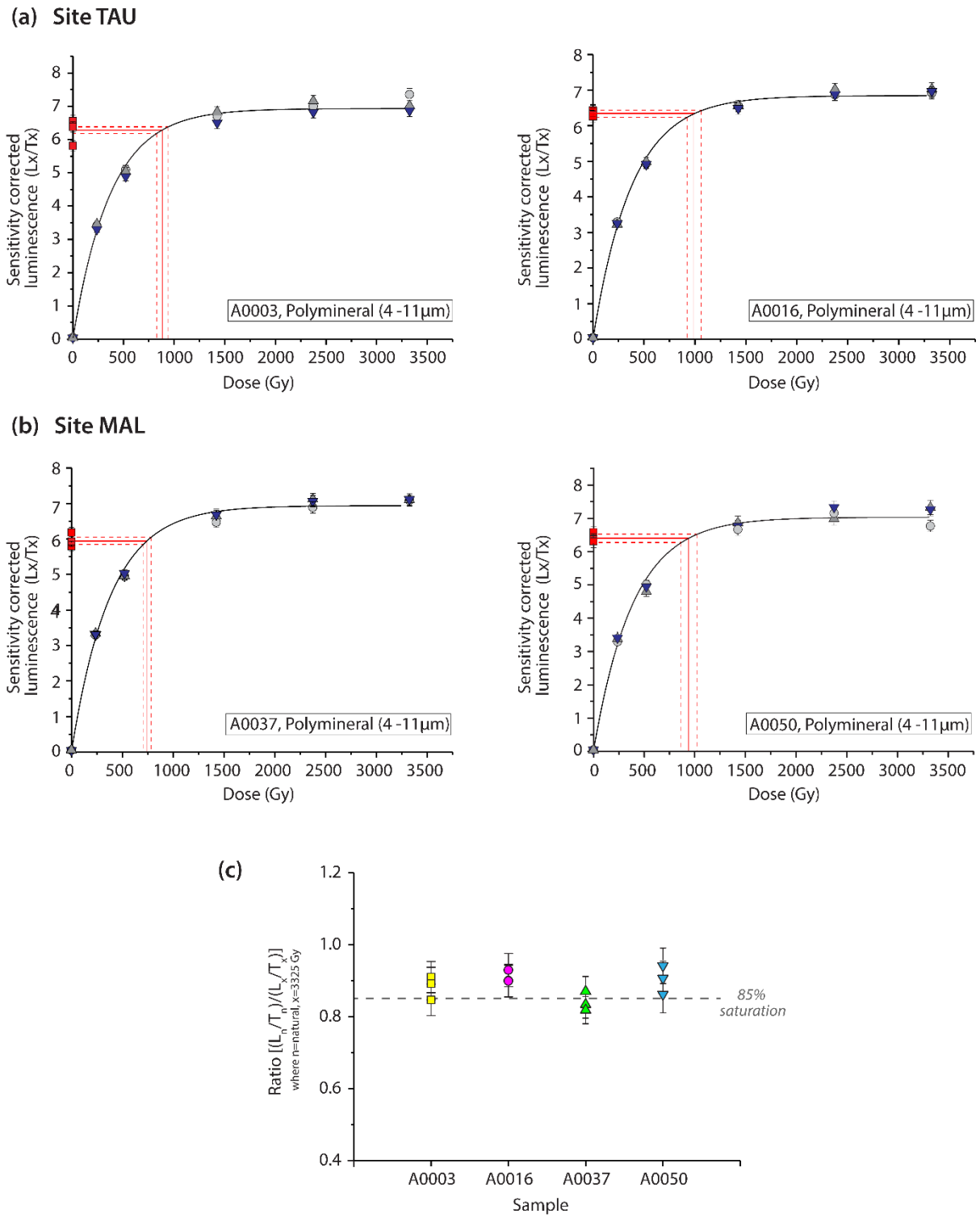

Fig. 3.4. Dose response curve for fine-grained polymineral samples at high doses (>3000 Gy) for selected samples from two sites: (a) site TAU, samples A0003 (depth 1.5 m) and A0016 (depth 7.5 m); and (b) site MAL, samples A0037 (depth 1 m) and A0050 (depth 5.1 m). (c) Ratio of natural sensitivity-corrected $pIRIR_{290}$ signal to that emitted at a dose of c. 3325 Gy for the aforementioned samples, taken from the top and bottom of the TAU and MAL sections.

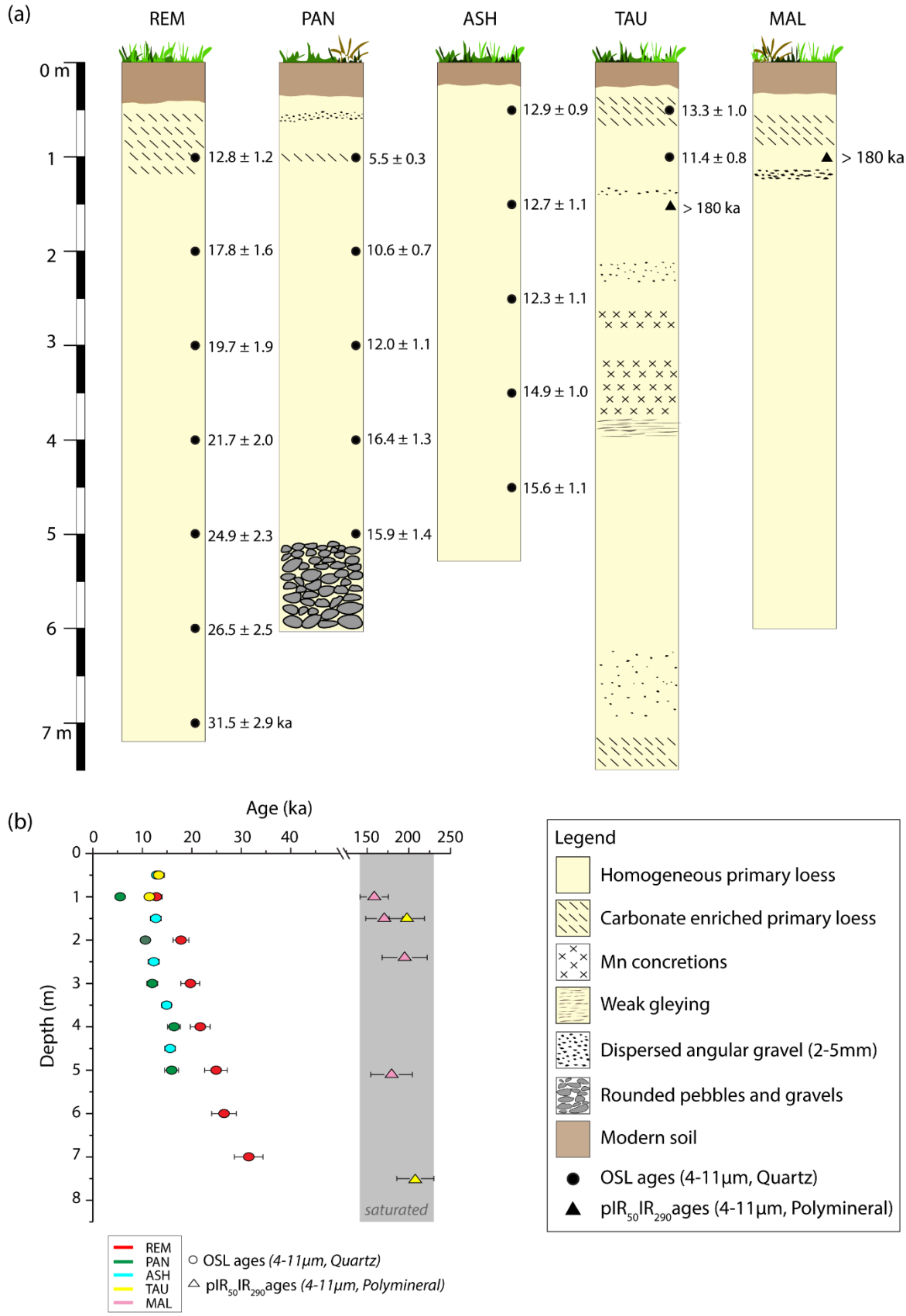

Fig. 3.5. (a) Stratigraphy of all the sites with the luminescence ages obtained in this study. (b) Plot of optical ages (2σ uncertainty) as a function of depth for all sites.

3.4.3. Age modelling and mass accumulation rates

Figure 3.6 shows the location of our sites, as well as of published sites from ACA and CLP, for which we calculated mass accumulation rates (MARs) from luminescence-based chronologies (quartz OSL and feldspar pIRIR ages). We limited our calculations of MARs to the last 60 kyr since (i) our investigations in this region suggest an upper limit to reliable dating of quartz in this region (based on saturation of the quartz OSL signal) of c. 70 ka, and (ii) most published loess sites in ACA and the CLP span this time period, so allowing for a representative evaluation of loess depositional dynamics across these regions.

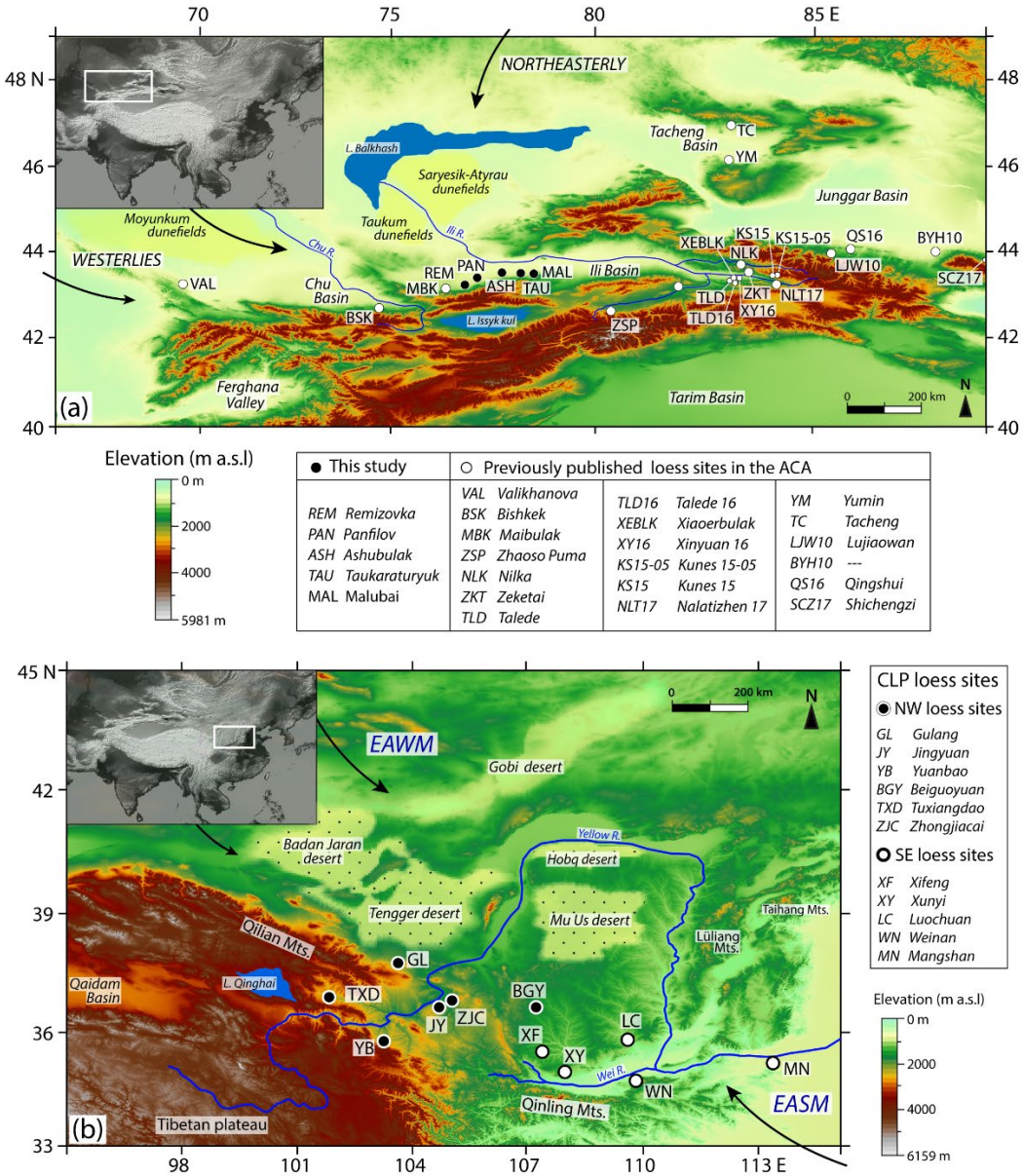

Fig. 3.6. Location and regional settings of all reliably dated loess sites in (a) ACA and (b) the CLP, for which we calculated MARs. References of all the published loess sites are listed in Table A5 of the supplementary material.

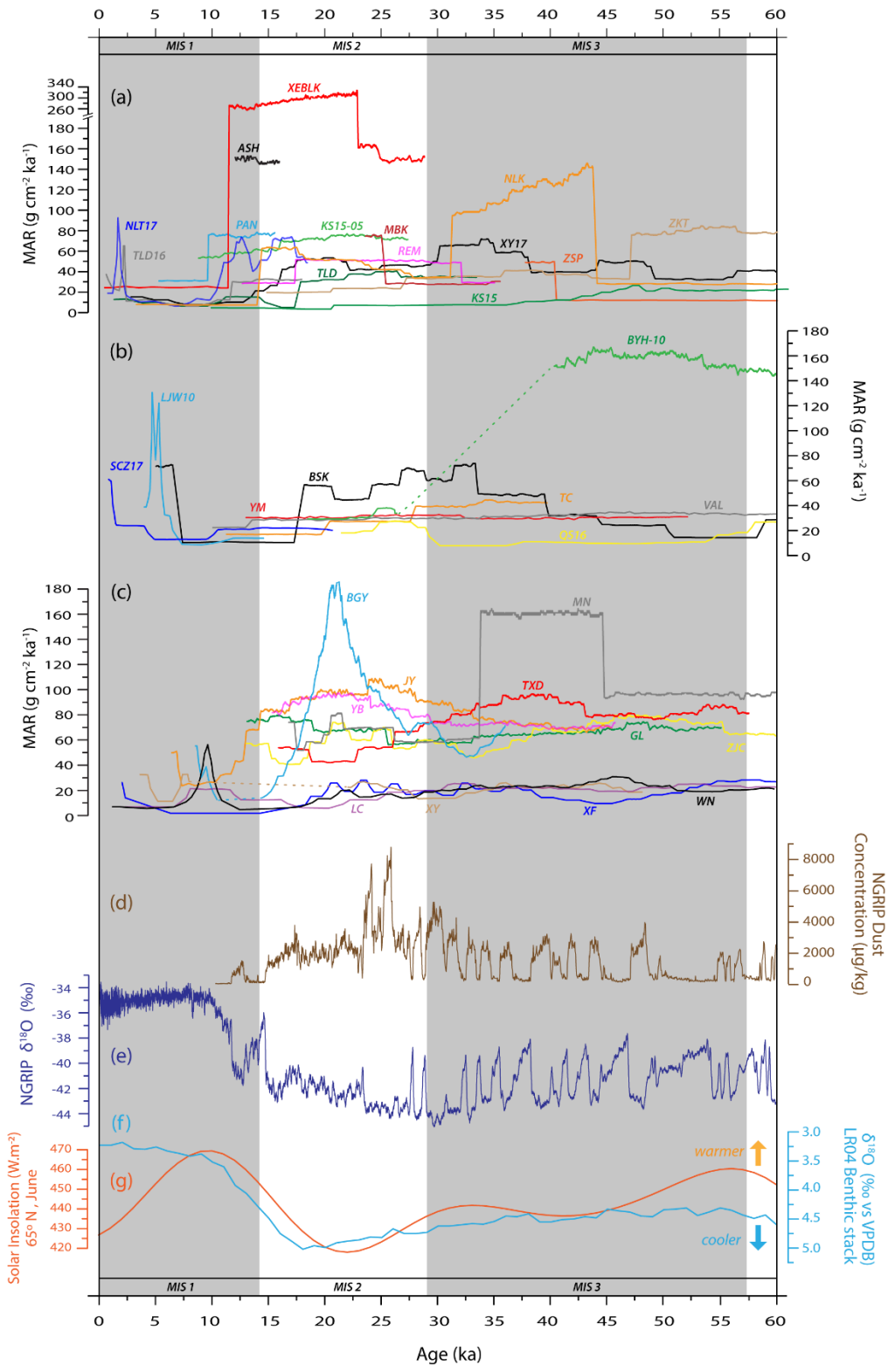

Fig. 3.7. Comparison of MARs over the past 60 ky for loess sites in (a) the Ili Basin (b) other enclosed basins in ACA and (c) the CLP. Note the uniform y-axis, with the exception of extremely high MARs at XEBLK in the Ili Basin. We compare the loess accumulation rates with (d) NGRIP dust flux (Ruth et al., 2007), (e) NGRIP $\delta^{18}O$ (Rasmussen et al., 2014), (f) stacked benthic foraminifera $\delta^{18}O$ marine record LR04 (Lisiecki and Raymo, 2005) and (g) June insolation at 65°N (Berger and Loutre, 1991). The dashed lines in the MARs represents a depositional unconformity/ hiatus at the respective site.

The MARs of sites in the Ili Basin, elsewhere in ACA, and across the CLP are illustrated with respect to concentrations of dust within the Greenland NGRIP ice core (Ruth et al., 2007), stable oxygen isotope records from NGRIP (Rasmussen et al., 2014) and the global marine stack (Lisiecki and Raymo, 2005), and June solar insolation at 65°N (Berger and Loutre, 1991) in Fig. 3.7. We observe substantial differences in absolute accumulation as well as the timing of peaks in accumulation between sites in the Ili Basin and across ACA more widely (Fig. 3.7a, b). There are similar differences across the CLP (Fig. 3.7c). Furthermore, based on our calculations of MARs from 11 sites across the CLP, we observe a distinct difference between sites located in the northwest (NW) and those in the southeast (SE). The geographic difference in loess accumulation in the CLP has previously been reported for various time periods (Lu and Sun, 2000; Kohfeld and Harrison, 2003; Xu et al., 2018; Liu et al., 2020).

3.5. Discussion

3.5.1. Spatio-temporal variation in loess deposition along the Central Tien Shan (Zailisky Alatau region)

Our new dataset adds chronologic constraints for five loess sites (including new data from REM) from the virtually unexplored Zailisky Alatau piedmont in the western portion of the Ili Basin. Our sites bridge the geographic gap between the relatively intensely studied eastern Ili Basin (E et al., 2012; Kang et al., 2015; Song et al., 2012, 2015; Li et al., 2016b, 2018a; Wang et al., 2019a,b; Li et al, 2020), and several dated sites further west at Maibulak (MBK) – also along the Zailisky Alatau (Fitzsimmons et al., 2017), Bishkek (BSK) in the Chu River valley (Youn et al., 2014) and Valikhanova (VAL) on the eastern slopes of the Karatau Range (Fitzsimmons et al., 2017)(Fig. 3.6a).

We identified phases of loess accumulation and illustrated these with respect to altitude, deposit thickness and distance from the range front in a schematic diagram in Fig. 3.8. Geographically, the four sites of MBK, REM, PAN and ASH lie west of the Ili Gate and in the more open part of the basin. TAU and MAL lie at approximately the narrowest part of the basin (the “Gate”) and are comparatively sheltered from northerly winds. The sites of PAN, ASH, TAU and MAL lie at similar elevations (~700-800 m a.s.l.); both MBK and REM are situated at higher altitudes (1070 m a.s.l.). The distances of the sites from the range front are also variable. MBK in the west overlies an alluvial fan c. 350 m from the range front and c. 2 km northward of a steeper break in slope. REM is situated atop a spur of the foothills which rises c. 200 vertical metres above the plain, and c. 5 km from the major break in slope representing the transition to bedrock ranges. PAN and ASH lie the greatest distance from the range front, c. 7.5-8 km to its north. TAU is located c. 1 km northward of the first ridge of the Zailisky Alatau, and MAL lies c. 150 m north of a bedrock spur and c. 2.3 km north of the main range. With the exception of REM, where the range front is oriented approximately

SSW-NNE, all sites are situated northward of an east-west trending break in slope. We hypothesise that (1) location within the basin, (2) distance from the range front and (3) its strike are all likely to have played a role in the potential of individual sites to trap aeolian sediment through time.

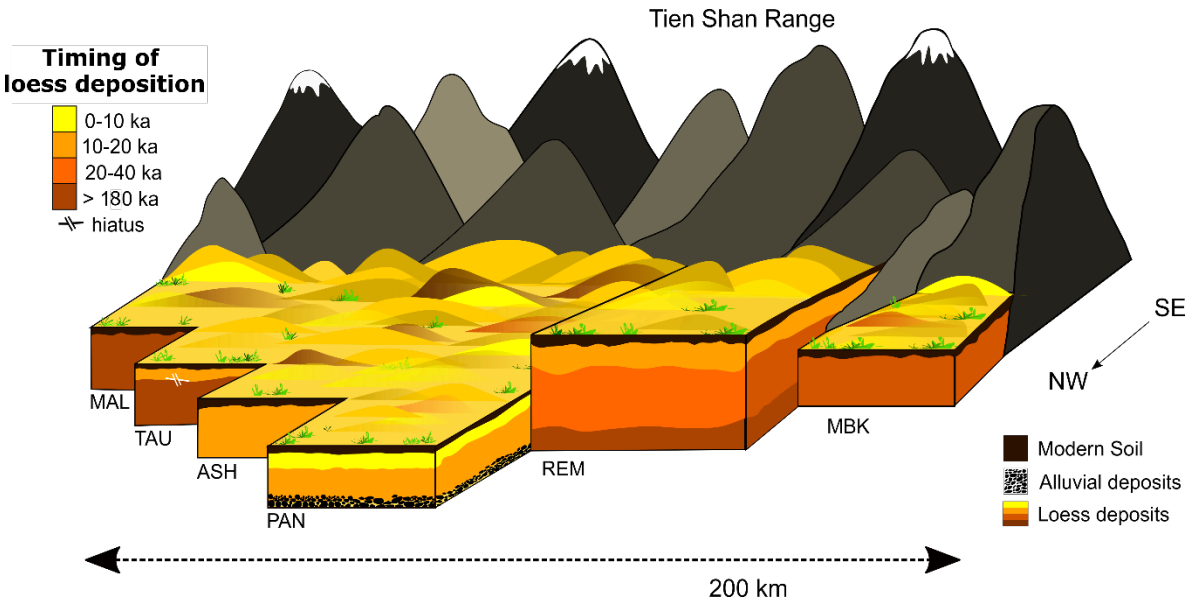

Fig. 3.8. Schematic 3D representation of the timing of loess accumulation phases along the Zalisky Alatau range in the Central Tien Shan, southeast Kazakhstan.

The westernmost sites, MBK and REM, range in age between 12–45 ka (this study; Fitzsimmons et al., 2017, 2018). Although the loess at REM extends downward toward older ages (Machalett et al., 2006; Sprafke et al, 2018), the lack of high-resolution dating >45 ka prevents our consideration of accumulation during earlier periods. By contrast, the two central sites, PAN and ASH, are substantially younger in age and span much shorter periods of time; 17–5 ka and 15–12 ka respectively. The site of TAU, situated c. 20 km east of ASH, preserves c. 1 m of loess accumulation during a similar time period to ASH (c. 11–13 ka) and overlies an unconformity with substantial hiatus, below which the loess exceeds 180 ka. The easternmost Zailisky Alatau site of MAL pre-dates 180 ka and yielded no Late Pleistocene deposits. We hypothesise that the location of TAU and MAL within the more sheltered Ili Gate area led to reduced loess accumulation over the late Pleistocene compared with the more exposed western sites. Increased wind strength related to a “funnelling” effect by the enclosing mountain ranges may also have led to the erosional unconformities observed at TAU and MAL.

While loess grain size is often used as a proxy for wind intensity through time (An et al., 1991a; Porter and An, 1995; Sun and An, 2005; Vandenberghe et al., 2013), our observations from the Ili Basin loess deposits strongly suggest that additional controls, such as geomorphic setting, sediment availability and supply to individual sites, also influence aeolian flux and grain size. We compared changes in GSI from three study sites (REM, PAN and ASH) with those from the published site of NLK in the eastern part of the basin (Li et al., 2018c), focussing on the time period c. 12–16 ka (Fig. 3.9). GSI values during this interval range from 0.30-0.40 at REM, 0.40-0.65 at PAN, 0.25-0.45 at ASH, and 0.30-0.60 at NLK. We observe that not only the magnitude of variability in GSI but also the mean value differs between sites. Sediments at PAN are coarser than at ASH, despite the relative proximity of these two sites. GSI values are less variable at REM in the west, than at NLK in the east (Fig. 3.9). These differences within the same time interval along the piedmont suggest spatial variability in sediment supply, transport to and deposition at an individual site. For example, the proximity of both NLK and PAN to active fluvial channels may account for relatively greater amounts of proximal transport of coarser grains (Li et al., 2018c) than can be transported to the other sites. The higher elevation of REM relative to the other sites may account for the overall finer GSI values and smaller range of GSI at the site reflecting a greater reliance on distal transport and sorting.

The geomorphic context of individual sites is likely to influence not only grain size characteristics and variability through time, but also aeolian flux, expressed here as MARs (Fig. 3.9). For the 12–16 ka time period, aeolian flux at ASH far exceeds that at any other site, with PAN experiencing the next highest rate of accumulation. We suggest that its relatively low elevation, distance from alluvial fans and range front, and a strengthened westerly trajectory of dust-laden winds at the Ili Gate resulted in higher accumulation here than at any other site along the piedmont for which we have data. On the other hand, whilst MARs at PAN are lower than at nearby ASH, its GSI range is higher and may reflect greater inmixing of proximal fluvial material with distal accumulation. This observation raises questions regarding hitherto popular correlation of proxies such as grain size and aeolian flux with wind strength in loess deposits generally. The older deposits at MAL and TAU yield GSIs in the 0.4-0.9 range, which is greater than that observed at the other sites. This may relate to the proximity of TAU and MAL to a seismically active range front (Chilik fault), which can introduce coarser clasts to the loess via slope transport. These observations highlight the need to first interrogate the geomorphic setting of individual sites for their potential to reflect local or larger scale processes according to proposed research questions.

We observe along the Zailisky Alatau transect, a ‘patchwork’ loess piedmont of spatially variable timing of peaks in deposition, flux and grain size. This most likely reflects the result of complex interactions between local and continental wind regimes and associated dust transport, topographic (including palaeotopographic) context, and local sediment supply.

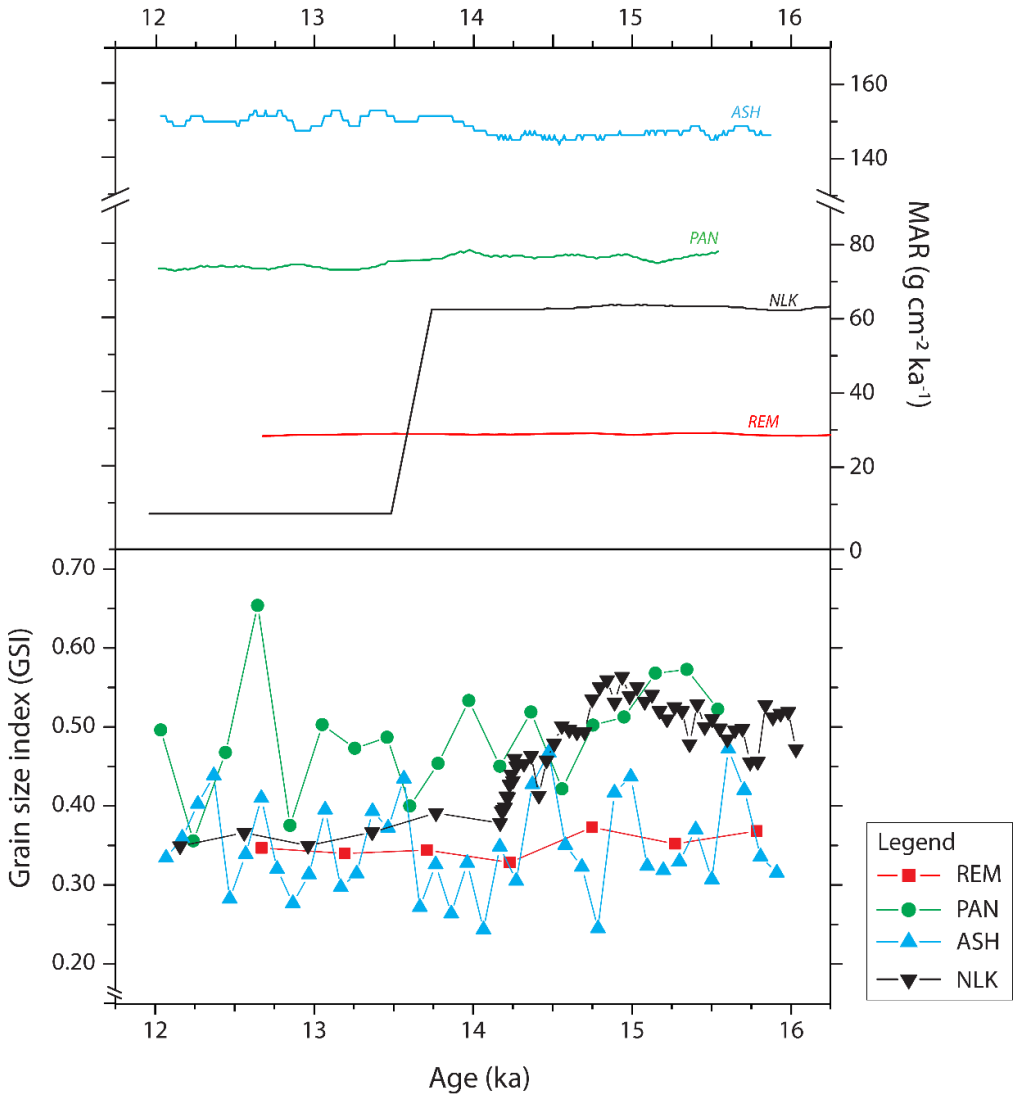

Fig. 3.9. Comparison of MAR and GSI for late MIS2 (12–16 ka) from four loess sites (REM, PAN, ASH and NLK) from an east-west transect along the Zalisky Alatau, SE Kazakhstan. The GSI for NLK were calculated from published data (Li et al., 2018c).

3.5.2. Loess sedimentation dynamics across the Ili Basin: Overcoming individual site bias to reconstruct the interplay between the Westerlies and Siberian High Pressure system

The ACA piedmonts, especially the Ili Basin, lie at a pivotal topographic point which exposes the region both to the mid-latitude Westerly winds and the Siberian High Pressure, the latter manifesting here in the form of northerly winds associated with the seasonal migration of the high-altitude polar jet (Fitzsimmons et al., 2020). The Westerlies rarely penetrate eastward of the Tien Shan range; loess deposited in this part of ACA therefore represents a strategic record of aeolian transport and deposition associated with both climate subsystems. Published correlations from the eastern Ili Basin loess linking grain size with penetration of

westerly air flow suggest that the influence of the Westerlies was neither consistent nor strong over the Late Pleistocene (Li et al., 2018c). The loess deposits of the Ili Gate/Zailisky Alatau region investigated in this study, coupled with data from the eastern Ili Basin, can provide more meaningful information relating to the interplay between the Westerlies and Siberian High climate systems through time.

Here we examine the degree to which loess profiles across the entire Ili Basin record past environmental conditions in the form of accumulation rates. In Fig. 3.7a, we show MARs from our new datasets from REM, PAN and ASH, in addition to those from 11 published sites (E et al., 2012; Kang et al., 2015; Song et al., 2012; 2015; Li et al., 2016b 2018a, 2020; Fitzsimmons et al., 2017, 2018; Wang et al., 2019a,b), presenting a 60 ky record from the eastern headwaters of the Basin to the 'Ili Gate'.

We observe substantial differences in absolute MAR's between sites, not only over the 60 ky range but also over shorter timescales such as the deglacial and MIS 3 interstadials. We hypothesise that absolute MAR's are likely to reflect differences in topographic settings between individual sites. Absolute sedimentation rates at NLK, for example, are approximately five times those observed at the sites KS15 and XY17 during late MIS 3 (40 – 27 ka). NLK is located on the banks of the Kax River (Kashi; Song et al., 2015), whereas KS15 is located in the easternmost Ili Basin and on the upper terraces of the Kunes River (Li et al., 2018a). While both these rivers, tributaries of the Ili, derive from glacial sources, the closer proximity of NLK to the river banks implies a higher sediment availability during MIS 3, when glaciers in the Tien Shan expanded in response to increased moisture transport to ACA (Koppes et al., 2008). The topographic setting of KS15 is also likely to have resulted in relatively low aeolian flux during other time periods. The site KS15-05 (Wang et al., 2019a), located c. 3 km east of KS15 (Fig. 3.6 and Fig. 3.7a), yielded MARs three times higher than at KS15 during late MIS 2 and early MIS 1 and is likely to relate to the closer proximity of the former to the active river channel.

There is also considerable variability in the timing of peaks in loess accumulation across the basin. For example, despite the proximity of the two eastern Ili Basin sites NLK and ZKT (Fig. 3.7a), the former yields peak MARs during late MIS3 (c. 45-30 ka) and the latter peaks during early MIS3 (c. 60-47 ka). These site-specific variations in loess sedimentation rates raise questions regarding how representative the MARs of individual sites may be for understanding regional climatic variations. We propose instead that aggregated trends in loess MARs from multiple sites across a basin are more likely to reflect changes in climate dynamics, so providing the best means to overcome the bias of individual sites based on their local setting.

We observe generally increased sedimentation across the entire Ili Basin during interstadial MIS 3 (29–57 ka; Lisiecki and Raymo, 2005); this extends on findings from previous studies

which noted primary loess accumulation at this time in the Zailisky Alatau area (Fitzsimmons et al., 2018). Fitzsimmons et al. (2018) hypothesised that increased loess flux during late MIS 3 (c. 40–27 ka) was due to general increased sediment availability and wind strength at this time. Increased sediment supply was likely to be linked to glacial advances in northern and eastern Tien Shan (Kong et al., 2009; Li et al., 2011, 2014; Chen et al., 2015) driven by increased moisture transport by the Westerlies, and also recorded in weak pedogenesis within the loess (Song et al., 2012, 2015; Fitzsimmons et al., 2018). Furthermore, it has been proposed that the Siberian High, which intensified during late MIS 3 (Ding et al., 1995; Hao et al., 2012), would have compressed the Westerlies against the Tien Shan ranges and increased wind strength into the Ili valley (Fitzsimmons et al., 2018). The combination of increased sediment availability and wind strength in the Ili Basin would therefore have contributed to the increased loess accumulation observed in aggregate during this period (Fig. 3.7a). Local katabatic winds might also have played an important role during this phase, resulting in localised effects on the timing and peaks of loess sedimentation.

We also observe generally increased accumulation rates in aggregate during MIS 2 (29–14 ka, Lisecki and Raymo, 2005) (Fig. 3.7a). These conditions coincide with globally cold climates prevailing during the Last Glacial Maximum (26–19 ka LGM; Clark et al., 2009). In the Ili Basin the conditions were not only cooler, but also more arid: stable carbon isotopic ($\delta_{13}C_{org}$) reconstructions for palaeovegetation in the valley indicate an increase in more arid-adapted C_4 vegetation (Ran and Feng, 2014). Cold, dry, windy climate appears to have resulted in coarser grain sizes within a number of loess sequences across the Ili Basin (Song et al., 2015; Li et al., 2016b, 2018c). Climate simulations models indicate windier LGM conditions, due either to stronger mid-latitude Westerlies (Sun et al., 2012) or an intensified Siberian High (Cheng et al., 2021). Glacial expansion during MIS 2 in the Central and Eastern Tien Shan (Kong et al., 2009; Li et al., 2011; 2014; Lifton et al., 2014; Blomdin et al., 2016), also resulted in increased production of silt and according availability within the Ili catchments for dust entrainment and transport.

Our analyses also suggest relatively widespread increase in MARs across most Ili Basin sites during the warming conditions of the global deglacial period (19–11 ka, Clark et al., 2012) (Fig. 3.7a). Those sites which do not show any increase (KS15 and ZSP) are likely to be more influenced by their topographic setting; both are located in the easternmost or upper reaches of the basin with minimal exposure to Westerly air flow (and in general records very low accumulation rates). Elsewhere, short-lived phases of increased flux of coarser grain size fractions have been correlated to abrupt climatic events such as the Younger Dryas (c. 12–11 ka) at several sites during the deglacial period (e.g. NLK: Li et al., 2018c; XEBLK: Li et al., 2016b), and have been hypothesised to associate with increased Westerly penetration eastward into the Ili Basin. Climate simulations (Wyrwoll et al., 2016) suggest that the strength of the Siberian High was reduced at this time. Such conditions would have increased the influence of the Westerlies on the Ili Basin, including increasing rainfall; increased

deglacial moisture availability is supported by more dominant C_3 vegetation signatures in the basin (Ran and Feng, 2014). We suggest that sediment availability was greater than during the LGM due to increased runoff promoted both by glacial melt under warmer conditions and increased precipitation transported by the Westerlies.

3.5.3. Variability in loess accumulation rates across mid-latitude Asia: Implications for interpreting loess archives from Central Asia to the Chinese Loess Plateau

Continental mid-latitude Asia, with its extensive deserts and widespread loess deposits, is believed to be one of the major contributors to the global dust cycle (Narsima, 2007; Kok et al., 2021). It is therefore imperative that we better understand the processes driving dust flux and their contribution to Northern Hemisphere climate dynamics. One major step towards our understanding of these processes involves quantifying Quaternary dust accumulation. Loess MARs provide the closest approximation of the 'dust parameter' over Pleistocene timescales. Given the issues raised by our analysis of the Ili Basin piedmont deposits, we compared loess MARs elsewhere in continental mid-latitude Asia over the same time period (0–60 ka), with a focus on the Chinese Loess Plateau (CLP) and published sites across ACA more widely. In doing so we further assess spatial and temporal inhomogeneity in loess MARs and the degree to which regional characteristics such as topography and climate influence MARs.

The CLP of central northern China was the first loess region to be recognised as a significant terrestrial palaeoclimate archive (Liu, 1962), and is now one of the most intensively studied loess areas in the world (An et al., 1991a,b; Porter and An, 1995; Ding et al., 2002; Kohfeld and Harrison, 2003; Sun and An, 2005; Stevens et al., 2008, 2013, 2018). Unlike the Central Asian piedmonts, the CLP forms an extensive, continuous plateau exceeding 200 m thickness in parts and centred on the southern half of the Ordos Loop of the Yellow River (Yang and Ding, 2010). The loess is believed to derive from denudation associated with uplift of the Tibetan highlands (Sun and Liu, 2000; Sun, 2002; Smalley et al 2014); its connection with the ice sheets of the Tibetan "third pole" underpins the assumption linking primary loess with glacial phases. The dominant sources of loess to the CLP are sediments derived from the Tibetan plateau, transported by the Yellow River prior to entrainment as dust (Stevens et al., 2013; Nie et al., 2015; 2018; Bird et al 2015; 2020); a significant proportion is recycled along the length of the river system as it flows along the plateau (Licht et al., 2016). The climate of the CLP is strongly influenced by the East Asian winter and summer monsoons (EAWM and EASM respectively). Northwesterly winds associated with the Siberian High Pressure system produce cold, dry, dust-bearing EAWM winter conditions (Liu and Ding, 1998; Maher, 2016), which alternate with rain-bearing southeasterly EASM summer monsoonal air flow (An et al., 1991b; Yang et al., 2015). Grain size analyses suggest that loess particles coarsen with

strengthening EAWM during glacial conditions (Sun et al., 2012; Stevens et al., 2018). Several studies report a southeastward decrease in loess flux which correlates with decreasing grain size, and has been linked to the strength of the EAWM (Lu and Sun, 2000; Vriend et al., 2011; Liu et al., 2020). However, several high-resolution luminescence dating studies challenge the prevailing assumption that CLP loess accumulation is uniformly driven by the strength of the EAWM (Stevens et al., 2006, 2007; Xu et al., 2018).

Fig. 3.7c shows MARs from 11 selected sites (Lai and Wintle, 2006; Lu et al., 2007 Stevens et al., 2008, 2016; Buylaert et al., 2008; Sun et al., 2012; Kang et al., 2013; Qiu and Zhou, 2015; Fig. 3.6b) across the CLP, following a northwest-southeast (NW-SE) transect over the period c. 0–60 ka. We observe a distinct difference in net loess accumulation, as well as in the timing in peak MARs, between the northwest and southeast sites. MARs in the northwestern sites are approximately three times higher than those in the southeast.

As we observed for the sites in the Ili Basin, the geomorphic context in the CLP appears to influence both absolute accumulation and timing of peaks in accumulation at individual sites. For example, among northwestern sites, JY shows higher accumulation rates than ZJC and GL, and likely relates to the proximity to the Yellow River; JY is located on the upper terraces of the river, whereas ZJC and GL are both situated further from fluvial source, south and north of the river respectively. In contrast to the generally low accumulation rates of southeastern sector, the site of MN, located on the banks of the Yellow River, has net accumulation comparable to the northwestern sites (Qui and Zhou, 2015; see Fig. 3.7c). In general, sites in close proximity to the Yellow River, as well as those close to the desert deflation zones, record higher MARs than those more distal to these likely sources. It appears that despite the role of the EAWM as a dust transport vector (Vriend et al, 2011; Liu et al., 2020), net accumulation of loess across the CLP is also locally influenced by proximity to source sediment, whether fluvial or aeolian. Nevertheless, desert marginal sites, such as Jingbian (Stevens et al., 2018), also record erosional unconformities; this effect has been proposed to result from increased erosional capacity of the EAWM in those regions. Not all records of MARs can be easily explained by climate mechanisms or by geomorphic context, however; the extremely high MAR at BGY during LGM (Fig. 3.7c) may relate to local preservation potential associated with expansion and contraction of the EASM (Buylaert et al., 2008).

The timing of MAR peaks in aggregate across the CLP gives a more nuanced insight into the climate dynamics acting in the region than previously obtained. We observe a divergence in the timing of peaks in loess accumulation between the northwest and southeast. In the northwest, loess accumulation increases during c. 18–11 ka and decreases at c. 11–6 ka (Fig. 3.7c), whereas the opposite is observed in the southeast sites. This alternating pattern has previously been attributed to a persistent weakening of the EAWM and gradual strengthening of the EASM during the early Holocene, with the opposite proposed for the deglacial (Xu et al., 2018; Kang et al., 2020). We suggest that the increase in MARs of the CLP

southeastern sites during early Holocene may relate to their proximity to the Wei River, which drains the Qinling Mountains and is more strongly influenced by the EASM; aeolian flux in this region would therefore respond more closely to sediment availability relating to increased runoff during strengthened monsoon conditions. Overall, the CLP experienced an increase in MARs during the LGM and is consistent with widespread glaciation on the Tibetan Plateau (Owen et al., 2003a,b, 2006; Owen and Dortsch, 2014), although relative changes in the southeast sites was less pronounced, likely due to distance from the Yellow River and northern deserts. Loess MARs decreased altogether during MIS 3 (c. 57–29 ka, Lisiecki and Raymo, 2005), most likely due to relatively weakened EAWM wind strength, although sediment supply was sustained by suspended load fluvial outwash linked to glaciations on the Tibetan plateau (Owen et al., 2003a; Owen and Dortch, 2014; Rother et al., 2017) in response to increased monsoonal precipitation. The sustained supply of sediment to the CLP can be observed in the generally higher MARs at the northwestern sites proximal to the river.

In addition to our analyses of MARs across the Ili Basin and CLP, we also calculated MARs from 8 other published loess sites across ACA (Fig. 3.6a and Fig. 3.7b). These sites not only represent similar piedmont settings to those found in the Ili Basin but are also influenced by similar climatic contexts. The westernmost sites of BSK (Youn et al., 2014) and VAL (Fitzsimmons et al., 2017) lie in the foothills of the Kyrgyz Tien Shan and Karatau Range respectively (Fig. 3.6a). The sites of LJW10 (Li et al., 2015), SCZ17 (Duan et al., 2020) and BYH10 (Li et al., 2016a) are located along the northern piedmonts of the eastern Tian Shan, south of the Junggar Basin (and the Gurbantunggut desert), and TC and YM are situated in the westward opening Tacheng Basin, bound by the northern edge of the Dzungarian Alatau and the Tarbagatai Range to the north (Fig. 3.6a; Li et al., 2019b)

As observed elsewhere, both absolute MAR values and the timing of peak accumulation are highly variable across the greater ACA. In the west, BSK experienced increased accumulation during late MIS3, continuing into the LGM, while VAL yields substantially lower MARs which remained consistent from late MIS 3 into the LGM. The higher accumulation rates at BSK are most likely due to its proximity to the glacially derived Chu river. Glacial expansion in the Kyrgyz Tien Shan during MIS 3 (Koppes et al., 2008) likely generated the fine-grained sediment for loess deposition at BSK, whereas the Karatau Range, from which the VAL sediments were sourced, was never glaciated and is much more arid, resulting in substantially less sediment supply. Both Tacheng Basin sites yield low, almost constant MARs (c. 30-40 g $cm^{-2}ka^{-1}$) throughout the past c. 60 ky (Li et al., 2019b). It is likely that these records relate to the lack of glaciation in the surrounding mountains, resulting in a dependence on the desert to the west as a source of dust (Li et al., 2019b). By contrast, the sites located in the Northern Tien Shan foothills yield variable depositional characteristics (Fig. 3.6a and Fig. 3.7b). The site of QS-16 yielded an LGM peak in accumulation; by comparison, the site of BYH-10, located further east, experienced peak MARs from early to mid-MIS 3 an order of magnitude greater than at QS-16, followed by a hiatus and subsequent

LGM MAR values comparable with QS-16 (Fig. 3.7b). LGM deposition in the northern Tien Shan area has been linked to regionally arid conditions and strengthened Westerlies which increased aeolian flux (Li et al., 2016a, 2020). The substantial difference in absolute MAR values at BYH-10 and QS-16 is most likely linked to their individual topographic and geomorphic setting; the former is located on the exposed northern piedmont of the Bogda Shan (eastern Tien Shan) which drains a number of glacially fed rivers, whereas QS-16 is sheltered from the prevailing westerly winds by the Borohoro mountains and at a greater distance from the northern dust source regions.

It is clear from our MAR review of the Ili Basin, wider ACA, and CLP that absolute accumulation rates and timing at a given site may be influenced by both synoptic-scale climate and local geomorphic settings in the form of proximity to dust sources, topography and sediment availability. At the same time, the timing of peaks in loess accumulation as an aggregate of multiple sites represents a reliable response to climate.

3.6. Conclusion

This study provides high resolution chronological frameworks for five new loess sites in the vastly understudied piedmonts of the Zalisky-Alatau (Central Tien Shan). Our new dataset provides the spatial coverage necessary to interrogate the timing and rate of loess deposition along the Ili Basin piedmonts as a whole, whereas previously only the eastern part of the basin and isolated western sites could be analysed. We observe substantial variability in the timing and rate of loess deposition across our new sites, which raises questions regarding to what degree the timing and rate of accumulation at individual sites can be taken as an indicator of past climate in this region. Our observations across the Ili Basin as a whole indicate a patchwork of loess deposition. Absolute sedimentation rates at a given site respond both to local topographic context and sediment availability and to climate. The timing of peaks in accumulation, irrespective of absolute MAR values and particularly when viewed in aggregate across a number of sites, represent a response to variability in wind dynamics driven by the Northern Hemispheric climate subsystems. This interpretation was supported by our analyses of MAR's from loess sites across wider ACA and the CLP over the past 60 kyr. We find that aggregate MARs from multiple sites provide a more robust tool for understanding past climate dynamics across a region and overcomes individual site bias.

Acknowledgements

AKD would like to gratefully acknowledge the following persons and institutions for their support: Steffi Hesse and Victoria Krippner at the Max Planck Institute for Evolutionary

Anthropology (MPI-EVA), Leipzig, Germany, for access to the HF laboratory, and Giovanni Muttoni for the use of magnetic susceptibility measurement facilities at the Alpine Palaeomagnetism Laboratory (Peveragno, Italy). Thanks also to A. Umarkhojiyev, A. Kossenko, and A Sirch for assistance in the field. This study was also supported by internal program No. RVO67985831 of the Institute of Geology CAS, Prague.

References

Albani, S., & Mahowald, N. M. (2019). Paleodust Insights into Dust Impacts on Climate. Journal of Climate, 32(22), 7897–7913. doi: 10.1175/JCLI-D-18-0742.1

An, Zhisheng, Kukla, G., Porter, S. C., & Xiao, J. (1991a). Late quaternary dust flow on the Chinese Loess Plateau. Catena, 18(2), 125–132. doi: 10.1016/0341-8162(91)90012-M

An, Zhisheng, Kukla, G. J., Porter, S. C., & Xiao, J. (1991b). Magnetic susceptibility evidence of monsoon variation on the Loess Plateau of central China during the last 130,000 years. Quaternary Research, 36(1), 29–36. doi: 10.1016/0033-5894(91)90015-W

Andreae, M. O., & Rosenfeld, D. (2008). Aerosol–cloud–precipitation interactions. Part 1. The nature and sources of cloud-active aerosols. Earth-Science Reviews, 89(1), 13–41. doi: https://doi.org/10.1016/j.earscirev.2008.03.001

Antoine, P., Rousseau, D.-D., Moine, O., Kunesch, S., Hatté, C., Lang, A., Tissoux, H., & Zöller, L. (2009). Rapid and cyclic aeolian deposition during the Last Glacial in European loess: A high-resolution record from Nussloch, Germany. Quaternary Science Reviews, 28(25), 2955–2973. https://doi.org/10.1016/j.quascirev.2009.08.001

Arimoto, R. (2001). Eolian dust and climate: Relationships to sources, tropospheric chemistry, transport and deposition. Earth-Science Reviews, 54(1), 29–42. doi: https://doi.org/10.1016/S0012-8252(01)00040-X

Avram, A., Constantin, D., Veres, D., Kelemen, S., Obreht, I., Hambach, U., Marković, S. B., & Timar-Gabor, A. (2020). Testing polymineral post-IR IRSL and quartz SAR-OSL protocols on Middle to Late Pleistocene loess at Batajnica, Serbia. Boreas, 49(3), 615–633. https://doi.org/10.1111/bor.12442

Banerjee, D., Murray, A. S., Bøtter-Jensen, L., & Lang, A. (2001). Equivalent dose estimation using a single aliquot of polymineral fine grains. Radiation Measurements, 33(1), 73–94. doi: 10.1016/S1350-4487(00)00101-3

Berger, A., & Loutre, M. F. (1991). Insolation values for the climate of the last 10 million years. Quaternary Science Reviews, 10(4), 297–317. doi: 10.1016/0277-3791(91)90033-Q

Bird, A., Stevens, T., Rittner, M., Vermeesch, P., Carter, A., Andò, S., Garzanti, E., Lu, H., Nie, J., Zeng, L., Zhang, H., & Xu, Z. (2015). Quaternary dust source variation across the Chinese Loess Plateau. Palaeogeography, Palaeoclimatology, Palaeoecology, 435, 254–264. https://doi.org/10.1016/j.palaeo.2015.06.024

Bird, A., Millar, I., Rodenburg, T., Stevens, T., Rittner, M., Vermeesch, P., & Lu, H. (2020). A constant Chinese Loess Plateau dust source since the late Miocene. Quaternary Science Reviews, 227, 106042. doi: 10.1016/j.quascirev.2019.106042

Blaauw, M., & Christen, J. A. (2011). Flexible paleoclimate age-depth models using an autoregressive gamma process. Bayesian Analysis, 6(3), 457–474. doi: 10.1214/11-BA618

Blomdin, R., Stroeven, A. P., Harbor, J. M., Lifton, N. A., Heyman, J., Gribenski, N., Petrakov, D. A., Caffee, M. W., Ivanov, M. N., Hättestrand, C., Rogozhina, I., & Usubaliev, R. (2016). Evaluating the timing of former glacier expansions in the Tian Shan: A key step towards robust spatial correlations. Quaternary Science Reviews, 153, 78–96. https://doi.org/10.1016/j.quascirev.2016.07.029

Blott, S. J., & Pye, K. (2001). GRADISTAT: a grain size distribution and statistics package for the analysis of unconsolidated sediments. Earth Surface Processes and Landforms, 26(11), 1237–1248. doi: https://doi.org/10.1002/esp.261

Buylaert, J. P., Murray, A. S., Vandenberghe, D., Vriend, M., Corte, F. D., & haute, P. V. den. (2008). Optical dating of Chinese loess using sand-sized quartz: Establishing a time frame for Late Pleistocene climate changes in the western part of the Chinese Loess Plateau. Quaternary Geochronology, 3(1), 99–113. doi: https://doi.org/10.1016/j.quageo.2007.05.003

Buylaert, J.-P., Jain, M., Murray, A. S., Thomsen, K. J., Thiel, C., & Sohbati, R. (2012). A robust feldspar luminescence dating method for Middle and Late Pleistocene sediments. Boreas, 41(3), 435–451. doi: https://doi.org/10.1111/j.1502-3885.2012.00248.x

Buylaert, J.-P., Yeo, E.-Y., Thiel, C., Yi, S., Stevens, T., Thompson, W., Frechen, M., Murray, A., & Lu, H. (2015). A detailed post-IR IRSL chronology for the last interglacial soil at the Jingbian loess site (northern China). LED14 Proceedings, 30, 194–199. https://doi.org/10.1016/j.quageo.2015.02.022

Chen, Y., Li, Y., Wang, Y., Zhang, M., Cui, Z., Yi, C., & Liu, G. (2015). Late Quaternary glacial history of the Karlik Range, easternmost Tian Shan, derived from 10Be surface exposure and optically stimulated luminescence datings. Quaternary Science Reviews, 115, 17–27. doi: 10.1016/j.quascirev.2015.02.010

Cheng, L., Song, Y., Wu, Y., Liu, Y., Liu, H., Chang, H., Zong, X., & Kang, S. (2021). Drivers for Asynchronous Patterns of Dust Accumulation in Central and Eastern Asia and in Greenland During the Last Glacial Maximum. Geophysical Research Letters, 48(5). https://doi.org/10.1029/2020GL091194

E, ChongYi., Lai, Z., Sun, Y., Hou, G., Yu, L., & Wu, C. (2012). A luminescence dating study of loess deposits from the Yili River basin in western China. Quaternary Geochronology, 10, 50–55. doi: https://doi.org/10.1016/j.quageo.2012.04.022

Clark, P. U., Dyke, A. S., Shakun, J. D., Carlson, A. E., Clark, J., Wohlfarth, B., Mitrovica, J. X., Hostetler, S. W., & McCabe, A. M. (2009). The Last Glacial Maximum. Science, 325(5941), 710. https://doi.org/10.1126/science.1172873

Clark, P. U., Shakun, J. D., Baker, P. A., Bartlein, P. J., Brewer, S., Brook, E., Carlson, A. E., Cheng, H., Kaufman, D. S., Liu, Z., Marchitto, T. M., Mix, A. C., Morrill, C., Otto-Bliesner, B. L., Pahnke, K., Russell, J. M., Whitlock, C., Adkins, J. F., Blois, J. L., … Williams, J. W. (2012). Global climate evolution during the last deglaciation. Proceedings of the National Academy of Sciences, 109(19), E1134. https://doi.org/10.1073/pnas.1116619109

Dave, A. K., Courty, M.-A., Fitzsimmons, K. E., & Singhvi, A. K. (2019). Revisiting the contemporaneity of a mighty river and the Harappans: Archaeological, stratigraphic and chronometric constraints. Quaternary Geochronology, 49, 230–235. doi: 10.1016/j.quageo.2018.05.002

Ding, Z., Liu, T., Rutter, N. W., Yu, Z., Guo, Z., & Zhu, R. (1995). Ice-Volume Forcing of East Asian Winter Monsoon Variations in the Past 800,000 Years. Quaternary Research, 44(2), 149–159. Cambridge Core. doi: 10.1006/qres.1995.1059

Ding, Z. L., Derbyshire, E., Yang, S. L., Yu, Z. W., Xiong, S. F., & Liu, T. S. (2002). Stacked 2.6-Ma grain size record from the Chinese loess based on five sections and correlation with the deep-sea δ18O record. Paleoceanography, 17(3), 5-1-5–21. doi: https://doi.org/10.1029/2001PA000725

Duan, F., An, C., Wang, W., Herzschuh, U., Zhang, M., Zhang, H., Liu, Y., Zhao, Y., & Li, G. (2020). Dating of a late Quaternary loess section from the northern slope of the Tianshan Mountains (Xinjiang, China) and its paleoenvironmental significance. Quaternary International, 544, 104–112. https://doi.org/10.1016/j.quaint.2020.02.034

Durcan, J. A., King, G. E., & Duller, G. A. T. (2015). DRAC: Dose Rate and Age Calculator for trapped charge dating. Quaternary Geochronology, 28, 54–61. doi: 10.1016/j.quageo.2015.03.012

Fenn, K., Durcan, J. A., Thomas, D. S. G., & Banak, A. (2020). A 180 ka record of environmental change at Erdut (Croatia): A new chronology for the loess–palaeosol sequence and its implications for environmental interpretation. Journal of Quaternary Science, 35(4), 582–593. doi: 10.1002/jqs.3201

Fitzsimmons, K. E., Marković, S. B., & Hambach, U. (2012). Pleistocene environmental dynamics recorded in the loess of the middle and lower Danube basin. Quaternary Science Reviews, 41, 104–118. doi: 10.1016/j.quascirev.2012.03.002

Fitzsimmons, K. E., & Hambach, U. (2014). Loess accumulation during the last glacial maximum: Evidence from Urluia, southeastern Romania. Quaternary International, 334–335, 74–85. doi: 10.1016/j.quaint.2013.08.005

Fitzsimmons, K. E. (2017). Reconstructing palaeoenvironments on desert margins: New perspectives from Eurasian loess and Australian dry lake shorelines. Quaternary Science Reviews, 171, 1–19. doi: 10.1016/j.quascirev.2017.05.018

Fitzsimmons, K. E., Iovita, R., Sprafke, T., Glantz, M., Talamo, S., Horton, K., Beeton, T., Alipova, S., Bekseitov, G., Ospanov, Y., Deom, J.-M., Sala, R., & Taimagambetov, Z. (2017). A chronological framework connecting the early Upper Palaeolithic across the Central Asian piedmont. Journal of Human Evolution, 113, 107–126. https://doi.org/10.1016/j.jhevol.2017.07.006

Fitzsimmons, K. E., Sprafke, T., Zielhofer, C., Günter, C., Deom, J.-M., Sala, R., & Iovita, R. (2018). Loess accumulation in the Tian Shan piedmont: Implications for palaeoenvironmental change in arid Central Asia. Quaternary International, 469, 30–43. doi: 10.1016/j.quaint.2016.07.041

Fitzsimmons, K. E., Nowatzki, M., Dave, A. K., & Harder, H. (2020). Intersections between wind regimes, topography and sediment supply: Perspectives from aeolian landforms in Central Asia. Palaeogeography, Palaeoclimatology, Palaeoecology, 540, 109531. doi: 10.1016/j.palaeo.2019.109531

Frechen, M., Schweitzer, U., & Zander, A. (1996). Improvements in sample preparation for the fine grain technique. Ancient TL, 14(2), 15–17.

Galbraith, R. F., Roberts, R. G., Laslett, G. M., Yoshida, H., & Olley, J. M. (1999). Optical dating of single and multiple grains of quartz from Jinmium rock shelter, northern Australia: Part I, experimental design and statistical models. Archaeometry, 41(2), 339–364. Scopus. doi: 10.1111/j.1475-4754.1999.tb00987.x

Grützner, C., Walker, R. T., Abdrakhmatov, K. E., Mukambaev, A., Elliott, A. J., & Elliott, J. R. (2017). Active Tectonics Around Almaty and along the Zailisky Alatau Rangefront. Tectonics, 36(10), 2192–2226. doi: https://doi.org/10.1002/2017TC004657

Guérin, G., Mercier, N., & Adamiec, G. (2011). Dose-rate conversion factors: Update. Ancient TL, 29(1), 5–8.

Hao, Q., Wang, L., Oldfield, F., Peng, S., Qin, L., Song, Y., Xu, B., Qiao, Y., Bloemendal, J., & Guo, Z. (2012). Delayed build-up of Arctic ice sheets during 400,000-year minima in insolation variability. Nature, 490(7420), 393–396. https://doi.org/10.1038/nature11493

Hong, B., Gasse, F., Uchida, M., Hong, Y., Leng, X., Shibata, Y., An, N., Zhu, Y., & Wang, Y. (2014). Increasing summer rainfall in arid eastern-Central Asia over the past 8500 years. Scientific Reports, 4. Scopus. https://doi.org/10.1038/srep05279

Jain, M., & Singhvi, Ashok. K. (2001). Limits to depletion of blue-green light stimulated luminescence in feldspars: Implications for quartz dating. Radiation Measurements, 33(6), 883–892. doi: 10.1016/S1350-4487(01)00104-4

Jia, J., Liu, H., Gao, F., & Xia, D. (2018). Variations in the westerlies in Central Asia since 16 ka recorded by a loess section from the Tien Shan Mountains. Palaeogeography, Palaeoclimatology, Palaeoecology, 504, 156–161. doi: 10.1016/j.palaeo.2018.05.02

Kang, S., Wang, X., & Lu, Y. (2013). Quartz OSL chronology and dust accumulation rate changes since the Last Glacial at Weinan on the southeastern Chinese Loess Plateau: Quartz OSL chronology and dust accumulation rates, SE Chinese Loess Plateau. Boreas, 42, 815-829. doi: 10.1111/bor.12005

Kang, S., Wang, X., Lu, Y., Liu, W., Song, Y., & Wang, N. (2015). A high-resolution quartz OSL chronology of the Talede loess over the past ∼30 ka and its implications for dust accumulation in the Ili Basin, Central Asia. Quaternary Geochronology, 30, 181–187. doi: 10.1016/j.quageo.2015.04.006

Kang, S., Du, J., Wang, N., Dong, J., Wang, D., Wang, X., Qiang, X., & Song, Y. (2020). Early Holocene weakening and mid- to late Holocene strengthening of the East Asian winter monsoon. Geology, 48(11), 1043–1047. https://doi.org/10.1130/G47621.1

Kohfeld, K. E., & Harrison, S. P. (2000). How well can we simulate past climates? Evaluating the models using global palaeoenvironmental datasets. Quaternary Science Reviews, 19(1–5), 321–346. doi: 10.1016/S0277-3791(99)00068-2

Kohfeld, K. E., & Harrison, S. P. (2003). Glacial-interglacial changes in dust deposition on the Chinese Loess Plateau. Quaternary Science Reviews, 22(18), 1859–1878. doi: 10.1016/S0277-3791(03)00166-5

Kok, J. F., Adebiyi, A. A., Albani, S., Balkanski, Y., Checa-Garcia, R., Chin, M., Colarco, P. R., Hamilton, D. S., Huang, Y., Ito, A., Klose, M., Li, L., Mahowald, N. M., Miller, R. L., Obiso, V., Pérez García-Pando, C., Rocha-Lima, A., & Wan, J. S. (2021). Contribution of the world's main dust source regions to the global cycle of desert dust. Atmospheric Chemistry and Physics Discussions, 2021, 1–34. https://doi.org/10.5194/acp-2021-4

Konert, M., & Vandenberghe, J. (1997). Comparison of laser grain size analysis with pipette and sieve analysis: A solution for the underestimation of the clay fraction. Sedimentology, 44(3), 523–535. doi: 10.1046/j.1365-3091.1997.d01-38.x

Kong, P., Fink, D., Na, C., & Huang, F. (2009). Late Quaternary glaciation of the Tianshan, Central Asia, using cosmogenic 10Be surface exposure dating. Quaternary Research, 72(2), 229–233. doi: 10.1016/j.yqres.2009.06.002

Koppes, M., Gillespie, A. R., Burke, R. M., Thompson, S. C., & Stone, J. (2008). Late Quaternary glaciation in the Kyrgyz Tien Shan. Quaternary Science Reviews, 27(7), 846–866. doi: 10.1016/j.quascirev.2008.01.009

Kukla, G., Heller, F., Ming, L. X., Chun, X. T., Sheng, L. T., & Sheng, A. Z. (1988). Pleistocene climates in China dated by magnetic susceptibility. Geology, 16(9), 811–814. doi: 10.1130/0091-7613(1988)016<0811:PCICDB>2.3.CO;2

Lai, Z., Wintle, A. G., & Thomas, D. S. G. (2007). Rates of dust deposition between 50 ka and 20 ka revealed by OSL dating at Yuanbao on the Chinese Loess Plateau. Palaeogeography, Palaeoclimatology, Palaeoecology, 248(3), 431–439. doi: https://doi.org/10.1016/j.palaeo.2006.12.013

Lai, Z.-P., & Wintle, A. G. (2006). Locating the boundary between the Pleistocene and the Holocene in Chinese loess using luminescence. The Holocene, 16(6), 893–899. doi: 10.1191/0959683606hol980rr

Li, Yingkui, Liu, G., Kong, P., Harbor, J., Chen, Y., & Caffee, M. (2011). Cosmogenic nuclide constraints on glacial chronology in the source area of the Urumqi River, Tian Shan, China. Journal of Quaternary Science, 26(3), 297–304. doi: 10.1002/jqs.1454

Li, Yingkui, Liu, G., Chen, Y., Li, Y., Harbor, J., Stroeven, A. P., Caffee, M., Zhang, M., Li, C., & Cui, Z. (2014). Timing and extent of Quaternary glaciations in the Tianger Range, eastern Tian Shan, China, investigated using

10Be surface exposure dating. Quaternary Science Reviews, 98, 7–23. https://doi.org/10.1016/j.quascirev.2014.05.009

Li, G., Wen, L., Xia, D., Duan, Y., Rao, Z., Madsen, D. B., Wei, H., Li, F., Jia, J., & Chen, F. (2015). Quartz OSL and K-feldspar pIRIR dating of a loess/paleosol sequence from arid central Asia, Tianshan Mountains, NW China. Quaternary Geochronology, 28, 40–53.doi: https://doi.org/10.1016/j.quageo.2015.03.011

Li, Guoqiang, Rao, Z., Duan, Y., Xia, D., Wang, L., Madsen, D. B., Jia, J., Wei, H., Qiang, M., Chen, J., & Chen, F. (2016)a. Paleoenvironmental changes recorded in a luminescence dated loess/paleosol sequence from the Tianshan Mountains, arid central Asia, since the Penultimate Glaciation. Earth and Planetary Science Letters, 448, 1–12. https://doi.org/10.1016/j.epsl.2016.05.008

Li, Yun, Song, Y., Lai, Z., Han, L., & An, Z. (2016)b. Rapid and cyclic dust accumulation during MIS 2 in Central Asia inferred from loess OSL dating and grain-size analysis. Scientific Reports, 6(1), 32365. doi: 10.1038/srep32365

Li, Guoqiang, Chen, F., Xia, D., Yang, H., Zhang, X., Madsen, D., Oldknow, C., Wei, H., Rao, Z., & Qiang, M. (2018)a. A Tianshan Mountains loess-paleosol sequence indicates anti-phase climatic variations in arid central Asia and in East Asia. Earth and Planetary Science Letters, 494, 153–163. https://doi.org/10.1016/j.epsl.2018.04.052

Li, Yue, Song, Y., Fitzsimmons, K. E., Chen, X., Wang, Q., Sun, H., & Zhang, Z. (2018)b. New evidence for the provenance and formation of loess deposits in the Ili River Basin, Arid Central Asia. Aeolian Research, 35, 1–8. doi: https://doi.org/10.1016/j.aeolia.2018.08.002

Li, Y., Song, Y., Fitzsimmons, K. E., Chang, H., Orozbaev, R., & Li, X. (2018)c. Eolian dust dispersal patterns since the last glacial period in eastern Central Asia: Insights from a loess-paleosol sequence in the Ili Basin. Climate of the Past, 14(3), 271–286. doi: 10.5194/cp-14-271-2018

Li, Yue, Song, Y., Qiang, M., Miao, Y., & Zeng, M. (2019)a. Atmospheric Dust Variations in the Ili Basin, Northwest China, During the Last Glacial Period as Revealed by a High Mountain Loess-Paleosol Sequence. Journal of Geophysical Research: Atmospheres, 124(15), 8449–8466. doi: 10.1029/2019JD030470

Li, Y., Song, Y., Yin, Q., Han, L., & Wang, Y. (2019)b. Orbital and millennial northern mid-latitude westerlies over the last glacial period. Climate Dynamics, 53(5–6), 3315–3324. doi: 10.1007/s00382-019-04704-5

Li, Guoqiang, Yang, H., Stevens, T., Zhang, X., Zhang, H., Wei, H., Zheng, W., Li, L., Liu, X., Chen, J., Xia, D., Oldknow, C., Ye, W., & Chen, F. (2020). Differential ice volume and orbital modulation of Quaternary moisture patterns between Central and East Asia. Earth and Planetary Science Letters, 530, 115901. doi: https://doi.org/10.1016/j.epsl.2019.115901

Licht, A., Dupont-Nivet, G., Pullen, A., Kapp, P., Abels, H. A., Lai, Z., Guo, Z., Abell, J., & Giesler, D. (2016). Resilience of the Asian atmospheric circulation shown by Paleogene dust provenance. Nature Communications, 7(1), 12390. https://doi.org/10.1038/ncomms12390

Lifton, N., Beel, C., Hättestrand, C., Kassab, C., Rogozhina, I., Heermance, R., … Stroeven, A. P. (2014). Constraints on the late Quaternary glacial history of the Inylchek and Sary-Dzaz valleys from in situ cosmogenic 10Be and 26Al, eastern Kyrgyz Tian Shan. Quaternary Science Reviews, 101, 77–90. doi: 10.1016/j.quascirev.2014.06.032

Lisiecki, L. E., & Raymo, M. E. (2005). A Pliocene-Pleistocene stack of 57 globally distributed benthic δ18O records. Paleoceanography, 20(1). doi: 10.1029/2004PA001071

Liu, T. (1962). The huangtu (loess) of China. Acta Geol. Sinica, 42, 1–14.

Liu, T. S. (1985). Loess and Environment. China Ocean Press (Beijing).

Liu, T., & Ding, Z. (1998). Chinese loess and the paleomonsoon. Annual Review of Earth and Planetary Sciences, 26(1), 111–145. doi: 10.1146/annurev.earth.26.1.111

Liu, Y., Liu, X., Ma, L., Kang, S., Qiang, X., Guo, F., & Sun, Y. (2020). Temporal–spatial variations in aeolian flux on the Chinese Loess Plateau during the last 150 ka. Geological Magazine, 157(5), 757–767. doi: 10.1017/S0016756819001067

Łomotowski, J., Burszta-Adamiak, E., Kęszycka, M., Jary, Z. (2008). In: Metody i techniki optyczne w badaniach zawiesin, Badania Sy. Instytut Badań Systemowych PAN, Warszawa. (n.d.).

Lu, H., & Sun, D. (2000). Pathways of dust input to the Chinese Loess Plateau during the last glacial and interglacial periods. Catena, 40(3), 251–261. doi: 10.1016/S0341-8162(00)00090-4

Lu, Y. C., Wang, X. L., & Wintle, A. G. (2007). A new OSL chronology for dust accumulation in the last 130,000 yr for the Chinese Loess Plateau. Quaternary Research, 67(1), 152–160. doi: 10.1016/j.yqres.2006.08.003

Lydolph, P. E. (1977). Climates of the Soviet Union. Amsterdam; New York: Elsevier Scientific Pub. Co.

Machalett, B., Frechen, M., Hambach, U., Oches, E. A., Zöller, L., & Marković, S. B. (2006). The loess sequence from Remisowka (northern boundary of the Tien Shan Mountains, Kazakhstan)—Part I: Luminescence dating. Quaternary International, 152–153, 192–201. doi: 10.1016/j.quaint.2005.12.014

Machalett, Björn, Oches, E. A., Frechen, M., Zöller, L., Hambach, U., Mavlyanova, N. G., … Endlicher, W. (2008). Aeolian dust dynamics in central Asia during the Pleistocene: Driven by the long-term migration, seasonality, and permanency of the Asiatic polar front: Aeolian dust dynamics in Central Asia. Geochemistry, Geophysics, Geosystems, 9(8), n/a-n/a. doi: 10.1029/2007GC001938

Maher, B. A. (2016). Palaeoclimatic records of the loess/palaeosol sequences of the Chinese Loess Plateau. Quaternary Science Reviews, 154, 23–84. doi: 10.1016/j.quascirev.2016.08.004

Marković, S. B., Stevens, T., Kukla, G. J., Hambach, U., Fitzsimmons, K. E., Gibbard, P., … Svirčev, Z. (2015). Danube loess stratigraphy—Towards a pan-European loess stratigraphic model. Earth-Science Reviews, 148, 228–258. doi: 10.1016/j.earscirev.2015.06.005

Martin, J. H. (1990). Glacial-interglacial CO 2 change: The Iron Hypothesis. Paleoceanography, 5(1), 1–13. doi: 10.1029/PA005i001p00001

Martínez-García, A., Sigman, D. M., Ren, H., Anderson, R. F., Straub, M., Hodell, D. A., … Haug, G. H. (2014). Iron Fertilization of the Subantarctic Ocean During the Last Ice Age. Science, 343(6177), 1347. doi: 10.1126/science.1246848

Muhs, D. R. (2007). Loess deposits, origins and properties. In Encyclopedia of Quaternary Science (pp. 1405–1418). Elsevier. doi: 10.1016/B0-44-452747-8/00158-7

Murray, A. S., & Wintle, A. G. (2000). Luminescence dating of quartz using an improved single-aliquot regenerative-dose protocol. Radiation Measurements, 32(1), 57–73. doi: https://doi.org/10.1016/S1350-4487(99)00253-X

Murray, A. S., & Wintle, A. G. (2003). The single aliquot regenerative dose protocol: Potential for improvements in reliability. Radiation Measurements, 37(4), 377–381. doi: https://doi.org/10.1016/S1350-4487(03)00053-2

Narisma, G. T., Foley, J. A., Licker, R., & Ramankutty, N. (2007). Abrupt changes in rainfall during the twentieth century. Geophysical Research Letters, 34(6). doi: https://doi.org/10.1029/2006GL028628

Nie, J., Stevens, T., Rittner, M., Stockli, D., Garzanti, E., Limonta, M., Bird, A., Andò, S., Vermeesch, P., Saylor, J., Lu, H., Breecker, D., Hu, X., Liu, S., Resentini, A., Vezzoli, G., Peng, W., Carter, A., Ji, S., & Pan, B. (2015). Loess Plateau storage of Northeastern Tibetan Plateau-derived Yellow River sediment. Nature Communications, 6(1), 8511. https://doi.org/10.1038/ncomms9511

Nie, J., Pullen, A., Garzione, C. N., Peng, W., & Wang, Z. (2018). Pre-Quaternary decoupling between Asian aridification and high dust accumulation rates. Science Advances, 4(2), eaao6977. doi: 10.1126/sciadv.aao6977

Obruchev, V. A. (1945). Loess types and their origin. American Journal of Science, 243(5), 256–262. doi: 10.2475/ajs.243.5.256

Owen, Lewis A., Finkel, R. C., Haizhou, M., Spencer, J. Q., Derbyshire, E., Barnard, P. L., & Caffee, M. W. (2003)a. Timing and style of Late Quaternary glaciation in northeastern Tibet. Geological Society of America Bulletin, 115(11), 1356. doi: 10.1130/B25314.1

Owen, L.A., Ma, H., Derbyshire, E., Spencer, J. Q., Barnard, P. L., Zeng, Y. N., … Caffee, M. W. (2003)b. The timing and style of Late Quaternary glaciation in the La Ji Mountains, NE Tibet: Evidence for restricted glaciation during the latter part of the Last Glacial. Zeitschrift Fur Geomorphologie, Supplementband, 130, 263–276.

Owen, L.A., Finkel, R. C., Haizhou, M., & Barnard, P. L. (2006). Late Quaternary landscape evolution in the Kunlun Mountains and Qaidam Basin, Northern Tibet: A framework for examining the links between glaciation, lake level changes and alluvial fan formation. Quaternary International, 154–155, 73–86. Scopus. doi: 10.1016/j.quaint.2006.02.008

Owen, Lewis A., & Dortch, J. M. (2014). Nature and timing of Quaternary glaciation in the Himalayan–Tibetan orogen. Quaternary Science Reviews, 88, 14–54. doi: 10.1016/j.quascirev.2013.11.016

Pécsi, M. (1990). Loess is not just the accumulation of dust. Quaternary International, 7–8, 1–21. doi: https://doi.org/10.1016/1040-6182(90)90034-2

Porter, S. C., & An, Z. (1995). Correlation between climate events in the North Atlantic and China during the last glaciation. Nature, 375(6529), 305–308. doi: 10.1038/375305a0

Prescott, J. R., & Hutton, J. T. (1994). Cosmic ray contributions to dose rates for luminescence and ESR dating: Large depths and long-term time variations. Radiation Measurements, 23(2), 497–500. doi: 10.1016/1350-4487(94)90086-8

Pye, K. (1987). Aeolian Dust and Dust Deposits. Academic Press, London.

Qiu, F., & Zhou, L. (2015). A new luminescence chronology for the Mangshan loess-palaeosol sequence on the southern bank of the Yellow River in Henan, central China. Quaternary Geochronology, 30, 24–33. doi: 10.1016/j.quageo.2015.06.014

Ran, M., & Feng, Z. (2013). Holocene moisture variations across China and driving mechanisms: A synthesis of climatic records. Quaternary International, 313–314, 179–193. doi: 10.1016/j.quaint.2013.09.034

Rasmussen, S. O., Bigler, M., Blockley, S. P., Blunier, T., Buchardt, S. L., Clausen, H. B., … Winstrup, M. (2014). A stratigraphic framework for abrupt climatic changes during the Last Glacial period based on three synchronized Greenland ice-core records: Refining and extending the INTIMATE event stratigraphy. Quaternary Science Reviews, 106, 14–28. doi: 10.1016/j.quascirev.2014.09.007

Rother, H., Stauch, G., Loibl, D., Lehmkuhl, F., & Freeman, S. P. H. T. (2017). Late Pleistocene glaciations at Lake Donggi Cona, eastern Kunlun Shan (NE Tibet): Early maxima and a diminishing trend of glaciation during the last glacial cycle. Boreas, 46(3), 503–524. doi: 10.1111/bor.12227

Ruth, U., Bigler, M., Röthlisberger, R., Siggaard-Andersen, M.-L., Kipfstuhl, S., Goto-Azuma, K., … Steffensen, J. P. (2007). Ice core evidence for a very tight link between North Atlantic and east Asian glacial climate. Geophysical Research Letters, 34(3). doi: 10.1029/2006GL027876

Schaetzl, R. J., Bettis, E. A., Crouvi, O., Fitzsimmons, K. E., Grimley, D. A., Hambach, U., … Zech, R. (2018). Approaches and challenges to the study of loess—Introduction to the LoessFest Special Issue. Quaternary Research 89 (3), 563-618. doi: 10.1017/qua.2018.15

Schaffernicht, E. J., Ludwig, P., & Shao, Y. (2020). Linkage between dust cycle and loess of the Last Glacial Maximum in Europe. Atmospheric Chemistry and Physics, 20(8), 4969–4986. doi: 10.5194/acp-20-4969-2020

Schulte, P., Sprafke, T., Rodrigues, L., & Fitzsimmons, K. E. (2018). Are fixed grain size ratios useful proxies for loess sedimentation dynamics? Experiences from Remizovka, Kazakhstan. Aeolian Research, 31(B), 131–140. doi: 10.1016/j.aeolia.2017.09.002

Schurr, B., Ratschbacher, L., Sippl, C., Gloaguen, R., Yuan, X., & Mechie, J. (2014). Seismotectonics of the Pamir. Tectonics, 33(8), 1501–1518. doi: 10.1002/2014TC003576

Selander, J., Oskin, M., Ormukov, C., & Abdrakhmatov, K. (2012). Inherited strike-slip faults as an origin for basement-cored uplifts: Example of the Kungey and Zailiskey ranges, northern Tian Shan. Tectonics, 31(4). doi: https://doi.org/10.1029/2011TC003002

Singhvi, A. K., Bluszcz, A., Bateman, M. D., & Rao, M. S. (2001). Luminescence dating of loess–palaeosol sequences and coversands: Methodological aspects and palaeoclimatic implications. Recent Research on Loess and Palaeosols, Pure and Applied, 54(1), 193–211. doi: 10.1016/S0012-8252(01)00048-4

Smalley, I. (1995). Making the material: The formation of silt sized primary mineral particles for loess deposits. Quaternary Science Reviews, 14(7), 645–651. doi: https://doi.org/10.1016/0277-3791(95)00046-1

Smalley, I. J., Kumar, R., O'Hara Dhand, K., Jefferson, I. F., & Evans, R. D. (2005). The formation of silt material for terrestrial sediments: Particularly loess and dust. Sedimentary Geology, 179(3), 321–328. doi: 10.1016/j.sedgeo.2005.06.011

Smalley, I., O'Hara-Dhand, K., & Kwong, J. (2014). China: Materials for a loess landscape. Catena, 117, 100–107. doi: 10.1016/j.catena.2013.11.016

Song, Yougui, Li, C., Zhao, J., Cheng, P., & Zeng, M. (2012). A combined luminescence and radiocarbon dating study of the Ili loess, Central Asia. Quaternary Geochronology, 10, 2–7. doi: 10.1016/j.quageo.2012.04.005

Song, Yougui, Chen, X., Qian, L., Li, C., Li, Y., Li, X., … An, Z. (2014). Distribution and composition of loess sediments in the Ili Basin, Central Asia. Quaternary International, 334–335, 61–73. doi: 10.1016/j.quaint.2013.12.053

Song, Yougui, Lai, Z., Li, Y., Chen, T., & Wang, Y. (2015). Comparison between luminescence and radiocarbon dating of late Quaternary loess from the Ili Basin in Central Asia. Quaternary Geochronology, 30, 405–410. doi: 10.1016/j.quageo.2015.01.012

Sprafke, T., Fitzsimmons, K. E., Grützner, C., Elliot, A., Marquer, L., & Nigmatova, S. (2018). Reevaluation of Late Pleistocene loess profiles at Remizovka (Kazakhstan) indicates the significance of topography in evaluating terrestrial paleoclimate records. Quaternary Research, 89(3), 674–690. doi: 10.1017/qua.2017.103

Stevens, Thomas, Armitage, S. J., Lu, H., & Thomas, D. S. G. (2006). Sedimentation and diagenesis of Chinese loess: Implications for the preservation of continuous, high-resolution climate records. Geology, 34(10), 849–852. doi: 10.1130/G22472.1

Stevens, Thomas, Thomas, D. S. G., Armitage, S. J., Lunn, H. R., & Lu, H. (2007). Reinterpreting climate proxy records from late Quaternary Chinese loess: A detailed OSL investigation. Earth-Science Reviews, 80(1), 111–136. doi: https://doi.org/10.1016/j.earscirev.2006.09.001

Stevens, Thomas, Lu, H., Thomas, D. S. G., & Armitage, S. J. (2008). Optical dating of abrupt shifts in the late Pleistocene East Asian monsoon. Geology, 36(5), 415. doi: 10.1130/G24524A.1

Stevens, T., Carter, A., Watson, T. P., Vermeesch, P., Andò, S., Bird, A. F., Lu, H., Garzanti, E., Cottam, M. A., & Sevastjanova, I. (2013). Genetic linkage between the Yellow River, the Mu Us desert and the Chinese Loess Plateau. Quaternary Science Reviews, 78, 355–368. https://doi.org/10.1016/j.quascirev.2012.11.032

Stevens, Thomas, Buylaert, J.-P., Lu, H., Thiel, C., Murray, A., Frechen, M., Yi, S., & Zeng, L. (2016). Mass accumulation rate and monsoon records from Xifeng, Chinese Loess Plateau, based on a luminescence age model: Monsoon records from Chinese Loess Plateau. Journal of Quaternary Science, 31(4), 391–405. https://doi.org/10.1002/jqs.2848

Stevens, T., Buylaert, J.-P., Thiel, C., Újvári, G., Yi, S., Murray, A. S., … Lu, H. (2018). Ice-volume-forced erosion of the Chinese Loess Plateau global Quaternary stratotype site. Nature Communications, 9(1), 983. doi: 10.1038/s41467-018-03329-2

Stevens, T. (2019). Applications in loessic environments. In Handbook of Luminescence Dating. Ed. M. Bateman and I. Bailiff. Caithness, Whittles Publishing, 153-190.

Stoops, G. (2003). Guidelines for Analysis and Description of Soil and Regolith Thin Sections. Soil Science Society of America, Madison, Wisconsin, 184 p.

Sun, J. (2002). Source Regions and Formation of the Loess Sediments on the High Mountain Regions of Northwestern China. Quaternary Research, 58(3), 341–351. doi: https://doi.org/10.1006/qres.2002.2381

Sun, J., & Liu, T. (2000). Stratigraphic Evidence for the Uplift of the Tibetan Plateau between ∼1.1 and ∼0.9 myr Ago. Quaternary Research, 54(3), 309–320. doi: https://doi.org/10.1006/qres.2000.2170

Sun, Y., & An, Z. (2005). Late Pliocene-Pleistocene changes in mass accumulation rates of eolian deposits on the central Chinese Loess Plateau. Journal of Geophysical Research, 110(D23), D23101. doi: 10.1029/2005JD006064

Sun, Y., Clemens, S. C., Morrill, C., Lin, X., Wang, X., & An, Z. (2012). Influence of Atlantic meridional overturning circulation on the East Asian winter monsoon. Nature Geoscience, 5(1), 46–49. doi: 10.1038/ngeo1326

Thiel, C., Buylaert, J.-P., Murray, A., Terhorst, B., Hofer, I., Tsukamoto, S., & Frechen, M. (2011). Luminescence dating of the Stratzing loess profile (Austria) – Testing the potential of an elevated temperature post-IR IRSL protocol. Quaternary International, 234(1), 23–31. doi: https://doi.org/10.1016/j.quaint.2010.05.018

Timar, A., Vandenberghe, D., Panaiotu, E. C., Panaiotu, C. G., Necula, C., Cosma, C., & van den haute, P. (2010). Optical dating of Romanian loess using fine-grained quartz.Quaternary Geochronology, 5(2), 143–148. doi: 10.1016/j.quageo.2009.03.003

Timar-Gabor, A., Buylaert, J.-P., Guralnik, B., Trandafir-Antohi, O., Constantin, D., Anechitei-Deacu, V., Jain, M., Murray, A. S., Porat, N., Hao, Q., & Wintle, A. G. (2017). On the importance of grain size in luminescence dating using quartz.Radiation Measurements, 106, 464–471. https://doi.org/10.1016/j.radmeas.2017.01.009

Újvári, G., Kovács, J., Varga, G., Raucsik, B., & Marković, S. B. (2010). Dust flux estimates for the Last Glacial Period in East Central Europe based on terrestrial records of loess deposits: A review. Quaternary Science Reviews, 29(23), 3157–3166. doi: 10.1016/j.quascirev.2010.07.005

Vandenberghe, J. (2013). Grain size of fine-grained windblown sediment: A powerful proxy for process identification. Earth-Science Reviews, 121, 18–30. doi: 10.1016/j.earscirev.2013.03.001

Vriend, M., Prins, M. A., Buylaert, J.-P., Vandenberghe, J., & Lu, H. (2011). Contrasting dust supply patterns across the north-western Chinese Loess Plateau during the last glacial-interglacial cycle. Quaternary International, 240(1), 167–180. doi: https://doi.org/10.1016/j.quaint.2010.11.009

Wang, L., Jia, J., Xia, D., Liu, H., Gao, F., Duan, Y., Wang, Q., Xie, H., & Chen, F. (2019)a. Climate change in arid central Asia since MIS 2 revealed from a loess sequence in Yili Basin, Xinjiang, China. Quaternary International, 502, 258–266. https://doi.org/10.1016/j.quaint.2018.02.032

Wang, L., Jia, J., Zhao, H., Liu, H., Duan, Y., Xie, H., Zhang, D. D., & Chen, F. (2019)b. Optical dating of Holocene paleosol development and climate changes in the Yili Basin, arid central Asia. The Holocene, 29(6), 1068–1077. https://doi.org/10.1177/0959683619831432

Wintle, A. G., & Murray, A. S. (2006). A review of quartz optically stimulated luminescence characteristics and their relevance in single-aliquot regeneration dating protocols. Radiation Measurements, 41(4), 369–391. doi: 10.1016/j.radmeas.2005.11.001

Wyrwoll, K.-H., Wei, J., Lin, Z., Shao, Y., & He, F. (2016). Cold surges and dust events: Establishing the link between the East Asian Winter Monsoon and the Chinese loess record. Quaternary Science Reviews, 149, 102–108. doi: https://doi.org/10.1016/j.quascirev.2016.04.015

Xu, Z., Stevens, T., Yi, S., Mason, J. A., & Lu, H. (2018). Seesaw pattern in dust accumulation on the Chinese Loess Plateau forced by late glacial shifts in the East Asian monsoon. Geology, 46(10), 871–874. doi: 10.1130/G45105.1

Yang, S., & Ding, Z. (2010). Drastic climatic shift at ∼2.8Ma as recorded in eolian deposits of China and its implications for redefining the Pliocene-Pleistocene boundary. Plio-Pleistocene Correlation and Global Change, 219(1), 37–44. doi: 10.1016/j.quaint.2009.10.029

Yang, S., Ding, Z., Li, Y., Wang, X., Jiang, W., & Huang, X. (2015). Warming-induced northwestward migration of the East Asian monsoon rain belt from the Last Glacial Maximum to the mid-Holocene. Proceedings of the National Academy of Sciences, 112(43), 13178. doi: 10.1073/pnas.1504688112

Yang, H., Li, G., Huang, X., Wang, X., Zhang, Y., Jonell, T. N., Jin, M., Chen, C., Zhao, W., Zhang, H., Wang, Z., & Deng, Y. (2020). Loess depositional dynamics and paleoclimatic changes in the Yili Basin, Central Asia, over the past 250 ka. Catena, 195, 104881. https://doi.org/10.1016/j.catena.2020.10488

Youn, J. H., Seong, Y. B., Choi, J. H., Abdrakhmatov, K., & Ormukov, C. (2014). Loess deposits in the northern Kyrgyz Tien Shan: Implications for the paleoclimate reconstruction during the Late Quaternary. Catena, 117, 81–93. doi: https://doi.org/10.1016/j.catena.2013.09.007

4. Chapter 4

A novel proxy for tracking the provenance of dust based on paired E'-peroxy paramagnetic defect centres in fine-grained quartz

Aditi K. Dave[1], Alida Timar-Gabor[2,3], Zuzanna Kabacińska[2], Giancarlo Scardia[4], Nosir Safaraliev[5], Saida Nigmatova[6], Kathryn E. Fitzsimmons[1]

[1]Research Group for Terrestrial Palaeoclimates, Max Planck Institute for Chemistry, Hahn-Meitner-Weg 1, 55128 Mainz, Germany
[2]Faculty of Environmental Sciences and Engineering, Babes Bolyai University, Cluj-Napoca, Romania
[3]Interdisciplinary Research Institute on Bionanoscience, Babes Bolyai University, Cluj-Napoca, Romania
[4]Instituto de Geociências e Ciências Exatas, Universidade Estadual Paulista, 13506-900 Rio Claro, SP, Brazil
[5]Tajik National University, 17 Rudaki Avenue, Dushanbe 734025, Tajikistan
[6]Institute of Geological Sciences K. Satpaeva, Ministry for Education and Science of the Republic of Kazakhstan, Almaty, Kazakhstan

Status:

Submitted to Geophysical Research Letters

Key Points

- New sediment provenance tool exploits the E' and peroxy paramagnetic defects in quartz
- Positive correlation of E' and peroxy intensities of fine-grained quartz reaffirms the hypothesis they arise from natural Schottky-Frenkel defect pairs
- New proxy successfully differentiates quartz in loess from two different basins in Central Asia
- Has potential applications for identifying climate-driven source change through time in loess and other sedimentary sequences

Abstract

Crystal lattice defects in quartz have long been exploited for age determination, yet also show potential for sediment provenance studies. Here we introduce a novel method for tracking aeolian dust provenance by utilising the natural accumulation of E' and peroxy defect centres in quartz. Our approach is based on the premise that E' and peroxy centres arise from Schottky-Frenkel defect pairs, and that their concentration increases with increasing age of the quartz-bearing source rock, as previously observed. We propose that these defect centres can be utilised as a characteristic feature of the source rock, to be compared with sediments derived from it. We observe a positive correlation between E' and

peroxy centre intensity in fine-grained quartz, supporting the hypothesis that they indeed arise from Frenkel defect pairs. We successfully apply our new protocol to distinguish fine-grained quartz extracted from loess from two regions in Central Asia which are known to derive from different source material. Our method offers great potential for identifying variability in source both spatially and through time, down sedimentary sequences.

Plain Language Summary

Identifying the origins of dust deposits allows us to reconstruct sediment transport pathways, which are essential for understanding past atmospheric circulation patterns. Towards this goal, we propose to exploit the characteristics of two naturally occurring defect centres in crystalline quartz: the E' and peroxy centres. These centres occur as pairs and are hypothesised to increase with the age of the quartz-bearing rock. By this logic, the E' and peroxy centres can be used to determine the lithic origins of sedimentary quartz in a similar way to detrital zircon-based provenance techniques, while analysing a more ubiquitous mineral (quartz). We applied our approach, which uses a simplified protocol for measurement in contrast to earlier studies, to successfully distinguish between loess (wind-blown dust deposits) from two different basins in Central Asia. This study holds great potential in its application not only for loess sequences, but also to other sedimentary archives.

Keywords: Provenance, Quartz, Defect centres, Loess, Electron Spin Resonance

4.1. Introduction

Identifying the original source rocks of sediments is important for the elucidation of sediment cycling. In the case of aeolian sediments, pinpointing provenance has the additional advantage of facilitating the reconstruction of transport pathways that relate to atmospheric circulation, and thereby changes in climate dynamics through time. Aeolian loess deposits have long been recognized as valuable archives of past climates in terrestrial environments (Kukla, 1988; Schaetzl et al., 2018). Since loess sequences represent the long-term accumulation of aeolian dust, identifying their provenance provides a vector for dust transport pathways, and therefore an important proxy for reconstructing changes in atmospheric circulation through time. A number of established tools are commonly used to identify the source of dust in loess deposits. These include grain-size analysis, in particular grain sorting and end-member modelling, to elucidate transport modes and likely source area types (Vandenberghe, 2013; Nottebaum et al., 2015; Li et al., 2018); major and trace elemental composition of bulk dust (Sun et al., 2002; Újvári et al., 2008); radiogenic isotope signatures (Sr and Nd) characteristic of clay minerals (Chen et al., 2007; Rao et al., 2015); and

detrital zircon age profiles (Pullen et al., 2011). Whilst these methods are widely used to identify relative changes in dust sources through time, they rely either on materials found in very low concentrations (detrital zircons, radiogenic isotopes in clays), undiagnostic physical characteristics (grain size parameters), or aggregated bulk measurements from multiple size fractions which are likely to have been transported from both distal and proximal sources (major and trace elements). Furthermore, post-depositional weathering can alter the in situ chemical signature within loess, rendering certain analytical techniques, if uncorrected, inaccurate for provenance (Yang et al., 2001).

Given the limitations of the above-mentioned provenance techniques, recent years have seen increasing interest in the characteristics of mineral quartz as a tool for linking dust sources and sinks. There are obvious advantages in using quartz as a provenance tool: it is not only ubiquitous, but also highly resistant to weathering and diagenesis (Goldich, 1938). A number of quartz-specific petrographic, isotopic and geochemical provenance methods have been proposed (Bernet & Basset, 2005; Nagashima et al., 2007, 2017; Shimada et al., 2013, Ackerson et al., 2015). Of these, the electron spin resonance (ESR) signal of the heat-treated E' (hereafter referred to as HT-E') centre, and crystallinity index (CI), of fine-grained quartz have been increasingly applied to aeolian quartz (Nagashima et al., 2007, 2011, 2013; Sun et al., 2007, 2008, 2013; Isozaki et al., 2020). ESR allows measurement of the intensity of paramagnetic (containing an unpaired electron) species in a material (Ikeya, 1993). Lattice defects and impurities in quartz give rise to various paramagnetic defect centres. E' is one such centre and is well characterised (Weil, 1984), comprising an unpaired electron in an oxygen vacancy (≡*Si*·) which is known to arise from diamagnetic oxygen vacancies (*Si*=*Si*, Fiegl et al., 1974). The most commonly used ESR protocol characterises HT-E' intensity (Toyoda & Hattori, 2000; Nagashima et al., 2007; Toyoda et al., 2016) by measuring E' intensity following gamma (γ) irradiation and thermal treatment. It is based on the premise that γ-irradiation and heating facilitate the conversion of quartz diamagnetic oxygen vacancies into paramagnetic E' centres resolvable by ESR and expressed as HT-E'. The HT-E' intensity is assumed to reflect the total number of oxygen vacancies, which is characteristic of rock type and consequently of the source rock from which the quartz is derived (Toyoda & Hattori, 2000; Toyoda et al., 2016). The HT-E' signal has also been observed to increase with rock age (Toyoda et al., 1992). By contrast, CI reflects the crystallisation conditions of quartz in source rocks (Nagashima et al., 2007). The combined HT-E' intensity and CI of sedimentary quartz is interpreted to reflect the age, formation and crystallisation conditions of quartz in the source rock, and therefore acts as a provenance tool (Nagashima et al., 2017; Toyoda et al., 2016). Several studies speculating on the role of aluminum (Al) in forming the HT-E' centre (Usami et al., 2009), and the prevailing hypothesis on the ionising radiation responsible for increase in the E' signal within the host rock (Rink & Odom, 1991; Toyoda et al., 1992; Toyoda et al., 2001) nevertheless suggests a need to further interrogate the mechanisms driving the formation of the quartz HT-E' centre.

Here we investigate a simplified new provenance method based on the natural characteristics of two paramagnetic centres, the E' and peroxy centres, using ESR. Our simplified protocol is based on the premise that E' and peroxy centres arise from Schottky-Frenkel (SF) defect pairs in quartz, and increase with the age of the quartz-bearing granitic host rock (Odom & Rink, 1989). We apply our method to natural loess sediments from inland Asia.

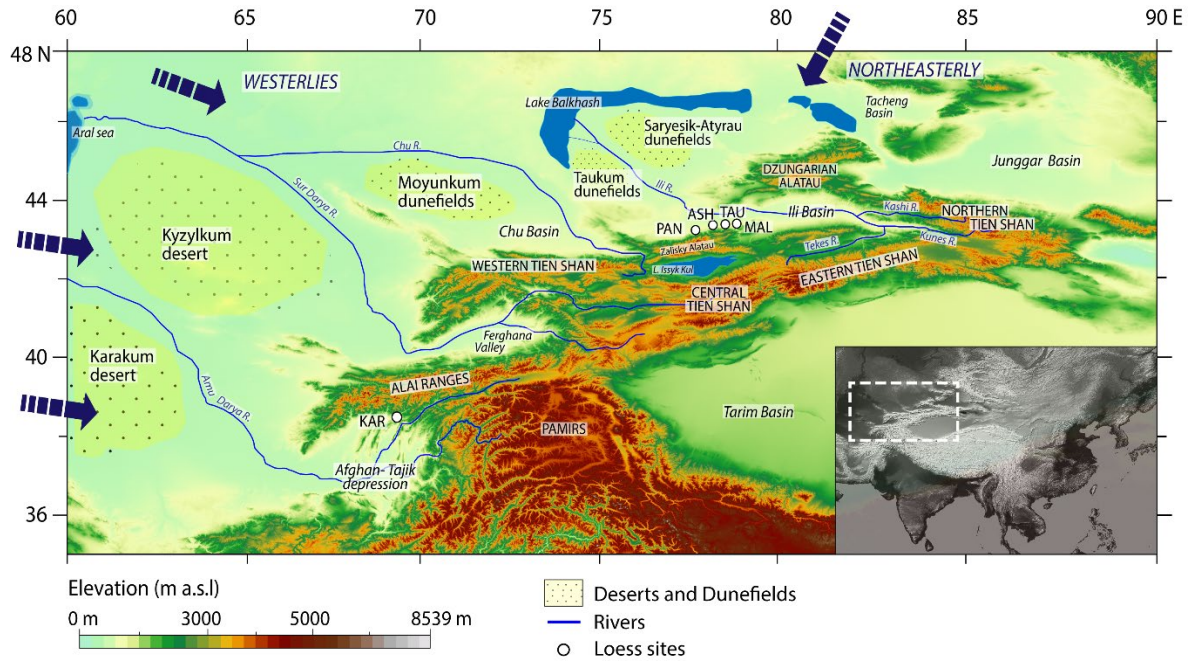

Fig. 4.1. Regional setting and location of the loess sites under study.

Inland Asia has been one of the regional foci for investigations using ESR signals of quartz as a provenance technique, since it represents one of the world's major atmospheric dust sources past and present (Kok et al., 2021). The basins to the north, east and west of the Asian high mountains lie in topographic rain shadows and represent substantial sinks for glacially- and fluvially-derived sediment from the uplands (Schaetzl et al., 2018; Fig. 4.1). In particular, the loess deposits of arid Central Asia (ACA) and the Chinese Loess Plateau (CLP) reach hundreds of metres in thickness (Liu, 1985; Li et al., 2015) and represent long-term substantial accumulation, and by extension likely distal export of aeolian dust. Distinguishing between the various potential dust sources in inland Asia is important at multiple scales. At a regional level it is essential to identify changes in source down loess sequences, and thereby to reconstruct variability in dust transport pathways and atmospheric circulation through time. At global scales, distinguishing dust sources from loess helps us understand the relative contributions of different basins to the generic "Asian" mineral dust identified in Greenland

ice cores (Svensson et al., 2000; Bory et al., 2003) and Pacific Ocean marine sediments (Nakai et al., 1993; Letelier et al., 2019). The combined quartz HT-E' intensity and CI method (Nagashima et al., 2007) has been applied to discern fine-grained quartz from several major deserts and loess sequences in East Asia (Sun et al., 2007, 2008, 2013; Isozaki et al., 2020), however the sources and contribution to global dust budget of the ACA loess piedmonts and deserts remain largely unexplored.

In this study, we characterise the natural E' and peroxy centre intensities of loess from two basins in ACA, the Ili basin and Tajik depression of southeast (SE) Kazakhstan and Tajikistan respectively (Fig. 4.1). Recent studies based on geochemical fingerprinting and back trajectory analysis indicate that these two loess regions derive sediment from different source areas (Li et al., 2018; Li et al., 2019; Fitzsimmons et al., 2020). The potential significance of the region for global atmospheric dust loads past and present, coupled with the likely discrete sources for the basins, make these two basins well suited for a targeted spatial and temporal comparison of quartz characteristics for provenance using our new method.

4.2. Material and Methods

We undertook measurements on fine-grained (4–11 µm) quartz extracted from loess samples collected from five sections in Central Asia (Fig. B1 in appendix B). Four of these sections, Panfilov (PAN), Ashubulak (ASH), Taukaraturyuk (TAU) and Malubai (MAL), are located along a ~200 km east-west transect of the Zalisky-Alatau range in the Ili basin of SE Kazakhstan. The fifth site, Karamaidan (KAR), is a c. 60 m-thick partial section of a c. 130 m-thick loess-paleosol sequence, located in the foothills of the Gissar mountain range on the northern margins of the Tajik Depression, in southern Tajikistan (Fig. 4.1). We analysed a total of 114 samples, 59 from SE Kazakhstan and 55 from Tajikistan. A detailed account of sampling, site description, sample preparation and instrumentation, measurement protocols and the parameters of ESR centres is provided in the Supporting Information (SI) in appendix B.

We performed two sets of experiments on the fine-grained quartz:

(i) To test our new approach, we measured the natural intensity of E' and peroxy centres for all samples, without the γ-irradiation and/or thermal treatment required for the HT-E' approach (Toyoda & Hattori, 2000). We hereafter refer to these measurements as the natural E' and peroxy intensity.

(ii) To understand and compare the difference between the natural E' and HT-E' intensity of quartz, we also measured the HT-E' intensity following published protocols (Toyoda & Hattori, 2000; Nagashima et al., 2007) for all our samples. This involved irradiating all samples with a γ-dose of 2000 Gy, followed by heating the samples to 350 °C for 15

minutes to obtain the maximum E' intensity. In addition, to further test our approach and evaluate the need for γ-irradiation and thermal treatment prior to E' measurement, we investigated the variation of ESR centres (E', peroxy and Al-hole) with γ-irradiation (varying from 0 to 40000 Gy) and temperature (300, 350 and 400 °C) from two representative samples, one from Kazakhstan (A0016, TAU) and the other Tajikistan (A0329, KAR). Detailed descriptions of experimental parameters are given in the SI.

4.3. Results and Discussion

4.3.1. Paired E'-peroxy centres in quartz: Methodological considerations linking quartz crystal defect dynamics to provenance

The formation and characteristics of E' and peroxy centres in natural and artificial quartz have long been the subject of empirical study (Weeks, 1956; McMorris, 1970; Stapelbroek et al., 1979; Friebele et al., 1979). Odom and Rink (1989), however, were the first to observe that E' and peroxy signals in quartz increase with the age of granitic host rocks. Based on positive correlations between E' and peroxy intensities (Odom & Rink, 1989) and calculations of alpha recoil lattice damage, Rink and Odom (1991) proposed that these defect centres arise from SF defect pairs formed by alpha-recoil nuclei, emitted by alpha-emitting elements (U and Th) and accumulated in rocks through time. If this principle holds true for all rock types and the mechanisms for defect formation are understood, then the E' and peroxy signals have obvious applications not only as geochronometers (Odom & Rink, 1989) but also for sediment provenance as explored here.

Our measurements of the natural E' and peroxy intensities of 114 Kazakh and Tajik samples indicate that the natural intensity of E' and peroxy centres yield a positive correlation, with a Pearson coefficient of 0.72 (Fig. 4.2a). This supports the hypothesis that these ESR centres indeed arise from SF defect pairs in quartz as per Odom and Rink (1989), and justifies our exploration of both E' and peroxy natural signals for their application as indicators of provenance.

Although intuitive, measurement of 'natural' signals for provenance remains largely unexplored. Our provenance approach, based on natural E' and peroxy signals, represents a simpler protocol than the hitherto established method based on HT-E' intensity (Toyoda et al., 2016, and references therein). In order to systematically assess the difference between natural (our study) and heat-treated (HT-) E' (established protocols) intensity of samples, we additionally measured the HT-E' intensity for all 114 samples using published protocols (Toyoda & Hattori, 2000; Nagashima et al, 2007). Fig. 4.2b compares the natural E' and HT-E' results for all samples. We observe that γ-irradiation and heating simply increases the signal

intensity beyond the natural E' in all samples. This indicates that the natural E' intensity produces the same inherited provenance characteristics as HT-E' intensity.

Our results suggest that sample pre-treatment by γ-irradiation and heating is unnecessary for ESR-based quartz provenance methods. Nevertheless, it is necessary to more directly test whether this is indeed the case. According to the proposed mechanism for formation of the HT-E' (Toyoda & Ikeya, 1991; Toyoda & Hattori, 2000), γ-irradiation creates hole-supplying Al-hole centres (which arise from Al impurities in quartz), and post-irradiation heating causes the migration of holes from the Al-hole centres. The released holes recombine with one of the two electrons of the diamagnetic oxygen vacancies, giving rise to an oxygen vacancy with an unpaired electron, i.e. an E' centre. Therefore, the HT-E' signal refers to the total E' concentration obtained after irradiation and thermal treatment. The established HT-E' provenance protocols (Toyoda et al., 2016, and references therein) propose that γ-irradiation and heating essentially convert all diamagnetic oxygen vacancies - which are characteristic of a rock - into E' centres. We therefore undertook a series of irradiation and heating experiments on two representative samples, A0016 (Kazakhstan) and A0329 (Tajikistan), to systematically assess the effects of γ-irradiation and thermal treatment on ESR centres (E', peroxy, Al-hole centre), and whether such pre-treatment is necessary for ESR-based provenance studies.

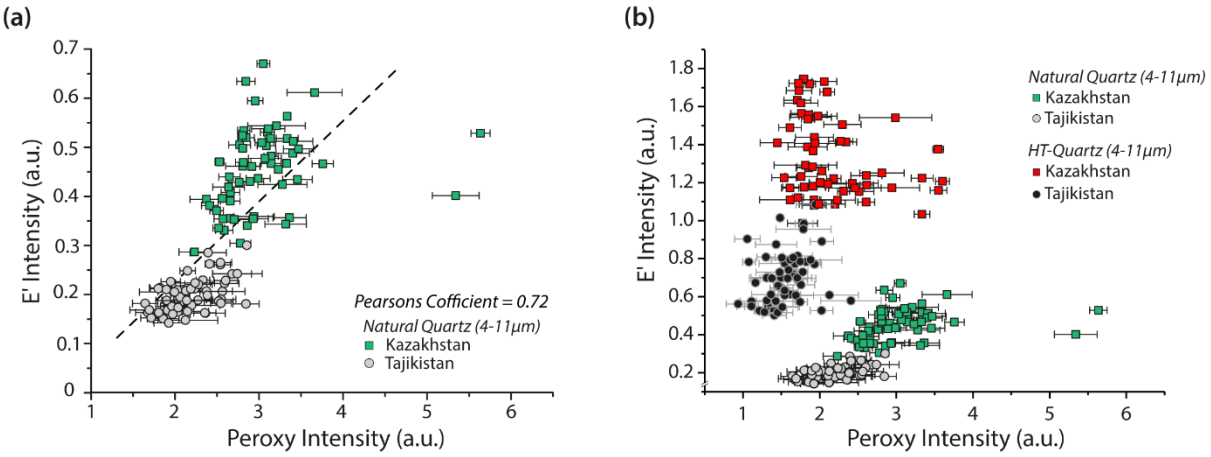

Fig. 4.2. (a) Cross-plot of natural E' and peroxy centre intensities of fine-grained quartz from Kazakhstan and Tajikistan based on our new approach; (b) Comparison between natural and heat-treated (HT) E' and peroxy intensities.

First, we tested the effect of γ-irradiation on the ESR intensity of natural E', peroxy and Al-hole centres. We irradiated 11 aliquots of each sample with a γ dose varying from 0 to 40000 Gy and measured the intensity of each ESR centre. We observe that, overall, the natural E'

intensity does not change with γ-irradiation (Fig. 4.3a,b). Our observations corroborate with results obtained from fine-grained quartz from other regions (eastern Europe and North America; Fig. B2 in appendix B). Likewise, the natural intensity of the peroxy centre for both samples does not vary with γ dose (Fig. B3 in appendix B). We note that the uncertainty on peroxy measurements (Fig. B3) is 10-20% higher than for the natural E', which has an uncertainty of <1%. This is most likely due to the weak peroxy signal observed in our samples. By contrast, the natural Al-hole centre intensity increases exponentially with increasing γ dose (Fig. B4 in appendix B).

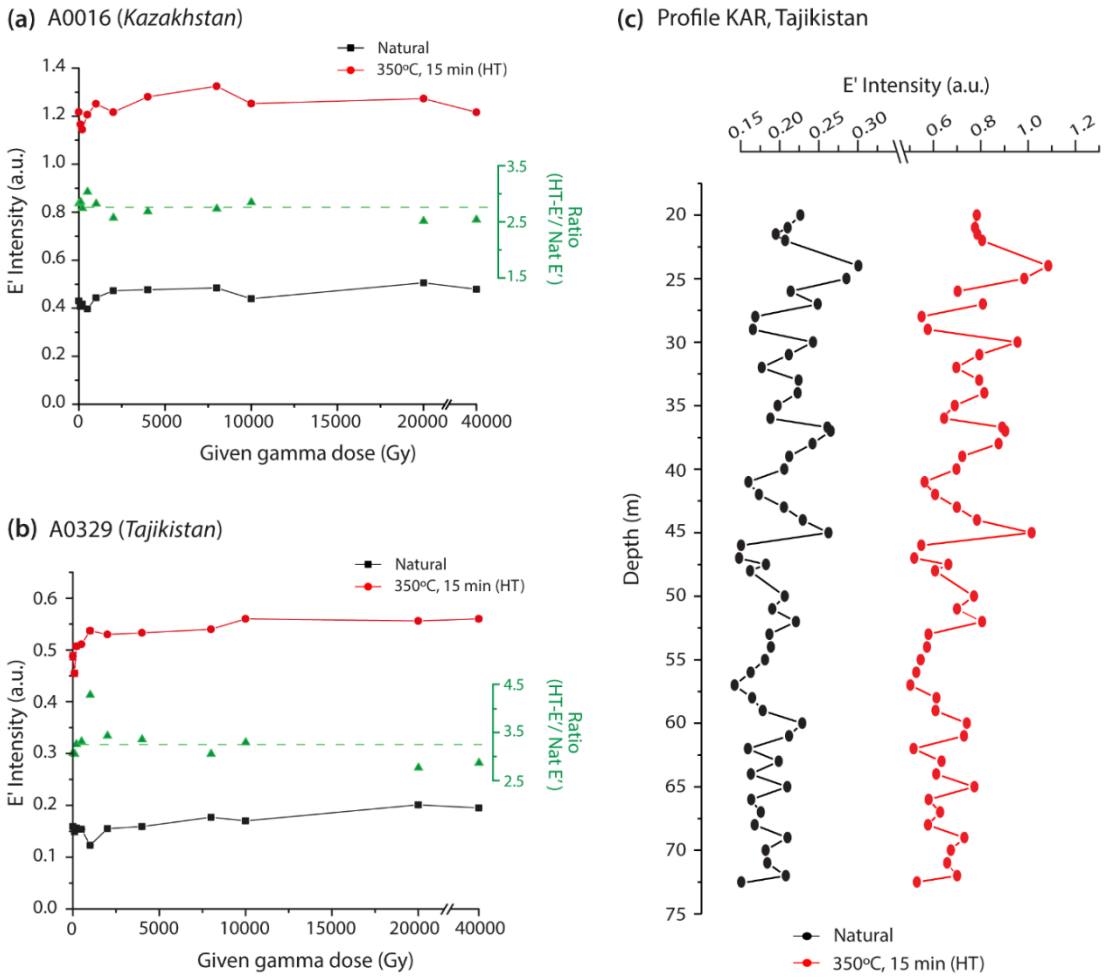

Fig. 4.3. Variation in natural E' and HT-E' (350 °C for 15 min) intensity with γ dose for sample (a) A0016 and (b) A0329. (c) Variation in natural and HT-E' intensity with depth (or increasing 'natural' dose) at site KAR.

We then tested the effect of temperature on irradiated quartz E' and peroxy centres for the same two representative samples (A0016 and A0329). All γ-irradiated aliquots (n=11) of each

sample were heated to 300, 350 and 400 °C for 15 min, followed by measurement of the resulting E' and peroxy centre intensities. In both samples, E' intensity increases with temperature up to a peak at 350 °C, after which the E' signal decreases (Fig. B5a,b in appendix B). The E' intensity at any given temperature does not change with increased dose (Fig. B5c,d in appendix B), which can also be seen in the constant ratio of HT-E' to natural E' intensity for both samples (Fig. 4.3a,b compares E' intensity of natural quartz and that heated to 350 °C). The peroxy signal shows minimal change in average intensity with increased temperature (Fig. B6 in appendix B). However, the generally weak peroxy signals produce high scatter in the data, rendering assessment of peroxy intensity response to increasing temperature difficult.

Our experiments on fine-grained quartz have two important implications for measuring natural E' as a provenance signal. First, E' and HT-E' intensity remains unchanged with increasing γ-dose, and the ratio between the two signals remains constant (Fig. 4.3). This suggests that heating increases net E' intensity, and irradiation has no effect. This is the case not only for our samples from two regions in Central Asia, but also for detrital quartz from modern river sediments (Wei et al., 2017). We conclude that natural E' reflects the quartz characteristics just as well as the HT-E' signal and argue that γ-irradiation and heating is not necessary. Secondly, in both of our samples, the intensity of the Al-hole centre increases with increasing γ-dose, in contrast to natural E' and HT-E'. If we assume the proposed formation mechanism of HT-E' centre to be true (Toyoda & Ikeya, 1991; Toyoda & Hattori, 2000), our observations would imply that the number of diamagnetic oxygen vacancies in our samples is less than number of holes released from Al-centres upon heating, even for unirradiated samples. This makes the γ-irradiation step unnecessary.

We argue that the intensity of both natural and HT-E' in fine-grained quartz is not dose-dependent, based on our irradiation experiments (Fig. 4.3a,b). We therefore argue that the γ-irradiation step recommended in the established HT-E' measurement protocol is redundant. We provide further evidence that the E' signal is independent from dose by investigating the effect of natural (environmental) irradiation, by examining the natural and HT-E' intensity variation with depth down the c. 60 m thick loess section at KAR, Tajikistan. Details of the stratigraphy and magnetic susceptibility of the KAR profile can be found in the SI in appendix B. Based on previous work (Forster & Heller, 1994) and our own magnetic susceptibility measurements, we correlated the sampled part of the KAR profile to marine oxygen isotope stages (MIS) 19-9 (c. 800–300 ka; Lisiecki & Raymo, 2005). This correlation renders the samples from this section beyond the limits of quartz Optically Stimulated Luminescence (OSL) dating. We therefore estimated the minimum natural (burial) ionising radiation received by the uppermost sample to c. 1000 Gy using the post-Infrared Infrared Stimulated Luminescence protocol (pIRIR, Table B1; Buylaert et al., 2012) on polymineral fine-grained fraction (refer SI in appendix B for details, Fig. B7). Assuming age (which corresponds to burial

time) increases with depth, this result implies that all samples below the uppermost sample received natural irradiation in excess of 1000 Gy. We then plotted the natural E' and HT-E' intensity with depth and observe no incremental increase. This implies that the E' signals are independent of natural irradiation (Fig. 4.3c), which further supports the results of our laboratory γ-irradiation based studies.

4.3.2. Applications in aeolian environments: Examples from Central Asia

The ultimate aim of sedimentary provenance analysis is to identify the parent rock assemblages from which sediments derive (Weltje & Enyatten, 2004). In case of aeolian quartz, if the parent rocks or sedimentary sources can be linked to the loess deposit in question, the vector responsible for dust transport can be established, and by extension the most likely climate circulation patterns prevailing at the time of accretion may be inferred. Our study provides a critical step towards achieving the aim of identifying provenance within sediments by establishing a simplified protocol exploiting characteristic signatures based on defect centres in quartz.

Our suite of samples forms two distinct spectral clusters depending on geographic region (Fig. 4.2a). Of the two natural ESR signals measured, the natural E' intensity yields the greatest difference between the two regions (Fig. 4.2). The more diffused peroxy signatures are a result of inherently weak peroxy signal in our samples and may perhaps, also reflect the hypothesis that 'peroxy' signals, as measured, may represent the overlap of a peroxy radical (≡*Si*-O-O·, POR) and non-bridging oxygen hole centre (≡*Si*–O·, NBOHC) (based on observations by Salh, 2011; Skuja et al., 2020; Fig. B8). Nevertheless, the peroxy signals from the two regions are statistically distinguishable; further investigations relating to this hypothesis are beyond the scope of this paper. We observe higher natural E' and peroxy signals in the Kazakh loess than for the Tajik samples. This suggests that the Kazakh quartz is sourced from older rocks as compared to the Tajik quartz, since the E' and peroxy centres are known to accumulate with time, as per Odom and Rink (1989). The suggestion that the Kazakh source rock is older is consistent with the rocks of the central Tien Shan, which are of Palaeozoic age or older (Tursungaziev & Petrov, 2008), and represent the likely source material to the Kazakh loess piedmont (Li et al., 2018; Fitzsimmons et al., 2020). These are older than the predominantly Mesozoic and younger rocks of the Gissar Mountains and northwestern Pamirs (Vlasov et al., 1991), which provide the most likely protoliths for the Tajik loess (Li et al., 2019). The formation of two separate clusters for two independently sourced regions of different protolith age provides support for our proposed approach as a provenance tool.

In addition to differentiating likely source regions for different loess sites, we ultimately aim to identify potential changes in source through time down long loess sequences such as those found in inland Asia. Fig. 4.4a shows down-profile variations in natural E' intensity of loessic quartz at KAR in Tajikistan, a site which preserves multiple primary loess and buried

soil (paleosol) horizons (refer SI in appendix B for details). We observe distinct differences in the natural E' and peroxy signature in loess versus paleosol horizons (Fig. 4.4b). Recent work using trace element concentrations and meteorological re-analysis of loess in Tajikistan suggests that its provenance is site-dependent and likely to be dominated by proximal montane sources (Li et al., 2016), with some contribution from distal sources such as the Karakum desert (Li et al., 2019). The relative contributions of distal and proximal sources to loess deposits in Tajikistan may have changed over glacial-interglacial timescales as a result of changes in the dynamics and intensity of atmospheric circulation. We suggest that our observed changes in paired E'-peroxy characteristics represent variability in the dominant source signature of quartz between the primary (glacial) loess and paleosol (interglacial) horizons. At this stage, without more targeted investigations of potential source rocks, we cannot identify whether the change in the dominant source signature through time at KAR is a result of proximal and/ or distal transport of dust. Nevertheless, our observations hold promise for more focused investigations of source signature based on our provenance method.

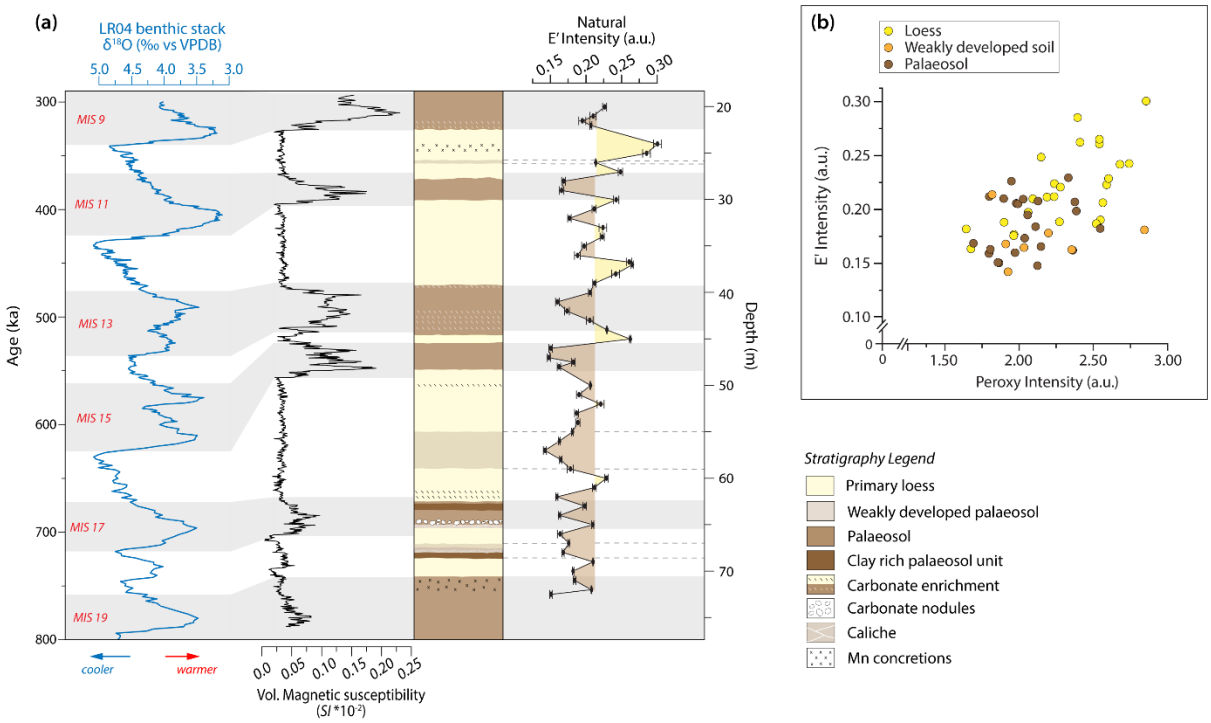

Fig. 4.4. (a) Down-profile variability in intensity of E' centres of fine-grained (4–11 µm) quartz at KAR, Tajikistan. The LR04 benthic δ18O stack is obtained from Lisiecki and Raymo (2005) (b) Natural E' and peroxy variation in samples from various stratigraphic sections (identified here as loess, palaeosol, and weakly developed palaeosols) at KAR (Tajikistan) based on field stratigraphic description and magnetic susceptibility data.

4.4. Conclusion

We propose a new method for determining the provenance of sedimentary quartz based on the natural accumulation of E' and peroxy centres. We confirm, based on empirical measurements of 114 fine-grained loessic quartz samples which yield a positive correlation between the natural E' and peroxy signals, that these centres arise from SF defect pairs. Samples from the Ili basin of SE Kazakhstan yield signals distinct from those from the Tajik basin in Tajikistan, indicating a difference in provenance consistent with previously published studies. The higher intensity E' and peroxy signals from the Kazakh samples, which are likely derived from older rocks than the Tajik loess, also strongly suggest that their concentrations increase with increasing age of the source rock. Furthermore, down-profile measurements at the KAR site in Tajikistan indicate a shift in source between primary loess and paleosol horizons, most likely in response to changes in atmospheric circulation associated with climatic oscillations. Our observations suggest this to be a robust new technique for sediment provenance, that can be applicable to a range of settings, exploiting the characteristics of one of the most ubiquitous minerals found in nature: quartz.

Acknowledgements

AK Dave would like to thank the Luminescence Laboratory at the Max Planck Institute for Evolutionary Anthropology, Leipzig, Germany for access to the HF etching laboratory. We also thank the following colleagues for their assistance during fieldwork in Tajikistan: S Yusupov, A Safarov, RS Pavlatov and ZN Nadjmudinov (Tajik National University); C Prudhomme, A Engström Johansson, L Marquer, Z Perić, S de Graaf, M Notwatzki and K Reetz (Max Planck Institute for Chemistry).

References

Ackerson, M. R., Tailby, N. D., & Watson, E. B. (2015). Trace elements in quartz shed light on sediment provenance. Geochemistry, Geophysics, Geosystems, 16(6), 1894–1904. https://doi.org/10.1002/2015GC005896

Bernet, M., & Bassett, K. (2005). Provenance analysis by single-quartz-grain SEM-CL/optical microscopy. Journal of Sedimentary Research, 75(3), 492–500. https://doi.org/10.2110/jsr.2005.038

Bory, A. J.-M., Biscaye, P. E., & Grousset, F. E. (2003). Two distinct seasonal Asian source regions for mineral dust deposited in Greenland (NorthGRIP). Geophysical Research Letters, 30(4). https://doi.org/10.1029/2002GL016446

Buylaert, J.-P., Jain, M., Murray, A. S., Thomsen, K. J., Thiel, C., & Sohbati, R. (2012). A robust feldspar luminescence dating method for Middle and Late Pleistocene sediments. Boreas, 41(3), 435–451. https://doi.org/10.1111/j.1502-3885.2012.00248.x

Chen, J., Li, G., Yang, J., Rao, W., Lu, H., Balsam, W., Sun, Y., & Ji, J. (2007). Nd and Sr isotopic characteristics of Chinese deserts: Implications for the provenances of Asian dust. Geochimica et Cosmochimica Acta, 71(15), 3904–3914. https://doi.org/10.1016/j.gca.2007.04.033

Feigl, F. J., Fowler, W. B., & Yip, K. L. (1974). Oxygen vacancy model for the E1′ center in SiO2. Solid State Communications, 14(3), 225–229. https://doi.org/10.1016/0038-1098(74)90840-0

Fitzsimmons, K. E., Nowatzki, M., Dave, A. K., & Harder, H. (2020). Intersections between wind regimes, topography and sediment supply: Perspectives from aeolian landforms in Central Asia. Palaeogeography, Palaeoclimatology, Palaeoecology, 540, 109531. https://doi.org/10.1016/j.palaeo.2019.109531

Forster, Th., & Heller, F. (1994). Loess deposits from the Tajik depression (Central Asia): Magnetic properties and paleoclimate. Earth and Planetary Science Letters, 128(3–4), 501–512. https://doi.org/10.1016/0012-821X(94)90166-X

Friebele, E. J., Griscom, D. L., Stapelbroek, M., & Weeks, R. A. (1979). Fundamental defect centers in glass: The peroxy radical in irradiated, high-purity, fused silica. Physical Review Letters, 42(20), 1346–1349.

Goldich, S. S. (1938). A Study in Rock-Weathering. The Journal of Geology, 46(1), 17–58. https://doi.org/10.1086/624619

Ikeya, M. (1993). New Applications of Electron Spin Resonance: Dating, Dosimetry and Microscopy. World Scientific. https://doi.org/10.1142/1854

Isozaki, Y., Tada, R., Sun, Y., Zheng, H., Toyoda, S., Sugiura, N., Karasuda, A., & Hasegawa, H. (2020). Origin of aeolian dust emitted from the Tarim Basin based on the ESR signal intensity and crystallinity index of quartz: The recycling system of fine detrital material within the basin. Geological Magazine, 157(5), 707–718. Cambridge Core. https://doi.org/10.1017/S0016756820000242

Kok, J. F., Adebiyi, A. A., Albani, S., Balkanski, Y., Checa-Garcia, R., Chin, M., Colarco, P. R., Hamilton, D. S., Huang, Y., Ito, A., Klose, M., Li, L., Mahowald, N. M., Miller, R. L., Obiso, V., Pérez García-Pando, C., Rocha-Lima, A., & Wan, J. S. (2021). Contribution of the world's main dust source regions to the global cycle of desert dust. Atmospheric Chemistry and Physics Discussions, 2021, 1–34. https://doi.org/10.5194/acp-2021-4

Kukla, G., Heller, F., Ming, L. X., Chun, X. T., Sheng, L. T., & Sheng, A. Z. (1988). Pleistocene climates in China dated by magnetic susceptibility. Geology, 16(9), 811–814. https://doi.org/10.1130/0091-7613(1988)016<0811:PCICDB>2.3.CO;2

Letelier, R. M., Björkman, K. M., Church, M. J., Hamilton, D. S., Mahowald, N. M., Scanza, R. A., Schneider, N., White, A. E., & Karl, D. M. (2019). Climate-driven oscillation of phosphorus and iron limitation in the North Pacific Subtropical Gyre. Proceedings of the National Academy of Sciences, 116(26), 12720-12728. https://doi.org/10.1073/pnas.1900789116

Li, Y., Song, Y., Yan, L., Chen, T., & An, Z. (2015). Timing and Spatial Distribution of Loess in Xinjiang, NW China. PLOS ONE, 10(5), e0125492. https://doi.org/10.1371/journal.pone.0125492

Li, Y., Song, Y., Chen, X., Li, J., Mamadjanov, Y., & Aminov, J. (2016). Geochemical composition of Tajikistan loess and its provenance implications. Palaeogeography, Palaeoclimatology, Palaeoecology, 446, 186–194. https://doi.org/10.1016/j.palaeo.2016.01.025

Li, Y., Song, Y., Fitzsimmons, K. E., Chen, X., Wang, Q., Sun, H., & Zhang, Z. (2018). New evidence for the provenance and formation of loess deposits in the Ili River Basin, Arid Central Asia. Aeolian Research, 35, 1–8. https://doi.org/10.1016/j.aeolia.2018.08.002

Li, Y., Song, Y., Kaskaoutis, D. G., Chen, X., Mamadjanov, Y., & Tan, L. (2019). Atmospheric dust dynamics in southern Central Asia: Implications for buildup of Tajikistan loess sediments. Atmospheric Research, 229, 74–85. https://doi.org/10.1016/j.atmosres.2019.06.013

Lisiecki, L. E., & Raymo, M. E. (2005). A Pliocene-Pleistocene stack of 57 globally distributed benthic δ18O records. Paleoceanography, 20(1). https://doi.org/10.1029/2004PA001071

Liu, T. S. (1985). Loess and Environment. China Ocean Press (Beijing).

Mcmorris, D. W. (1970). ESR Detection of Fossil Alpha Damage in Quartz. Nature, 226(5241), 146–148. https://doi.org/10.1038/226146b0

Nagashima, K., Tada, R., Tani, A., Toyoda, S., Sun, Y., & Isozaki, Y. (2007). Contribution of aeolian dust in Japan Sea sediments estimated from ESR signal intensity and crystallinity of quartz. Geochemistry, Geophysics, Geosystems, 8(2). https://doi.org/10.1029/2006GC001364

Nagashima, K., Tada, R., Tani, A., Sun, Y., Isozaki, Y., Toyoda, S., & Hasegawa, H. (2011). Millennial-scale oscillations of the westerly jet path during the last glacial period. Journal of Asian Earth Sciences, 40(6), 1214–1220. https://doi.org/10.1016/j.jseaes.2010.08.010

Nagashima, K., Tada, R., & Toyoda, S. (2013). Westerly jet-East Asian summer monsoon connection during the Holocene. Geochemistry, Geophysics, Geosystems, 14(12), 5041–5053. Scopus. https://doi.org/10.1002/2013GC004931

Nagashima, K., Nishido, H., Kayama, M., Kurosaki, Y., Ohgo, S., & Hasegawa, H. (2017). Composition of Asian dust from cathodoluminescence spectral analysis of single quartz grains. Geology, 45(10), 879–882. https://doi.org/10.1130/G39237.1

Nakai, S., Halliday, A. N., & Rea, D. K. (1993). Provenance of dust in the Pacific Ocean. Earth and Planetary Science Letters, 119(1), 143–157. https://doi.org/10.1016/0012-821X(93)90012-X

Nottebaum, V., Stauch, G., Hartmann, K., Zhang, J., & Lehmkuhl, F. (2015). Unmixed loess grain size populations along the northern Qilian Shan (China): Relationships between geomorphologic, sedimentologic and climatic controls. Quaternary International, 372, 151–166. Scopus. https://doi.org/10.1016/j.quaint.2014.12.071

Odom, A. L., & Rink, W. J. (1989). Natural accumulation of Schottky-Frenkel defects: Implications for a quartz geochronometer. Geology, 17(1), 55–58. https://doi.org/10.1130/0091-7613(1988)017<0055:NAOSFD>2.3.CO;2

Pullen, A., Kapp, P., McCallister, A. T., Chang, H., Gehrels, G. E., Garzione, C. N., Heermance, R. V., & Ding, L. (2011). Qaidam Basin and northern Tibetan Plateau as dust sources for the Chinese Loess Plateau and paleoclimatic implications. Geology, 39(11), 1031–1034. https://doi.org/10.1130/G32296.1

Rao, W., Tan, H., Chen, J., Ji, J., Chen, Y., Pan, Y., & Zhang, W. (2015). Nd–Sr isotope geochemistry of fine-grained sands in the basin-type deserts, West China: Implications for the source mechanism and atmospheric transport. Geomorphology, 246, 458–471. https://doi.org/10.1016/j.geomorph.2015.06.043

Rink, W. J., & Odom, A. L. (1991). Natural alpha recoil particle radiation and ionizing radiation sensitivities in quartz detected with EPR: Implications for geochronometry. International Journal of Radiation Applications and Instrumentation. Part D. Nuclear Tracks and Radiation Measurements, 18(1), 163–173. https://doi.org/10.1016/1359-0189(91)90108-T

Salh, R. (2011). Defect Related Luminescence in Silicon Dioxide Network: A Review. In S. Basu (Ed.), Crystalline Silicon—Properties and Uses. InTech. https://doi.org/10.5772/22607

Schaetzl, R. J., Bettis, E. A., Crouvi, O., Fitzsimmons, K. E., Grimley, D. A., Hambach, U., Lehmkuhl, F., Marković, S. B., Mason, J. A., Owczarek, P., Roberts, H. M., Rousseau, D.-D., Stevens, T., Vandenberghe, J., Zárate, M., Veres, D., Yang, S., Zech, M., Conroy, J. L., … Zech, R. (2018). Approaches and challenges to the study of loess—Introduction to the LoessFest Special Issue. Quaternary Research, 89(3), 563-618. doi:10.1017/qua.2018.15

Shimada, A., Takada, M., & Toyoda, S. (2013). Characteristics of ESR signals and TLCLs of quartz included in various source rocks and sediments in Japan: A clue to sediment provenance. Geochronometria, 40(4), 334–340. https://doi.org/10.2478/s13386-013-0111-z

Skuja, L., Ollier, N., & Kajihara, K. (2020). Luminescence of non-bridging oxygen hole centers as a marker of particle irradiation of α-quartz. Radiation Measurements, 135, 106373. https://doi.org/10.1016/j.radmeas.2020.106373

Stapelbroek, M., Griscom, D. L., Friebele, E. J., & Sigel, G. H. (1979). Oxygen-associated trapped-hole centers in high-purity fused silicas. Electronic Properties and Structure of Amorphous Solids, 32(1), 313–326. https://doi.org/10.1016/0022-3093(79)90079-6

Sun, J. (2002). Provenance of loess material and formation of loess deposits on the Chinese Loess Plateau. Earth and Planetary Science Letters, 203(3), 845–859. https://doi.org/10.1016/S0012-821X(02)00921-4

Sun, Y., Tada, R., Chen, J., Chen, H., Toyoda, S., Tani, A., Isozaki, Y., Nagashima, K., Hasegawa, H., & Ji, J. (2007). Distinguishing the sources of Asian dust based on electron spin resonance signal intensity and crystallinity of quartz. Atmospheric Environment, 41(38), 8537–8548. https://doi.org/10.1016/j.atmosenv.2007.07.014

Sun, Y., Tada, R., Chen, J., Liu, Q., Toyoda, S., Tani, A., Ji, J., & Isozaki, Y. (2008). Tracing the provenance of fine-grained dust deposited on the central Chinese Loess Plateau. Geophysical Research Letters, 35(1), L01804. https://doi.org/10.1029/2007GL031672

Sun, Y., Chen, H., Tada, R., Weiss, D., Lin, M., Toyoda, S., Yan, Y., & Isozaki, Y. (2013). ESR signal intensity and crystallinity of quartz from Gobi and sandy deserts in East Asia and implication for tracing Asian dust provenance. Geochemistry, Geophysics, Geosystems, 14(8), 2615–2627. https://doi.org/10.1002/ggge.20162

Svensson, A., Biscaye, P. E., & Grousset, F. E. (2000). Characterization of late glacial continental dust in the Greenland Ice Core Project ice core. Journal of Geophysical Research: Atmospheres, 105(D4), 4637–4656. https://doi.org/10.1029/1999JD901093

Toyoda, S., & Ikeya, M. (1991). Thermal stabilities of paramagnetic defect and impurity centers in quartz: Basis for ESR dating of thermal history. Geochemical Journal, 25(6), 437–445. https://doi.org/10.2343/geochemj.25.437

Toyoda, S., Ikeya, M., Morikawa, J., & Nagatomo, T. (1992). Enhancement of oxygen vacancies in quartz by natural external β and γ ray dose: A possible ESR Geochronometer of Ma-Ga range. Geochemical Journal, 26(3), 111–115. https://doi.org/10.2343/geochemj.26.111

Toyoda, S., & Hattori, W. (2000). Formation and decay of the E1′ center and of its precursor. Applied Radiation and Isotopes, 52(5), 1351–1356. https://doi.org/10.1016/S0969-8043(00)00094-4

Toyoda, S., Rink, W. J., Yonezawa, C., Matsue, H., & Kagami, T. (2001). In situ production of alpha particles and alpha recoil particles in quartz applied to ESR studies of oxygen vacancies. TL/ESR Special, 20(5), 1057–1061. https://doi.org/10.1016/S0277-3791(00)00018-4

Toyoda, S., Nagashima, K., & Yamamoto, Y. (2016). ESR signals in quartz: Applications to provenance research – A review. Quaternary International, 397, 258–266. https://doi.org/10.1016/j.quaint.2015.05.048

Tursungaziev, B. T., & Petrov, O. B. (Eds.), (2008). Geological Map of the Kyrgyz Republic, 1:500,000. Bishkek.

Újvári, G., Varga, A., & Balogh-Brunstad, Z. (2008). Origin, weathering, and geochemical composition of loess in southwestern Hungary. Quaternary Research, 69(3), 421–437. https://doi.org/10.1016/j.yqres.2008.02.001

Usami, T., Toyoda, S., Bahadur, H., Srivastava, A. K., & Nishido, H. (2009). Characterization of the E1′ center in quartz: Role of aluminum hole centers and oxygen vacancies. Physica B: Condensed Matter, 404(20), 3819–3823. https://doi.org/10.1016/j.physb.2009.07.075

Vandenberghe, J. (2013). Grain size of fine-grained windblown sediment: A powerful proxy for process identification. Earth-Science Reviews, 121, 18–30. https://doi.org/10.1016/j.earscirev.2013.03.001

Vlasov, N., Yu, G., Dyakov, A., and Cherev, E.S. (1991). Geological Map of the Tajik SSR and Adjacent Territories: Saint Petersburg, Russia, Vsesojuznoi Geologic Institute of Leningrad, scale 1:500,000.

Weeks, R. A. (1956). Paramagnetic Resonance of Lattice Defects in Irradiated Quartz. Journal of Applied Physics, 27(11), 1376–1381. https://doi.org/10.1063/1.1722267

Wei, C., Li, C., Liu, C., Li, W., Zhang, Z., Zhang, H., Zhao, J., & Zhang, L. (2017). Nature ESR signals of quartz E' center shed new light on river sediments provenance: A case study in southeast margin of the Tibet Plateau. Third Pole: The Last 20,000 Years - Part III, 454, 38–44. https://doi.org/10.1016/j.quaint.2017.08.044

Weil, J. A. (1984). A review of electron spin spectroscopy and its application to the study of paramagnetic defects in crystalline quartz. Physics and Chemistry of Minerals, 10(4), 149–165. https://doi.org/10.1007/BF00311472

Weltje, G. J., & von Eynatten, H. (2004). Quantitative provenance analysis of sediments: Review and outlook. Quantitative Provenance Analysis of Sediments, 171(1), 1–11. https://doi.org/10.1016/j.sedgeo.2004.05.007

Yang, J.-D., Chen, J., Tao, X.-C., Li, C.-L., Ji, J.-F., & Chen, Y. (2001). Sr isotope ratios of acid-leached loess residues from Luochuan, China: A tracer of continental weathering intensity over the past 2.5 Ma. Geochemical Journal, 35(6), 403–412. https://doi.org/10.2343/geochemj.35.403

5. Chapter 5

Variation in luminescence characteristics and paramagnetic defect centres in fine-grained quartz from a loess-palaeosol sequence in Tajikistan: Implications for provenance studies in aeolian environments

Aditi K. Dave[1], Alida Timar-Gabor[2,3], Giancarlo Scardia[4], Nosir Safaraliev[5], Kathryn E. Fitzsimmons[1]

[1]Research Group for Terrestrial Palaeoclimates, Max Planck Institute for Chemistry, Hahn-Meitner-Weg 1, 55128 Mainz, Germany
[2]Faculty of Environmental Sciences and Engineering, Babes Bolyai University, Cluj-Napoca, Romania
[3]Interdisciplinary Research Institute on Bionanoscience, Babes Bolyai University, Cluj-Napoca, Romania
[4]Instituto de Geociências e Ciências Exatas, Universidade Estadual Paulista, 13506-900 Rio Claro, SP, Brazil
[5]Tajik National University, 17 Rudaki Avenue, Dushanbe 734025, Tajikistan

Status:

In preparation

Keywords: Loess, Provenance, Luminescence sensitivity, ESR centres, Tajikistan, Central Asia

Abstract

Trapped charge characteristics in quartz are of increasing interest for their utility as indicators of sediment provenance. These include sensitivity of Optically stimulated luminescence (OSL) and Thermoluminescence (TL) signal and paramagnetic E' defect centres in quartz. Up until now, these methods have largely been used independently in provenance investigations, especially in aeolian systems. Variations in quartz OSL and TL signal sensitivity in loess-palaeosol sequences has been linked to shifts in sediment source corresponding to climatic fluctuations. However, the processes responsible for observed OSL and TL sensitivity variation in quartz, including its link to the original rock source and/or its sedimentary history, remains a topic of contention. On the other hand, the intensity of E' defect centre in quartz is known to reflect the provenance of quartz, and is also routinely utilised as a provenance indicator in aeolian studies. In this study we aim to understand the variations in E' intensity and OSL/TL sensitivity by direct comparison of these characteristics in fine-grained quartz from a c. 60 m thick loess-paleosol sequence in Tajikistan. In doing so, we investigate the natural processes that may have led to variability in trapped-charge characteristics over the c. 500 ky timespan covered by the sequence.

5.1. Introduction

Deposits of aeolian dust, or loess, have long been recognised as excellent terrestrial archives of past environmental change (Liu, 1985; Kukla et al., 1988; Schaetzl et al., 2018). These deposits form stacked sequences of primary loess and buried soils – commonly known as loess-palaeosol sequences - that are largely hypothesised to reflect colder, drier, more windy phases, and more humid, warmer, less windy periods respectively (Marković et al., 2015). Whilst evidence of *in situ* past climatic conditions can be extracted from the physical and chemical characteristics of loess sediments (e.g. Fitzsimmons et al., 2012 and references therein), identifying the source of loess – its provenance – is equally valuable for elucidating dust transport pathways, so providing insights into past wind dynamics and atmospheric circulation in a region (Ding et al., 2000; Muhs et al., 2008). A number of provenance techniques have been applied to distinguish source change in loess, including isotopic (Smith et al., 2003; Rao et al., 2006; Miyazaki et al., 2016) and geochemical (Sun, 2002; Buggle et al., 2008; Újvári et al., 2008) approaches. However, these methods are derived from bulk sample, which can lead to indeterminate results (Újvári et al., 2012). The limitations of radiogenic and elemental approaches in loess provenance studies have led to an increased interest in targeting specific minerals, such as zircon (Stevens et al., 2010; Fenn et al., 2018) and quartz (Nagashima et al., 2007, 2017; Sun et al., 2008). Provenance techniques based on detrital zircon U-Pb ages in loess are, however, often limited by very low concentrations of zircon grains (Fenn et al., 2018). By contrast, quartz is ubiquitous, and its resistance to chemical weathering provides an excellent material for provenance analysis in loess sediments.

In recent years there has been an increased focus on exploring lattice defects and impurities in quartz as potential indicators of sedimentary history and transport processes (Preusser et al., 2006; Pietsch et al., 2008; Fitzsimmons, 2011; Sawakuchi et al., 2012; Gliganic et al., 2017) and provenance (Nagashima et al., 2007; 2017; Toyoda et al., 2016; Sawakuchi et al., 2018). A range of characteristics are exploited for this purpose. These include various components of the optically stimulated luminescence (OSL) and thermoluminescence (TL) signals (Tsukamoto et al., 2011; Jeong and Choi, 2012), including its sensitivity characteristics (Zheng et al., 2009; Lü and Sun, 2011; Sawakuchi et al., 2012, 2018; Zular et al., 2015; Li and Zhou, 2020), or specific intrinsic or impurity-related defect centres in quartz such as E', Al-hole and Ti-Li centres using electron spin resonance (ESR; Nagashima et al., 2007; Sun et al., 2007, 2008; Shimada et al., 2013; Tissoux et al., 2015; Wei et al., 2020; Wang et al., 2020).

Luminescence sensitivity is conventionally defined as the luminescence emitted per unit dose per unit mass of the sample, and is an intrinsic property of the quartz crystal. Sensitivity has the advantage of being rapidly measured using luminescence dating readers, facilities which are increasingly widely available. Luminescence sensitivity of quartz is linked to (i) the thermal history of the quartz-bearing source rocks, which forms the basis of its use as a provenance indicator (Fitzsimmons, 2011; Sawakuchi et al., 2011); and (ii) the sedimentary

history of the grain, whereby quartz is sensitised by repeated processes of erosion, transport, storage and burial (Pietsch et al., 2008; Fitzsimmons et al., 2010). As such, the technique shows promise for application in long profiles of aeolian loess. Recent investigations of quartz OSL and TL sensitivity down two loess profiles in Tajikistan (Li and Zhou, 2020), as well as loess sequences from the Chinese loess plateau (CLP; Lü et al., 2014, 2021) yielded distinctions in the sensitivity of quartz between loess and palaeosol units. The variability observed within individual profiles has been interpreted to relate to the impact of climatic fluctuations on geomorphic processes, such as the contraction and expansion of nearby deserts leading to sensitivity change related to transport distance from the source (deserts) to the sink (loess) (Lü et al., 2014, 2021); increased glacial erosion in mountain regions during cold phases leading to increased production of low sensitivity quartz (Lü et al., 2014); and preferential weathering of certain rock types in response to long-term climate fluctuations which lead to availability of quartz of different origin for loess deposition (Li and Zhou, 2020).

One of the most commonly used ESR-based quartz provenance technique utilises the heat-treated E' centre (or HT-E'; Toyoda et al., 2016 and references therein), which refers to the total concentration of E' centres measured after γ-irradiation and thermal treatment. This technique is based on the premise that HT-E' reflects the total number of oxygen vacancies (*Si=Si*, Feigl et al., 1974) and increases with rock age, a quantity which is characteristic of the source rock (Toyoda and Hattori, 2000; Toyoda et al., 2016). In combination with the crystallinity index of quartz (Nagashima et al., 2007; Toyoda et al., 2016), the HT-E' signature has been applied to distinguish between quartz from different inland Asian desert sources (Sun et al., 2007; 2008) and ocean sediment cores (Nagashima et al., 2011; Wang et al., 2020). We recently proposed a simplified provenance technique based on natural (not heat-treated) E' and peroxy centre intensity in sedimentary quartz (Dave et al., submitted; hereon referred to as Chapter 4), also assumed to increase with the age of the rock (Odom and Rink, 1989). In that study we successfully differentiated loess deposits from two different basins in Central Asia, as well as identified temporal variations in provenance in response to climatic variations at a long loess sequence (Karamaidan: KAR) in Tajikistan.

Luminescence sensitivity and ESR-based quartz-defect approaches relate to different intrinsic processes within the crystal lattice. While sensitivity arises from luminescence emitted as a result of the recombination process (when an electron recombines with a hole, Aitken, 1998; Yukihara and McKeever, 2011), ESR measures the concentration of defect centres that may arise as a result of dislocation, irradiation and/or substitution effects in a quartz crystal lattice (Ikeya, 1993). Both methods can nevertheless be used to infer sediment provenance. Here we compare luminescence sensitivity and natural E' and peroxy defect centres in quartz directly in order to independently assess changes in provenance down the KAR loess sequence in Tajikistan, Central Asia. This allows us to not only independently assess the two techniques as provenance indicators, but also to integrate our insights from these methods to better understand loess source variability and depositional dynamics in piedmont regions.

5.2. Material and Methods

5.2.1. Site setting and sampling

The site of Karamaidan (KAR; 38° 34’ 33.47’’ N, 69° 16’ 40.79’’ E, 1629 m a.s.l.) lies in the foothills of the Gissar Range, on the northern margins of the Afghan-Tajik depression (Fig. 5.1) and 45 km east of Dushanbe, the capital city of Tajikistan. The Afghan-Tajik depression is a seismically active sedimentary basin, the northern part of which is interrupted by a series of north-south oriented folds and ridges (McNab et al., 2019) that are traversed by a number of rivers arising from the glaciated Alai, Trans-Alai and Pamir ranges. These drainage systems are tributaries to the Amu Darya River and provide vast glacio-/fluvial outwash and alluvial plains that act as dust source regions (Li et al., 2019). The KAR site is situated between two such rivers, the *Kofarnihon* to the north and the *Vakhsh* to the south. The piedmont of the Gissar Range therefore provides an optimal setting for dust trapping and deposition. The Karakum and Kzylkum deserts located to the west and northwest act as additional dust sources for the Afghan-Tajik depression (Li et al., 2019). Given this setting, the margins of the depression preserve some of the thickest loess deposits in Eurasia, several of which represent quasi-continuous deposition over the last million years (Forster and Heller, 1994; Dodonov and Baiguzina, 1995; Ding et al., 2002). The loess deposits at KAR provide one such record, known to preserve a record of climate change over the past 1 Ma (Forster and Heller, 1994).

KAR provides us with an ideal test site to investigate long term variations in dust source and their relationship to changing climatic conditions. The KAR profile represents a >100 m thick package of alternating primary loess and buried soils (Forster and Heller, 1994) exposed as a result of a recent landslide following seismic activity. In this study we investigate a c. 56 m package from the lower part of the KAR section, comprising six loess and five palaeosol units, with three additional weak to moderately developed soils observed within the loess units (Fig. 5.2). Sediments from the base of the section record the Brunhes-Matuyama magnetic reversal, and therefore the section is inferred to span > 800 ka (Forster and Heller, 1994). The relative chronology of the c. 56 m subsection sampled for this study has been previously described in Chapter 4 and is interpreted to span marine isotope stages (MIS) 9-19, based on the correlation of in-situ magnetic susceptibility measurements with the global marine isotope stack (Lisiecki and Raymo, 2005; Fig. 5.2). A description of the stratigraphy of the subsection, magnetic susceptibility measurements and relative chronology can be found in the supplementary information (SI) in appendix C.

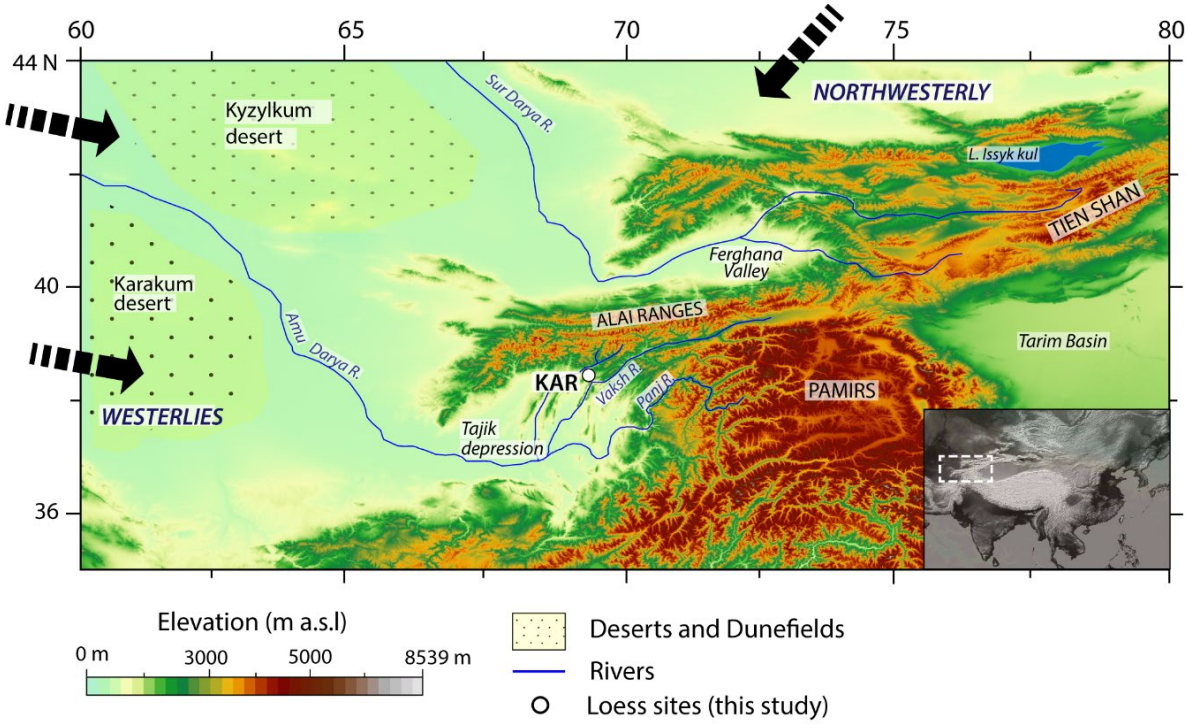

Fig. 5.1. (a) Regional setting and location of study site KAR within western Central Asia.

Sampling at KAR was carried out by abseil down the exposed vertical cliff to ensure continuous down-profile observations and sampling. Prior to sampling, we cleaned back more than 1 horizontal metre of sediment from the cliff face to prevent contamination by recent displacement and to expose undisturbed stratigraphy. We collected a total of 55 samples every 0.5 to 1 m by hammering opaque steel tubes into the cleaned and exposed vertical section.

5.2.2. Luminescence measurements

We processed our samples under subdued red-light conditions in dedicated laboratories at the Johannes Gutenberg University and Max Planck Institute for Chemistry in Mainz to extract fine grain (4-11um) quartz and polymineral grains using published procedures (Frechen et al., 1996) outlined in the SI (appendix C)

We conducted luminescence sensitivity measurements on 55 fine-grained quartz and polymineral samples at the Max Planck Institute for Chemistry, using an automated Riso TL-DA-20 reader equipped with a $^{90}Sr/^{90}Y$ beta source calibrated to a dose rate of 0.095±0.02 Gy/s. Samples were stimulated using blue LEDs (470±30 nm, 80 mW/cm^2) and IR (870 ± 30 nm, 300 mW/cm^2), and the emitted luminescence signal was detected by an EMI 9235QA photomultiplier tube fitted with a 7.5 mm Hoya U-340, and a combination of Schott BG-39 and BG-3 filters, to detect quartz and feldspar emissions respectively. We prepared 6-8

aliquots per sample for measurement by pipetting the fine-grained sample (quartz or polymineral), suspended in acetone, onto stainless steel discs. All measurements were performed with an applied beta dose of 47.5 Gy; the mass of each aliquot was measured before and after mounting the sample using a Mettler balance with a precison of 0.001 mg. Since luminescence sensitivity entails the measurement of the luminescence emitted (counts, cts) per unit dose (Gy) per unit mass (mg), the luminescence measurements from all aliquots were normalized to the applied beta dose and the corresponding aliquot mass. The sensitivity is expressed as cts/Gy/mg and uncertainties as 1σ.

The protocols for measurement of fine-grained quartz OSL and TL sensitivity (modified after Sawakuchi et al., 2018 and Li and Zhou, 2020), and the Infrared stimulated luminescence (IRSL) and post Infrared-optically stimulated luminescence (pIR-OSL) of polymineral grains (after Sawakuchi et al., 2018) are outlined in Table 5.1. A detailed description can be found in the SI in appendix C. TL sensitivity was measured by integrating the TL signal from 60°C to 120 °C. The OSL sensitivity was calculated from the integral of the first 0.8 s of the OSL signal, from which the average integral of the last 10 s of OSL signal was subtracted. The IRSL signals from the feldspar component of the polymineral aliquots were evaluated from the integral of the the first 3.6 s, from which the average integral of the last 10 s of OSL signal was subtracted. The pIR-OSL signal from the quartz component of the polymineral aliquots was calculated from the initial 0.8s following subtraction of the average from the last 10 s.

Table 5.1. Protocol for luminescence sensitivity measurements from fine-grained quartz and polymineral samples (modified after Sawakuchi et al., 2018; Li and Zhou, 2020).

Step	Protocol for quartz
1	OSL 125°C, Blue LED 100s @5°C/s
2	β dose= 47.5 Gy
3	TL 240°C, 10s
4	IRSL 50°C, 50s
5	OSL 125°C, Blue LEDs for 100s

Step	Protocol for polyminerals
1	OSL 125°C for 100s @5°C/s
2	β irradiation, given dose= 47.5 Gy
3	Preheat at 240°C for 10s
4	IRSL at 60°C for 300s
5	OSL (Blue LED) at 125°C for 100s
6	OSL (Blue LED) at 125°C for 100s

5.2.3. Electron spin resonance measurements

ESR allows the measurement of paramagnetic (containing an unpaired electron) species in a material. In this study we focus on the natural intensity of two paramagnetic defect centres

in fine-grained quartz from KAR: the E' centre (an unpaired electron occupying an oxygen vacancy; Feigl et al., 1974) and the peroxy centre. The measurement of these centres was previously reported in Chapter 4 and a summarised account of sample measurement procedures and parameters is presented in the SI (appendix C). ESR measurements were carried out using an X-band Brucker EMX Plus Spectrometer at Babes Bolyai University in Cluj-Napoca, Romania.

5.3. Results

Figure 5.2 illustrates the down-profile variations in luminescence sensitivity of the OSL and TL signal and E' defect centre intensity of fine-grained quartz, and the pIR-OSL signal sensitivity and the ratio of [IRSL]/[pIR-OSL] from polymineral fine grains. We observe that the quartz luminescence sensitivity of the 110^{o}C TL and OSL signals is higher in the palaeosol horizons compared to primary loess units, and correlate with the variability in magnetic susceptibility. The clear distinction in luminescence sensitivity between loess and soil horizons can also be observed in the cross plot shown in Fig. 5.3a. The luminescence sensitivity of the pIR-OSL signal from the quartz component of the polymineral fraction exhibits the same trend as that obtained from the OSL signal of pure quartz (Fig. 5.2).

The ratio of [IRSL]/[pIR-OSL] in polymineral grains has been proposed as a proxy for the relative enrichment of quartz within the sediment and was used to indicate the weathering intensity in a loess-palaeosol sequences in the CLP (Wang and Miao, 2006). Down-profile variability in the ratio of [IRSL]/[pIR-OSL] from fine-grained polymineral aliquots at KAR shows a decrease within paleosol horizons and an increase in loess horizons (Fig. 5.2). This result indicates an enhanced quartz content in the paleosols due to weathering of feldspar minerals within these units. We also note a decrease in feldspar content within the soil units in the down-profile luminescence sensitivity variations of the polymineral IRSL signal (Fig. C1, refer SI in appendix C). The difference in relative quartz enrichment between soil and loess units can also be seen in Fig. 5.3b. The ratio of [IRSL]/[pIR-OSL] is also able to distinguish between the weakly developed soil units (c. 25.4-25.7m, c. 55-59 and c.68-69 depth) and highly weathered, slightly clayey loess (c. 45 m), which was not observed in our magnetic susceptibility measurements (Fig. 5.2).

Down-profile variations in the intensity of the natural E' signal of fine-grained quartz indicate lower intensity in the soil units and higher values in the loess horizons (Fig. 5.2). These changes are more pronounced above c. 60 m depth. Below c. 60 m, the natural E' intensity is generally lower but fluctuates at a higher frequency. These changes are inconsistent with the observed stratigraphy (Fig. 5.2). The variation in peroxy intensity of fine-grained quartz with

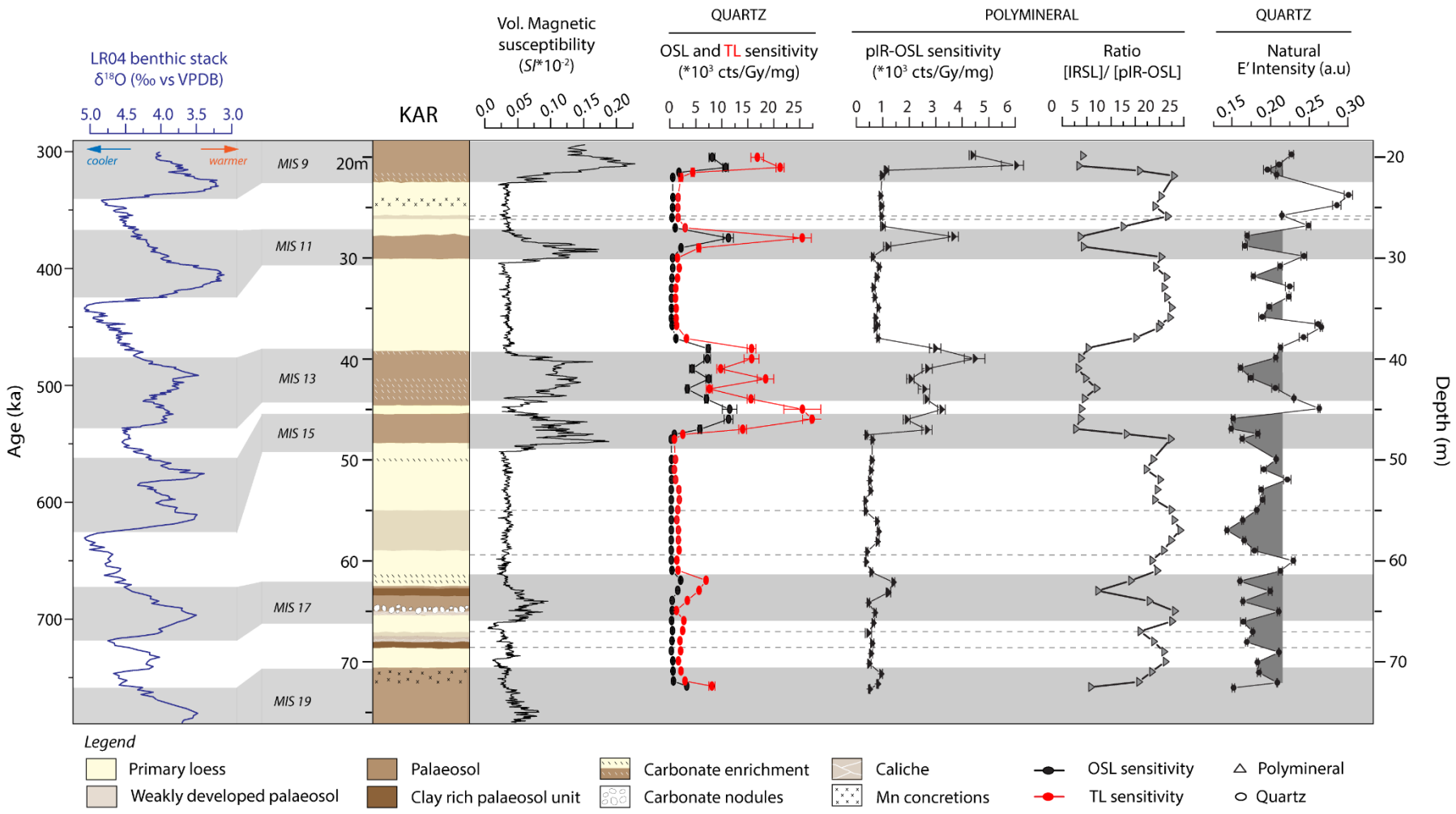

Fig. 5.2. Down-profile variations in magnetic susceptibility, OSL and TL signal sensitivity from quartz, sensitivity of the pIR-OSL signal in polyminerals, ratio of [IRSL]/[pIR-OSL] signal from the polymineral samples, and natural E' intensity for the KAR loess sequence. Stratigraphy of KAR and its correlation to the global benthic curve (Lisiecki and Raymo, 2005) is based on in-situ magnetic susceptibility measurements at the site (modified after Chapter 4).

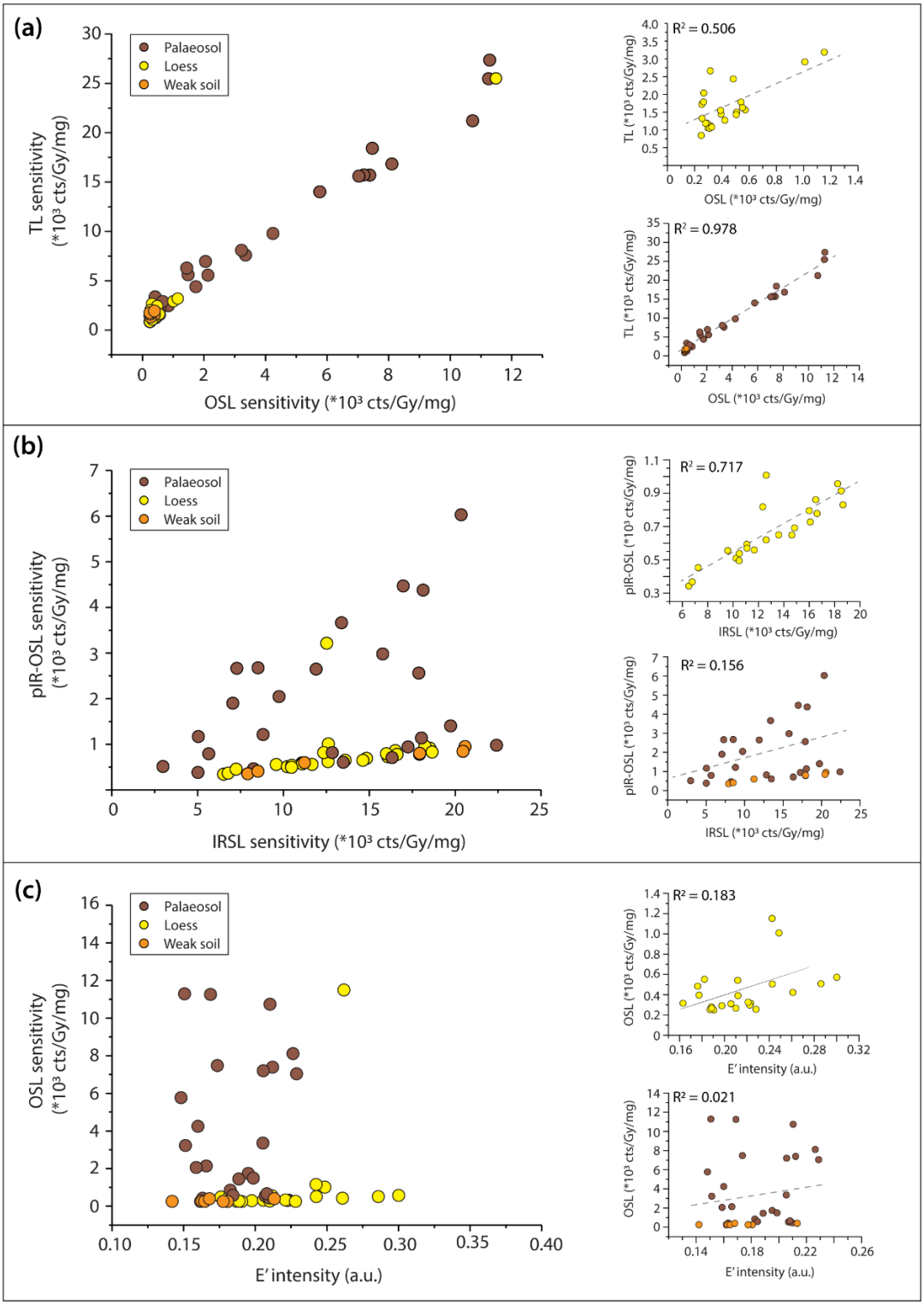

Fig. 5.3. (a) Plot comparing the sensitivity of OSL and 110°C TL signal from fine-grained quartz with respect to unit type; (b) plot comparing the sensitivity of pIR-OSL and IRSL signals from polymineral fine grains with respect to stratigraphic unit type; (c) Plot comparing E' intensity and sensitivity of the OSL signal from fine-grained quartz with respect to stratigraphy. Note: The anomalous value of the loess sample (A0302), that occurs as an 'outlier' in the above plots (as it exhibits sensitivity characteristics similar to that seen in soil units) is not plotted during individual comparisons of loess and soil units.

depth correlates with the variations in natural E' values (Fig. C2, appendix C). The plot of natural E' vs. peroxy also highlights the difference between loess and soil units (Fig. 5.4a, after Chapter 4). Comparison of natural E'-peroxy intensity with luminescence sensitivity of the OSL and TL signal from quartz, in general, shows inverse trends between loess and soil units (Fig. 5.2 and Fig. 5.4). E' and peroxy intensity is lower in the soil horizons whereas both OSL and TL signal intensity is distinctly higher, and vice versa for the loess horizons. Although the trends in natural E' and luminescence sensitivity appear to be anticorrelated (see Fig. 5.2 and Fig. 5.4), the relationship between the natural E' signature and the OSL sensitivity of quartz remains inconclusive. Independent comparison between the E' and OSL sensitivity in soil and loess units yields no correlation or a low positive correlation respectively (Fig. 5.3c). This inconsistency is likely to result from fluctuation of the natural E' values at a higher frequency with depth, particularly within the loess units (Fig. 5.2) whereas luminescence sensitivity varies very little within a given loess horizon.

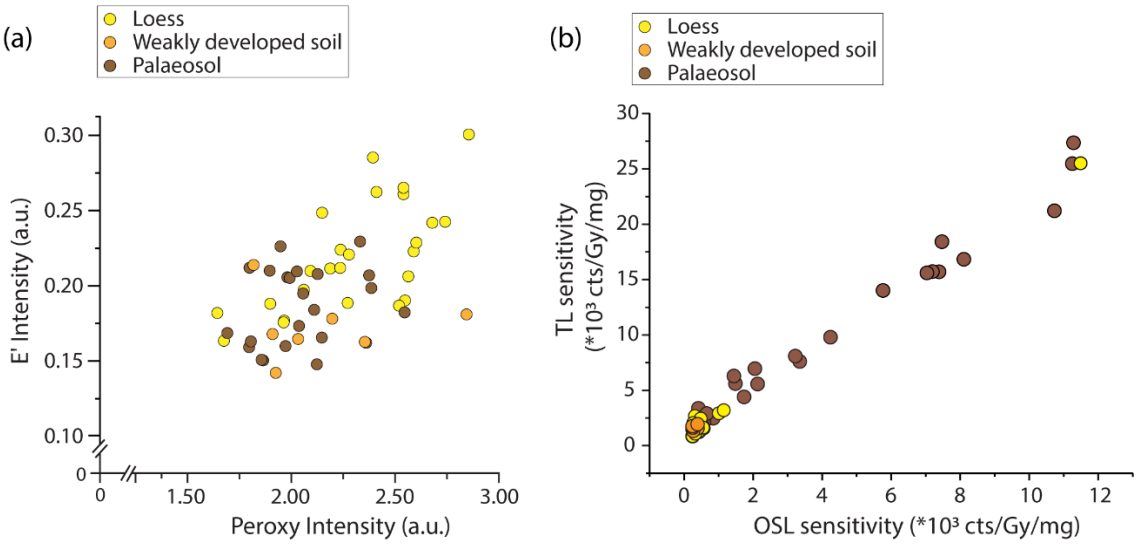

Fig. 5.4. Variation in (a) natural E' and peroxy defect centres and (b) sensitivity of OSL and TL signals in fine grain quartz with respect to stratigraphic unit type.

5.4. Discussion

The aim of sediment provenance analysis is ultimately to identify the parent rock from which sediments are derived. However, the process of sediment cycling is complicated by multiple factors that affect the fate of the material from source to sink (Weltje and von Eynatten, 2004; Allen, 2008). With this in mind, one of the first considerations for the application of a provenance technique should lie in its sensitivity to detect changes in sediment composition, and therefore source, at a site. Here we compared two different approaches based on

trapped charge within fine-grained aeolian quartz which appear to reflect different aspects of the sediment cycling process. The natural E' signal from quartz measures a single defect type and largely reflects the signature of the host rock (through its age: Wei et al., 2020; Chapter 4). By contrast, the OSL and TL signals are more complex and may reflect either the signature of the parent rock (through its thermal history: Fitzsimmons, 2011; Sawakuchi et al., 2011; 2018), and/or its sedimentary and transport history (Pietsch et al., 2008; Fitzsimmons et al., 2010). Consequently, at any given point in a sedimentary setting, the quartz OSL and TL luminescence sensitivity may be recording the influence of both, and the degree of influence of each is decided by whichever is the dominating factor at that time (Fitzsimmons, 2011; Sawakuchi et al., 2011; Lü and Sun, 2011). Recent studies based on multi-spectroscopic techniques (Sharma et al., 2017), as well as laboratory-based experiments on repeated irradiation and bleaching of natural quartz (Li and Zhou, 2020; Bartyik et al., 2021) show that it exhibits preferential sensitisation, the magnitude of which may vary depending on the quartz source. Thus, a combined approach based on measurement of both the natural E' intensity and luminescence sensitivity of the OSL and TL signals may allow us not only to understand the influence of natural factors on luminescence sensitivity, but also gain an insight into depositional processes in sedimentary environments such as loess deposits.

Climate modelling studies and down-profile grain size variations in loess-palaeosol sequences in southern Tajikistan suggest stronger Westerly winds during glacial periods as compared to interglacials; thereby indicating dust transport from distal sources during glacial periods (Vandenberghe et al., 2006). Based on these studies, we suggest that the low natural E' intensities observed at KAR in the warmer, more humid soil units (interglacial conditions) is linked to proximal source signature. There are also phases within loess accumulating glacial stages, particularly during interstadial periods which oversaw weak pedogenesis, when E' intensity values were also low and which likewise indicate a net input of proximal source material (Fig. 5.2). At the same time, throughout the KAR profile, natural E' intensities, while variable, are relatively low, which suggests that proximal source sediments dominate the net background sediment contribution to the site throughout its depositional history. This observation is in tune with recent observations made by Li et al (2019) that propose an increased likelihood of proximally sourced dust in loess deposits in the Tajik basin based on elemental geochemistry data from loess and modern meteorological analysis. Nevertheless, during glacial phases there is a stronger shift towards quartz with higher E' intensities (Fig. 5.2), particularly above c. 60m depth. Below this depth the distinction between primary loess and paleosols based on E' intensity is less pronounced. This is most likely due to the presence of multiple paleosol horizons, low sedimentation rates, and compaction of the sediment which may have contributed to over-printing of the quartz E' signature. Furthermore, the c. 60 m depth marker at KAR coincides with the end of the mid-Pleistocene transition (MPT; Clark et al., 2006), after which the Earth's climate shifted to lower frequency (c. 100 kyr), higher amplitude glacial-interglacial cycles. The MPT transition has been observed to

manifest in other loess regions as more distinct loess-paleosol oscillations with higher sedimentation rates (e.g. Fitzsimmons et al., 2012, Marković et al 2015), which may explain the more distinct high E' intensity values within the glacial loess above c. 60 m at KAR.

The natural E' intensity values from fine grained quartz adds nuance to, and raises questions about, the interpretation derived from the OSL and TL sensitivity record at KAR. Within the primary loess and weak paleosol sediments accreted during the glacial periods, OSL and TL sensitivity remains consistently low in relation to quartz from the more strongly developed interglacial paleosols which record high sensitivity values. These consistent oscillations in luminescence sensitivity deviate from the more variable E' signatures described above. The net background input of proximally sourced material to the site, proposed based on our E' results, accounts for the comparatively constant sensitivity of the quartz OSL and TL signal observed in the loess units at KAR. However, it is unclear how one can account for source shifts during glacial periods – as observed by variations in the E' signal - when the OSL and TL sensitivity shows minimal variation.

We hypothesise that the net OSL and TL sensitivity remains unaffected by the source shifts recorded in the E' signature. We suggest that this is because E' is a more sensitive proxy which measures a specific defect centre in quartz, whereas luminescence sensitivity is emitted from multiple traps as a result of recombination of electron and hole centres (Aitken, 1998; Yukihara and McKeever, 2011). As a result, the proximal signal dominates the OSL and TL sensitivity values and masks more subtle source changes.

It is likewise unclear what caused the increase in OSL and TL sensitivity observed during the accretion and formation of interglacial paleosols. We propose this to be due to repeated bleaching and irradiation associated with extended periods of pedogenesis, aided by reduced sedimentation rates. This would also explain the high degree of scatter observed in quartz OSL and TL sensitivity within the paleosol horizons as compared to primary loess (Fig. 5.3a). Our premise is also supported by recent study from Li and Zhou (2020), who observed a three-fold increase in OSL sensitivity of fine grain quartz from Tajik loess, after repeated laboratory induced irradiation and bleaching cycles. In addition, many other studies based on laboratory irradiation and bleaching of natural quartz from different regions also show sensitisation of quartz (Moska and Murray, 2006; Pietsch et al., 2008). Although preliminary, a support for our hypothesis can be found in the natural E' and peroxy, and luminescence characteristics of loessic quartz from weakly developed soil horizons, as discussed in the supplementary information (appendix C)

In general, the down-profile variations in quartz E' and peroxy intensity variations are anti-correlated to the OSL and TL sensitivity at KAR (Fig. 5.4). However, independent analysis of samples from loess and soil units yields inconclusive results. We observe a weak positive correlation for loess samples, while samples from the paleosol horizons do not exhibit any

correlation (Fig. 5.3c). At the same time, in a previous study, Tsukamoto et al (2011) observed a weak positive correlation between HT-E' intensity and the ratio of the fast to the sum of fast and medium component of OSL signal from quartz derived from ocean sediment. Therefore, the relationship between E' and OSL sensitivity, offers potential for future provenance studies, but needs further investigation.

5.5. Conclusion

This study utilises the natural E' and peroxy characteristics of quartz as a provenance indicator to investigate the observed variations in luminescence (OSL and TL) sensitivity down a long loess-palaeosol sequence in Tajikistan. Previous studies link down-profile variations in luminescence sensitivity with climatic fluctuations that occur over glacial-interglacial timescales (Lü et al., 2014, 2021; Li and Zhou, 2020). However, the cause for the observed sensitivity in quartz is debated (Lü et al., 2014, 2021; Li and Zhou, 2020). Our results suggest that the high OSL and TL sensitivity of quartz in the buried soil (palaeosol) horizon is likely to reflect sensitisation of quartz due to repeated irradiation and bleaching cycles during pedogenesis. At the same time, sensitivity variations that may have otherwise occurred due to changes in sediment source during glacial periods as indicated by natural E' intensity of quartz, are likely to be masked by the dominant input of proximally derived material. Nevertheless, the OSL and TL sensitivity of quartz from aeolian environments holds great potential for identifying spatial variability in luminescence characteristics between sites (Lü et al., 2021).

Acknowledgements

AKD would like to thank the Luminescence Laboratory at the Max Planck Institute for Evolutionary Anthropology, Leipzig, Germany for access to the HF etching laboratory, and R Schiebel at the Max Planck Institute for Chemistry (MPIC) for access to a high precision balance. We also thank the following colleagues for their assistance during fieldwork: S Yusupov, A Safarov, ZN Nadjmudinov and RS Pavlatov (Tajik National University); C Prud'homme, A Engström Johansson, L Marquer, Z Perić, S de Graaf, M Notwatzki and K Reetz (MPIC).

References

Aitken, M.J., 1998. An introduction to Optical dating: The dating of quaternary sediments by the use of photon-stimulated luminescence. Oxford University Press, Oxford.

Allen, P. A. (2008). From landscapes into geological history. Nature, 451(7176), 274–276. https://doi.org/10.1038/nature06586

Bartyik, T., Magyar, G., Filyó, D., Tóth, O., Blanka-Végi, V., Kiss, T., Marković, S., Persoiu, I., Gavrilov, M., Mezősi, G., & Sipos, G. (2021). Spatial differences in the luminescence sensitivity of quartz extracted from Carpathian
Basin fluvial sediments. Quaternary Geochronology, 64, 101166. https://doi.org/10.1016/j.quageo.2021.101166

Buggle, B., Glaser, B., Zöller, L., Hambach, U., Marković, S., Glaser, I., & Gerasimenko, N. (2008). Geochemical characterization and origin of Southeastern and Eastern European loesses (Serbia, Romania, Ukraine).
Quaternary Science Reviews, 27(9), 1058–1075. https://doi.org/10.1016/j.quascirev.2008.01.018

Ding, Z. L., Rutter, N. W., Sun, J. M., Yang, S. L., & Liu, T. S. (2000). Re-arrangement of atmospheric circulation at about 2.6Ma over northern China: Evidence from grain size records of loess-palaeosol and red clay sequences. Quaternary Science Reviews, 19(6), 547–558. https://doi.org/10.1016/S0277-3791(99)00017-7

Ding, Z. L., Derbyshire, E., Yang, S. L., Yu, Z. W., Xiong, S. F., & Liu, T. S. (2002). Stacked 2.6-Ma grain size record from the Chinese loess based on five sections and correlation with the deep-sea δ18O record. Paleoceanography, 17(3), 5-1-5–21. https://doi.org/10.1029/2001PA000725

Dodonov, A. E., & Baiguzina, L. L. (1995). Loess stratigraphy of Central Asia: Palaeoclimatic and palaeoenvironmental aspects. Aeolian Sediments in the Quaternary Record, 14(7), 707–720. https://doi.org/10.1016/0277-3791(95)00054-2

Feigl, F. J., Fowler, W. B., & Yip, K. L. (1974). Oxygen vacancy model for the E1′ center in SiO2. Solid State Communications, 14(3), 225–229. https://doi.org/10.1016/0038-1098(74)90840-0

Fenn, K., Stevens, T., Bird, A., Limonta, M., Rittner, M., Vermeesch, P., Andò, S., Garzanti, E., Lu, H., Zhang, H., & Lin, Z. (2018). Insights into the provenance of the Chinese Loess Plateau from joint zircon U-Pb and garnet geochemical analysis of last glacial loess. Quaternary Research, 89(3), 645–659. https://doi.org/10.1017/qua.2017.86

Fitzsimmons, K. E., Rhodes, E. J., & Barrows, T. T. (2010). OSL dating of southeast Australian quartz: A preliminary assessment of luminescence characteristics and behaviour. Quaternary Geochronology, 5(2), 91–95. https://doi.org/10.1016/j.quageo.2009.02.009

Fitzsimmons, K. (2011). An assessment of the luminescence sensitivity of Australian quartz with respect to sediment history. Geochronometria, 38(3), 199–208. https://doi.org/10.2478/s13386-011-0030-9

Fitzsimmons, K. E., Marković, S. B., & Hambach, U. (2012). Pleistocene environmental dynamics recorded in the loess of the middle and lower Danube basin. Quaternary Science Reviews, 41, 104–118. https://doi.org/10.1016/j.quascirev.2012.03.002

Forster, Th., & Heller, F. (1994). Loess deposits from the Tajik depression (Central Asia): Magnetic properties and paleoclimate. Earth and Planetary Science Letters, 128(3–4), 501–512. https://doi.org/10.1016/0012-821X(94)90166-X

Frechen, M., Schweitzer, U., & Zander, A. (1996). Improvements in sample preparation for the fine grain technique. Ancient TL, 14(2), 15–17.

Gliganic, L. A., Cohen, T. J., Meyer, M., & Molenaar, A. (2017). Variations in luminescence properties of quartz and feldspar from modern fluvial sediments in three rivers. Quaternary Geochronology, 41, 70–82. https://doi.org/10.1016/j.quageo.2017.06.005

Ikeya, M. (1993). New Applications of Electron Spin Resonance: Dating, Dosimetry and Microscopy. World Scientific. https://doi.org/10.1142/1854

Jeong, G. Y., & Choi, J.-H. (2012). Variations in quartz OSL components with lithology, weathering and transportation. Quaternary Geochronology, 10, 320–326. https://doi.org/10.1016/j.quageo.2012.02.023

Kukla, G., Heller, F., Ming, L. X., Chun, X. T., Sheng, L. T., & Sheng, A. Z. (1988). Pleistocene climates in China dated by magnetic susceptibility. Geology, 16(9), 811–814. https://doi.org/10.1130/0091-7613(1988)016<0811:PCICDB>2.3.CO;2

Li, Y., Song, Y., Kaskaoutis, D. G., Chen, X., Mamadjanov, Y., & Tan, L. (2019). Atmospheric dust dynamics in southern Central Asia: Implications for buildup of Tajikistan loess sediments. Atmospheric Research, 229, 74–85. https://doi.org/10.1016/j.atmosres.2019.06.013

Li, Y., & Zhou, L. (2020). Variations of thermally and optically stimulated luminescence sensitivity of loess and pedocomplex samples from southern Tajikistan, Central Asia. Geochronometria, 0(0), 000010151520150118. https://doi.org/10.1515/geochr-2015-0118

Lisiecki, L. E., & Raymo, M. E. (2005). A Pliocene-Pleistocene stack of 57 globally distributed benthic δ18O records. Paleoceanography, 20(1). https://doi.org/10.1029/2004PA001071

Liu, T. S. (1985). Loess and Environment. China Ocean Press (Beijing).

Lü, T., & Sun, J. (2011). Luminescence sensitivities of quartz grains from eolian deposits in northern China and their implications for provenance. Quaternary Research, 76(2), 181–189. https://doi.org/10.1016/j.yqres.2011.06.015

Lü, T., Sun, J., Li, S.-H., Gong, Z., & Xue, L. (2014). Vertical variations of luminescence sensitivity of quartz grains from loess/paleosol of Luochuan section in the central Chinese Loess Plateau since the last interglacial. Quaternary Geochronology, 22, 107–115. https://doi.org/10.1016/j.quageo.2014.04.004

Lü, T., Sun, J., Feathers, J. K., & Sun, D. (2021). Spatiotemporal variations and implications of luminescence sensitivity of quartz grains on the Chinese Loess Plateau since the last interglaciation. Quaternary Research, 99, 190–203. Cambridge Core. https://doi.org/10.1017/qua.2020.53

Marković, S. B., Stevens, T., Kukla, G. J., Hambach, U., Fitzsimmons, K. E., Gibbard, P., Buggle, B., Zech, M., Guo, Z., Hao, Q., Wu, H., O'Hara Dhand, K., Smalley, I. J., Újvári, G., Sümegi, P., Timar-Gabor, A., Veres, D., Sirocko, F., Vasiljević, D. A., … Svirčev, Z. (2015). Danube loess stratigraphy—Towards a pan-European loess stratigraphic model. Earth-Science Reviews, 148, 228–258. https://doi.org/10.1016/j.earscirev.2015.06.005

McNab, F., Sloan, R. A., & Walker, R. T. (2019). Simultaneous orthogonal shortening in the Afghan-Tajik Depression. Geology, 47(9), 862–866. https://doi.org/10.1130/G46090.1

Miyazaki, T., Kimura, J.-I., & Katakuse, M. (2016). Geochemical records from loess deposits in Japan over the last 210 kyr: Lithogenic source changes and paleoclimatic indications. Geochemistry, Geophysics, Geosystems, 17(7), 2745–2761. https://doi.org/10.1002/2016GC006322

Moska, P., & Murray, A. S. (2006). Stability of the quartz fast-component in insensitive samples.Radiation Measurements, 41(7), 878–885. https://doi.org/10.1016/j.radmeas.2006.06.005

Muhs, D. R., Bettis, E. A., Aleinikoff, J. N., McGeehin, J. P., Beann, J., Skipp, G., Marshall, B. D., Roberts, H. M., Johnson, W. C., & Benton, R. (2008). Origin and paleoclimatic significance of late Quaternary loess in Nebraska: Evidence from stratigraphy, chronology, sedimentology, and geochemistry. Geological Society of America Bulletin, 120(11–12), 1378–1407. https://doi.org/10.1130/B26221.1

Nagashima, K., Nishido, H., Kayama, M., Kurosaki, Y., Ohgo, S., & Hasegawa, H. (2017). Composition of Asian dust from cathodoluminescence spectral analysis of single quartz grains. Geology, 45(10), 879–882. https://doi.org/10.1130/G39237.1

Nagashima, K., Tada, R., Tani, A., Sun, Y., Isozaki, Y., Toyoda, S., & Hasegawa, H. (2011). Millennial-scale oscillations of the westerly jet path during the last glacial period. Journal of Asian Earth Sciences, 40(6), 1214–1220. https://doi.org/10.1016/j.jseaes.2010.08.010

Nagashima, K., Tada, R., Tani, A., Toyoda, S., Sun, Y., & Isozaki, Y. (2007). Contribution of aeolian dust in Japan Sea sediments estimated from ESR signal intensity and crystallinity of quartz. Geochemistry, Geophysics, Geosystems, 8(2). https://doi.org/10.1029/2006GC001364

Odom, A. L., & Rink, W. J. (1989). Natural accumulation of Schottky-Frenkel defects: Implications for a quartz geochronometer. Geology, 17(1), 55–58. https://doi.org/10.1130/0091-7613(1988)017<0055:NAOSFD>2.3.CO;2

Pietsch, T. J., Olley, J. M., & Nanson, G. C. (2008). Fluvial transport as a natural luminescence sensitiser of quartz. Quaternary Geochronology, 3(4), 365–376. https://doi.org/10.1016/j.quageo.2007.12.005

Preusser, F., Ramseyer, K., & Schlüchter, C. (2006). Characterisation of low OSL intensity quartz from the New Zealand Alps. Radiation Measurements, 41(7), 871–877. https://doi.org/10.1016/j.radmeas.2006.04.019

Rao, W., Yang, J., Chen, J., & Li, G. (2006). Sr-Nd isotope geochemistry of eolian dust of the arid-semiarid areas in China: Implications for loess provenance and monsoon evolution. Science Bulletin, 51(12), 1401–1412. https://doi.org/10.1007/s11434-006-2008-1

Sawakuchi, A. O., Blair, M. W., DeWitt, R., Faleiros, F. M., Hyppolito, T., & Guedes, C. C. F. (2011). Thermal history versus sedimentary history: OSL sensitivity of quartz grains extracted from rocks and sediments. Quaternary Geochronology, 6(2), 261–272. https://doi.org/10.1016/j.quageo.2010.11.002

Sawakuchi, A. O., Guedes, C. C. F., DeWitt, R., Giannini, P. C. F., Blair, M. W., Nascimento, D. R., & Faleiros, F. M. (2012). Quartz OSL sensitivity as a proxy for storm activity on the southern Brazilian coast during the Late Holocene. Quaternary Geochronology, 13, 92–102. https://doi.org/10.1016/j.quageo.2012.07.002

Sawakuchi, A. O., Jain, M., Mineli, T. D., Nogueira, L., Bertassoli, D. J., Häggi, C., Sawakuchi, H. O., Pupim, F. N., Grohmann, C. H., Chiessi, C. M., Zabel, M., Mulitza, S., Mazoca, C. E. M., & Cunha, D. F. (2018). Luminescence of quartz and feldspar fingerprints provenance and correlates with the source area denudation in the Amazon River basin. Earth and Planetary Science Letters, 492, 152–162. https://doi.org/10.1016/j.epsl.2018.04.006

Schaetzl, R. J., Bettis, E. A., Crouvi, O., Fitzsimmons, K. E., Grimley, D. A., Hambach, U., Lehmkuhl, F., Marković, S. B., Mason, J. A., Owczarek, P., Roberts, H. M., Rousseau, D.-D., Stevens, T., Vandenberghe, J., Zárate, M., Veres, D., Yang, S., Zech, M., Conroy, J. L., … Zech, R. (2018, May). Approaches and challenges to the study of loess—Introduction to the LoessFest Special Issue. Quaternary Research; Cambridge University Press. https://doi.org/10.1017/qua.2018.15

Sharma, S. K. (2017). Understanding the Reasons for Variations in Luminescence Sensitivity of Natural Quartz Using Spectroscopic and Chemical Studies. Proceedings of the Indian National Science Academy, 92(0). https://doi.org/10.16943/ptinsa/2017/49024

Shimada, A., Takada, M., & Toyoda, S. (2013). Characteristics of ESR signals and TLCLs of quartz included in various source rocks and sediments in Japan: A clue to sediment provenance. Geochronometria, 40(4), 334–340. https://doi.org/10.2478/s13386-013-0111-z

Smith, J., Vance, D., Kemp, R. A., Archer, C., Toms, P., King, M., & Zárate, M. (2003). Isotopic constraints on the source of Argentinian loess – with implications for atmospheric circulation and the provenance of Antarctic dust during recent glacial maxima. Earth and Planetary Science Letters, 212(1), 181–196. https://doi.org/10.1016/S0012-821X(03)00260-7

Stevens, T., Palk, C., Carter, A., Lu, H., & Clift, P. D. (2010). Assessing the provenance of loess and desert sediments in northern China using U-Pb dating and morphology of detrital zircons. Geological Society of America Bulletin, 122(7–8), 1331–1344. https://doi.org/10.1130/B30102.1

Sun, J. (2002). Provenance of loess material and formation of loess deposits on the Chinese Loess Plateau. Earth and Planetary Science Letters, 203(3), 845–859. https://doi.org/10.1016/S0012-821X(02)00921-4

Sun, Y., Tada, R., Chen, J., Chen, H., Toyoda, S., Tani, A., Isozaki, Y., Nagashima, K., Hasegawa, H., & Ji, J. (2007). Distinguishing the sources of Asian dust based on electron spin resonance signal intensity and crystallinity of quartz. Atmospheric Environment, 41(38), 8537–8548. https://doi.org/10.1016/j.atmosenv.2007.07.014

Sun, Y., Tada, R., Chen, J., Liu, Q., Toyoda, S., Tani, A., Ji, J., & Isozaki, Y. (2008). Tracing the provenance of fine-grained dust deposited on the central Chinese Loess Plateau. Geophysical Research Letters, 35(1), L01804. https://doi.org/10.1029/2007GL031672

Toyoda, S., & Hattori, W. (2000). Formation and decay of the E1′ center and of its precursor. Applied Radiation and Isotopes, 52(5), 1351–1356. https://doi.org/10.1016/S0969-8043(00)00094-4

Toyoda, S., Nagashima, K., & Yamamoto, Y. (2016). ESR signals in quartz: Applications to provenance research – A review. Quaternary International, 397, 258–266. https://doi.org/10.1016/j.quaint.2015.05.048

Tsukamoto, S., Nagashima, K., Murray, A. S., & Tada, R. (2011). Variations in OSL components from quartz from Japan sea sediments and the possibility of reconstructing provenance. Loess in Eurasia, 234(1), 182–189. https://doi.org/10.1016/j.quaint.2010.09.003

Újvári, G., Varga, A., & Balogh-Brunstad, Z. (2008). Origin, weathering, and geochemical composition of loess in southwestern Hungary. Quaternary Research, 69(3), 421–437. https://doi.org/10.1016/j.yqres.2008.02.001

Vandenberghe, J., Renssen, H., van Huissteden, K., Nugteren, G., Konert, M., Lu, H., Dodonov, A., & Buylaert, J.-P. (2006). Penetration of Atlantic westerly winds into Central and East Asia. Quaternary Science Reviews, 25(17), 2380–2389. https://doi.org/10.1016/j.quascirev.2006.02.017

Wang, X., & Miao, X. (2006). Weathering history indicated by the luminescence emissions in Chinese loess and paleosol. Quaternary Science Reviews, 25(13), 1719–1726. https://doi.org/10.1016/j.quascirev.2005.11.009

Wang, K., Tada, R., Zheng, H., Irino, T., Zhou, B., & Saito, K. (2020). Provenance changes in fine detrital quartz in the inner shelf sediments of the East China Sea associated with shifts in the East Asian summer monsoon front during the last 6 kyrs. Progress in Earth and Planetary Science, 7(1), 5. https://doi.org/10.1186/s40645-019-0319-5

Wei, C., Yin, G., Li, Y., Liu, C., Li, W., & Guo, R. (2020). Quartz electron spin resonance signal intensity of Al and Ti–Li centers as a provenance indicator: An example from the Yangtze River Basin. Quaternary International, 562, 76–84. https://doi.org/10.1016/j.quaint.2020.06.023

Weltje, G. J., & von Eynatten, H. (2004). Quantitative provenance analysis of sediments: Review and outlook. Quantitative Provenance Analysis of Sediments, 171(1), 1–11. https://doi.org/10.1016/j.sedgeo.2004.05.007

Yukihara, E. G., & McKeever, S. W. S. (2011). Optically Stimulated Luminescence: Fundamentals and Applications. John Wiley & Sons, Ltd. https://doi.org/10.1002/9780470977064

Zheng, C. X., Zhou, L. P., & Qin, J. T. (2009). Difference in luminescence sensitivity of coarse-grained quartz from deserts of northern China. Radiation Measurements, 44(5), 534–537. https://doi.org/10.1016/j.radmeas.2009.02.013

Zular, A., Sawakuchi, A. O., Guedes, C. C. F., & Giannini, P. C. F. (2015). Attaining provenance proxies from OSL and TL sensitivities: Coupling with grain size and heavy minerals data from southern Brazilian coastal sediments. Radiation Measurements, 81, 39–45. https://doi.org/10.1016/j.radmeas.2015.04.010

6. Chapter 6

Conclusions and Outlook

6.1. Conclusion

This thesis employs trapped charge techniques to reconstruct the timing and provenance of loess deposits in the piedmonts of Central Asia. The luminescence technique is used as a dating tool to provide an absolute chronological framework for the loess sites. While, electron spin resonance (ESR) technique provides a powerful method for measuring different paramagnetic centres in quartz grains, by means of which, this thesis establishes a novel approach for provenance using E' and peroxy centres in quartz. This method provides a new provenance tool to not only distinguish between loess from two different regions, but also offers potential towards understanding long term variations in source change within a loess-palaeosol sequence. In addition, this thesis explores the trapped charge characteristics of quartz using both luminescence and ESR techniques, in parallel down a long loess sequence, to gain a more nuanced insight into how these different trapped-charge indicators reflect source change through time. These investigations are supported by stratigraphic data, grain size analysis, magnetic susceptibility measurements and micromorphology, which provide a robust foundation for interpretation of past climate and processes of dust transport and deposition in the piedmonts of Central Asia.

One of the key issues in Arid Central Asia (ACA) loess records is the high degree of variability in the timing and peaks of loess accumulation between sites. This challenges previous assumptions linking aeolian flux to cold dry (glacial) phases, and consequently its variability over glacial-interglacial time scales (Li et al., 2016, 2018, 2020; Fitzsimmons et al., 2018). Recent studies (Li et al., 2018) also found the ACA records to be asynchronous with aeolian flux in the Chinese Loess Plateau (CLP). This prompted the first investigation in Chapter 3, where we systematically assess how loess mass accumulation rates (MARs) respond to climatic and geological controls in piedmont regions. We provide a high-resolution chronological framework based on luminescence ages for five new sites in the vastly understudied piedmonts of the central Ili basin (along the Zalisky Alatau range front). This new dataset provides the 'missing' spatial coverage needed to interrogate loess depositional dynamics in the Ili basin as a whole, whereas up until now these interpretations were based only on data from the eastern, and a few isolated western sites of the Ili basin. Our new ages from the five sites in the central Ili basin show spatio-temporal inhomogeneity in timing and rate of deposition, with diverse histories of accumulation varying from the mid-Holocene to beyond the last interglacial. Therefore, to understand aeolian dynamics over regional scales, we constructed MARs for the past 60 ky by combining luminescence ages from 30 other published sites in the Ili basin and from neighbouring basins in the ACA as well as the CLP.

This allows for a local (individual sites) to regional scale (multiple sites across the ACA and CLP) interrogation of MARs based on its response to local geomorphic setting, topography and climate-controlled wind regimes and sediment supply. This local to regional scale examination of MAR's across different piedmont settings, suggests that the response of loess MARs can be viewed as a composite of – 'net' loess accumulation and the 'timing of peaks' in loess accumulation, which are driven both by climate dynamics and local geomorphic setting. Nevertheless, the absolute sedimentation rates at a given site respond to local topographic and geomorphic context, sediment availability and to climate. While, the 'timing of peaks' in accumulation, when viewed in aggregate across a number of sites, largely represents a response to variability in wind dynamics driven by large scale climate dynamics in the region.

Although intuitive, the role of geomorphic setting and its influence on palaeoclimate proxy indices in loess is often underestimated, especially in the investigation of individual sites. Our study highlights such a scenario (see Chapter 3, Fig. 3.9) by comparing four loess sites in the Ili basin with different geomorphic settings (e.g. proximity to fluvial channels and mountain ranges, altitude) over the same time interval. We observe that geomorphic setting not only influences grain size characteristics but also MARs through time. The resulting spatial variability in MARs and grain size most likely reflects a complex interaction between local and larger-scale wind regimes and associated dust transport, topographic (and palaeotopographic) context, and local sediment supply. This example highlights the need to interrogate geomorphic setting of individual sites for their potential to reflect local or large-scale processes depending on the planned research question.

Another important aspect in loess research, is determining the provenance of aeolian dust. This is important at two scales. At a global scale loess deposits and other aeolian landforms are major contributors to global atmospheric dust load, past and present. Therefore, fingerprinting dust from different regions can help in understanding their relative contribution towards dust found in ice cores and marine sediments (Nakai et al., 1993; Biscaye et al., 1997). At a regional scale, identifying the source of loess sediments and the change in loess through time, provides a means to reconstruct dust transport pathways and consequently, atmospheric circulation in the region. In Chapter 4 of this thesis, we propose a new method for identifying sediment provenance based on quartz, one of the most ubiquitous minerals on the Earth's surface and an essential component of aeolian dust. We exploit two paramagnetic defect centres in quartz, the E' and peroxy centre, as a proxy for provenance using ESR. Our approach is based on observations by Odom and Rink (1989) that the E' and peroxy centres in natural quartz arise from Schottky-Frenkel defect pairs, and their intensity is proportional to the age of the granitic quartz host rock. We applied this new measurement protocol to a suite of 114 fine-grained quartz loess samples from two sedimentary basins in Kazakhstan and Tajikistan respectively, which are known to have different dust source regions and derive from source rocks of very different ages. We successfully distinguished between quartz from these two regions based on the new paired

E'-peroxy approach. We also observe that the E' and peroxy intensities show a positive correlation and loess samples derived from older rocks (in Kazakhstan) yield stronger signals than those sourced from younger rocks (Tajikistan). These observations reaffirm the basis of our approach that these centres arise from Schottky-Frenkel defect pairs and increase with the age of the rocks.

Furthermore, we compared the characteristics of the natural E' signature of quartz in our samples to the heat-treated (HT)-E' signal that is routinely used in ESR-based provenance studies (Toyoda and Hattori, 2000). Our investigations show that γ-irradiation and thermal treatment (used in HT-E' measurement) are unnecessary, and the natural E' signature represents the same inherent provenance characteristics as the HT-E' signal for our samples. Therefore, we present a substantially simplified measurement protocol for provenance analysis using quartz.

We further applied this new method to investigate source change down a long loess-palaeosol sequence at Karamaidan in Tajikistan, by taking down-profile measurements of natural E' and peroxy intensity of quartz. Our results reveal differences between primary loess and buried soil (palaeosol) horizons, which we propose reflects changes in dominant dust source, transport pathways and therefore, atmospheric circulation on glacial-interglacial timescales. Our new provenance technique is clearly highly applicable to long aeolian records, but also holds great potential for application to other sedimentary systems.

The successful application of our new provenance method based on E' and peroxy centres in quartz, prompted its comparison with other trapped charge provenance techniques. Luminescence sensitivity of quartz has increasingly been utilised either as an indicator of provenance and/or to derive the sedimentary history of grains (Pietsch et al., 2008; Fitzsimmons, 2011; Sawakuchi et al., 2011; 2018). Recent investigations on luminescence sensitivity of the optically stimulated luminescence (OSL) and thermoluminescence (TL) signals in quartz from loess-palaeosol sequences in the CLP and Tajikistan reveal a distinct difference between soil and loess units (Lü et al., 2014, 2021; Li and Zhou, 2020). The variability observed within individual loess profiles has been interpreted to relate to the impact of climatic fluctuations on geomorphic processes, such as the (i) contraction and expansion of neighbouring deserts leading to sensitivity change, as result of varying transport distance from the source (deserts) to the sink (loess) (Lü et al., 2014, 2021), (ii) increased glacial erosion in mountain regions during cold phases leading to increased production and availability of low sensitivity quartz (Lü et al., 2014), and (iii) preferential weathering of rocks in response to climatic fluctuations, leading to sediment compositions with distinct quartz signature (Li and Zhou, 2020).

In Chapter 5, we investigate both the E'-peroxy intensities and luminescence sensitivity characteristics of fine grain quartz in parallel down a long loess sequence from southern

Tajikistan, to gain a more nuanced insight into how these different trapped-charge indicators reflect source change through time. We observe a distinct increase in OSL and TL sensitivity of quartz within buried soil units (palaesols) as compared to the primary loess units. Based on interpretations of natural E' and peroxy intensity in quartz as a provenance indicator, we attribute the increased OSL/TL sensitivity in soil units largely to repeated cycles of natural irradiation and bleaching, facilitated by low deposition rates during pedogenesis. Thus, the comparison between these two techniques not only allows us to independently assess their utility as provenance indicators, but also provides an insight into the influence of geomorphic processes on trapped charge characteristics in quartz.

In addition, in Chapter 5 we also investigate the ratio [IRSL]/[pIR-OSL] from polymineral samples that is considered as a proxy to indicate enrichment of quartz (Wang and Miao, 2006), as a result of weathering of feldspar grains during soil formation. Down-profile variations in [IRSL]/[pIR-OSL] ratio at KAR shows agreement with the magnetic susceptibility measurements and the stratigraphic observations at the site. In addition, this ratio is highly sensitive to weathering during soil formation, as it also identified weakly developed soil horizons, which remained otherwise undetected in magnetic susceptibility measurements. This suggests the potential of [IRSL]/[pIR-OSL] ratio from polymineral grains as a screening tool to assess and detect buried soil horizons in loess-palaeosol units.

6.2. Outlook and future research perspectives

This thesis has made two important contributions towards the understanding of aeolian landscape-climate interaction in piedmont regions, particularly in Central Asia. *First,* a nuanced understanding of loess MARs in response to climatic, geomorphic and topographic controls. A synthesis of MARs from 33 sites across ACA and CLP, show that spatio-temporal variability in MARs results from a complex interaction of wind regimes, topography, and local sediment supply and availability. Based on this local to regional perspective on MARs across various piedmont settings, we suggest the response of loess MARs as a composite of – 'net sedimentation' and 'timing of peaks in accumulation'. The latter, when derived from an aggregate of sites, acts as an indicator of large-scale climate dynamics in a region. *Second*, a new proxy for provenance of quartz based on natural intensity of E' and peroxy paramagnetic centres. This new technique provides a simplified measurement protocol as compared to previously applied ESR-based provenance methods. This new approach successfully distinguished quartz from two different basins in Central Asia as well as identified source change down loess-palaeosol sequences. Hence together, the spatio-temporal dynamics of loess accumulation and source change in ACA has important implications towards understanding the nature of interaction and interplay between two major drivers of the

Northern Hemisphere climate: the mid latitude Westerlies and the Siberian High-Pressure system.

Overall, the results presented in this thesis have important implications, not only for loess deposits in Central Asia, but also for loess research in general. The meticulous assessment of the causal link between loess MARs and climate, in context of geomorphic and topographic constraints, provides a framework for systematic evaluation and interpretation of MARs from loess sites. The successful application of our new provenance technique opens new avenues for investigation into further applications of this method in loess research as well as to other sedimentary systems. It also prompts a need for further research into fundamental understanding of defect dynamics in natural quartz.

In addition to the work presented in this thesis, a suite of surface samples (modern) and rocks from the Ili basin of SE Kazakhstan were also investigated. The preliminary results are presented in Appendix D. The results from this thesis, coupled with insights from our preliminary investigations presents an array of potential areas of investigations for future research in this field. Some of these studies include:

a) Reconstruction of aeolian transport pathways: Present and Past

The identification of potential dust sources in a region allows us to link source areas to loess deposits, which in turn can help discern the dominant dust transport pathway, and by extension, the most likely climate circulation pattern prevailing at that time. In a recent study, Fitzsimmons et al (2020), used back-trajectory models to identify likely dust transport pathways to the piedmonts of the Zalisky Alatau (in the central Ili basin). Based on this study, surface samples were collected from various depositional and potential source contexts across the Ili basin (during July 2019 field expedition). We examined ESR signature of various paramagnetic centres (E', peroxy and Al-hole) in quartz of different grain sizes from surface samples (refer appendix D). These were compared to modern (surface) loess and loess dated between the mid-Holocene to late Pleistocene from this region. Our preliminary investigations yield two important results: i) the signature of modern (surface) loess samples agrees with samples sourced from the western part of the basin, suggesting a predominantly Westerly influence in the basin during present times (Fig. D2, appendix D). This is in tune with the dust transport models for the region (Fitzsimmons et al., 2020) and (ii) comparison of mid-Holocene and Pleistocene age loess samples with surface samples, indicates a change in source, implying that dust transport pathways most likely changed dominance through time (Fig. D3, appendix D). Thus, our new provenance approach provides a powerful tool to reconstruct aeolian transport pathways through time.

Another important aspect in aeolian studies is understanding the mechanisms that drive aeolian processes, i.e., the entrainment, transport, and deposition of dust, that are vital towards understanding the links between the resulting depositional landforms and climate

dynamics in a region. Our preliminary investigations on ESR characteristics of quartz of different grain sizes shows significant difference between the clustering of fine and coarse grains from different catchments which highlights the difference in entrainment and transport processes for different grain sizes (Fig. D2 in appendix D). Thus, the new provenance approach developed in this thesis opens exciting new avenues of research in aeolian environments.

b) Defect dynamics in 'source' rocks

Our understanding of the behaviour (in response to dose) and characteristics of different defect centres (E', peroxy, Al-hole centres) in quartz derived from rocks of different types and ages is very limited. The characteristics of some of these centres (E' and peroxy) are known to vary with age of granitic rocks (Odom and Rink, 1989; Toyoda and Ikeya, 1991; Toyoda and Hattori, 2000). However, not much is known about the effect of (i) metamorphism, (ii) rate of cooling during rock formation, and (iii) natural deformation (e.g. faults) on the initial formation and/or rate of formation of these defect centres in quartz (Rink and Odom, 1990). Our preliminary analysis of different types of rocks (Fig. D4, in appendix D) suggests that the concentration of defect centres depends not only on the age, but also the type of rock and thus, suggests a need for further investigation in understanding the defect centre dynamics in rocks. Such investigations will greatly contribute towards better characterisation of the signature of source rocks for future provenance work.

(c) Establishing a calibration standard for ESR-based provenance studies

Current research in the application of ESR-based provenance techniques either doesn't use calibration, or uses different types of calibration sources. Although, this does not affect individual study or results; however, it limits the scope and potential impact of this research field. Not having a global standard calibration for ESR-based provenance studies, prevents inter-comparison of data between different laboratories; but more importantly, it prevents comparison and/ or coupling of datasets generated by different laboratories. This results in generation of large datasets for provenance from different regions of the world, which sadly, remain incomparable. Hence, it is crucial that all research groups in this field make a collective effort towards establishing a calibration standard for ESR-based provenance studies.

(d) Understanding the link between E' and OSL sensitivity

E' intensity and OSL sensitivity characteristics of quartz are often independently used parameters in provenance studies of quartz. Studies based on high temperature annealing experiments on natural quartz observe that heating quartz to > 500^{o}C anneals the E' centre, while there is a subsequent increase in OSL intensity (Poolton, 2000). This phenomenon was then closely investigated by multi-spectroscopic studies on quartz (Schilles et al., 2001),

which suggest that luminescence is generally sensitized in quartz by removal of the E' centre, which acts either as non-radiative recombination centres, or as luminescence centres emitting in the deep UV. They also compete with other acceptors during recombination processes. This illustrates the complex relationship between these parameters. Also, how these parameters change under natural processes (in nature) is not known. Only a limited number of studies have attempted a correlation between E' and luminescence characteristics of quartz in natural systems (Tsukamoto et al., 2011; Chapter 5 of this thesis), however the results presented in these studies need further investigation and at present, remain inconclusive. Therefore, there is need for fundamental understanding of the nature of relationship between these trapped charge parameters in natural systems.

(e) Beyond dust deposits: Applying the 'paired E'-peroxy' approach to other sedimentary systems

This thesis has successfully utilised the E' and peroxy centre intensity as a proxy for provenance in fine grain quartz extracted from loess deposits. In addition, our preliminary work with modern surface sediments of different grain sizes indicates the ability of this technique to distinguish quartz of different grain sizes from different catchment areas within a basin. Hence, the new ESR-based approach for provenance of quartz developed in this thesis offers great potential for its application to other sedimentary systems (e.g. lacustrine and fluvial systems, and ocean sediments).

References

Biscaye, P. E., Grousset, F. E., Revel, M., Van der Gaast, S., Zielinski, G. A., Vaars, A., & Kukla, G. (1997). Asian provenance of glacial dust (stage 2) in the Greenland Ice Sheet Project 2 Ice Core, Summit, Greenland. Journal of Geophysical Research: Oceans, 102(C12), 26765–26781. https://doi.org/10.1029/97JC01249

Fitzsimmons, K. (2011). An assessment of the luminescence sensitivity of Australian quartz with respect to sediment history. Geochronometria, 38(3), 199–208. https://doi.org/10.2478/s13386-011-0030-9

Fitzsimmons, K. E., Nowatzki, M., Dave, A. K., & Harder, H. (2020). Intersections between wind regimes, topography and sediment supply: Perspectives from aeolian landforms in Central Asia. Palaeogeography, Palaeoclimatology, Palaeoecology, 540, 109531. https://doi.org/10.1016/j.palaeo.2019.109531

Fitzsimmons, K. E., Sprafke, T., Zielhofer, C., Günter, C., Deom, J.-M., Sala, R., & Iovita, R. (2018). Loess accumulation in the Tian Shan piedmont: Implications for palaeoenvironmental change in arid Central Asia. Quaternary International, 469, 30–43. https://doi.org/10.1016/j.quaint.2016.07.041

Li, G., Rao, Z., Duan, Y., Xia, D., Wang, L., Madsen, D. B., Jia, J., Wei, H., Qiang, M., Chen, J., & Chen, F. (2016). Paleoenvironmental changes recorded in a luminescence dated loess/paleosol sequence from the Tianshan Mountains, arid central Asia, since the Penultimate Glaciation. Earth and Planetary Science Letters, 448, 1–12. https://doi.org/10.1016/j.epsl.2016.05.008

Li, G., Chen, F., Xia, D., Yang, H., Zhang, X., Madsen, D., Oldknow, C., Wei, H., Rao, Z., & Qiang, M. (2018). A Tianshan Mountains loess-paleosol sequence indicates anti-phase climatic variations in arid central Asia and in East Asia. Earth and Planetary Science Letters, 494, 153–163. https://doi.org/10.1016/j.epsl.2018.04.052

Li, G., Yang, H., Stevens, T., Zhang, X., Zhang, H., Wei, H., Zheng, W., Li, L., Liu, X., Chen, J., Xia, D., Oldknow, C., Ye, W., & Chen, F. (2020). Differential ice volume and orbital modulation of Quaternary moisture patterns between Central and East Asia. Earth and Planetary Science Letters, 530, 115901. https://doi.org/10.1016/j.epsl.2019.115901

Li, Y., & Zhou, L. (2020). Variations of thermally and optically stimulated luminescence sensitivity of loess and pedocomplex samples from southern Tajikistan, Central Asia. Geochronometria, 0(0), 000010151520150118. https://doi.org/10.1515/geochr-2015-0118

Lü, T., Sun, J., Li, S.-H., Gong, Z., & Xue, L. (2014). Vertical variations of luminescence sensitivity of quartz grains from loess/paleosol of Luochuan section in the central Chinese Loess Plateau since the last interglacial. Quaternary Geochronology, 22, 107–115. https://doi.org/10.1016/j.quageo.2014.04.004

Lü, T., Sun, J., Feathers, J. K., & Sun, D. (2021). Spatiotemporal variations and implications of luminescence sensitivity of quartz grains on the Chinese Loess Plateau since the last interglaciation. Quaternary Research, 99, 190–203. Cambridge Core. https://doi.org/10.1017/qua.2020.53

Nakai, S., Halliday, A. N., & Rea, D. K. (1993). Provenance of dust in the Pacific Ocean. Earth and Planetary Science Letters, 119(1), 143–157. https://doi.org/10.1016/0012-821X(93)90012-X

Odom, A. L., & Rink, W. J. (1989). Natural accumulation of Schottky-Frenkel defects: Implications for a quartz geochronometer. Geology, 17(1), 55–58. https://doi.org/10.1130/0091-7613(1988)017<0055:NAOSFD>2.3.CO;2

Pietsch, T. J., Olley, J. M., & Nanson, G. C. (2008). Fluvial transport as a natural luminescence sensitiser of quartz. Quaternary Geochronology, 3(4), 365–376. https://doi.org/10.1016/j.quageo.2007.12.005

Poolton, N. R. J., Smith, G. M., Riedi, P. C., Bulur, E., Bøtter-Jensen, L., Murray, A. S., & Adrian, M. (2000). Luminescence sensitivity changes in natural quartz induced by high temperature annealing: A high frequency EPR and OSL study. Journal of Physics D: Applied Physics, 33(8), 1007–1017. https://doi.org/10.1088/0022-3727/33/8/318

Rink, W. J., & Odom, A. L. (1991). Natural alpha recoil particle radiation and ionizing radiation sensitivities in quartz detected with EPR: Implications for geochronometry. International Journal of Radiation Applications and Instrumentation. Part D. Nuclear Tracks and Radiation Measurements, 18(1), 163–173. https://doi.org/10.1016/1359-0189(91)90108-T

Sawakuchi, A. O., Blair, M. W., DeWitt, R., Faleiros, F. M., Hyppolito, T., & Guedes, C. C. F. (2011). Thermal history versus sedimentary history: OSL sensitivity of quartz grains extracted from rocks and sediments. Quaternary Geochronology, 6(2), 261–272. https://doi.org/10.1016/j.quageo.2010.11.002

Sawakuchi, A. O., Jain, M., Mineli, T. D., Nogueira, L., Bertassoli, D. J., Häggi, C., Sawakuchi, H. O., Pupim, F. N., Grohmann, C. H., Chiessi, C. M., Zabel, M., Mulitza, S., Mazoca, C. E. M., & Cunha, D. F. (2018). Luminescence of quartz and feldspar fingerprints provenance and correlates with the source area denudation in the Amazon River basin. Earth and Planetary Science Letters, 492, 152–162. https://doi.org/10.1016/j.epsl.2018.04.006

Schilles, T., Poolton, N. R. J., Bulur, E., Bøtter-Jensen, L., Murray, A. S., Smith, G. M., Riedi, P. C., & Wagner, G. A. (2001). A multi-spectroscopic study of luminescence sensitivity changes in natural quartz induced by high-temperature annealing. Journal of Physics D: Applied Physics, 34(5), 722–731. https://doi.org/10.1088/0022-3727/34/5/310

Toyoda, S., & Hattori, W. (2000). Formation and decay of the E1′ center and of its precursor. Applied Radiation and Isotopes, 52(5), 1351–1356. https://doi.org/10.1016/S0969-8043(00)00094-4

Toyoda, S., & Ikeya, M. (1991). Thermal stabilities of paramagnetic defect and impurity centers in quartz: Basis for ESR dating of thermal history. Geochemical Journal, 25(6), 437–445. https://doi.org/10.2343/geochemj.25.437

Tsukamoto, S., Nagashima, K., Murray, A. S., & Tada, R. (2011). Variations in OSL components from quartz from Japan sea sediments and the possibility of reconstructing provenance. Quaternary International, 234(1), 182–189. https://doi.org/10.1016/j.quaint.2010.09.003

Wang, X., & Miao, X. (2006). Weathering history indicated by the luminescence emissions in Chinese loess and paleosol. Quaternary Science Reviews, 25(13), 1719–1726. https://doi.org/10.1016/j.quascirev.2005.11.009

Other contributions during this PhD

During my PhD, I had the opportunity to contribute with my expertise in luminescence to other publications not included in this thesis. These publications include:

Fitzsimmons, K.E., Nowatski, M., Dave, A.K., Harder, H. (2020). Intersections between wind regimes, topography and sediment supply: Perspectives from aeolian landforms in Central Asia. Palaeogeography, Palaeoclimatology, Palaeoecology 540, 109-531.

Fitzsimmons, K.E., Nowatski, M., Dave, A.K., Harder, H. (2020). Corrigendum to 'Intersections between wind regimes, topography and sediment supply: Perspectives from aeolian landforms in Central Asia'. Palaeogeography, Palaeoclimatology, Palaeoecology 540, 109-531.

Schaetzl, R.J., Bettis, E.A., Crouvi, O., Fitzsimmons, K.E., Grimley, D.A., Hambach, U., Lehmkuhl, F., Marković, S.B., Mason, J.A., Owczarek, P., Roberts, H.M., Rousseau, D.-D., Stevens, T., Vandenberghe, J., Zarate, M., Veres, D., Yang, S., Zech, M., Conroy, J.L., Dave, A.K., Faust, D., Hao, Q., Obreht, I., Prud'homme, C., Smalley, I., Tripaldi, A., Zeeden, C., Zech, R. (2018). Approaches and challenges to the study of loess. Quaternary Research (89), 563-618.

Appendix A

Supplementary Information for Chapter 1

The patchwork loess of Central Asia: Implications for interpreting aeolian dynamics and past climate circulation in piedmont regions

1. Optically stimulated luminescence (OSL) dating

1.1. Sample preparation

All the samples were processed and measured under subdued red-light conditions at the Institute of Geosciences, Johannes Gutenberg University and the Max Planck Institute for Chemistry (MPIC) in Mainz, Germany. Different grain size fractions were extracted by wet-sieving. However due to the lack of sufficient coarse grains (>45 µm), fine grain (4-11 µm) samples were prepared for OSL analysis using established protocols (Frechen et al., 1996). For the preparation of fine grain (4-11 µm) fraction – the <63 µm sediment was treated with 10% HCl followed by 10% H_2O_2 to remove carbonates and organics respectively. The sediment was then treated with 0.1N sodium oxalate to remove clays. The 4-11 µm polymineral fraction was obtained from the bulk fraction (<63 µm) by settling using Stokes law. This polymineral fine grain fraction was treated with 37% Hexafluorosilicic acid (H_2SiF_6) for 7 days to remove feldspar and washed with 10% HCl to remove fluoride precipitates to obtain fine grained (4-11 µm) quartz rich fraction (Jackson et al, 1976). All aliquots were prepared by depositing a suspension of 4-11 µm quartz fraction using acetone on 9.7 mm stainless steel discs. The purity of the quartz extracts for all samples was verified by the near background signal observed on IR stimulation of the sample after a given dose (~19 Gy) for all the samples (Duller, 2003).

1.2. Luminescence Measurements

All luminescence measurements were made using an automated Risø TL-DA-20 reader equipped with a $^{90}Sr/^{90}Y$ beta sources (Thomsen et al., 2006) calibrated to a dose rate of 0.095 ± 0.02 Gy/s. The sample was stimulated using blue LED (470±30 nm, 80 mW/cm^2) and IR LED (870 ± 30 nm, 300 mW/cm^2) and the emitted luminescence signal was detected by EMI 9235QA photomultiplier tube fitted with a 7.5 mm Hoya U-340 and a combination of Schott BG-39 and BG-3 filters to detect quartz and feldspar emissions respectively.

The natural and regenerated quartz OSL decay curves show a rapid decay in the initial 1s of stimulation indicating the dominance of the fast component in the OSL signal. This can also

be seen with its comparison to normalised quartz OSL signal from calibration quartz (Fig. A2). Furthermore, unlike observations made in previous studies (Li et al., 2018) regarding the dim nature of silt sized quartz extract (38-63 µm), the natural and regenerative OSL decay curves obtained from fine grained (4-11 µm) quartz are sufficiently bright for OSL measurements, although the intensity varies between the different samples. The change in sensitivity (brightness) of the quartz from different size fractions as well as between different samples of similar size fractions (e.g. Kang et al., 2015; Li et al 2018.; this study) is not well understood and requires further study. In order to negate any suspicion of feldspar contamination to the quartz-dominant OSL signal, an additional IR stimulation was added prior to every blue stimulation in the classic single aliquot regenerative protocol (SAR; Murray and Wintle, 2000, 2003) - commonly referred to as DSAR (or Double-SAR; Banerjee et al, 2001). This approach was developed and commonly applied to obtain quartz-dominated post-IR OSL signal from a feldspar contaminated or polymineral fraction (Banerjee et al., 2001; Roberts and Wintle, 2001; Jain and Singhvi, 2001). Some studies have previously reported discrepancies between the equivalent dose values evaluated from polymineral post IR-OSL signal compared to that from chemically purified quartz OSL signal (Zhang and Zhao, 2007; Zhang et al., 2007), which has been related to IR exposure time and bleaching temperature utilised prior to blue stimulation in the DSAR protocol. Since in our study, we apply the DSAR protocol on chemically pure fine grain quartz, we do not expect any such discrepancy. Nevertheless, we optimise the performance of the DSAR as well as verify the applicability of the DSAR protocol on our samples by comparing the equivalent dose obtained from a simple SAR protocol and that obtained from the DSAR protocol (at different IR bleaching times and temperatures) on a selected fine grain quartz sample (A0034).

Prior to any luminescence measurements, preheat plateau tests were performed on three discs each of two samples, A0021 and A0034, from profile PAN and ASH respectively at 180, 220, 240, 260 and 280^{o}C (Fig. 3.3a). The results indicate an acceptable preheat plateau range between 240 to 260^{o}C, hence a preheat of 260^{o}C with a cut heat of 240^{o}C for 10s was chosen for further tests and equivalent dose measurements for all fine grain quartz samples.

In order to test and optimise the performance of the DSAR protocol 3 discs each of A0034 was run for a combination of two different IR bleaching temperatures (50^{o}C and 70^{o}C) with two different IR bleaching times (40s and 100s) in the DSAR protocol (Table A2). The results obtained from these tests along with that obtained from running a simple SAR protocol are summarised in Fig.3.3b. These results (as also observed by Zhang and Zhao, 2007) show that short IR exposure times of 40 to 100s seconds do not have much impact on the D_e's, however it seems that a lower IR bleaching temperature of 50^{o}C is more suitable for the application of the DSAR method to our samples. Hence, an IR stimulation of 100s at 50^{o}C was chosen for all equivalent dose measurements using DSAR protocol. To further check the applicability of the DSAR protocol, dose recovery tests was performed on 3-5 discs each of sample A0025 (site PAN) and A0034 (site ASH) using the DSAR (with an IR stimulation at 50^{o}C for 100s) and a

simple SAR protocol. After bleaching the samples with Blue LEDs at room temperature for 80s, a radiation dose of ~47.5 Gy (close to their corresponding equivalent dose) was given to the samples. This laboratory dose was then measured using the SAR and DSAR protocol for both the samples and the resulting ratio of recovered laboratory dose to given dose was found to be within 10% of unity for both the samples irrespective of the applied protocols (Fig. 3.3c). This further affirms the suitability of the DSAR protocol for age determination of fine grain samples for our samples.

Equivalent dose (D_e) was determined from 16-22 aliquots each, of 19 fine grained quartz samples from four sites using the DSAR protocol (Table 3.1). The steps of the DSAR protocol are listed in Table A2. The robustness of the DSAR protocol on individual aliquots is tested with a set of intrinsic performance steps (recycling and recuperation) included after all the irradiation steps in every measurement. The recycling ratio (ratio of repeated dose to corresponding regenerative dose) was found to be within 10% of unity for all samples. While the recuperation ratio was <2% of the natural OSL signal for all aliquots, suggesting negligible thermal transfer of charge during OSL measurements. The dose response curves for all samples were fitted with a single saturating exponential function to obtain the best fit based on reduced chi square parameter. The early and late background subtraction method (Cunningham and Wallinga, 2010) for D_e determination was tested for all samples and no apparent change in D_e value was observed. Hence, we utilise the initial 0.8 s after subtracting the last 8s from the background OSL signal for calculation of the net OSL signal from each aliquot. The Central Age Model (Galbraith et al., 1999) was used to calculate the D_e for all samples.

Initial application of DSAR protocol on sample A0003 (site TAU, depth = 1 m) and A0038 (site MAL, depth = 1m) exhibited a flattening of the quartz OSL dose response curve indicating a near saturation of the quartz in nature. However, Timar-Gabor et al (2017) observed that the SAR dose response curve (DRC) constructed from the OSL fast component of fine grain quartz was described by a sum of two saturating exponential function and did not undergo saturation at high doses (>10000 Gy), even though it may have attained saturation with respect to its limit for dating under natural conditions. In order to ascertain that the quartz in our samples was in saturation and evaluate its saturation limit, we constructed the DRCs with a high dose range (c. upto 1500 Gy) for selected samples from the top and bottom of the profiles at site TAU (A0003, depth=1.5m; A0016, depth=7m) and MAL (A0037, depth=1m; A0050, depth=5.1m) respectively (Fig. A3). All four samples, yield an 'apparent' equivalent dose estimate of c.180-190 Gy (c.70 ka), which corresponds to the natural saturation values of fine grain quartz in this region (Table 3.1 and Fig. A3).

In cases where apparent natural saturation of the fine-grained quartz-OSL signal was observed, elevated temperature post-infrared infrared stimulated luminescence (pIR-IRSL) dating of polymineral fine grains was undertaken (protocol outlined in Table A2; Theil et al,

2011). Based on the observations made by Thomsen et al (2008) and Murray et al (2009) and following the work of Theil et al (2011), a pIR-IRSL protocol, with a preheat of 320^{o}C for 60 s, followed by an IR stimulation at 50^{o}C for 200s (IR_{50}) and subsequent measurement of the pIR-IRSL signal at 290^{o}C for 200 s ($pIRIR_{290}$) was employed for all polymineral fine grain samples. A high temperature bleach at 325^{o}C for 100 s was performed after each cycle to remove any residual charge. The equivalent dose was evaluated using the net signal obtained from the initial 2.4 s of stimulation after subtraction of the background from the last c. 20 s. Since initial D_e measurements yielded a high natural dose, we constructed dose response curves extending over a high dose range (upto c. 3325 Gy, after Buylaert et al., 2012) to evaluate the D_e from polymineral fine grains. We performed this analysis on 3 aliquots each of the same set of samples from TAU (A0003 and A0016) and MAL (A0038 and A0050) as used in the quartz saturation experiment. The results are summarised in Fig. 3.4a,b. We assessed the closeness of the natural pIRIR signal to saturation by taking a ratio of the sensitivity corrected natural pIRIR signal to that obtained at c. 3225 Gy (Fig. 3.4c; after Avram et al., 2020). The D_e's of all the samples fall between 88-92%, which is greater than $2D_o$. D_o refers to the characteristic dose obtained from the exponential function used to fit the dose response curve and $2D_o$ refers to the dose value defined as 85% of maximum intensity for quartz OSL signal (Wintle and Murray, 2006). The $2D_o$ value is recommended as the upper limit for quartz OSL dating as any uncertainty in the natural signal leads to a higher asymmetric uncertainty in the evaluated D_e values (Wintle and Murray, 2006). Since, no such equivalent criteria exists for pIRIR signals, we evaluate our samples based on the same criteria as quartz OSL. Therefore, the $pIRIR_{290}$ ages from TAU and MAL are considered as minimum ages and are summarised in Table A3.

1.3. Dose rate calculations

Environmental radiation dose rates were calculated from the U, Th and K concentrations obtained from bulk sediment samples using high resolution gamma spectrometry. Radionuclide concentrations were converted to dry dose rates using conversion factors of Guerin et al. (2011). The in-situ moisture in the samples varied between 5-12% and the saturated water content varied between 15-25% for all sample, hence the dose rates for all the samples were attenuated for moisture using in-situ water content of 10 ± 5%. The cosmic ray component of the dose rates was determined from sample depths and uniform values for sediment density and site altitude, latitude and longitude, following Prescott and Hutton (1994). An alpha efficiency value (a-value) of 0.038 ± 0.002 for fine grained quartz and 0.086 ± 0.004 for poly mineral fine grains was utilised for all calculations (Rees-Jones, 1995). Given the size of fine grains (4-11), the contribution of internal alpha activity to dose rate is assumed to be negligibly small and ignored for all calculations. All dose rate calculations were performed using DRAC v.1.2 (Durcan et al., 2015). The radionuclide activities of U and Th

were evaluated for possible disequilibrium and the results are presented in Table A4 and discussed in section 1.3.2.

1.3.1. Water content of loess samples

The measured water content of most samples from the study sites varies from 5-12%. The sampling for luminescence dating samples was done during the summer of 2017 and there is a possibility that the measured *in situ* water content from the samples are underestimated due to evaporation following the cleaning of the section and storage of the samples. Water saturation experiments performed on sediments from the study sites suggests a maximum water saturation of 20±5 %. Hence, we utilise a water content of 10±5% for all our dose rate calculations (Buylaert et al., 2015; Li et al., 2016b).

1.3.2. Disequilibrium

The radionuclide activities ($Bq.kg^{-1}$) and daughter to parent ratios obtained by high resolution gamma spectrometry of ^{238}U and ^{232}Th decay chains from all the samples are summarised in Table A4. We investigate the secular disequilibrium assumption in the ^{238}U decay chain by assessing the ratio of the activity concentrations of ^{210}Pb to ^{226}Ra. ^{210}Pb:^{226}Ra activity ratios indicate long term in-situ loss of ^{222}Rn during burial time. The gamma dose rate for all the samples in this study was calculated assuming secular equilibrium. If the level of disequilibrium, as seen in the activity ratios of ~0.8 for ^{210}Pb:^{226}Ra in Table A4 had existed throughout the burial period, then the total dose rate would be ~2% lower than the ones calculated here (based on Olley et al, 1996). Such a change in dose rate would not affect the ages significantly and would be consistent within a 2σ error limit.

2. Assumptions and considerations: Age-depth modelling and mass accumulation rates

2.1. Optical ages for age depth modelling

A total of 33 loess sites, 14 sites from the Ili basin (including 3 sites from this study), 8 sites from other neighbouring basins in Arid Central Asia (ACA) and 11 representative sites from the Chinese loess Plateau (CLP) were chosen for this study. Table A5 contains a summary of the sites evaluated in this study as well as the references from where the optical ages have been obtained. To ensure a meaningful and robust comparison of MAR between the sites, only sites with a high resolution (≤ 1.5 m) absolute chronology were selected. Luminescence ages based on quartz OSL and feldspar pIRIR signal were evaluated for a period of 60-0 kyr. We did not consider any luminescence ages based on IR_{50} signal as well as any radiocarbon ages for purposes of age-depth modelling.

2.2. Bacon modelling parameters

Bayesian age depth modelling was performed using R package Bacon (Blaauw and Christen, 2011) using optical ages from various sites summarised in Table A5. Bacon uses Bayesian statistics to reconstruct accumulation histories for deposits by combining absolute ages with prior information like accumulation rate and its variability over time (memory, derived from autocorrelation). Inverse accumulation rates (sedimentation times, yrs.cm^{-1}) are estimated from millions of Markov Chain Monte Carlo (MCMC) iterations, and these rates form the age depth model. Th Inverse accumulation rates are controlled by prior information which have been set with default values: accumulation shape = 1.5 and accumulation mean = 20 for the gamma distribution and memory mean =0.7 and memory strength =4 for beta distribution, that describe the memory effects or autocorrelation of the inverse sedimentation rates. The thickness parameter in bacon is set as 10 or 20 depending on the length of the profile being analysed. In cases where hiatuses have been identified by the authors, relevant changes were made to specify hiatuses at given depths in the model. In case of hiatuses >10 ka years, the bacon model was run to get individual age vs depth model for each section within the site.

The resulting modelled depths and weighted mean ages from the Bacon-derived age-depth models were used to evaluate sedimentation rates (cmka^{-1}; SR) according to the equation:

$$SR = \frac{d_2 - d_1}{t_2 - t_1}$$

Where, d_2, d_1 and t_2, t_1 refer to consecutive depths and corresponding modelled mean ages respectively.

Comparison of past dust records from different loess deposits with each other and with other global dust flux records from ice cores and ocean sediments requires the evaluation of loess mass accumulation rates (MAR, gm^{-2}a^{-1}), which are computed using the equation:

$$MAR = SR \times \rho_{dry} \times f_{eol}$$

where SR refers to sedimentation rate (m/a), ρ_{dry} is the dry bulk density (gm^{-3}) and f_{eol} refers to the sediment fraction that is aeolian in nature (Kohfield and Harrison, 2000); f_{eol} = 1 for all calculations, since we assume that loess is almost entirely aeolian in nature. Dry bulk density for sediments varies with nature of sediment, depth and grain size; the systematic use of these parameters in previously published literature is based on approximate estimates from the region or on values from neighbouring loess sites. Furthermore, information on down-section variation of dry bulk density in loess is sparse and usually a constant value is assumed for an entire profile. In all the sites evaluated in this study, most studies use dry bulk density values based on approximate regional estimates, which vary from 1.2 gcm^{-3} (in palaeosols)

upto 1.8 gcm^{-3} (in loess) depending on the site and region (ACA: Jia et al., 2018; Wang et al., 2019; Li et al., 2019b; CLP: Kohfeld and Harrison, 2003). This variation can alone add an uncertainty of upto 20% to the MAR values at the site. We keep this in mind while drawing conclusions based on comparison of MAR's between different sites.

Sites where, high deposition occurs during short time intervals (e.g. XEBLK - Li et al, 2016a, ASH - this study) can lead to a modelled dataset with high frequency variations (noise) around the mean value. In such cases for simplicity and better representation, we use a 10-point running average through the dataset. Our evaluation of MAR's from luminescence ages for most sites agrees (1σ uncertainty) with that evaluated by the respective authors of the original work. The differences (where applicable) occur due to the statistical approach utilised for age-depth modelling.

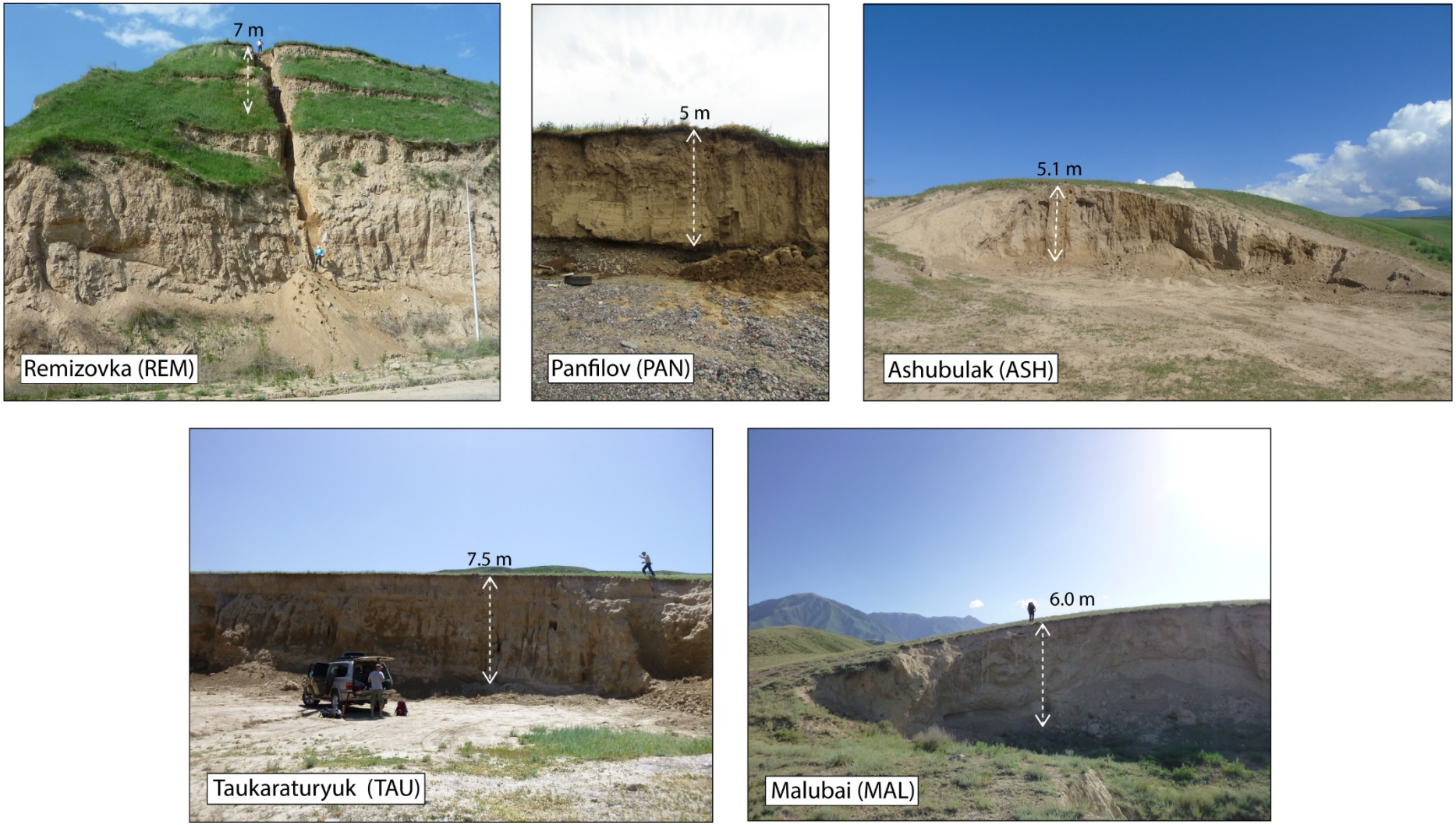

Fig. A1. Loess sites under study in the Ili basin of SE Kazakhstan.

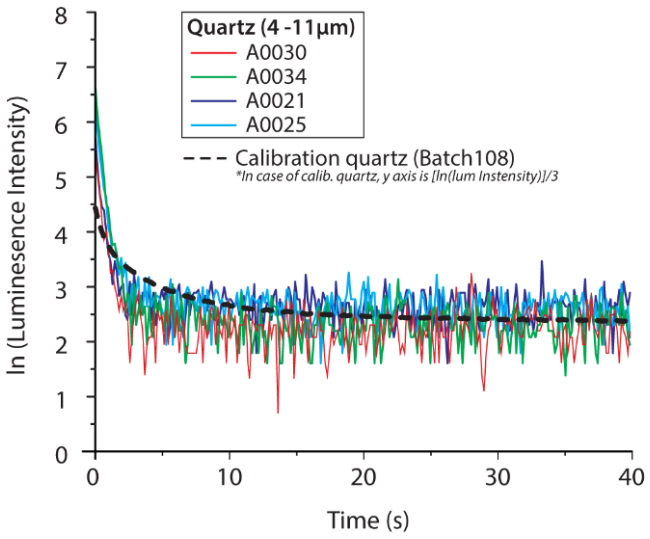

Fig. A2. Comparison of quartz OSL signal behaviour of fine grain calibration quartz with that from Central Asian loess sites, PAN and ASH.

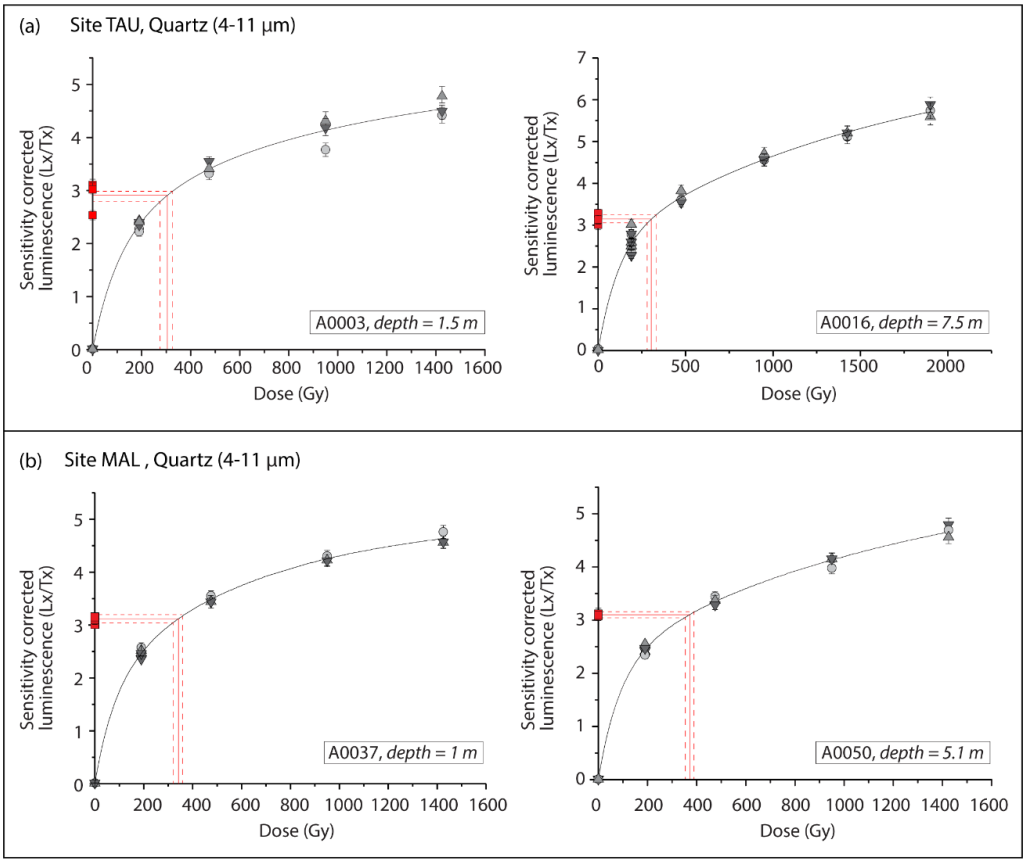

Fig. A3. Dose response curves (DRC) constructed at high doses (upto c.1500 Gy) in fine grain quartz from (a) site TAU and (b) site MAL. The DRCs were fitted using the sum of two saturating exponentials.

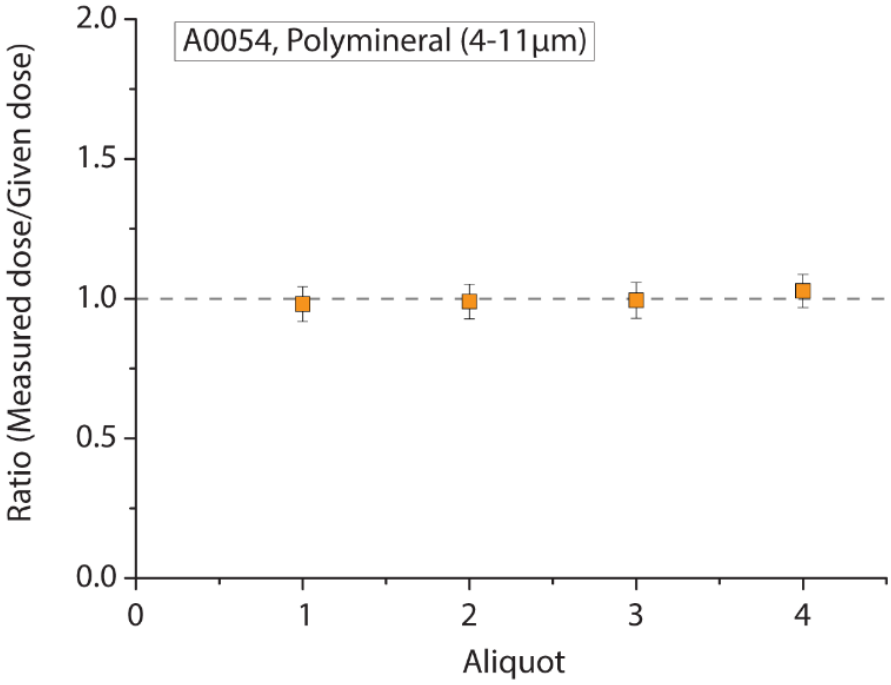

Fig. A4. Dose recovery tests for fine grained polymineral sample A0054 from site MAL.

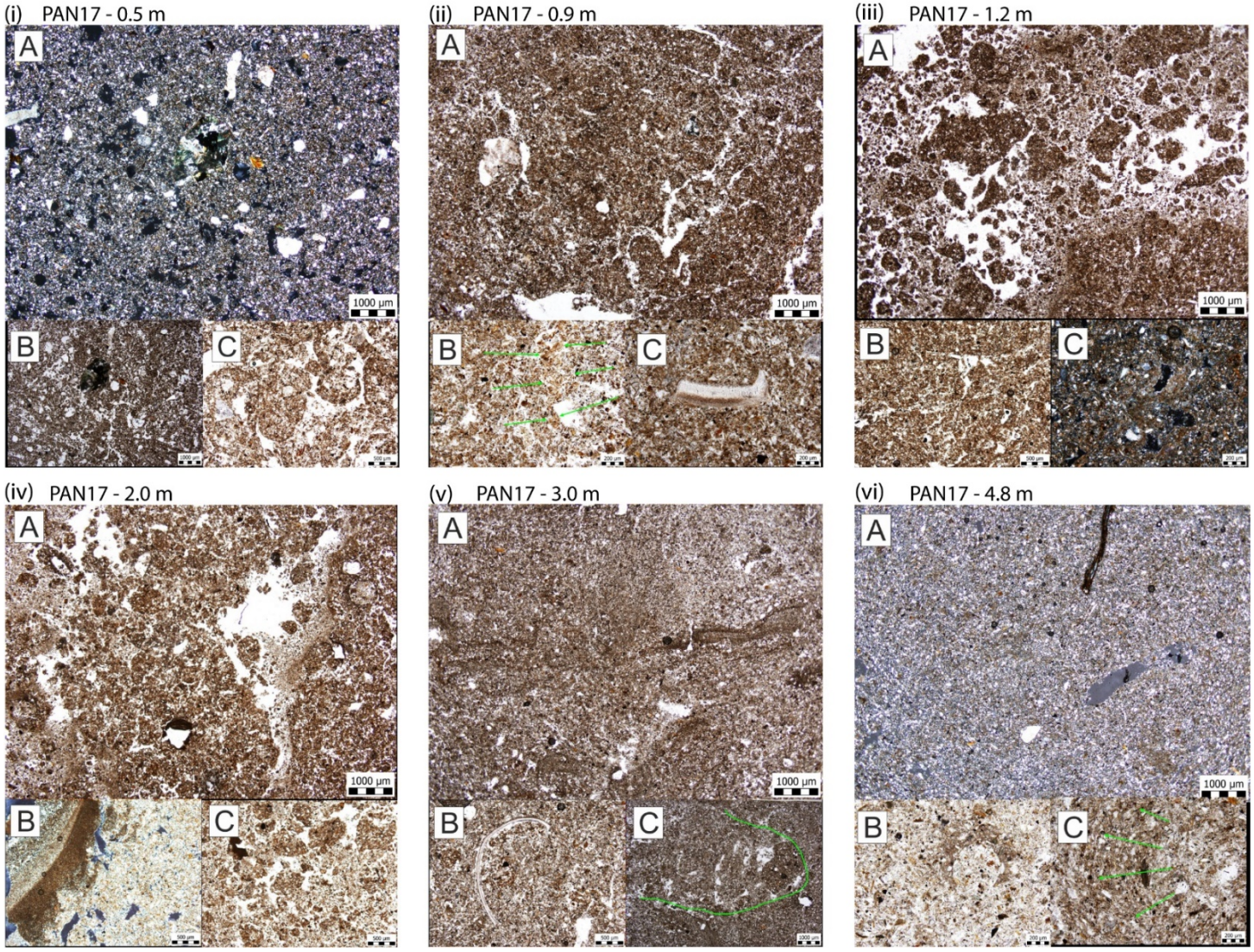

Fig. A5. Microphotographs of thin sections from profile PAN **(i)** PAN17-0.5 m: **A)** unsorted matrix (XPL). **B)** same photograph showing highly bioturbated matrix (PPL). **C)** excremental features (PPL).

(ii) PAN17-0.9 m: **A)** matrix with cracks, possibly a product of bioturbation (PPL**). B)** decomposed organic matter, probably root relict (PPL). **C)** shell fragment (PPL).

(iii) PAN17-1.2 m: **A)** Granular microstructure – problem in sampling? (PPL). **B)** passage features (PPL). **C)** vughs with hypocoating preserved within the aggregate (XPL).

(iv) PAN17-2.0 m: **A)** matrix rich in depletion features and redeposited soil crusts (PPL). **B)** Soil crust (XPL). **C)** silty aggregate fragments (PPL).

(v) PAN17-3.0 m: **A)** unsorted material with common presence of redeposited soil crusts (PPL). **B)** shell fragment (PPL). **C)** bioturbation (PPL).

(vi) PAN17-4.8 m: **A)** homogenous silty loam influenced by bioturbation (XPL). **B)** rare hypocoating (XPL). **C)** bioturbation (PPL).

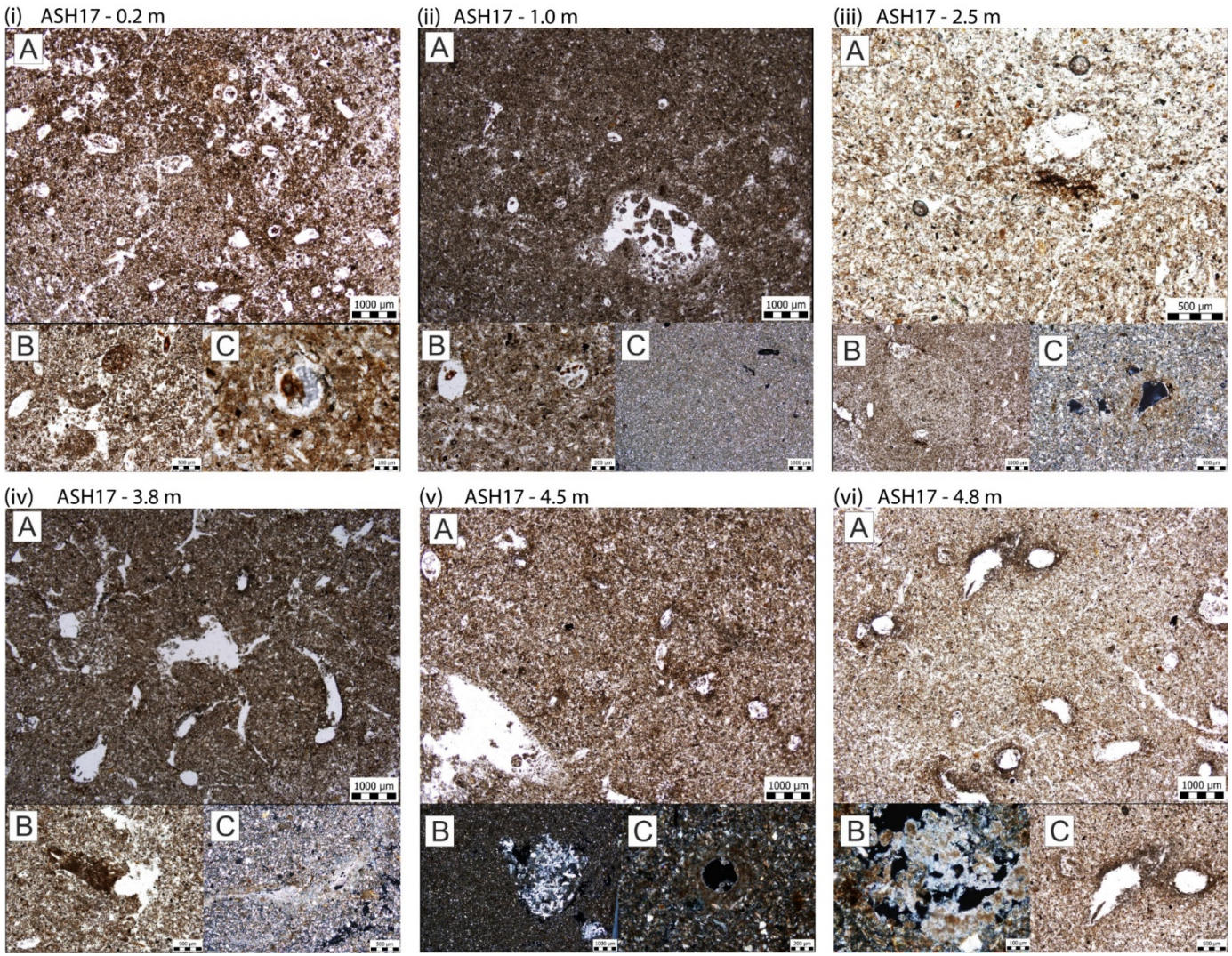

Fig. A6. Microphotographs of thin sections from profile ASH **(i)** ASH17-0.2 m: **A)** matrix influenced strongly by bioturbation (PPL). **B)** excremental features (PPL). **C)** multi-layered hypocoating with the root in the centre (PPL).

(ii) ASH17-1.0 m: **A)** homogenous silty loam influenced by bioturbation (PPL). **B)** Fresh roots preserved (PPL). **C)** homogeneous sorted matrix (XPL).

(iii) ASH17-2.5 m: **A)** dark brown concentrations of decomposed organic matter (PPL). **B)** calcium carbonate impregnations (XPL). **C)** hypocoating (XPL).

(iv) ASH17-3.8 m: **A)** homogeneous silty loam matrix with common bioturbation features (PPL). **B)** rare presence of soil crusts (PPL). **C)** calcium carbonate infill with possible presence of lublinite (XPL).

(v) ASH17-4.5 m: **A)** homogeneous silty loam matrix with common vughs and hypocoatings (PPL). **B)** gypsum crystals (XPL). **C)** calcium carbonate hypocoating (XPL).

(vi) ASH17-4.8 m: **A)** homogenous silty loam matrix with common vughs and hypocoatings (PPL). **B)** lublinite void infills (XPL). **C)** calcium carbonate hypocoating (XPL).

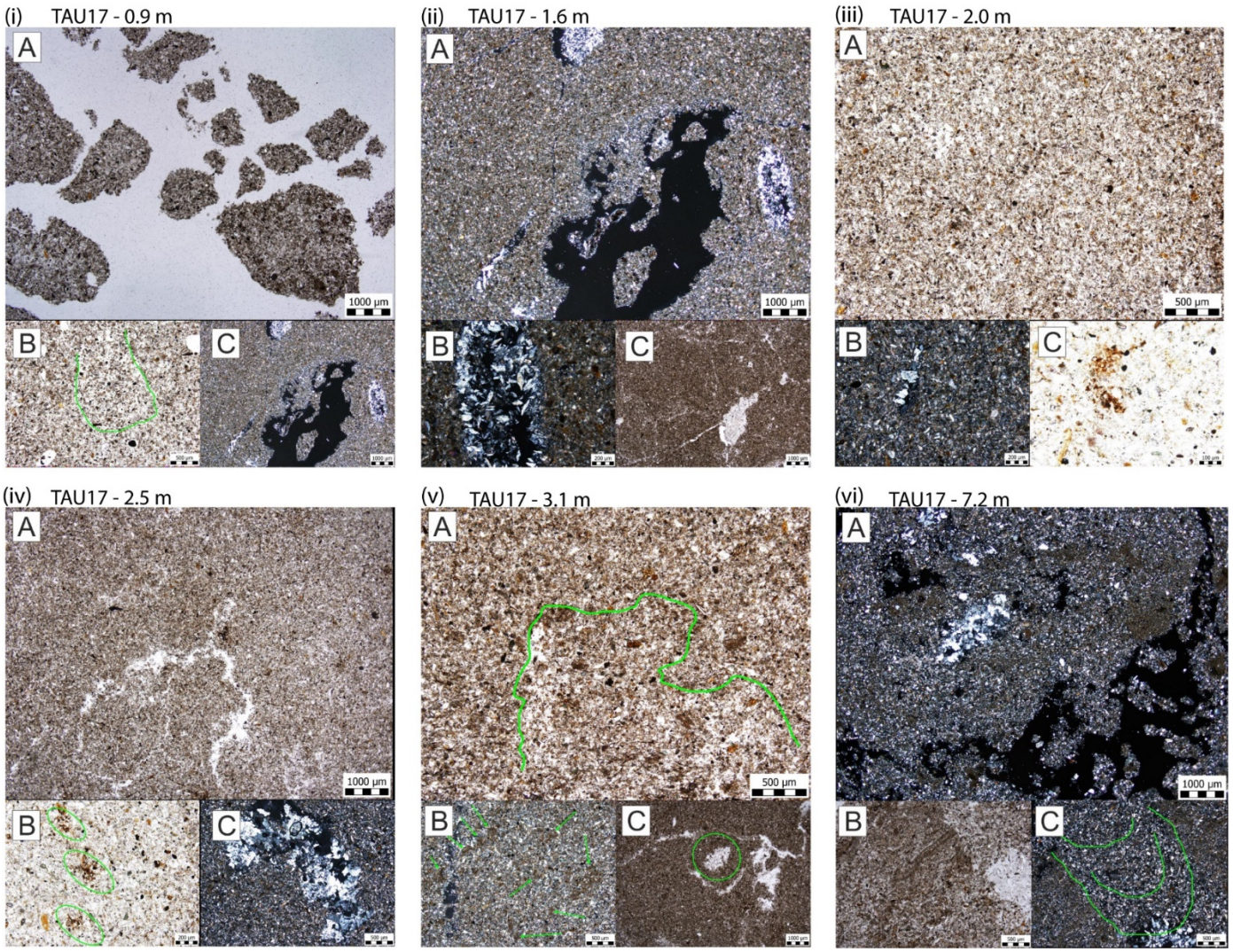

Fig. A7. Microphotographs of thin sections from site TAU **(i)** TAU17-0.9 m: **A)** granular microstructure – possibly a sampling error (PPL). **B)** passage features (PPL). **C)** vughs preserved within the aggregates and root fragments *(in green)* (PPL).

(ii) TAU17-1.6 m: **A)** homogeneous silty loam influenced by gypsum crystal growth (XPL). **B)** calcium carbonate impregnations (XPL). **C)** cracks as a result of crystal growth (PPL).

(iii) TAU17-2.0 m: **A)** homogeneous silty loam influenced by gypsum crystal growth (XPL). **B)** gypsum crystal growth (XPL). **C)** rare decomposed organic matter (PPL).

(iv) TAU17-2.5 m: **A)** homogenous silty loam matrix with cracks (XPL). **B)** decomposed organic matter (PPL). **C)** gypsum crystal growth (XPL).

(v) TAU17-3.1 m: **A)** homogeneous silty loam influenced by bioturbation (PPL). **B)** silty aggregates (XPL). **C)** subangular blocky microstructure and gypsum crystal growth *(green circle)* (PPL).

(vi) TAU17-7.2 m: **A)** packing voids through unsorted matrix rich in soil crust and gypsum crystal growth (XPL). **B)** soil crusts and gypsum crystal growth (PPL). **C)** bioturbation (XPL).

Table A1. Micromorphological description of selected samples from three loess sites (PAN, ASH and TAU) in the Ili basin, SE Kazakhstan.

Site	Micromorphological description of selected samples							
	Selected Sample (depth, m)	Fabric						Pedogenic features
		Microstructure	Matrix	Grain size description	Minerals	Roundness	Other features	
Panfilov (PAN)	0.5 m Fig. A5(i)	Complex microstructure (combination of granular and channel) with the simple packing, compound packing voids, channels and vughs.	Colour - Dark brown to brown; Bf - crystallitic	Unsorted with double spaced porphyric distribution; GSD corresponds to sandy loam with c/f$_{(50\mu m)}$= 60:40	Qzt, Ptg, aluminosilicate and opaque minerals	SR; some angular to sub-angular rock fragments	Decomposed organic matter, relicts of fresh roots	Passage and excremental features
	0.9 m Fig. A5(ii)	Complex microstructure with the cracks, vughs and channels.	Colour - brown; Bf-crystallitic	Moderately sorted with porphyric distribution; GSD corresponds to silty loam with c/f$_{(50\mu m)=}$ 40:60	Qzt, Ptg, aluminosilicate and opaque minerals	SR; some angular rock fragments	Decomposed organic matter, relicts of fresh roots, presence of shell fragments	Passage features, hypocoatings
	1.2 m Fig. A5(iii)	Presence of granular microstructure (problematic sampling issue?). Preserved pores most likely reflect the complex packing void; few vughs preserved within aggregates.	Colour - grey brown; Bf-crystallitic	Well sorted with porphyric distribution; GSD corresponds to silty loam with c/f$_{(50\mu m)=}$ 30:70	Qzt, Ptg, aluminosilicate and opaque minerals	SR	Decomposed organic matter	Rare passage features, hypocoatings
	2.0 m Fig. A5(iv)	Complex microstructure with complex packing voids and chambers; few vughs and channels are also preserved.	Colour - grey brown to brown, Bf - crystallitic	Moderately sorted to unsorted with double spaced porphyric distribution; GSD corresponds to silty loam with c/f$_{(50\mu m)}$= 40:60	Qzt, Ptg, aluminosilicate and opaque minerals	SR	Decomposed organic matter	Passage features, depletion features, calcium carbonate impregnations, redeposited soil crusts

	3.0 m Fig. A5(v)	Complex microstructure with the complex packing void, few vughs and cracks	Colour - Patchy brown and dark brown phases; Bf-crystallitic	Unsorted with the porphyric double spaced distribution; GSD corresponds to the sandy loam withc/$f_{(50\mu m)}$=60:40; presence of silty aggregates (compose 10% of sandy fraction)	Qzt, Ptg, aluminosilicate and opaque minerals	SR	Decomposed organic matter	Passage features, calcium carbonate impregnations, fragmented and redeposited soil crusts
	4.8 m Fig. A5(vi)	Complex microstructure with the few vughs, chambers and and channels, with a low amount of pores.	Colour - grey brown; Bf-crystallitic	Well sorted with the porphyric distribution and GSD corresponds to the silty loam withc/f $_{(50\mu m)}$= 60:40;presence of silty aggregates (compose 10% of sandy fraction)	Qzt, Ptg, aluminosilicate and opaque minerals	SR	Decomposed organic matter	Rare passage features
Ashubulak (ASH)	0.2 m Fig. A6(i)	Complex microstructure (combination of granular and channel) simple packing voids, compound packing voilds, channels and few vughs.	Colour - dark brown; Bf-crystallitic	Well sorted with porphyric distribution; GSD correspond to silty loam with c/$f_{(50\mu m)}$= 30:70.	Qzt, Ptg, aluminosilicate and opaque minerals	SR	Decomposed organic matter	Passage features, excremental features, partial and multilayered hypocoating.
	1.0 m Fig. A6(ii)	Complex microstructure with the complex packing void, few cracks, vughs and channels	Colour - grey brown; Bf-crystallitic	Well sorted with porphyric distribution and GSD corresponds to the silty loam with c/$f_{(50\mu m)}$= 30:70	Qzt, Ptg, aluminosilicate and opaque minerals	SR	Decomposed organic matter	Passage features
	2.5m Fig. A6(iii)	Channel microstructure with channels, vughs and chambers	Colour-brown with local dark brown patches; Bf-	Moderately sorted with porphyric distribution and GSD corresponds to silty loam with c/$f_{(50\mu m)}$=	Qzt, Ptg, aluminosilicate and opaque minerals	SR	Decomposed organic matter as black dotting	Passage features, calcium carbonate illuviation, hypocoating

			crystallic	30:70				
	3.8 m Fig. A6(iv)	Complex microstructure with the complex packing void, cracks, vughs and channels. Pores are very common	Colour - grey brown; Bf- crystallitic	Well sorted with porphyric distribution; GSD corresponds to the silty loam with the $c/f_{(50\mu m)}$= 30:70	Qzt, Ptg, aluminosilicate and opaque minerals	SR	Decomposed organic matter, relicts of fresh roots, rare presence of soil crusts	Passage features, hypocoating, infilling
	4.5 m Fig. A6(v)	vughy/channel microstructure with the vughs and channels.	Colour - grey brown; Bf- crystallitic	Well sorted with the porphyric distribution; GSD corresponds to the silty loam with $c/f_{(50\mu m)}$= 30:70	Qzt, Ptg, aluminosilicate and opaque minerals	SR	Decomposed organic matter, relicts of fresh roots	Rare passage features, hypocoating, gypsum crystal growth
	4.8 m Fig. A6(vi)	Channel microstructure with the vughs and channels.	Colour - grey brown; Bf- crystallitic	Well sorted with the porphyric distribution; GSD corresponds to the silty loam with $c/f_{(50\mu m)}$= 30:70	Qzt, Ptg, aluminosilicate and opaque minerals	SR	Decomposed organic matter, occasional relicts of fresh roots	Rare passage features, hypocoating, lignite void infillings, gypsum crystal growth
Taukaraturyuk (TAU)	0.9 m Fig. A7(i)	Granular microstructure (product of problematic sampling?). Preserved pores may be because of the complex packing void; few vughs preserved within the aggregates.	Colour - grey brown; Bf- crystallitic	Well sorted with the porphyric distribution; GSD corresponds to the silty loam with $c/f_{(50\mu m)}$= 30:70	Qzt, Ptg, aluminosilicate and opaque minerals	SR	Decomposed organic matter	Rare passage features
	1.6 m Fig. A7(ii)	Complex microstructure with the chambers and cracks.	Colour - grey brown; Bf - crystallitic	Well sorted with porphyric distribution and GSD corresponds to silty loam with with $c/f_{(50\mu m)}$= 30:70	Qzt, Ptg, aluminosilicate and opaque minerals, gypsum	SR, except gypsum crystals	Decomposed organic matter	Gypsum crystallisation

	2.0 m Fig. A7(iii)	Massive microstructure with only rare vughs	Colour - grey brown; Bf - crystallitic	Well sorted with the porphyric distribution and GSD corresponds to the silty loam with $c/f_{(50\mu m)}$= 30:70.	Qzt, Ptg, alumosilicate and opaque minerals, gypsum	SR, except gypsum crystals	Decomposed organic matter	Gypsum crystallisation
	2.5 m Fig. A7(iv)	Massive to cracky microstructure with only rare vughs	Colour - grey brown; Bf - crystallitic	Well sorted with the porphyric distribution and GSD corresponds to the silty loam with $c/f_{(50\mu m)}$= 30:70.	Qzt, Ptg, alumosilicate and opaque minerals, gypsum	SR, except gypsum crystals	Decomposed organic matter as black dotting, brownish organic matter	Occasional gypsum crystallisation
	3.1 m Fig. A7(v)	Subangular blocky microstructure with the complex packing void, few vughs and channels.	Colour - grey brown; Bf - crystallitic	Well sorted with porphyric distribution and GSD correspond to the silty loam with $c/f_{(50\mu m)}$= 60:40; presence of silty aggregates (compose up to 10 % of the sandy fraction)	Qzt, Ptg, alumosilicate and opaque minerals, gypsum	SR, except gypsum crystals	Decomposed organic matter	Rare passage features and gypsum crystal growth
	7.2 m Fig. A7(vi)	Subangular blocky microstructure with the complex packing void, chambers, plates as a part of fragmented soil crusts, few vughs and channels	Colour - Patchy brown and dark brown phases; Bf - crystallitic	Unsorted with porphyric double spaced distribution and GSD correspond to the sandy loam with the $c/f_{(50\mu m)}$= 60:40; coarse fraction mainly composed of soil fragments, gypsum crystals and rock fragments	Qzt, Ptg, alumosilicate and opaque minerals, gypsum, rock fragments	SR, except gypsum crystals	Decomposed organic matter	Passage features, calcium carbonate illuviation and local impregnations, fragmented and redeposited soil crust, gypsum crystal growth

*Terms: *Qzt* – quartz; *SR* – subrounded; *Bf* - Bifringence; *GSD* - Grain size distribution

Table A2. (a) DSAR and (b) SAR protocol used in the study for D_e determinations of fine-grained quartz grains (c) $pIR_{50}IR_{290}$ protocol used for the measurement of polymineral fine grains.

(a) Double-SAR protocol (Modified from Banerjee et al, 2001)		
Step	Treatment	Signal measured
1	Dose (Natural or laboratory)	-
2	Preheat 10s at 260 ^oC	
3	IR, 100s at 50^oC	
4	Blue OSL, 40s at 125 ^oC	L_n, or L_x
5	Test dose	
6	Cut heat 10s at 240 ^oC	
7	IR, 100s at 50^oC	
8	Blue OSL, 40s at 125 ^oC	T_n or T_x
9	Blue OSL, 40s 280 ^oC	

(b) SAR protocol (Murray and Wintle, 2000)		
Step	Treatment	Signal measured
1	Dose (Natural or laboratory)	-
2	Preheat 10s at 260 ^oC	
3	Blue OSL, 40s at 125 ^oC	L_n, or L_x
4	Test dose	
5	Cut heat 10s at 240 ^oC	
6	Blue OSL, 40s at 125 ^oC	T_n or T_x
7	Blue OSL, 40s 280 ^oC	
8	Return to step 1	

(c) $pIR_{50}IR_{290}$ protocol (after Thiel et al, 2011)		
Step	Treatment	Signal measured
1	Dose (Natural or laboratory)	-
2	Preheat 60s at 320 ^oC	
3	IRSL, 200s at 50^oC	
4	IRSL, 200s at 290 ^oC	L_n or L_x
5	Test dose	
6	Preheat 60s at 320 ^oC	
7	IRSL, 200s at 50^oC	T_n or T_x
8	IRSL, 200s at 290 ^oC	
9	IRSL, 100s at 325 ^oC	
10	Return to step 1	

Table A3. Equivalent dose, dose rate and post $IR_{50}IRSL_{290}$ ages on polymineral fine grains from the Ili basin study sites. The term n_e/n_t refers to the total number of accepted discs to the total number of discs measured

Site	Sample No.	Depth (m)	Moisture attenuated dose rate (Gy/ka)			Cosmic (Gy/ka)	Total Dose Rate (Gy/ka)	n_e/n_t	D_e (Gy)	Age (ka)
			Alpha	Beta	Gamma					
Taukaraturyuk (TAU)	A003	1.5 ± 0.05	1.1 ± 0.1	2.0 ± 0.1	1.2 ± 0.1	0.20 ± 0.02	4.5 ± 0.2	8/12	896.6 ± 54.0	197.6 ± 21.2
	A007	3.5 ± 0.05	1.3 ± 0.1	2.2 ± 0.2	1.3 ± 0.1	0.15 ± 0.02	5.1 ± 0.3	5/5	953.5 ± 65.7	188.7 ± 22.8
	A0012	6.0 ± 0.05	1.3 ± 0.1	2.3 ± 0.2	1.4 ± 0.1	0.11 ± 0.01	5.1 ± 0.2	5/5	1004.4 ± 66.9	197.3 ± 22.3
	A0016	7.5 ± 0.05	1.2 ± 0.1	2.3 ± 0.2	1.3 ± 0.1	0.10 ± 0.01	4.9 ± 0.2	5/5	1017.9 ± 63.5	207.7 ± 22.3
Malubai (MAL)	*A0037**	*1.0 ± 0.05*	*1.3 ± 0.2*	*2.0 ± 0.2*	*1.2 ± 0.1*	*0.21 ± 0.02*	*4.7 ± 0.2*	*4/4*	*959.0 ± 55.8*	*204.9 ± 22.8*
	A0037[#]	1.0 ± 0.05	–	–	–	–	6.0 ± 0.3	4/4	959.0 ± 55.8	158.5 ± 17.0
	A0038	1.5 ± 0.05	1.8 ± 0.2	2.5 ± 0.2	1.6 ± 0.1	0.20 ± 0.02	6.0 ± 0.3	3/3	1031.5 ± 83.6	170.5 ± 22.2
	A0040	2.4 ± 0.05	1.6 ± 0.2	2.5 ± 0.2	1.5 ± 0.1	0.18 ± 0.02	5.7 ± 0.3	4/5	1111.1 ± 98.6	195.0 ± 27.0
	A0050	5.1 ± 0.05	1.6 ± 0.2	2.5 ± 0.2	1.6 ± 0.1	0.13 ± 0.01	5.8 ± 0.3	4/5	1040.1 ± 91.0	179.3 ± 25.0

*Sample A0037 originally (in italics) has an unusually low Uranium content (See supplementary Table A4) compared to the rest of the section.

[#]We use the dose rate of the sample below A0037 (here A0038) to evaluate the more likely age of the sample.

Table A4. Radionuclide activities ($Bq.kg^{-1}$) and daughter to parent ratios obtained from high resolution gamma spectrometry measurements of the ^{238}U and ^{232}Th decay chains.

Sample No.	Depth (m)	^{238}U-Chain ($Bq.kg^{-1}$)			^{232}Th Chain ($Bq.kg^{-1}$)			Ratios - U chain		Ratios - Th	
		^{238}U	^{226}Ra	^{210}Pb	^{232}Th	^{228}Ra	^{228}Th	$^{226}Ra/^{238}U$	$^{210}Pb/^{226}Ra$	$^{228}Ra/^{232}Th$	$^{228}Th/^{228}Ra$
A0017	1	35 ± 5	43.5 ± 2.6	35 ± 4	47.1 ± 2.9	48 ± 3	46.6 ± 2.9	1.24	0.80	1.02	0.97
A0019	2	34 ± 4	36.9 ± 2.3	32 ± 4	42.4 ± 2.5	40 ± 3	43 ± 2.8	1.09	0.87	0.94	1.08
A0021	3	40 ± 5	39.5 ± 2.3	31 ± 4	44.2 ± 2.7	45 ± 3	44 ± 2.8	0.99	0.78	1.02	0.98
A0023	4	41 ± 5	39.7 ± 2.5	32 ± 4	43.2 ± 2.8	43 ± 3	43.3 ± 2.8	0.97	0.81	1.00	1.01
A0025	5	38 ± 5	39.5 ± 2.4	37 ± 5	47 ± 3	47 ± 3	47 ± 3	1.04	0.94	1.00	1.00
A0026	0.5	29 ± 5	36.5 ± 2.2	28 ± 4	40.7 ± 2.6	42 ± 2.8	40.3 ± 2.6	1.26	0.77	1.03	0.96
A0028	1.5	46 ± 5	40.5 ± 2.5	38 ± 5	44.2 ± 2.8	43 ± 3	44.6 ± 2.9	0.88	0.94	0.97	1.04
A0030	2.5	43 ± 6	40.3 ± 2.5	32 ± 4	45.2 ± 2.9	45 ± 3	45.2 ± 2.9	0.94	0.79	1.00	1.00
A0032	3.5	38 ± 5	42.3 ± 2.5	39 ± 4	48 ± 3	47 ± 3	49 ± 3	1.11	0.92	0.98	1.04
A0034	4.5	40 ± 5	40.9 ± 2.5	33 ± 4	46 ± 3	46 ± 3	46 ± 3	1.02	0.81	1.00	1.00
A001	0.5	29 ± 4	36.4 ± 2.3	30 ± 4	41.3 ± 2.6	42 ± 3	41 ± 2.7	1.26	0.82	1.02	0.98
A002	1	37 ± 5	44.2 ± 2.6	41 ± 5	47 ± 2.9	48 ± 3	46.7 ± 2.9	1.19	0.93	1.02	0.97
A003	1.5	46 ± 5	40.5 ± 2.4	36 ± 4	39.5 ± 2.5	39.1 ± 2.7	39.6 ± 2.5	0.88	0.89	0.99	1.01
A007	3.5	56 ± 5	50 ± 2.8	43 ± 4	42.8 ± 2.6	43 ± 3	43 ± 3	0.89	0.86	1.00	1.00
A0012	6	54 ± 5	48.1 ± 2.8	43 ± 4	45.3 ± 2.8	46 ± 3	45.2 ± 2.8	0.89	0.89	1.02	0.98
A0016	7.5	44 ± 4	41.2 ± 2.3	36 ± 3	47.4 ± 2.9	48 ± 3	47.3 ± 2.9	0.94	0.87	1.01	0.99
A0037	1	59 ± 6	58 ± 3	47 ± 5	36.5 ± 2.3	36.4 ± 2.5	36.5 ± 2.3	0.98	0.81	1.00	1.00
A0038	1.5	97 ± 8	60 ± 3	42 ± 5	38.4 ± 2.4	39 ± 2.6	38.3 ± 2.4	0.62	0.70	1.02	0.98
A0040	2.4	71 ± 8	62 ± 4	53 ± 6	45.6 ± 2.9	46 ± 3	45.6 ± 2.9	0.87	0.85	1.01	0.99
A0050	5.1	75 ± 8	60 ± 4	42 ± 5	48 ± 3	47 ± 3	48 ± 3	0.80	0.70	0.98	1.02

Table A5. List of sites from the ACA and CLP considered for age depth modelling and consequently for evaluation of MARs. The references in the table refer to the studies from which the luminescence ages for the sites have been obtained.

Site	Site names	Reference
Sites from the Ili basin, ACA		
MBK	Maibulak	Fitzsimmons et al (2017)
REM	Remizovka	This study; Fitzsimmons et al (2018)
PAN	Panfilov	This study
ASH	Ashubulak	This study
XEBLK	Xiaoerbulak	Li et al (2016)a
TLD	Talede	Kang et al (2015)
TLD16	Talede	Wang et al (2019)a
NLK	Nilka	Song et al (2015)
ZKT	Zeketai	E et al (2012)
KS15	Kunes-15	Li et al (2018)
KS15-05	Kunes15-05	Wang et al (2019)b
ZSP	Zhaoso Puma	Song et al (2012)
NLT17	Nalatizhen 17	Li et al (2020)
XY17	Xinyuan 17	Li et al (2020)
Sites from basins neighboring the Ili basin, ACA		
VAL	Valikhanova	Fitzsimmons et al (2017)
BSK	Bishkek	Youn et al (2014)
BYH10	--	Li et al (2016)b
LJW10	Lujiaowan	Li et al (2015)
SCZ17	Shichengzi	Duan et al (2020)
YM	Yumin	Li et al (2019)
TC	Tacheng	Li et al (2019)
QS16	Qingshui	Li et al (2020)
Sites from the Chinese loess Plateau		
GL	Gulang	Sun et al (2012)
JY	Jinguan	Sun et al (2012)
XF	Xifeng	Stevens et al (2016)
BGY	Beiguoyuan	Stevens et al (2008)
YB	Yuanbao	Lai and Wintle (2006)
TXD	Tuxiangdao	Buylaert et al (2008)
WN	Weinan	Kang et al (2013)
XY	Xunyi	Stevens et al (2008)
ZJC	Zhongjiacai	Buylaert et al (2008)
LC	Luochuan	Lu et al (2007)
MN	Mangshan	Qui and Zhou (2015)

References

Avram, A., Constantin, D., Veres, D., Kelemen, S., Obreht, I., Hambach, U., Marković, S. B., & Timar-Gabor, A. (2020). Testing polymineral post-IR IRSL and quartz SAR-OSL protocols on Middle to Late Pleistocene loess at Batajnica, Serbia. Boreas, 49(3), 615–633. https://doi.org/10.1111/bor.12442

Banerjee, D., Murray, A. S., Bøtter-Jensen, L., & Lang, A. (2001). Equivalent dose estimation using a single aliquot of polymineral fine grains. Radiation Measurements, 33(1), 73–94. doi: 10.1016/S1350-4487(00)00101-3

Blaauw, M., & Christen, J. A. (2011). Flexible paleoclimate age-depth models using an autoregressive gamma process. Bayesian Analysis, 6(3), 457–474. https://doi.org/10.1214/11-BA618

Buylaert, J. P., Murray, A. S., Vandenberghe, D., Vriend, M., Corte, F. D., & haute, P. V. den. (2008). Optical dating of Chinese loess using sand-sized quartz: Establishing a time frame for Late Pleistocene climate changes in the western part of the Chinese Loess Plateau. Quaternary Geochronology, 3(1), 99–113. doi: https://doi.org/10.1016/j.quageo.2007.05.003

Buylaert, J.-P., Jain, M., Murray, A. S., Thomsen, K. J., Thiel, C., & Sohbati, R. (2012). A robust feldspar luminescence dating method for Middle and Late Pleistocene sediments. Boreas, 41(3), 435–451. doi: https://doi.org/10.1111/j.1502-3885.2012.00248.x

Buylaert, J.-P., Yeo, E.-Y., Thiel, C., Yi, S., Stevens, T., Thompson, W., Frechen, M., Murray, A., & Lu, H. (2015). A detailed post-IR IRSL chronology for the last interglacial soil at the Jingbian loess site (northern China). Quaternary Geochronology, 194–199. https://doi.org/10.1016/j.quageo.2015.02.022

Cunningham, A. C., & Wallinga, J. (2010). Selection of integration time intervals for quartz OSL decay curves. Quaternary Geochronology, 5(6), 657–666. doi: 10.1016/j.quageo.2010.08.004

Duan, F., An, C., Wang, W., Herzschuh, U., Zhang, M., Zhang, H., Liu, Y., Zhao, Y., & Li, G. (2020). Dating of a late Quaternary loess section from the northern slope of the Tianshan Mountains (Xinjiang, China) and its paleoenvironmental significance. Quaternary International, 544, 104–112. https://doi.org/10.1016/j.quaint.2020.02.034

Duller, G. A. T. (2003). Distinguishing quartz and feldspar in single grain luminescence measurements. Radiation Measurements, 37(2), 161–165. https://doi.org/10.1016/S1350-4487(02)00170-1

Durcan, J. A., King, G. E., & Duller, G. A. T. (2015). DRAC: Dose Rate and Age Calculator for trapped charge dating. Quaternary Geochronology, 28, 54–61. doi: 10.1016/j.quageo.2015.03.012

E. ChongYi, Lai, Z., Sun, Y., Hou, G., Yu, L., & Wu, C. (2012). A luminescence dating study of loess deposits from the Yili River basin in western China. Quaternary Geochronology, 10, 50–55. doi: https://doi.org/10.1016/j.quageo.2012.04.022

Fitzsimmons, K. E., Iovita, R., Sprafke, T., Glantz, M., Talamo, S., Horton, K., … Taimagambetov, Z. (2017). A chronological framework connecting the early Upper Palaeolithic across the Central Asian piedmont. Journal of Human Evolution, 113, 107–126. doi: https://doi.org/10.1016/j.jhevol.2017.07.006

Fitzsimmons, K. E., Sprafke, T., Zielhofer, C., Günter, C., Deom, J.-M., Sala, R., & Iovita, R. (2018). Loess accumulation in the Tian Shan piedmont: Implications for palaeoenvironmental change in arid Central Asia. Aeolian Deposition and Earth Surface Systems, 469, 30–43. doi: 10.1016/j.quaint.2016.07.041

Frechen, M., Schweitzer, U., & Zander, A. (1996). Improvements in sample preparation for the fine grain technique. Ancient TL, 14(2), 15–17.

Galbraith, R. F., Roberts, R. G., Laslett, G. M., Yoshida, H., & Olley, J. M. (1999). Optical dating of single and multiple grains of quartz from Jinmium rock shelter, northern Australia: Part I, experimental design and statistical models. Archaeometry, 41(2), 339–364. Scopus. doi: 10.1111/j.1475-4754.1999.tb00987.x

Guérin, G., Mercier, N., & Adamiec, G. (2011). Dose-rate conversion factors: Update. Ancient TL, 29(1), 5–8.

Jackson, M. L., Sayin, M., & Clayton, R. N. (1976). Hexafluorosilicic Acid Reagent Modification for Quartz Isolation. Soil Science Society of America Journal, 40(6), 958–960. doi: 10.2136/sssaj1976.03615995004000060040x

Jain, M., & Singhvi, Ashok. K. (2001). Limits to depletion of blue-green light stimulated luminescence in feldspars: Implications for quartz dating. Radiation Measurements, 33(6), 883–892. doi: 10.1016/S1350-4487(01)00104-4

Kang, S., Wang, X., & Lu, Y. (2013). Quartz OSL chronology and dust accumulation rate changes since the Last Glacial at Weinan on the southeastern Chinese Loess Plateau: Quartz OSL chronology and dust accumulation rates, SE Chinese Loess Plateau. Boreas, 815-829. doi: 10.1111/bor.12005

Kang, S., Wang, X., Lu, Y., Liu, W., Song, Y., & Wang, N. (2015). A high-resolution quartz OSL chronology of the Talede loess over the past ∼30 ka and its implications for dust accumulation in the Ili Basin, Central Asia. Quaternary Geochronology, 30, 181–187. doi: 10.1016/j.quageo.2015.04.006

Jia, J., Liu, H., Gao, F., & Xia, D. (2018). Variations in the westerlies in Central Asia since 16 ka recorded by a loess section from the Tien Shan Mountains. Palaeogeography, Palaeoclimatology, Palaeoecology, 504, 156–161. https://doi.org/10.1016/j.palaeo.2018.05.021

Kohfeld, K. E., & Harrison, S. P. (2003). Glacial-interglacial changes in dust deposition on the Chinese Loess Plateau. Quaternary Science Reviews, 22(18), 1859–1878. https://doi.org/10.1016/S0277-3791(03)00166-5

Lai, Z.-P., & Wintle, A. G. (2006). Locating the boundary between the Pleistocene and the Holocene in Chinese loess using luminescence. The Holocene, 16(6), 893–899. doi: 10.1191/0959683606hol980rr

Li, G., Wen, L., Xia, D., Duan, Y., Rao, Z., Madsen, D. B., Wei, H., Li, F., Jia, J., & Chen, F. (2015). Quartz OSL and K-feldspar pIRIR dating of a loess/paleosol sequence from arid central Asia, Tianshan Mountains, NW China. Quaternary Geochronology, 28, 40–53. Scopus. https://doi.org/10.1016/j.quageo.2015.03.011

Li, Y., Song, Y., Lai, Z., Han, L., & An, Z. (2016)a. Rapid and cyclic dust accumulation during MIS 2 in Central Asia inferred from loess OSL dating and grain-size analysis. Scientific Reports, 6(1), 32365. doi: 10.1038/srep32365

Li, G., Rao, Z., Duan, Y., Xia, D., Wang, L., Madsen, D. B., Jia, J., Wei, H., Qiang, M., Chen, J., & Chen, F. (2016)b. Paleoenvironmental changes recorded in a luminescence dated loess/paleosol sequence from the Tianshan Mountains, arid central Asia, since the Penultimate Glaciation. Earth and Planetary Science Letters, 448, 1–12. https://doi.org/10.1016/j.epsl.2016.05.008

Li, G., Chen, F., Xia, D., Yang, H., Zhang, X., Madsen, D., Oldknow, C., Wei, H., Rao, Z., & Qiang, M. (2018). A Tianshan Mountains loess-paleosol sequence indicates anti-phase climatic variations in arid central Asia and in East Asia. Earth and Planetary Science Letters, 494, 153–163. https://doi.org/10.1016/j.epsl.2018.04.052

Li, Y., Song, Y., Yin, Q., Han, L., & Wang, Y. (2019). Orbital and millennial northern mid-latitude westerlies over the last glacial period. Climate Dynamics, 53(5–6), 3315–3324. doi: 10.1007/s00382-019-04704-5

Li, G., Yang, H., Stevens, T., Zhang, X., Zhang, H., Wei, H., Zheng, W., Li, L., Liu, X., Chen, J., Xia, D., Oldknow, C., Ye, W., & Chen, F. (2020). Differential ice volume and orbital modulation of Quaternary moisture

patterns between Central and East Asia. Earth and Planetary Science Letters, 530, 115901. https://doi.org/10.1016/j.epsl.2019.115901

Lu, Y. C., Wang, X. L., & Wintle, A. G. (2007). A new OSL chronology for dust accumulation in the last 130,000 yr for the Chinese Loess Plateau. Quaternary Research, 67(1), 152–160. doi: 10.1016/j.yqres.2006.08.003

Murray, A. S., & Wintle, A. G. (2000). Luminescence dating of quartz using an improved single-aliquot regenerative-dose protocol. Radiation Measurements, 32(1), 57–73. https://doi.org/10.1016/S1350-4487(99)00253-X

Murray, A. S., & Wintle, A. G. (2003). The single aliquot regenerative dose protocol: Potential for improvements in reliability. Radiation Measurements, 37(4), 377–381. https://doi.org/10.1016/S1350-4487(03)00053-2

Murray, A. S., Buylaert, J. P., Thomsen, K. J., & Jain, M. (2009). The effect of preheating on the IRSL signal from feldspar. Radiation Measurements, 44(5), 554–559. https://doi.org/10.1016/j.radmeas.2009.02.004

Olley, J. M., Murray, A., & Roberts, R. G. (1996). The effects of disequilibria in the uranium and thorium decay chains on burial dose rates in fluvial sediments. Quaternary Science Reviews, 15(7), 751–760. doi: 10.1016/0277-3791(96)00026-1

Prescott, J. R., & Hutton, J. T. (1994). Cosmic ray contributions to dose rates for luminescence and ESR dating: Large depths and long-term time variations. Radiation Measurements, 23(2), 497–500. doi: 10.1016/1350-4487(94)90086-8

Qiu, F., & Zhou, L. (2015). A new luminescence chronology for the Mangshan loess-palaeosol sequence on the southern bank of the Yellow River in Henan, central China. Quaternary Geochronology, 30, 24–33. doi: 10.1016/j.quageo.2015.06.014

Rees-Jones, J. (1995). Optical dating of young sediments using fine-grained quartz. Ancient TL, 13, 9–14.

Roberts, H. M., & Wintle, A. G. (2001). Equivalent dose determinations for polymineralic fine-grains using the SAR protocol: Application to a Holocene sequence of the Chinese Loess Plateau. Quaternary Science Reviews, 20(5), 859–863. doi: 10.1016/S0277-3791(00)00051-2

Song, YouGui, Lai, Z., Li, Y., Chen, T., & Wang, Y. (2015). Comparison between luminescence and radiocarbon dating of late Quaternary loess from the Ili Basin in Central Asia. Quaternary Geochronology, 30, 405–410. doi: 10.1016/j.quageo.2015.01.012

Song, Yougui, Li, C., Zhao, J., Cheng, P., & Zeng, M. (2012). A combined luminescence and radiocarbon dating study of the Ili loess, Central Asia. 13th International Conference on Luminescence and Electron Spin Resonance Dating - LED 2011 Dedicated to J. Prescott and G. Berger, 10, 2–7. doi: 10.1016/j.quageo.2012.04.005

Stevens, T., Buylaert, J.-P., Lu, H., Thiel, C., Murray, A., Frechen, M., … Zeng, L. (2016). Mass accumulation rate and monsoon records from Xifeng, Chinese Loess Plateau, based on a luminescence age model: Monsoon Records from Chinese Loess Plateau. Journal of Quaternary Science, 31(4), 391–405. doi: 10.1002/jqs.2848

Stevens, T., Lu, H., Thomas, D. S. G., & Armitage, S. J. (2008). Optical dating of abrupt shifts in the late Pleistocene East Asian monsoon. Geology, 36(5), 415. doi: 10.1130/G24524A.1

Sun, Y., Clemens, S. C., Morrill, C., Lin, X., Wang, X., & An, Z. (2012). Influence of Atlantic meridional overturning circulation on the East Asian winter monsoon. Nature Geoscience, 5(1), 46–49. doi: 10.1038/ngeo1326

Thomsen, K. J., Bøtter-Jensen, L., Denby, P. M., Moska, P., & Murray, A. S. (2006). Developments in luminescence measurement techniques. Radiation Measurements, 41(7), 768–773. doi: 10.1016/j.radmeas.2006.06.010

Thomsen, K. J., Murray, A. S., Jain, M., & Bøtter-Jensen, L. (2008). Laboratory fading rates of various luminescence signals from feldspar-rich sediment extracts. Radiation Measurements, 43(9), 1474–1486. https://doi.org/10.1016/j.radmeas.2008.06.002

Timar-Gabor, A., Buylaert, J.-P., Guralnik, B., Trandafir-Antohi, O., Constantin, D., Anechitei-Deacu, V., Jain, M., Murray, A. S., Porat, N., Hao, Q., & Wintle, A. G. (2017). Radiation Measurements, 106, 464–471. https://doi.org/10.1016/j.radmeas.2017.01.009

Wang, L., Jia, J., Zhao, H., Liu, H., Duan, Y., Xie, H., Zhang, D. D., & Chen, F. (2019)a. Optical dating of Holocene paleosol development and climate changes in the Yili Basin, arid central Asia. The Holocene, 29(6), 1068–1077. https://doi.org/10.1177/0959683619831432

Wang, L., Jia, J., Xia, D., Liu, H., Gao, F., Duan, Y., Wang, Q., Xie, H., & Chen, F. (2019)b. Climate change in arid central Asia since MIS 2 revealed from a loess sequence in Yili Basin, Xinjiang, China. Quaternary International, 502, 258–266. https://doi.org/10.1016/j.quaint.2018.02.032

Wintle, A. G., & Murray, A. S. (2006). A review of quartz optically stimulated luminescence characteristics and their relevance in single-aliquot regeneration dating protocols. Radiation Measurements, 41(4), 369–391. doi: 10.1016/j.radmeas.2005.11.001

Youn, J. H., Seong, Y. B., Choi, J. H., Abdrakhmatov, K., & Ormukov, C. (2014). Loess deposits in the northern Kyrgyz Tien Shan: Implications for the paleoclimate reconstruction during the Late Quaternary. Catena, 117, 81–93. doi: https://doi.org/10.1016/j.catena.2013.09.007

Zhang, J. F., & Zhou, L. P. (2007). Optimization of the 'double SAR' procedure for polymineral fine grains. Radiation Measurements, 42(9), 1475–1482. doi: 10.1016/j.radmeas.2007.06.007

Zhang, J.-F., Fan, C.-F., Wang, H., & Zhou, L.-P. (2007). Chronology of an oyster reef on the coast of Bohai Bay, China: Constraints from optical dating using different luminescence signals from fine quartz and polymineral fine grains of coastal sediments. Quaternary Geochronology, 2(1), 71–76. doi: 10.1016/j.quageo.2006.05.027

Appendix B

Supplementary information for Chapter 4

A novel proxy for tracking the provenance of dust based on paired E'-peroxy paramagnetic defect centres in fine-grained quartz

Introduction

The supplementary information of this paper contains two main texts

(i) Text 1 gives a detailed account of the sampling methodology, geomorphic setting and stratigraphy of the sites in section 1.1. The sample preparation, measurement protocols and parameters and instrumentation are described in Section 1.2 and 1.3 of this appendix.

(ii) Text 2 is an extended description of the experiments conducted in this study. The results of these experiments are discussed in the main paper (Chapter 4).

1. Materials and Methods

1.1. Sampling and Stratigraphy

We sampled a total of 114 sediment samples from five loess sections located in southeast (SE) Kazakhstan and the Tajik depression in Tajikistan. Of these, four loess sections (*PAN*-Panfilov, *ASH*-Ashubulak, *TAU*-Taukaraturyuk, and *MAL*-Malubai) are located along a c.200 km east-west transect in the piedmonts of the Zalisky Alatau in the Ili basin of SE Kazakhstan. One loess section, Karamaidan (KAR), is located in the northern margins of the Tajik depression in Tajikistan (Fig. 4.1). We undertook sampling of vertically exposed loess sections by abseil to ensure continuous down-profile stratigraphic observation and sampling. To prevent contamination by recent sediment movement, all the sections were cleaned back by at least 1-1.5 m to expose a clean, undisturbed section for sampling. Samples for Electron Spin Resonance (ESR) measurements were collected in a manner similar to that employed for luminescence dating, i.e., by hammering opaque steel tubes (10 cm-long, 3.5 cm-wide) into freshly cleaned loess sections. Samples at each of the Kazakh sites were sampled down-profile, every c. 0.3 to 0.5 m. A total of 59 samples were collected from four sites in the Ili basin of Kazakhstan, of which 10 samples were taken from PAN, 10 from ASH, 16 from TAU and 23 from MAL (16 samples from profile MAL-A and 7 samples from profile MAL-B). While

a total of 55 samples were collected sequentially every c. 0.5 to 1 m from a c. 60 m thick loess section at KAR in Tajikistan.

a) Ili basin, SE Kazakhstan

A detailed stratigraphic description of the loess sites in SE Kazakhstan can be found in Dave et al. (submitted; Chapter 3). The sites in SE Kazakhstan can be seen in Fig. B1 and a brief description of their stratigraphy is presented here.

Panfilov (PAN, 43° 22.295' N, 77° 07.670' E; 710 m a.s.l.) is located c. 40 km northeast of Almaty. It is a 5 m-thick loess section that overlies an c. 2 m-thick gravel bed.

Ashubulak (ASH, 43° 28.671' N, 77° 47.379' E; 760 m a.s.l.) is 5 m-thick loess section located ~50 km east of the PAN section. Both PAN and ASH sections are composed almost entirely of pale yellowish primary loess material and do not show any major soil bearing units, apart from the top c. 30 cm of disturbed modern soil.

Taukaraturyk (TAU, 43° 29.445' N, 78° 01.509' E; 769 m a.s.l.) is a 7.5 m-thick loess section located c. 20 km east of ASH. The upper c.30 cm is composed of humic soil unit with modern rootlets and insect holes. The rest of the section is composed of yellowish-beige primary loess with episodic occurrence of angular gravels (1-2 mm), occurring at depths of 1.5–2.0, 2.4–2.8 and 3.8–4.9 m. The occurrence of episodic coarse-grained material in the profile is most likely due to colluvial input from the nearby range front.

Malubai (MAL, 43° 26.312' N, 78° 19.763' E; 815 m a.s.l.) is located south to the city of Chilik (also known as Shelek) and c.25 km east of TAU. The loess section at MAL is composed of two profiles – A and B. Profile A is c. 6 m-thick loess section composed of pale yellowish primary loess, with the presence of an angular gravel layer (c. 0.5–2 cm in diameter) between depths 1.1–1.3 m. Profile B is located c. 6 m north of the main outcrop, Profile A. Profile B consists of two parallel, c. 2 and 1.5 m-thick sections, composed of primary loess, with a c. 2 cm thin layer made of angular gravels (c. 0.5–2 cm in diameter) with silty matrix at 0.40–0.45 m and an imbricated, angular cobble bed at c. 0.9–1.3 m.

Both MAL and TAU are located closer to the range front and this may explain episodic sedimentation of colluvial material within their respective profile. This is not the case at sites PAN and ASH, which are located along the peripheral edge of the piedmont loess deposits where they pinch out onto the Ili River floodplain.

b) Tajik depression, Tajikistan

The loess site of *Karamaidan* (KAR) is located c. 45 km east of the capital city of Dushanbe in Tajikistan. The site has been previously described and dated by palaeomagnetism, and it preserves a continuous record of climate change over the past 1 Ma (Forster & Heller, 1994). The exact exposures at Karamaidan studied by Forster and Heller (1994) are no longer recognisable, therefore, during the 2018 fieldwork in Tajikistan, three new stratigraphically

overlapping sections (total c. 130 m thick) were opened and cleaned. We independently constrained the continuity and overlap of these three sections by measuring the *in situ* magnetic susceptibility with portable Bartington MS3/MS2K magnetic susceptibility (MS) measuring equipment. Our MS composite log closely resembles the Karamaidan profile presented in Forster and Heller (1994) and spans the past >800 ka. Here, we study a c. 60 m-thick section at KAR, comprising of 6 soil and 5 loess units spanning MIS 19-9 (refer section 1.2 of this appendix for relative chronology of the site).

KAR (38° 34' 33.47'' N, 69° 16' 40.79'' E, 1629 m a.s.l.) begins at 19.6 m and continues down to the depth of 75 m. This section comprises 6 palaeosol and 5 loess units with 3 observed intercalating weak to moderately developed soil units. Visibly distinct dark reddish-brown, clayey palaeosol units were observed between depths 19.6–22.4 m, 27.9–30.1 m, 39.3–44.7 m, 45.3–48.4 m, 62.5–65.3 m, and 70.6–75 m. In the palaeosol unit at depth 62.5-65.3 m, the clay rich horizon overlies a carbonate-enriched layer consisting of nodules (up to 10 cm in diameter) between 64.3-64.3 followed by a caliche horizon up to 65.3 m. Alternately-occurring pale yellowish-beige primary loess units, with minor carbonate mottling occurs at depths 22.4–25.4 m, 30.1–39.3 m, 44.7–45.3 m, 48.4–62.5 m and 65.3–70.6 m. Intercalating weakly developed soil units within the loess were observed at c. 25.4–25.9 m, c. 55–59 m and c. 68.4–69.6 m.

1.2. Magnetic susceptibility at KAR: Relative chronology based on correlations with the global benthic record

Magnetic susceptibility (MS) measurements at the site KAR in Tajikistan were carried out using a portable Bartington Magnetic Susceptibility (MS) system. The Bartington MS system utilizes a MS3 meter combined with a MS2K field sensor (a high stability surface scanning sensor) for continuous down-profile measurement of the cleaned outcrop. This system allows for the measurement of volume magnetic susceptibility expressed in *SI* units. Each measurement down-profile was performed on a freshly cleaned, relatively smooth and flat surface, and was individually calibrated with air-temperature to compensate for temperature-induced drift. The measurements were taken continuously every 5 cm for the entire depth of c. 60 m. The resulting volume magnetic susceptibility dataset was correlated by visual comparison to the global benthic $\delta^{18}O$ curve (Lisiecki & Raymo, 2005) using the magnetostratigraphic constraints of Forster and Heller (1994), ascribing paleosols and loess intervals to global glacial and interglacial stages. The correlation of magnetic susceptibility to global benthic records for KAR indicates that the loess varies in age from MIS 19-9 (800 -300 ka, refer Fig. 4.4a of the main text in Chapter 4).

1.3. Sample preparation and Methodology

a) Sample preparation: Extraction of fine-grained Quartz

114 sediment samples from 4 sites in Kazakhstan and 1 site in Tajikistan were processed under subdued red-light conditions to obtain fine grained (4-11µm) quartz (according to standard luminescence dating preparation techniques; Frechen et al, 1996) at the Institute for Geosciences, Johannes Gutenberg University and the Max Planck Institute for Chemistry (MPIC) in Mainz, Germany. The fine-grained samples were prepared by treating the <63 µm sediment fraction with 10% HCl followed by 10% H_2O_2 to remove carbonates and organics respectively. The sediment was then treated with 0.1 N sodium oxalate to remove clays. The samples were rinsed at least three to four times with distilled water between each of the aforementioned steps. The fine-grained (4-11 µm) fraction was obtained from the chemically-treated bulk fraction (<63 µm) by settling using Stokes law. The separated 4-11 µm fraction was treated with 37% hexafluorosilicic acid (H_2SiF_6) for 7 days and consequently washed with 10% HCl (to remove fluoride precipitates) to obtain fine grain (4-11µm) quartz rich fraction. The etching of the fine grained polymineral fraction was performed at the Max Planck Institute for Evolutionary Anthropology at Leipzig, Germany.

b) Electron Spin Resonance: Instrumentation and Methodology

ESR investigations were carried out using an X band Bruker EMX Plus Spectrometer at the Babes Bolyai University, Cluj-Napoca, Romania. All measurements were made by filling a quartz glass tube with sample at the same volume, with a mass of 100±4 mg (less than 5% variation) for all samples. Consequently, all ESR measurements were normalized to 100 mg for inter-comparison. In all cases, we measure the peak-to-peak amplitude of the ESR signal to quantify the variation in defect concentration; as the peak-to-peak amplitude variation can be taken as a good approximation of the effective concentration of the defect centres in the sample (Chestnut, 1977). The natural spectra of the Al-hole centre is shown in Fig. B4 and that of E' and peroxy spectra in Fig. B8. Exposure of samples to sunlight was restricted to a minimum during measurements. Gamma irradiations were performed at room temperature at the Centre for Nuclear Technologies, Technical University of Denmark (DTU NUTECH) using a calibrated ^{60}Co-60 gamma cell, with a dose rate of about 2 Gy/s (dose rate to water) at the time of irradiation. Dose rate to quartz was estimated to be 0.941 (with relative uncertainty of 2.2%) of dose rate to water based on Monte Carlo simulation considering the irradiation geometry used.

Three types of defect centres were investigated in this study – E', Peroxy and Al-hole centre. Intensity of E' and peroxy defect centre was measured for all samples while Al-hole centre signals was quantified for selected samples. E' was recorded at room temperature at a

modulation amplitude of 0.5 G, conversion time of 75.13 ms and a microwave power of 0.02 mW. Each data point for E' is an average of 3 repeat measurements, wherein each repeat measurement is an average of 6 scans with a sweep time of 30 s each. The peroxy defect was measured at room temperature with a modulation amplitude of 1 G, conversion time of 40.96 ms and at a microwave power of 10 mW. Each peroxy data point is an average of 3 repeat measurements, each of which is an average of 3 scans with a sweep time of 120s. The peroxy signature was determined from the peak-to-peak height from g=2.003 to g=2.009 (Odom & Rink, 1989). The ESR intensity of the Al-hole centre was recorded at a temperature of 90 K, with a modulation amplitude of 1G, sweep time of 120 s and a microwave power of 2 mW. Each data point for Al-hole centre intensity is an average of 3 scans carried out by rotating the sample by 120 degree between each scan. The signal of Al-hole was quantified using peak-to-peak height from g=2.018 to g=1.993 (Toyoda & Falguères, 2003).

c) Optically stimulated luminescence (OSL): Evaluation of burial dose (in nature)

Correlation of magnetic susceptibility to global benthic records for site KAR suggests that the loess samples at the site vary in age from c. 800-300 ka (MIS 19-9; Refer section 1.2 of this appendix). It is well known that natural quartz OSL signal (or the accumulated dose in quartz) saturates between c. 100-300 Gy (Timar-Gabor & Wintle, 2013). Therefore, we investigated the burial dose in the polymineral fine grains as feldspars in polymineral aliquots, which are known to saturate at higher doses (Buylaert et al., 2012). Therefore, we attempted to evaluate the natural dose received by the sample during burial at the top (sample A0276, depth=20 m) and bottom (A0329, depth =72.5 m) of the profile.

In this study, we undertook post-infrared Infrared (pIRIR) stimulated luminescence measurements at high doses (up to 3325 Gy) for two polymineral fine-grained (4-11µm) samples from KAR, based on the protocol by Buylaert et al (2012) and summarized in Table B1. The polymineral fine grains for these measurements were derived from the same samples as their quartz equivalent. 3 polymineral aliquots each of the samples A0276 and A0329 were evaluated based on the protocol described in Table B1 and the results are summarized in Fig. B7. Figure B7 shows that sample A0276 is close to saturation, with a burial dose c. 970 Gy, whilst sample A0329 was completely saturated. This implies that the uppermost sample at site KAR has received a minimum natural burial dose of ≥1000 Gy, which increases with depth (assuming age increases with depth) at KAR.

The pIRIR measurements were made using an automated Risø TL-DA-20 reader equipped with a $^{90}Sr/^{90}Y$ beta sources. The sample was stimulated using IR LED (870 ± 30 nm, 300 mW/cm^2), and the emitted luminescence signal was detected by by EMI 9235QA photomultiplier tube using a combination of Schott BG-39 and BG-3 filters to detect feldspar emissions.

2. Extended description of Results

2.1. Experiments on selected samples, A0016 and A0329: Experimental setup and methodology

Two fine-grained (4-11µm) quartz samples were selected, one each from Kazakhstan (A0016, TAU) and Tajikistan (A0329, KAR), to investigae the effect of gamma (γ) irradiation and heating on the ESR centres: E', peroxy and Al-hole centres. Sample A0016 and A0329 were divided into 11 subsamples of c.100 mg each and irradiated with given γ-doses: 0 Gy (referred to as the natural sample), 100 Gy, 200 Gy, 500 Gy, 1000 Gy, 2000 Gy, 5000 Gy, 10000 Gy, 20000 Gy and 40000 Gy. In the first case, all aliquots of the irradiated samples were measured at room temperature to record the corresponding intensity of the E' and peroxy centres. The Al-hole measurements (on selected samples) were recorded at 90 K for all samples. In the second case, all the aliquots of sample A0016 and A0329 were heated stepwise at 300 ^{o}C, 350 ^{o}C, and 400^{o}C for 15 min each and the corresponding intensity of the E' and peroxy centres was measured after each heating step. The results of this experiment are summarized in Fig. B5 and Fig. B6.

2.2. Simulation of E', Peroxy and Al-hole signals

Of the three ESR signals investigated in this study, the E' signals obtained from our samples are well defined. However, the peroxy and Al-hole centres are comparatively weak. Therefore, in order to assess the behavior of the ESR signals in our samples with expected signal behaviour based on literature, we simulated the signatures of all the centres under study with known parameters from literature. The E' and peroxy signal was simulated using parameters from Ikeya (1993), while the simulation of Al-hole centre was based on the Al-hole signal from a natural quartz sample, EVA-1095, combined with parameters from literature (Nuttall & Weil, 1981; Ikeya, 1993). Sample EVA-1095 (125-212 µm) is a natural quartz sample from Lake Durthong, Australia (Fitzsimmons, 2017) and has a well characterised Al-hole centre, with relatively high concentration (Benzid & Timar-Gabor, 2020). Bruker WinEPR SimFonia software was used to perform the simulation and fitting.

In order to compare the effective apparent concentrations of the Al-hole centres in samples A0016 (Kazakhstan) and A0329 (Tajikistan), we used the 'simulated' Al-hole signal to obtain the effective Al-hole concentration. This was done, since the measurement of Al-hole concentration in natural fine grain quartz, especially a weak signal, is likely to have an interfering component from the peroxy signal, as also inferred from dating studies by Timar-Gabor et al. (2018). Therefore, the simulated signal was fitted to the measured Al-hole signal from two fine grained (4-11µm) quartz samples, A0016 (Kazakhstan) and A0329 (Tajikistan)

with a given γ dose of 0 Gy (natural sample) and 20000 Gy. These simulated signals were then integrated twice to obtain the effective Al-hole concentration (equal to the area under the curve). The results from simulations of the Al-hole centre and its effective concentration in the samples are summarized in Fig. B4. The results from Fig. B4 clearly illustrate that the concentration of Al-hole centre in Kazakh samples is higher than the Tajik samples. The simulations of the E' and peroxy centre with respect to their natural signals are shown in Fig. B8.

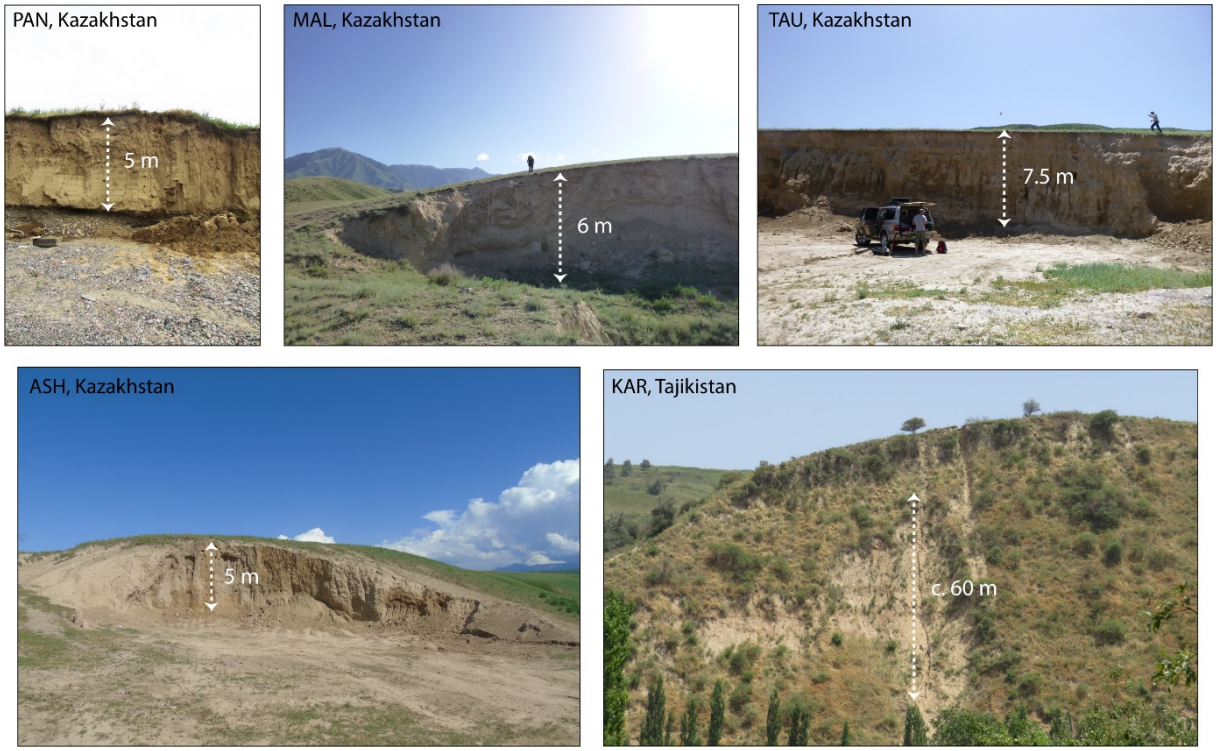

Fig. B1. Sites under study in the Ili basin of Kazakhstan (PAN, ASH, TAU and MAL; fieldwork 2017) and the Tajik depression (KAR) in Tajikistan (fieldwork 2018).

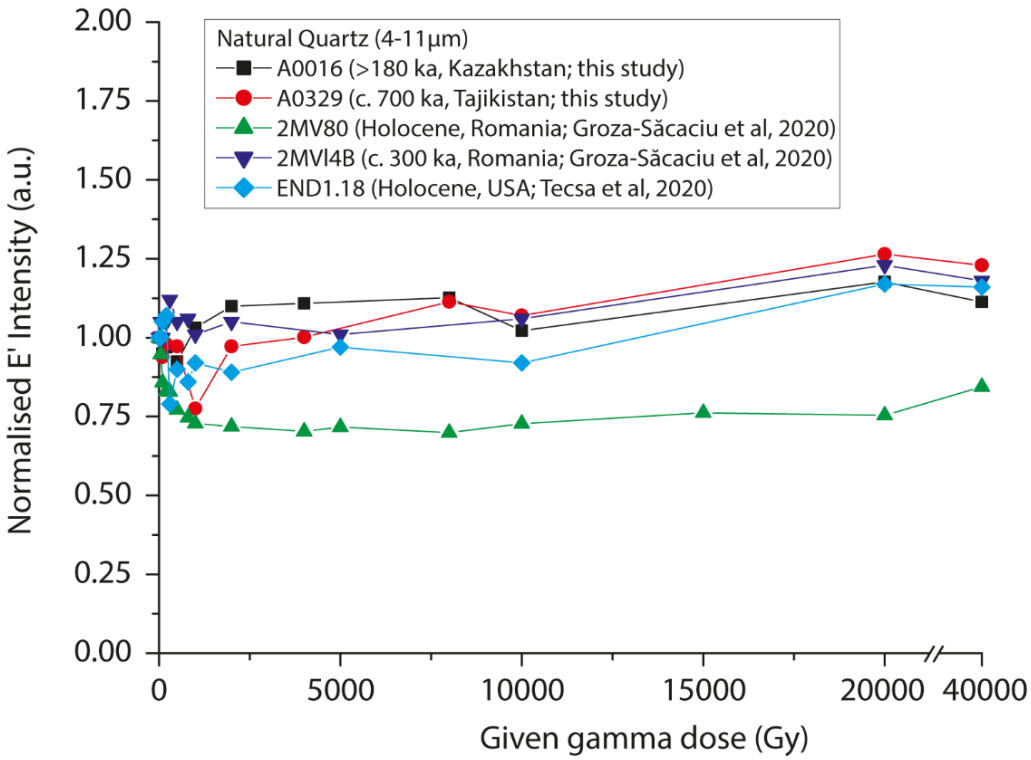

Fig. B2. Variation in intensity of E' centre with γ- irradiation. Here the E' intensity is normalized to its natural value for all measurements. The experiments were performed at room temperature on 4-11 µm natural quartz from different geographic locations.

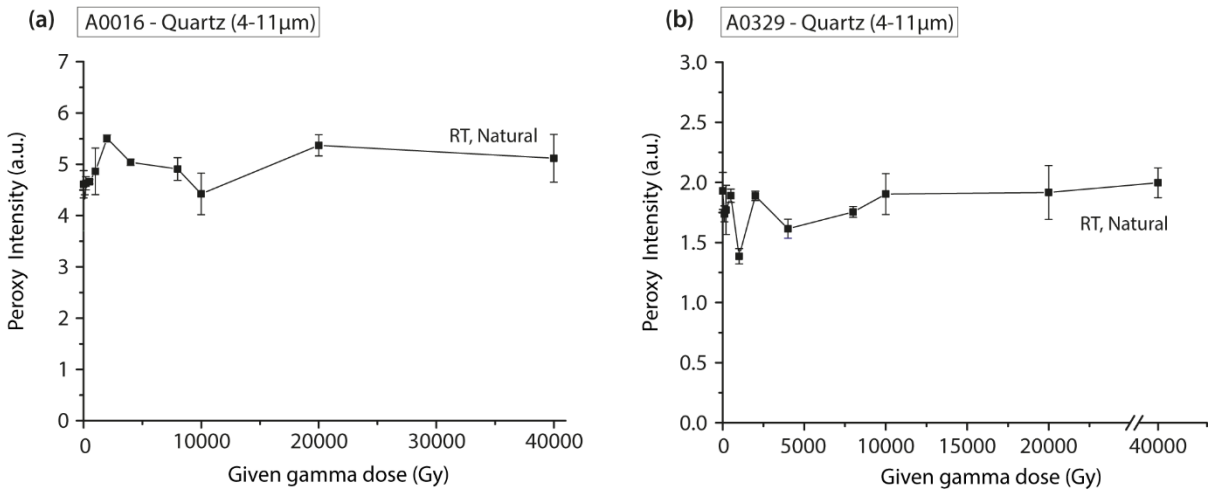

Fig. B3. Variation of natural peroxy intensity in fine grain quartz with γ- irradiation in samples (a) A0016 (Kazakhstan) and (b) A0329 (Tajikistan).

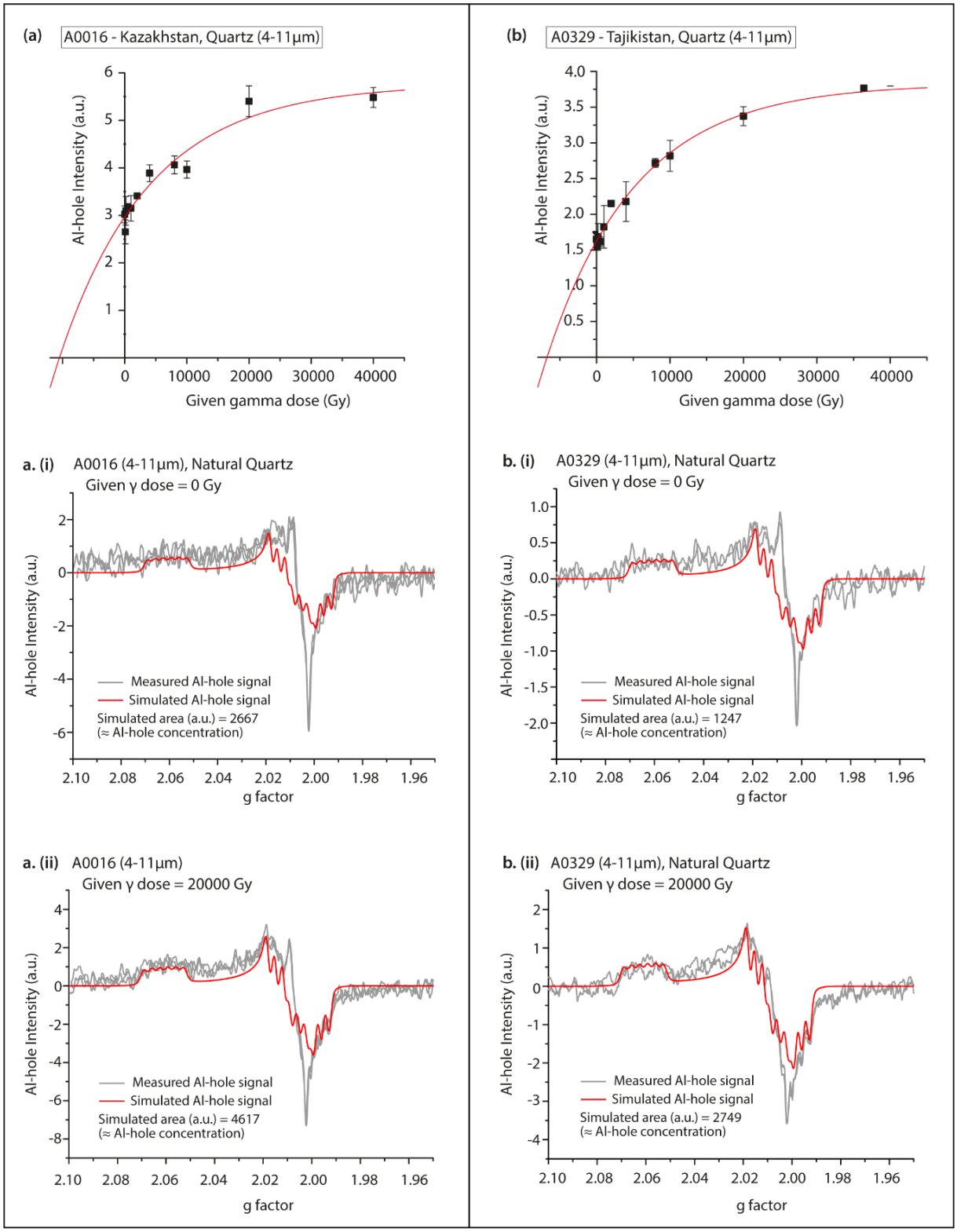

Figure B4. Variation in intensity of Al-hole centre with γ-dose for sample (a) A0016 and (b) A0329. Part (i) and (ii) show the difference between intensity of Al-hole centres in natural (0 Gy) and a γ-irradiated aliquot (20000 Gy) based on simulations for samples A0016 and A0329 respectively. All the intensities for AL-hole centre are baseline corrected.

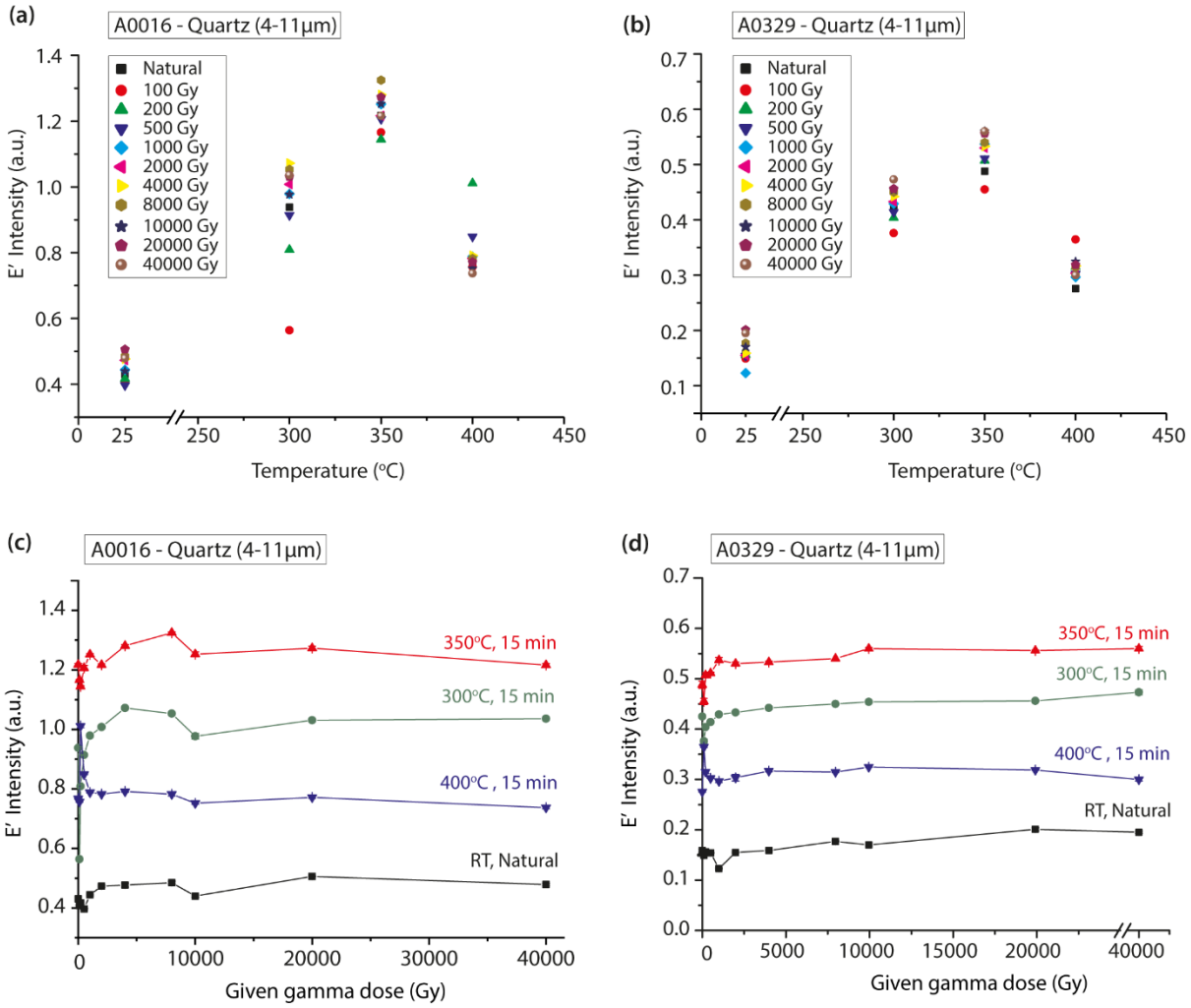

Fig. B5. Variation of E' intensity in γ-irradiated aliquots for sample (a) A0016 and (b) A00329 with temperature. Plot (c) and (d) show the variation of E' intensity with γ-irradiation with subsequent stepwise heating at 300°, 350° and 400°C for sample A0016 (Kazakhstan) and A0329 (Tajikistan) respectively.

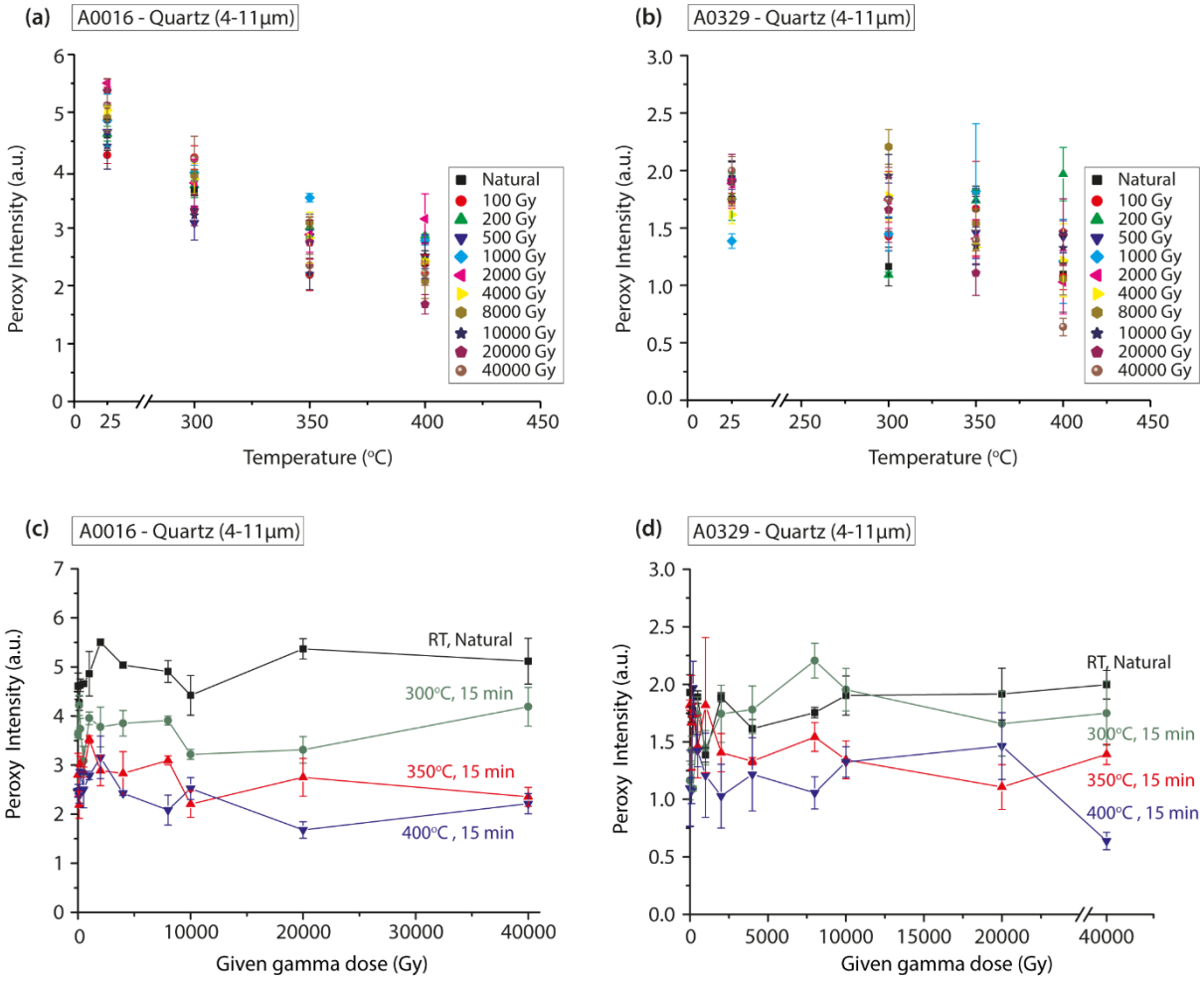

Fig. B6. Variation of peroxy intensity in γ-irradiated aliquots of sample (a) A0016 and (b) A00329 with temperature. Plot (c) and (d) show the variation of peroxy intensity with γ-irradiation with subsequent stepwise heating at 300°, 350° and 400°C for sample A0016 (Kazakhstan) and A0329 (Tajikistan) respectively.

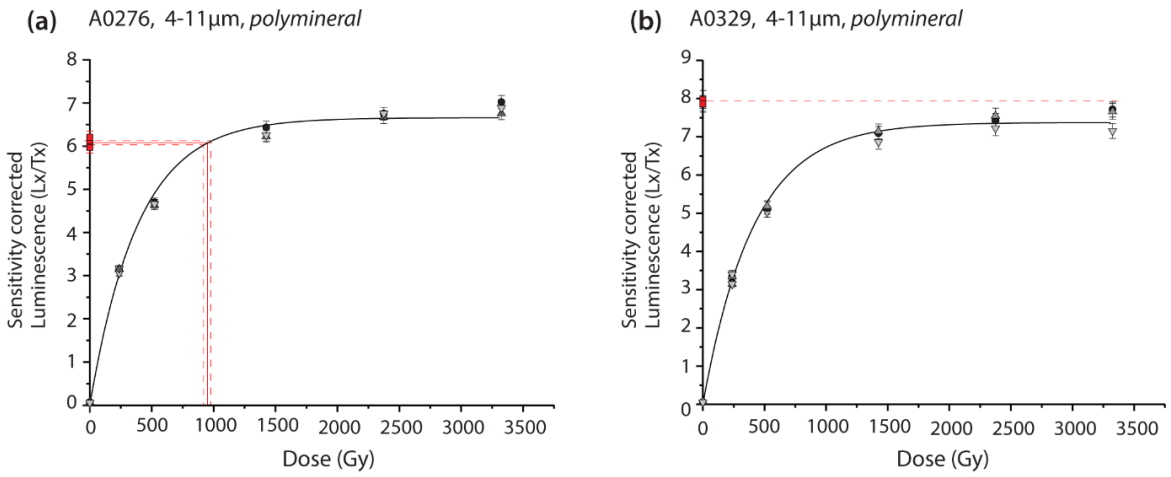

Fig. B7. Dose response curve of fine grain polymineral constructed using $pIRIR_{290}$ protocol (Buylaert et al., 2012) to estimate the burial dose in the samples (a) A0276 (uppermost sample) (b) A0329 (bottom sample) at KAR, Tajikistan.

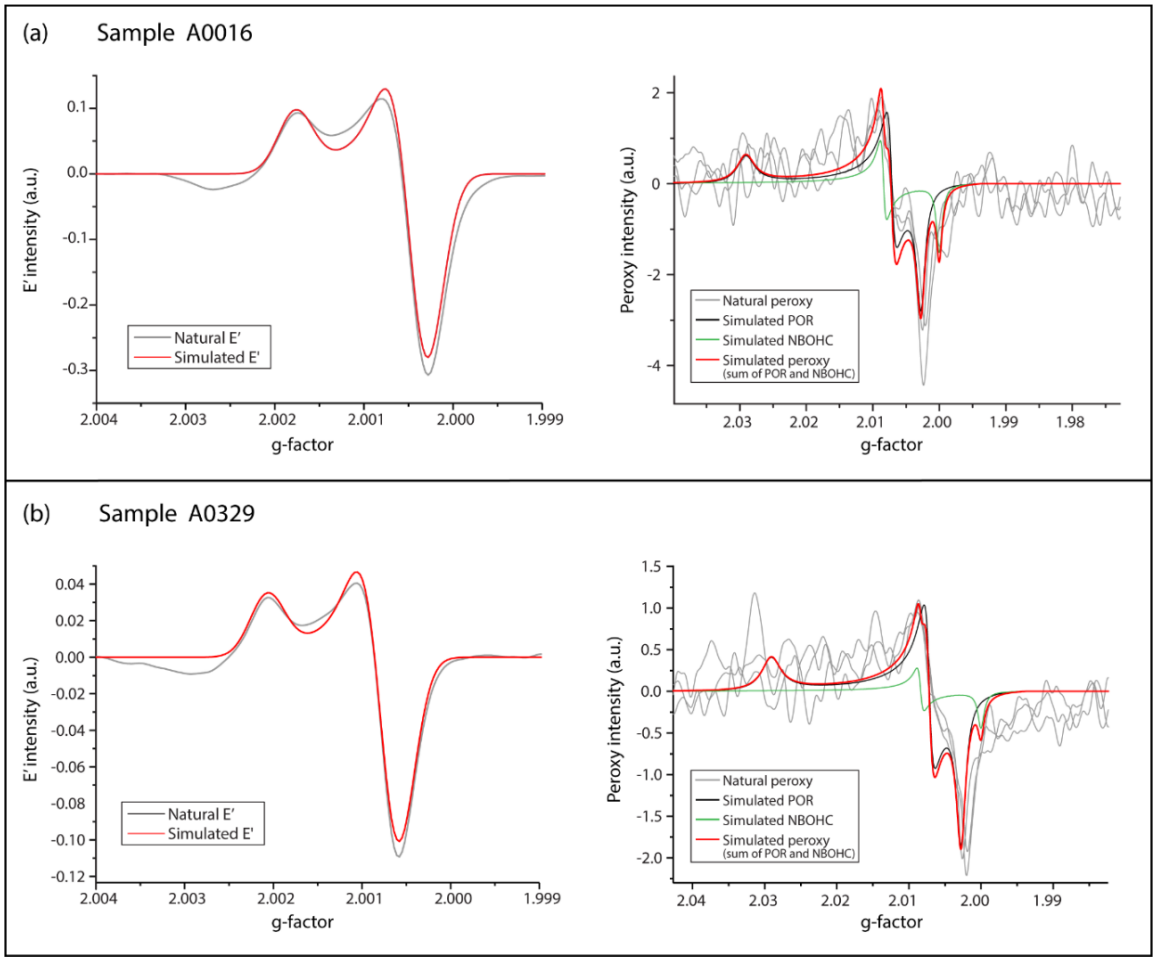

Fig. B8. Comparison of natural and simulated spectra of the E' and peroxy centre of sample (a) A0016 (Kazakhstan) and (b) A0329 (Tajikistan).

Table B1. Protocol for pIRIR investigations to evaluate the burial dose (or equivalent dose) from polymineral fine grain samples (after Buylaert et al., 2012).

$pIRIR_{290}$ protocol (Buylaert et al., 2012)		
Step	Treatment	Signal measured
1	Dose (Natural or laboratory)	-
2	Preheat 60s at 320 ^{o}C	-
3	IRSL, 200s at 50^{o}C	-
4	IRSL, 200s at 290 ^{o}C	L_n, or L_x
5	Test dose	-
6	Preheat 60s at 320 ^{o}C	-
7	IRSL, 200s at 50^{o}C	-
8	IRSL, 200s at 290 ^{o}C	T_n or T_x
9	IRSL, 100s at 325 ^{o}C	-
10	Return to step 1	-

References

Benzid, K., & Timar-Gabor, A. (2020). Phenomenological model of aluminium-hole ([AlO4/h+]0) defect formation in sedimentary quartz upon room temperature irradiation: Electron spin resonance (ESR) study. Radiation Measurements, 130, 106187. https://doi.org/10.1016/j.radmeas.2019.106187

Buylaert, J.-P., Jain, M., Murray, A. S., Thomsen, K. J., Thiel, C., & Sohbati, R. (2012). A robust feldspar luminescence dating method for Middle and Late Pleistocene sediments. Boreas, 41(3), 435–451. https://doi.org/10.1111/j.1502-3885.2012.00248.x

Chesnut, D. B. (1977). On the Use of the AW2 method for integrated line intensities from first-derivative presentations. Journal of Magnetic Resonance (1969), 25(2), 373–374. https://doi.org/10.1016/0022-2364(77)90032-4

Dave, A.K., Lisa, L., Scardia, G., Nigmatova, S., & Fitzsimmons, K. (submitted). The patchwork loess of Central Asia: Implications for interpreting aeolian dynamics and past climate circulation in piedmont regions. Quaternary Science Reviews.

Fitzsimmons, K. E. (2017). Reconstructing palaeoenvironments on desert margins: New perspectives from Eurasian loess and Australian dry lake shorelines. Quaternary Science Reviews, 171, 1–19. https://doi.org/10.1016/j.quascirev.2017.05.018

Forster, Th., & Heller, F. (1994). Loess deposits from the Tajik depression (Central Asia): Magnetic properties and paleoclimate. Earth and Planetary Science Letters, 128(3–4), 501–512. https://doi.org/10.1016/0012-821X(94)90166-X

Frechen, M., Schweitzer, U., & Zander, A. (1996). Improvements in sample preparation for the fine grain technique. Ancient TL, 14(2), 15–17.

Ikeya, M. (1993). New Applications of Electron Spin Resonance: Dating, Dosimetry and Microscopy. World Scientific. https://doi.org/10.1142/1854

Lisiecki, L. E., & Raymo, M. E. (2005). A Pliocene-Pleistocene stack of 57 globally distributed benthic δ18O records. Paleoceanography, 20(1). https://doi.org/10.1029/2004PA001071

Nuttall, R. H. D., & Weil, J. A. (1981). The magnetic properties of the oxygen–hole aluminum centers in crystalline SiO2.I.[AlO4]0. Canadian Journal of Physics, 59(11), 1696–1708. https://doi.org/10.1139/p81-227

Odom, A. L., & Rink, W. J. (1989). Natural accumulation of Schottky-Frenkel defects: Implications for a quartz geochronometer. Geology, 17(1), 55–58. https://doi.org/10.1130/0091-7613(1988)017<0055:NAOSFD>2.3.CO;2

Timar-Gabor, A., & Wintle, A. G. (2013). On natural and laboratory generated dose response curves for quartz of different grain sizes from Romanian loess. Quaternary Geochronology, 18, 34–40. https://doi.org/10.1016/j.quageo.2013.08.001

Timar-Gabor, A. (2018). Electron spin resonance characterisation of sedimentary quartz of different grain sizes. Radiation Measurements, 120, 59–65. https://doi.org/10.1016/j.radmeas.2018.06.023

Toyoda, S., & Falguères, C. (2003). The method to represent the ESR signal intensity of the aluminum hole center in quartz for the purpose of dating. Advances in ESR Applications, 20, 7–10.

Appendix C

Supplementary information for Chapter 5

Variation in luminescence characteristics and paramagnetic defect centres in fine-grained quartz from a loess-palaeosol sequence in Tajikistan: Implications for provenance studies in aeolian environments

1. Site setting and stratigraphy

The site of Karamaidan (KAR) is located c. 45 km east to the capital city of Dushanbe in Tajikistan. KAR is located in the northern end of the Afghan-Tajik depression, in the piedmonts of the Gissar Ranges, which lies south of the Alai Mountains and west of the Pamirs. The loess at the site of Karamaidan was previously described and dated using palaeomagnetism and is known to preserve a fairly continuous record of climate change over the past 1 Ma (Forster and Heller, 1994). Since the past excavations at the sites are more than two decades old, the exact stratigraphic sections studied by (Forster and Heller, 1994) are no longer recognisable. During the 2018 field campaign in Tajikistan, four new stratigraphically overlapping sections (>100 m thick; for reference refer Fig. 1.6 in Chapter 1) were opened and cleaned for logging and sampling. The continuity and overlap of the sections were independently confirmed by measuring the *in-situ* volume magnetic susceptibility using a portable Bartington magnetic susceptibility meter. The composite of these new sections closely resembled the Karamaidan profile presented by Forster and Heller (1994) and spans the past >800 ka. A detailed composite of all the sites will be presented elsewhere. In this study, we focus on a c. 56 m-thick subsection at KAR. This section comprises of six palaeosol and five loess units with three observed intercalating weak to moderately developed soil units.

The stratigraphy the KAR section can be seen in Fig. 5.2 of Chapter 5. The uppermost c. 3 m, from c.19.6 - 22.4 m consists of a dark-brown clay rich palaeosol with minor carbonate mottling. The carbonate content increases gradually with depth, with an intensely developed carbonate rich horizon at the base of the palaeosol unit between c. 21.6-22.4 m. Below 22.4, up to a depth of 27.9 m, consist of a c. 5.5 m pale beige silty primary loess unit. Minor carbonate is observed throughout this unit and minor Mn concretions occur between c. 24-25 m. An intercalating slightly clay-rich, brownish-beige carbonate rich weakly developed soil horizon occurs at a depth of c. 25.4-25.7 m. This loess unit is followed by a c. 2.2 m thick, palaeosol unit at depths c. 27.9 -30.1 m, comprising of a reddish-brown clay-rich palaeosol with substantial carbonate mottling throughout the unit. Below, c. 30.1 m, up to a depth of c. 39.3 m, comprises of a c. 9.2 m thick pale beige primary loess unit with minor carbonate

mottling which decreases gradually downward until c.35.3 m. From c. 39.3 - 44.7 m, a reddish-brown fine-grained clay rich horizon is observed. Minor carbonate mottling is observed throughout this unit with slightly higher carbonate enrichment between c. 39.4-39.5 m and c. 42.1-44.7 m and minor iron oxide concretions between c. 40.0 - 42.1 m. This is followed by a much paler c. 0.6 m thick, highly weathered, slightly clayey loess unit between c. 44.7-45.3 m. After this, between depths c. 45.3 – 48.4 m, a c. 3 m thick, reddish-brown clay rich palaeosol is observed, with localised carbonate enrichment occurring between depths c. 47.1-47.3 m and c. 48.2-48.4 m. From depth c. 48.4 – 62.5 m, c. 14.1 m thick pale beige primary loess unit is observed with minimal carbonate mottling but more localised carbonate enrichment between c. 50.3-50.6 m and c. 61.5-62.5 m. An intercalating slightly clayey, carbonate rich weakly developed soil horizon is observed at depth c. 55-59 m. This is followed by a c. 2.8 m thick reddish-brown clay rich palaeosol unit between c. 62.5-65.3 m. The upper 0.3 m of this unit is much paler in colour and less clayey compared to latter part of this unit, which comprises of a darker brownish-red, clay enriched horizon between c. 62.8-63.4 m. This is followed by a carbonate enriched zone, dominated by carbonate nodules (up to 10 cm in diameter) between c. 64.3 -64.9 m, which gradually transcends into a caliche horizon between c. 64.9-65.3 m. Below this, between c. 65.3-70.6 m, a carbonate mottled primary loess unit is observed, wherein the carbonate content decreases with depth. A slightly reddish appearance is observed below 66.3 m upto c. 70 m. Whether the reddish appearance of loess is a product of a soil forming clay horizon or an increased enrichment of iron oxides, remains unclear. An intercalating moderately developed soil, comprising of a reddish-brown clay rich unit followed by a c. 0.4 m thick caliche-like horizon is observed between c. 68.4-69.6 m. Lastly, depths c. 70.6 to 75 m, comprises of a reddish-brown palaeosol unit, which is much paler in colour, siltier and has higher Mn concretions in the upper c. 1.8 m. The lower part of this unit has a much darker brownish-red colour with minor carbonate mottling.

2. Magnetic Susceptibility measurements

The magnetic susceptibility (MS) measurements at KAR have previously been presented in Dave et al (submitted: Chapter 4 of this thesis). A brief summary of the methodology and instrumentation is reported here. The MS measurements at the site KAR were carried out using a portable Bartington Magnetic MS system, comprising of a MS3 meter combined with a MS2K field sensor. This system measures the volume magnetic susceptibility in SI units. The MS measurements at KAR were performed continuously every 5 cm down-profile for the entire depth of c. 56 m, and each measurement was individually calibrated with air-temperature to compensate for temperature induced drift. The volume magnetic susceptibility dataset obtained from our measurements was correlated by visual comparison to the global benthic $\delta^{18}O$ curve (Lisecki and Raymo, 2005) using the magnetostratigraphic

constraints of Forster and Heller (1994), therefore allowing the correlation of the paleosol and loess units at KAR with global glacial and interglacial stages.

3. Methodology and Instrumentation

3.1. Sample preparation

55 sediment samples were collected in opaque tubes every 0.5 - 1m down-profile at the site of KAR. The samples were processed and prepared according to standard luminescence dating preparation techniques (Frechen et al., 1996) to obtained fine grain (4-11 µm) quartz and polymineral fractions. All samples were processed under subdued red-light conditions at the Institute for Geosciences, Johannes Gutenberg University and the Max Planck Institute for Chemistry (MPIC) in Mainz, Germany. The sediment samples were wet-sieved to obtain the <63 µm sediment fraction. This fraction with treated with 10% HCl followed by 10% H_2O_2 to remove carbonates and organics respectively. This was followed by treatment with 0.1 N sodium oxalate to remove clays. The samples were rinsed at least three to four times with distilled water between each of the aforementioned steps. The polymineral fine grain (4-11 µm) fraction was obtained from the chemically treated bulk fraction (<63 µm) by settling using Stokes law. A portion of the polymineral 4-11 µm fraction was treated with 37% Hexafluorosilicic acid (H_2SiF_6) for 7 days and consequently washed with 10% HCl (to remove fluoride precipitate) to obtain fine grain (4-11µm) quartz rich fraction. The etching of the fine grained polymineral fraction was performed at the Max Planck Institute for Evolutionary Anthropology at Leipzig, Germany. The purity of the fine grain quartz samples was verified by a near background signal obtained on IR stimulation. During this process, 5 samples were identified with feldspar contamination and were re-etched with H_2SiF_6 for 7-days to obtain pure quartz fraction.

3.2. Methodology and Instrumentation

a) Electron Spin Resonance

The Electron spin resonance (ESR) investigations on fine grain (4-11µm) quartz at KAR have previously been reported in Chapter 4. A summary of the relevant methodology and instrumentation is presented here. ESR investigations were carried out using an X band Bruker EMX Plus Spectrometer at the Babes Bolyai University, Cluj-Napoca, Romania. All measurements were made using a quartz glass tube filled by maintaining the same volume, with the mass of 100±4 mg (less than 5% variation) for all samples and therefore, all ESR measurements were normalized to 100 mg for inter-comparison. Exposure of samples to sunlight was restricted to a minimum during measurements. In this study we measured two defect centres, the E' and peroxy centres in all our fine grain quartz samples. In both cases, we measure the peak-to-peak amplitude of the ESR signal of the respective defect centre to

quantify the variation in defect concentration. The peak-to-peak amplitude variation can be taken as a good approximation of the effective concentration of the defect centre in the sample (Chesnut, 1977). In case of E', the intensity of the signal was evaluated from peak-to-peak height of the signal with a baseline crossing at g=2.001. The intensity of the peroxy signal was quantified from the peak-to-peak height taken from g=2.003 to g=2.009 (Odom and Rink, 1989).

E' was recorded at room temperature at a modulation amplitude of 0.5 G, conversion time of 75.13 ms and a microwave power of 0.02 mW. Each data point for E' is an average of 3 repeat measurements, wherein each repeat measurement is an average of 6 scans with a sweep time of 30 s each. The peroxy defect was measured at room temperature with a modulation amplitude of 1 G, conversion time of 40.96 ms and at a microwave power of 10 mW. Each peroxy data point is an average of 3 repeat measurements, each of which is an average of 3 scans with a sweep time of 120s. The uncertainty in measurements in each sample is expressed as standard error.

b) Luminescence sensitivity measurements

All luminescence measurements were performed using an automated Risø TL-DA-20 reader equipped with a $^{90}Sr/^{90}Y$ beta sources (Thomsen et al., 2006) calibrated to a dose rate of 0.095 ± 0.02 Gy/s. The sample was stimulated using blue LED (470±30 nm, 80 mW/cm^2) and IR LED (870 ± 30 nm, 300 mW/cm^2) and the emitted luminescence signal was detected by EMI 9235QA photomultiplier tube fitted with a 7.5 mm Hoya U-340 and a combination of Schott BG-39 and BG-3 filters to detect quartz and feldspar emissions respectively. All measurements were performed at the Luminescence laboratory at the Max Planck Institute for Chemistry in Mainz, Germany. The aliquots for measurement were prepared by suspending fine grain sample (quartz or polymineral) in acetone on stainless steel discs. For all samples (quartz and polymineral), 6-8 aliquots per sample were used for luminescence sensitivity measurements. The weight of each aliquot was measured before and after mounting the sample using a Mettler Balance with a precision of 0.001 mg.

For the quartz fine grain samples, the luminesce sensitivity protocol is outlined in Table 5.1 (modified after Li and Zhou, 2020; Sawakuchi et al, 2018). This protocol aims at obtaining the TL and OSL sensitivity from pure fine grain quartz in response to a given dose (47.5 Gy). In this procedure, all aliquots were bleached with Blue LED's at 125^{o}C for 100 s to eliminate the natural luminescence signal. Following which, a beta dose of 47.5 Gy was given to all aliquots. The aliquots were then heated to 240^{o}C for 10 s to measure the TL signal; this step also serves as a preheat to eliminate any unstable signals. Infrared stimulation at 50^{o}C for 50 s was applied to check for any possible feldspar contamination. This was followed by a blue light stimulation at 125^{o}C for 100 s to measure the OSL signal from pure quartz. The heating

rate in all thermal treatments is 5°C/s. The TL sensitivity was measured by integrating the TL signal from 60°C to 120°C, while the OSL sensitivity was obtained from the initial 0.8 s after subtraction of the average from the last 10 s of the OSL emission. Each of these measurements was normalized by the beta dose (47.5 Gy) and the corresponding weight of the aliquot, finally expressing sensitivity as counts.$Gy^{-1}mg^{-1}$.

The luminescence sensitivity measurement protocol for polymineral fine grain samples is outlined in Table 5.1 (modified after Sawakuchi et al., 2018). This protocol aims at obtaining the IRSL sensitivity from the feldspar component and the post IR- OSL sensitivity from the quartz component of the polymineral fine grains in response to a given dose (47.5 Gy). In this protocol, all aliquots were bleached with blue stimulation at 125°C for 100 s to eliminate the naturally accumulated luminescence signal in the sample. After which, a beta dose of 47.5 Gy was given to all the aliquots of the sample. A preheat of 240°C for 10 s was applied to remove any unstable signals. Following which, an IR stimulation at 60°C for 300 s was applied to measure the feldspar signal in the polyminerals. This step (ideally) also allows the elimination of the feldspar contribution to the OSL signal, which is measured in the subsequent step (Banerjee et al, 2001; Jain and Singhvi, 2003). In the next step, OSL using blue stimulation at 125°C for 100 s was used to measure the quartz dominant post IR-OSL signal from the polymineral. In the last step, the OSL step was repeated to determine the background underlying the OSL signal in the previous step (Sawakuchi et al, 2018). Unlike the work of Sawakuchi et al (2018), we only use the last step to monitor the background of the OSL signal. The IRSL signal from feldspar was evaluated from the initial 3.2 s after subtraction of the corresponding average intensity from the last 10 s, while the post IR-OSL signal from the quartz fraction of the polymineral was determined from the initial 0.8 s after the subtraction of the average from the last 10 s. These intensity measurements were normalized by the given beta dose (47.5 Gy) and the weight of the aliquot to obtain the IRSL and post IR-OSL sensitivities from the feldspar and quartz component of the polymineral sample respectively (expressed as counts $Gy^{-1}mg^{-1}$).

4. Preliminary insights in support of the proposed hypothesis

Luminescence and ESR defect characteristics of quartz from weakly developed soil units

In this study, we propose that the observed sensitivity increase in quartz from soil horizons is due to repeated cycles of irradiation and bleaching, that occurs during soil formation. We also suggest that it is increasingly likely that the original (provenance) luminescence signature of the grains are masked by this effect. To shed light on this scenario, here we illustrate the example of luminescence and ESR defect characteristics of the quartz samples from the weakly developed soil units that occur within the loess accumulating glacial phases. *We note*

that these preliminary observations, can by no means be taken as proof of concept; nevertheless, these observations offer interesting insight

Fig. 5.4 (in the main text: Chapter 5) illustrates the natural E'and peroxy intensities and the luminescence sensitivity of the OSL and TL signal from quartz obtained from weakly developed soil units, in context of the signatures obtained from loess and palaeosol units. We observe that the quartz from the weak-soil units exhibit natural E' and peroxy characteristics similar to the well-developed palaeosol units. While, it shows OSL and TL sensitivities similar to that observed in loess units. Hence, if our hypothesis holds, then quartz from the weakly developed soil units, with a low E' value as also seen in soils (interglacials), reflect a dominant proximal source signature at the loess site. Whilst, as these units represent weak pedogenesis and have higher sedimentation rates, they are less likely to be sensitised by repeated cycles of irradiation and bleaching unlike the well-developed palaeosol units, and this can be seen in its low OSL and TL sensitivity.

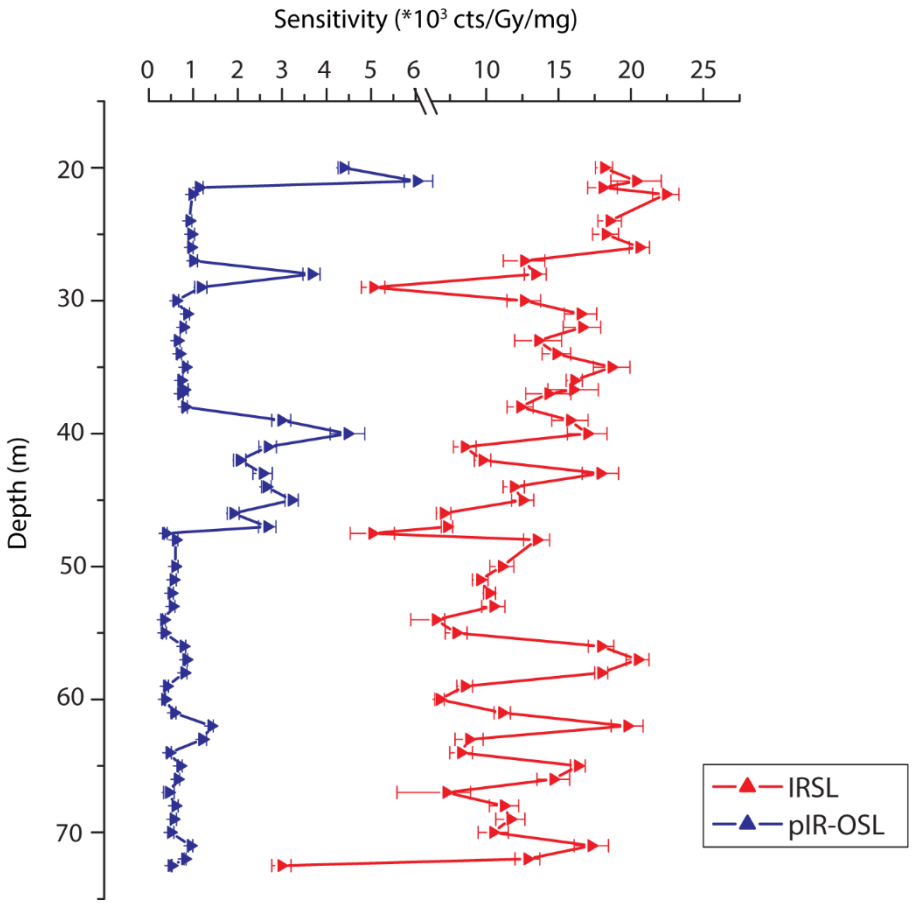

Fig. C1. Down-profile variation of luminescence sensitivity of IRSL and pIR-OSL signal from polymineral fine grains.

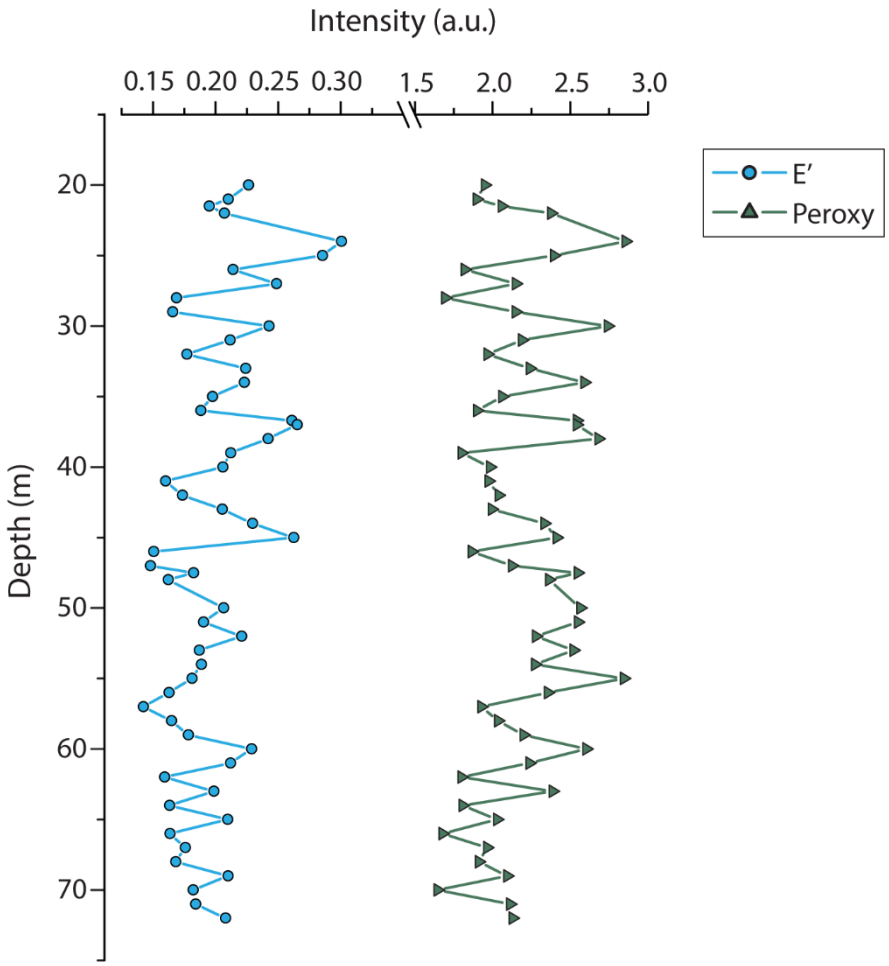

Fig. C2. Down-profile variations of natural E' and peroxy intensity from fine grain quartz (derived from Chapter 4).

References

Banerjee, D., Murray, A. S., Bøtter-Jensen, L., & Lang, A. (2001). Equivalent dose estimation using a single aliquot of polymineral fine grains. Radiation Measurements, 33(1), 73–94. https://doi.org/10.1016/S1350-4487(00)00101-3

Chesnut, D. B. (1977). On the Use of the AW2 method for integrated line intensities from first-derivative presentations. Journal of Magnetic Resonance (1969), 25(2), 373–374. https://doi.org/10.1016/0022-2364(77)90032-4

Forster, Th., & Heller, F. (1994). Loess deposits from the Tajik depression (Central Asia): Magnetic properties and paleoclimate. Earth and Planetary Science Letters, 128(3–4), 501–512. https://doi.org/10.1016/0012-821X(94)90166-X

Frechen, M., Schweitzer, U., & Zander, A. (1996). Improvements in sample preparation for the fine grain technique. Ancient TL, 14(2), 15–17.

Jain, M., & Singhvi, Ashok. K. (2001). Limits to depletion of blue-green light stimulated luminescence in feldspars: Implications for quartz dating. Radiation Measurements, 33(6), 883–892. https://doi.org/10.1016/S1350-4487(01)00104-4

Li, Y., & Zhou, L. (2020). Variations of thermally and optically stimulated luminescence sensitivity of loess and pedocomplex samples from southern Tajikistan, Central Asia. Geochronometria, 0(0), 000010151520150118. https://doi.org/10.1515/geochr-2015-0118

Lisiecki, L. E., & Raymo, M. E. (2005). A Pliocene-Pleistocene stack of 57 globally distributed benthic δ18O records. Paleoceanography, 20(1). https://doi.org/10.1029/2004PA001071

Odom, A. L., & Rink, W. J. (1989). Natural accumulation of Schottky-Frenkel defects: Implications for a quartz geochronometer. Geology, 17(1), 55–58. https://doi.org/10.1130/0091-7613(1988)017<0055:NAOSFD>2.3.CO;2

Sawakuchi, A. O., Jain, M., Mineli, T. D., Nogueira, L., Bertassoli, D. J., Häggi, C., Sawakuchi, H. O., Pupim, F. N., Grohmann, C. H., Chiessi, C. M., Zabel, M., Mulitza, S., Mazoca, C. E. M., & Cunha, D. F. (2018). Luminescence of quartz and feldspar fingerprints provenance and correlates with the source area denudation in the Amazon River basin. Earth and Planetary Science Letters, 492, 152–162. https://doi.org/10.1016/j.epsl.2018.04.006

Thomsen, K. J., Bøtter-Jensen, L., Denby, P. M., Moska, P., & Murray, A. S. (2006). Developments in luminescence measurement techniques. Radiation Measurements, 41(7), 768–773. https://doi.org/10.1016/j.radmeas.2006.06.010

Appendix D

Preliminary investigations of surface samples and rocks from the Ili basin of SE Kazakhstan

1. Reconstructing aeolian transport processes and pathways using paramagnetic centres in fine grain quartz: A case study from the Ili basin, southeast Kazakhstan

The understanding of aeolian processes, i.e., the entrainment, transport and deposition of wind-blown sediments, forms a crucial component towards linking resulting depositional landforms and climate dynamics in a region. The nature of these processes has varied over Quaternary timescales, and is dependent on changing sediment supply, existing topography and climatic parameters such as wind strength and moisture availability, at local to supra-regional spatial scales (Fitzsimmons et al, 2020). Therefore, in order to understand long-term interactions between aeolian-dominated landscapes and climate, there is a need to investigate the mechanisms driving wind-blown processes. In this context, the Ili basin of southeast (SE) Kazakhstan, with its extensive piedmont loess deposits and desert dunefields, provides an optimal study region for examining aeolian earth-surface processes and their links to climate. In addition, this region lies at the intersection of two major Northern hemisphere climate subsystems: the Westerlies and the Siberian High. Recent dust trajectory modelling study by Fitzsimmons et al (2020) suggest that the Westerlies and the Siberian high influenced Northerly winds are currently responsible for transporting dust to the piedmonts of the Ili basin (especially at our sites), implying multiple potential source areas, which may have changed dominance through time.

1.1. Sampling

A suite of 40 surface samples were collected from various depositional settings (floodplains, rivers, streams, alluvial plains, loess, dunefields) in the Ili basin of SE Kazakhstan during the field campaign in 2019. Two surface loess samples were also collected from sites PAN and ASH. The location of the different samples can be seen in Fig. D1. The sampling locations were chosen based on the potential dust source areas derived from the previously conducted dust trajectory modelling studies in the region (Fitzsimmons et al., 2020). These samples were collected from areas that were located away from agricultural or industrial influences to prevent contamination and potential mixing. All samples were processed under subdued red-light conditions (as done in the case of luminescence dating) at the Johannes Gutenberg University and the Max Planck Institute for Chemistry, Mainz.

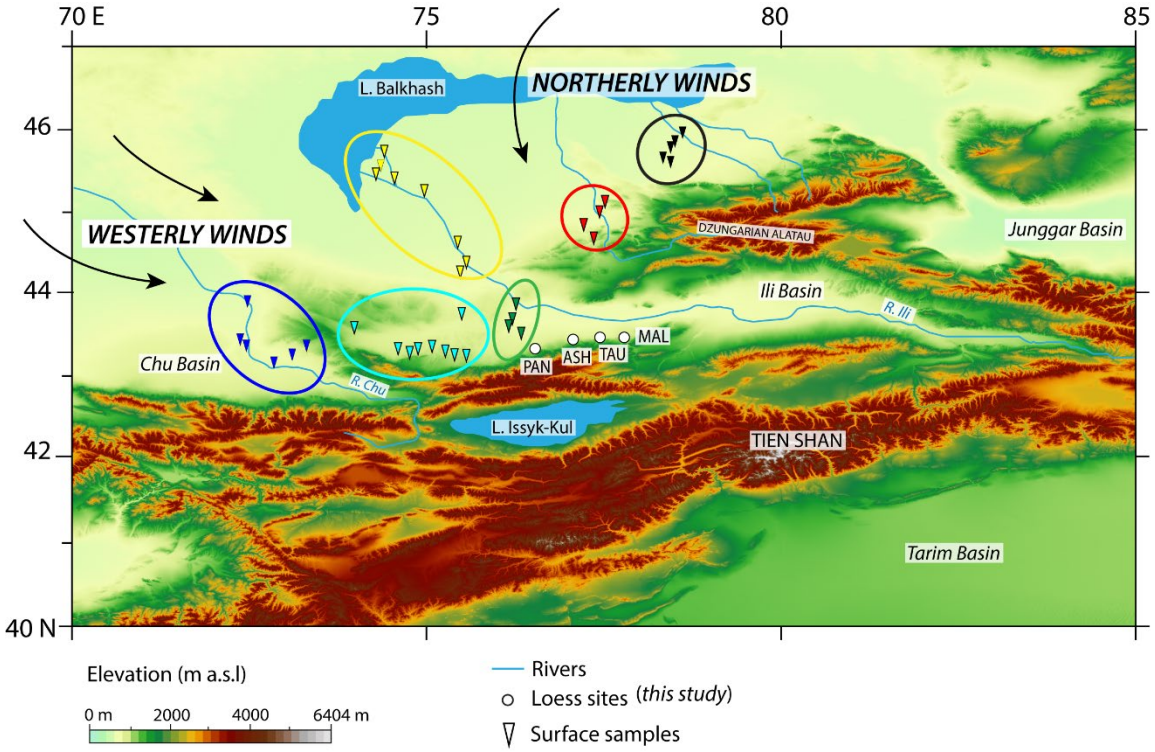

Fig. D1. Regional setting and location of samples investigated in this study. The coloured areas represent the samples from different drainage catchments within the Ili basin.

1.2. Material and Methods:

Sample preparation

40 sediment samples were processed according to established luminescence dating protocols to obtain quartz of three different grain sizes (4-11 µm, 63-90 µm and 90-212 µm; Frechen et al, 1996; Wintle, 1997). We note that not all samples yielded all the grain sizes in quantities required for purposes of Electron spin resonance (ESR) measurements (c.100-150 mg). The samples were wet sieved to obtain the three different grain size fractions (212-90 µm, 63-90 µm and <63 µm). The 63-90 µm and 90-212µm fractions were treated with 10% HCl and 10% H_2O_2 to remove carbonates and organics respectively. The pure quartz from these fractions was then separated by density separation (between 2.62-2.68 g/cm3) using Lithium polytungstate. Following which, pure quartz was obtained by etching the sample for 40 min in 40% hydrofluoric acid (HF). The <63 µm fraction was treated with 10% HCl followed by 10% H_2O_2 to remove carbonates and organics respectively. This was followed by treatment with 0.1 N sodium oxalate to remove clays. The samples were rinsed at least three to four times with distilled water between each of the aforementioned steps. The polymineral fine grain (4-11 µm) fraction was obtained from the chemically treated bulk fraction (<63 µm) by

settling using Stokes law. A portion of the polymineral 4-11 μm fraction was treated with 37% hexafluorosilicic acid (H_2SiF_6) for 7 days and consequently washed with 10% HCl (to remove fluoride precipitate) to obtain fine grain (4-11μm) quartz rich fraction. The etching of the fine grained polymineral fraction was performed at the Max Planck Institute for Evolutionary Anthropology at Leipzig, Germany.

Electron spin resonance (ESR) measurements

ESR investigations were carried out using an X band Bruker EMX Plus Spectrometer at the Babes Bolyai University, Cluj-Napoca, Romania. All measurements were made using a quartz glass tube filled by maintaining the same volume, with the mass of 100±4 mg (less than 5% variation) for fine grained quartz samples and a mass of 200±5 mg for all quartz samples > 63 μm. All ESR measurements were normalized to 100 mg for inter-comparison. Exposure of samples to sunlight was restricted to a minimum during measurements. In this study we measured two defect centres, the E' and peroxy centres for all the samples. In both cases, we measure the peak-to-peak amplitude of the ESR signal of the respective defect centre to quantify the variation in defect concentration. The peak-to-peak amplitude variation can be taken as a good approximation of the effective concentration of the defect centre in the sample (Chesnut, 1977). In case of E', the intensity of the signal was evaluated from peak-to-peak height of the signal with a baseline crossing at g=2.001. The intensity of the peroxy signal was quantified from the peak-to-peak height taken from g=2.003 to g=2.009 (Odom and Rink, 1989).

E' was recorded at room temperature at a modulation amplitude of 0.5 G, conversion time of 75.13 ms and a microwave power of 0.02 mW. Each data point for E' is an average of 3 repeat measurements, wherein each repeat measurement is an average of 6 scans with a sweep time of 30 s each. The peroxy defect was measured at room temperature with a modulation amplitude of 1 G, conversion time of 40.96 ms and at a microwave power of 10 mW. Each peroxy data point is an average of 3 repeat measurements, each of which is an average of 3 scans with a sweep time of 120s. The uncertainty in measurements in each sample is expressed as standard error.

1.3. Preliminary results and discussion

Fig. D2 shows the variation of natural E'and peroxy intensities in fine-grained (4-11 μm) and coarse grain quartz (212-90 μm) from surface samples, including fine grained quartz from surface (modern) loess samples from site PAN and ASH. In case of fine grain quartz (Fig. D2a), we observe that samples from the northern part (in black) are significantly different from the northwestern and western part of the Ili basin (for colour reference to sites, refer the map in Fig. D1). We also observe an overlap between samples from the west and northwest.

Comparison of the surface sediments with surface (modern) loess sample from PAN and ASH (Fig. D2a) suggests that modern (surface) loess at site PAN an ASH is most likely influenced by sediment sources located in west and north west, indicating a more dominant influence of dust transporting Westerly winds in the Ili basin in present times. This is in tune with the results obtained from dust transport models reconstructed by Fitzsimmons et al (2020) for piedmont loess sites in this region.

Fig. D2b shows the E' and peroxy intensity variations of coarse-grained (212-90 μm) quartz from surface samples. We observe a high degree of clustering of coarse grains compared to fine grains from the same catchment. This suggests that the coarse grains are more localised and are likely to reflect the signature of the catchment area. This observation corroborates with our understanding that coarse grains are unlikely to be transported over long distances by wind.

Fig. D3a compares the results of the fine grain quartz from surface sediments and modern (surface) loess at site PAN and ASH with loess dated to the past 20 ky at the same site. We observe that the quartz E'-peroxy signature from loess post 10 ka looks different from that dated to pre-10ka, and both look different from modern loess samples at the same site. On the other hand, Fig. D3b shows that loess dated to > 180 ka (refer Chapter 3 for luminescence dating results) from sites TAU and MAL (located c. 40-80 km west of PAN and ASH), mostly overlap with the signature of modern loess samples from PAN and ASH. This suggests a more dominant influence from sediment sources transported by the Westerlies more than > 180 ka, which may not have been the case during c. 5-18 ka. These results provide the first empirical evidence for change in source through time in loess deposits along the piedmonts of the Ili basin in SE Kazakhstan.

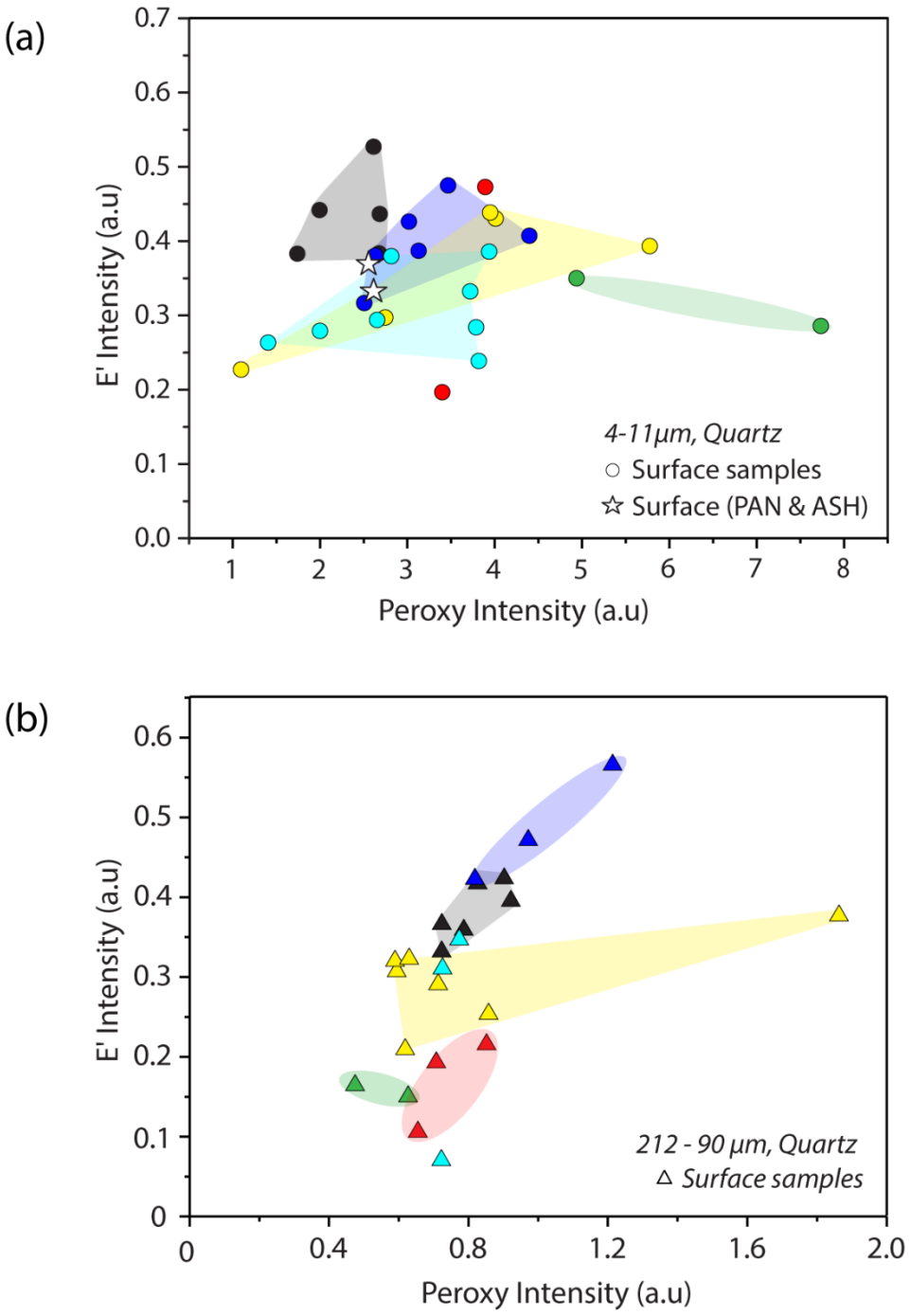

Fig. D2. Variation in natural E' and peroxy intensities in (a) fine grained quartz and (b) coarse grained quartz, extracted from surface sediments from various depositional settings across the Ili Basin of SE Kazakhstan.

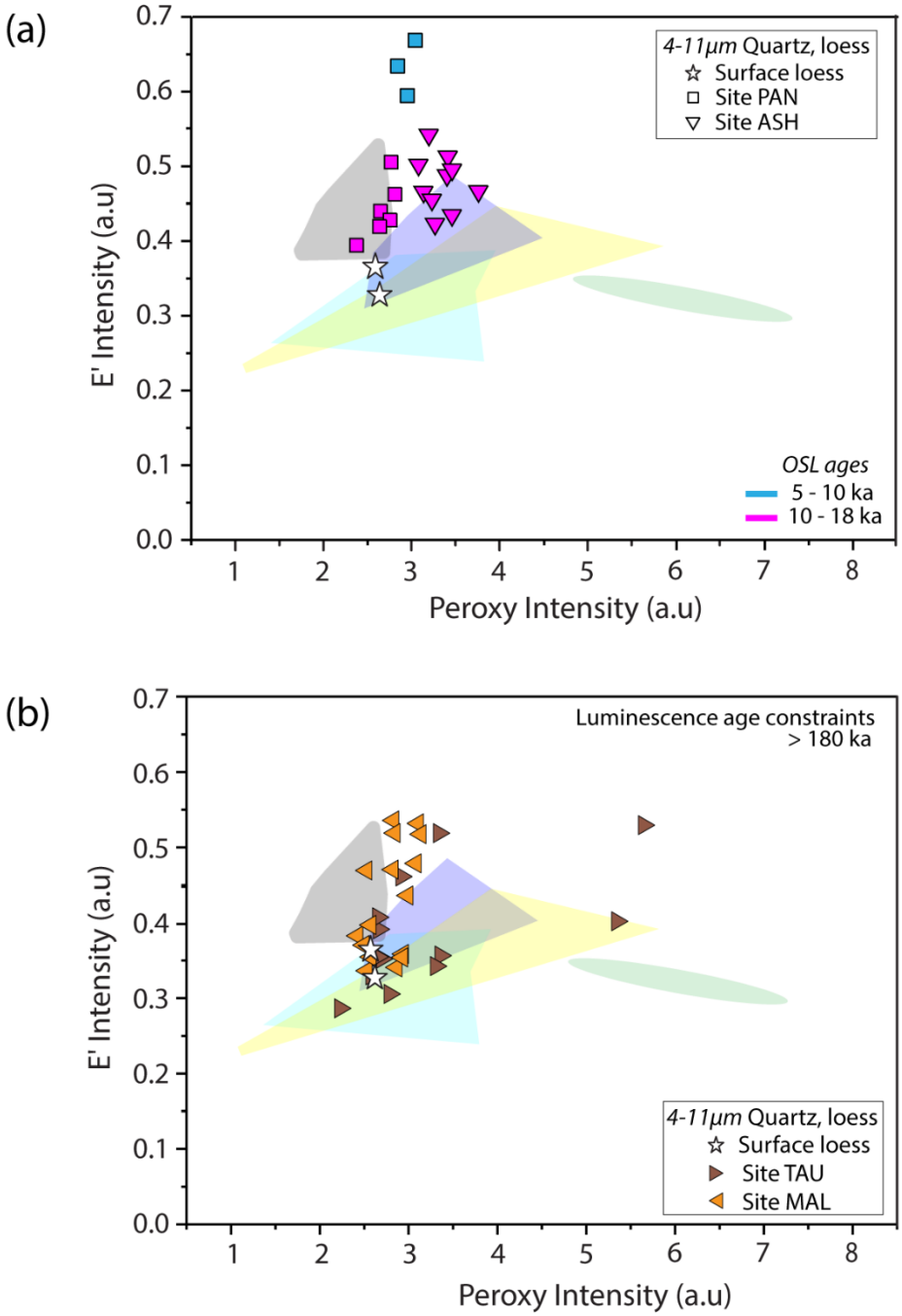

Fig. D3. Comparison of natural E' and peroxy intensities from fine grained surface sediments from different catchments areas within and around the Ili basin of SE Kazakhstan with, fine grained quartz from loess deposits dated between the mid-Holocene to beyond the last interglacial. The luminescence ages of the samples are obtained from Chapter 3.

2. Preliminary investigations on rocks

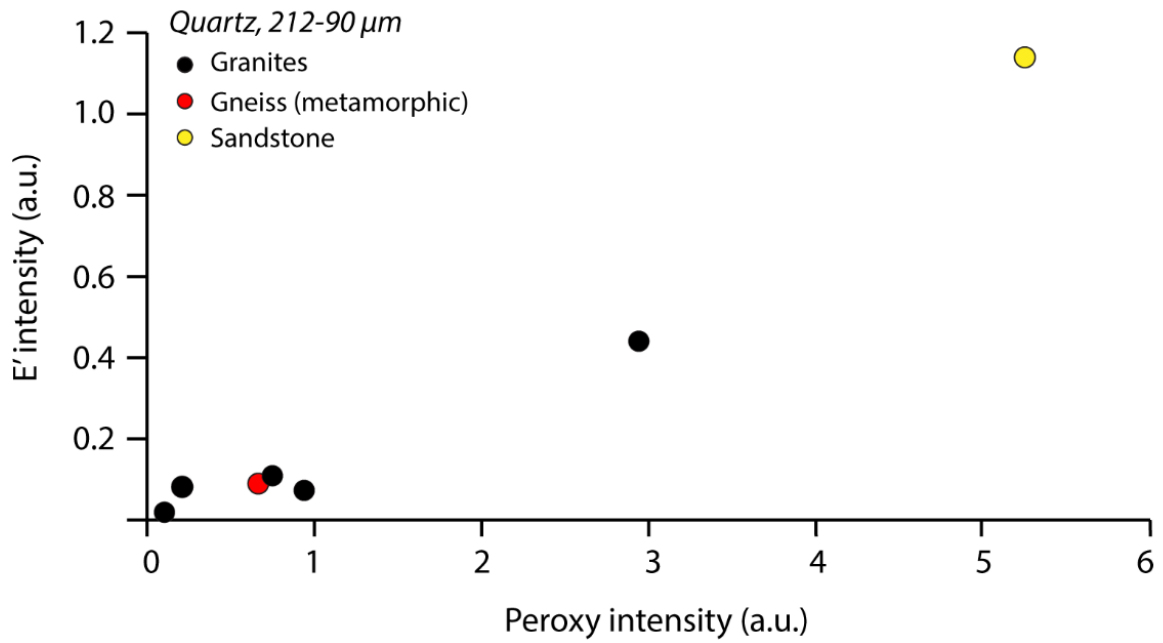

Fig. D4. Natural E' and peroxy intensity variations in 212-90 µm quartz extracted from rocks from the Tien Shan ranges surrounding the Ili basin of SE Kazkakhstan.

References

Chesnut, D. B. (1977). On the Use of the AW2 method for integrated line intensities from first-derivative presentations. Journal of Magnetic Resonance (1969), 25(2), 373–374. https://doi.org/10.1016/0022-2364(77)90032-4

Fitzsimmons, K. E., Nowatzki, M., Dave, A. K., & Harder, H. (2020). Intersections between wind regimes, topography and sediment supply: Perspectives from aeolian landforms in Central Asia. Palaeogeography, Palaeoclimatology, Palaeoecology, 540, 109531. https://doi.org/10.1016/j.palaeo.2019.109531

Frechen, M., Schweitzer, U., & Zander, A. (1996). Improvements in sample preparation for the fine grain technique. Ancient TL, 14(2), 15–17.

Odom, A. L., & Rink, W. J. (1989). Natural accumulation of Schottky-Frenkel defects: Implications for a quartz geochronometer. Geology, 17(1), 55–58. https://doi.org/10.1130/0091-7613(1988)017<0055:NAOSFD>2.3.CO;2

Wintle, A. G. (1997). Luminescence dating: Laboratory procedures and protocols. Radiation Measurements, 27(5), 769–817. https://doi.org/10.1016/S1350-4487(97)00220-5